UNIVERSITY OF CALIFORNIA

SANTA BARBARA

Traveling-wave Electroabsorption Modulators

By

Shengzhong Zhang

April 1999

A dissertation submitted in partial satisfaction
of the requirements for the degree of

Doctor of Philosophy

in

Electrical and Computer Engineering

Committee in Charge

Professor John E. Bowers, Chairperson
Professor Larry A. Coldren
Professor Nadir Dagli
Professor Evelyn L. Hu

The dissertation of Shengzhong Zhang is approved

Professor Larry A. Coldren

Professor Nadir Dagli

Professor Evelyn L. Hu

Professor John E. Bowers, Chairperson

April 1999

Traveling-wave Electroabsorption Modulators

April 1999

Department of Electrical and Computer Engineering
University of California, Santa Barbara
Santa Barbara, CA 93106

ACKNOWLEDEGMENTS

My studies at UCSB will be my most memorable days in my life, not only because of the beautiful place and the gorgeous weather, but also because of the wonderful experience I have had and the wonderful people I have met.

First of all, I am especially grateful to my adviser Professor John Bowers for his guidance and continuous support in the past years. I would also like to acknowledge my committee members, Professors Larry Coldren, Nadir Dagli, and Evelyn Hu for their helpful discussions and suggestions.

Dr. Radha Nagarajan brought me to the Ultrafast Optoelectronics group and deserves a special thank you. I learned a lot from him on the component and system performance of optical fiber communication systems.

I am especially indebted to Patrick Abraham and Yi-Jen Chiu for growing the high quality wafers for me. The very first wafer that I worked with was grown by Prashant Chavarkar. Without their work, this dissertation could not have been possible. I am also particularly grateful to Volkan Kaman for doing the tremendous work on the system measurements.

I am very grateful for all the help I received from the other people in UCSB as well. Yifeng Wu, Aaron Hawkins, Dan Tauber, Qinghong Li and Ernie Caine taught me how to use the RIE machines. Eva Strzelecka helped me to install the Ar source controller in RIE#1. Jack Ko, Yi-Jen Chiu and Ching-hui Chen showed me how to use the thermal and electron beam evaporators. Dan Cohen and Baki Acikel showed me on how to operate the SEM machine. Gerry Robinson, Beck Mason and Greg Fish are the process handbooks and they have full of tricks on making the process perfect. I am also grateful to the numerous help from other clean room folks. Among them were Bipul Agarwal, Yuliya Akulova, John Getty, James Guthrie, Syn-yem Hu, Yu-heng Jan, Thomas Liljeberg, Bin Liu, Rajasekhar Pullela, Naone Ryan and Kehl Sink. Many thanks to Jack Whaley, Bob Hill and Martin Vandenbroek for keeping the clean rooms working and for treating me well.

I am also very grateful to the people who helped me on the projects outside of the clean room. Tom Reynolds deserves special thanks for his help, friendship and dedication in maintaining everything well. Anders Peterson was my mentor on UNIX. Peter Blixt gave me initial directions on the system measurements. Mike Anzlowar designed the prototype package for my device. Siegfried Fleischer

helped me a huge amount on optical measurements. Lance Rushing taught me on how to write LabVIEW programs. I am grateful to Professor Dan Blumenthal for his help in the system measurements. I would like to thank Kirk Giboney for pioneering the traveling-wave theory in hybrid coplanar waveguide structures.

I cherish the friendship and numerous technical discussions with Yi-Jen Chiu and Bin Liu. Those good old days we spent together will always be a wonderful memory. I would like to thank as well all the other group mates and office mates for all their help and for all the pleasure to work with them. These group mates were Dubravoko Babic, Alexis Black, Pat Corvini, Xiaofeng Fan, Aaron Hawkins, Archie Holmes, Adil Karim, Adrian Keating, Chris LaBounty, Daniel Lasaosa, Thomas Liljeberg, Near Margalit, Rich Mirin, Jaochim Piprek, Maura Rabum, Rajeev Ram, Helen Reese, Ali Shakouri, Kehl Sink, Dan Tauber, Sufhosh Venkatesh, Gary Wang, Jon Wesselmann, Weishu Wu, Shanhua Xue, Gehong Zeng. The office mates from Professor Dan Blumental's group were Roopesh Doshi, Scott Humphries, Lavanya Rau, and Chris Scholz. I also appreciate the work by Vickie Edwards, Christina Loomis, Diana Thurman, and Kira Abrams in keeping things run as smoothly as possible.

And finally, many thanks to the clean-room friends for sharing the many quiet mid-night parties in the hated but also beloved yellow rooms. Good luck to all of you if you are still enjoying it.

VITA

September 1986 – July 1991	B. S. Electronic Engineering, Tsinghua University, Beijing, P. R. China
September 1991 – July 1994	M. S. Electronic Engineering, Tsinghua University, Beijing, P. R. China
July 1998 – September 1998	Technical Consultant, RSoft Inc., Ossining, New York
September 1994 -	Graduate Student Researcher, University of California, Santa Barbara

PUPLICATIONS

1. Sheng Z. Zhang, Volkan Kaman, Patrick Abraham, Yi-Jen Chiu, Adrian Keating, and John E. Bowers, "30 Gbit/s operation of a traveling-wave electroabsorption modulator," *Optical Fiber Communication Conference, OFC'99*, paper ThT3, San Diego, 1999.

2. Sheng Z. Zhang, Yi-Jen Chiu, Patrick Abraham, and John E. Bowers, "25 GHz polarization-insensitive electroabsorption modulators with traveling-wave electrodes," *Photon. Technol. Lett.,* vol.11, pp. 191-193, 1999.

3. Volkan Kaman, Sheng Z. Zhang, Adrian J. Keating, and John E. Bowers, "A 30 Gbit/s electrical TDM transmission system using a traveling-wave electroabsorption modulator," submitted to *Electron. Lett.*, 1999.

4. Joachim Piprek, Koichi Takiguchi, Alexis Black, Patrick Abraham, Adrian Keating, Volkan Kaman , Sheng Zhang, and John E. Bowers, "Analog Modulation of 1.55-micron Vertical-Cavity Lasers," *SPIE Proc. Vol. 3627*, "Vertical-Cavity Surface-Emitting Lasers III," eds. K. D. Choquette and C. Lei (1999), in press.

5. John E. Bowers, Sheng Z. Zhang, Patrick Abraham, Yi-Jen Chiu, and Volkan Kaman, "Low drive voltage, high speed traveling-wave electroabsorption modulators," Photonic Systems for Antenna Applications Symposium, PSAA-9, 1999.

6. Bin Liu, Ali Shakouri, P. Abraham, Y. J. Chiu, S. Zhang and John E. Bowers, "Fused InP-GaAs fused vertical coupler filters," *IEEE Photon. Technol. Lett.*, vol.11, pp.93-95, 1999.

7. S. Z. Zhang, Y. J. Chiu, P. Abraham and J. E. Bowers, "Polarization-insensitive multiple-quantum-well traveling-wave electroabsorption modulators with 18 GHz bandwidth and 1.2 V

driving voltage at 1.55 um," *IEEE Topical Meeting on Microwave Photonics*, Paper MC2, pp. 33-36, Princeton, New Jersey, 1998.

8. Yi-Jen Chiu, Sheng Z. Zhang, Siegfried B. Fleischer, John E. Bowers and Umesh K. Mishra, "1.55 um absorption, high speed, high saturation power, p-i-n photodetector using low-temperature grown GaAs," *IEEE Topical Meeting on Microwave Photonics*, Paper TuD3, Princeton, New Jersey, 1998.

9. K.D. Pedrotti, C.E. Chang, A. Price, S.M. Beccue, A.D. Campana, G. Gutierrez, D. Meeker, D. Wu, K.C. Wang, A. Metzger, P.M. Asbeck, D. Huff, N. Kwong, M. Swass, S.Z. Zhang and J. Bowers, "WEST 120-Gbit/s 3*3 wavelength-division multiplexed cross-connect," in *Tech. Dig. OFC'98*, pp. 66-67, 1998.

10. Syn-Yem Hu, S.Z. Zhang, J. Ko, J.E. Bowers and L.A. Coldren, "1.5 Gbit/s/channel operation of multiple-wavelength vertical-cavity photonic integrated emitter arrays for low-cost multimode WDM local-area networks," *Electron. Lett.*, vol.34, pp.768-770, 1998.

11. Yi-Jen Chiu, S.Z. Zhang, S.B. Fleischer, J.E. Bowers and U.K. Mishra, "GaAs-based, 1.55 mu m high speed, high saturation power, low-temperature grown GaAs p-i-n photodetector," *Electron. Lett.,* vol.34, pp.1253-1255, 1998.

12. Bin Liu, Ali Shakouri, P. Abraham, Y. J. Chiu, S. Zhang and John E. Bowers, “InP/GaAs fused vertical coupler filters,” in *Proc. LEOS '98*, pp.18-19, 1998.

13. Yi-Jen Chiu, Volkan Kaman, Sheng Z. Zhang, John E. Bowers and Umesh K. Mishra, “A novel 1.54 mm n-i-n photodetector based on low-temperature grown GaAs,” in *Proc. LEOS '98*, pp.155-156, 1998.

14. N.M. Margalit, S.Z. Zhang and J.E. Bowers, "Vertical cavity lasers for telecom applications," *IEEE Communications Magazine*, vol.35, pp.164-170, 1997.

15. S.Z. Zhang, N.M. Margalit, T.E. Reynolds and J.E. Bowers, "1.54- μm vertical-cavity surface-emitting laser transmission at 2.5 Gb/s," *IEEE Photon. Technol. Lett.,* vol.9, pp.374-376, 1997.

16. N.M. Margalit, J. Piprek, S. Zhang, D.I. Babic, K. Streubel, R.P. Mirin, J.R. Wesselmann and J.E. Bowers, "64 degrees C continuous-wave operation of 1.5- μm vertical-cavity laser," *IEEE J. of Selected Topics in Quantum Electronics*, vol.3, pp.359-365, 1997.

17. S.Z. Zhang, N.M. Margalit, T.E. Reynolds and J.E. Bowers, "1.54- μm vertical-cavity surface-emitting laser transmission at 2.5 Gb/s," *OSA Trends in Optics and Photonics (Vol. 12): System Technologies*, Alan E. Willner and Curtis R. Menyuk, ed., pp. 314-317, 1997.

18. S.Z. Zhang, N.M. Margalit, T.E. Reynolds and J.E. Bowers, "1.54- μm vertical-cavity laser transmission at 2.5 Gbit/s," *Tech. Dig. OFC'97*, paper TuD2, pp.11-12, 1997.

19. D. Huff, T. Schrans, K.C. Wang, K. Pedrotti, A. Price, D. Wu, J. Bowers, Sheng Zhang, P. Asbeck and A. Metzger, "WEST (WDM and electronic switching technology) project: 40 Gbit/s WDM system review," in *Proc. SPIE*, vol.3038, pp.60-66, 1997.

20. C.E. Chang, K.D. Pedrotti, A. Price, A.D. Campana, D. Meeker, S.M. Beccue, D. Wu, K.C. Wang, A. Metzger, P.M. Asbeck, D. Huff, N. Kwong, M. Swass, S.Z. Zhang and J. Bowers, "40 Gb/s WDM cross-connect with an electronic switching core: preliminary results from the WEST Consortium," in *Proc. LEOS '97*, pp.336-337, 1997.

21. S.Z. Zhang, N.M. Margalit, T.E. Reynolds and J.E. Bowers, "1.55 μm vertical cavity laser transmission over 200 km at 622 Mbit/s," *Electron. Lett.,* vol.32, pp.1597-1599, 1996.

22. N.M. Margalit, D.I. Babic, K. Streubel, R.P. Mirin, D.E. Mars, Sheng Zhang, J.E. Bowers and E.L. Hu, "Laterally oxidized long wavelength CW vertical-cavity lasers," in *Tech. Dig. OFC'96*, post deadline paper PD10, 1996.

23. S. Zhang, R. Nagarajan, A. Petersen and J. Bowers, "40 Gbit/s fiber optic transmission systems: are solitons needed?" in *Proc. SPIE*, vol.2684, pp.182-185, 1996.

24. Yi Luo, Weimin Si, Shengzhong Zhang, Di Chen and Jianhua Wang, "Fabrication of GaAlAs/GaAs gain-coupled distributed feedback lasers using the nature of MBE," *IEEE Photon. Technol. Lett.*, vol.6, pp.17-20, 1994.

25. Luo Yi, Zhang Shengzhong, Si Weimin, Chen Di, and Wang Jianhua, "A novel fabrication technique for GaAlAs/GaAs distributed feedback lasers based on molecular beam epitaxy," *Chinese Journal of Semiconductors*, vol.15, pp.694-699, 1994.

26. Luo Yi, Si Weimin, Zhang Shengzhong, Chen Di, Wang Jianhua and Pu Rui, "GaAlAs/GaAs multiquantum well gain-coupled distributed feedback lasers with absorptive gratings all grown by MBE," *Chinese Journal of Semiconductors*, vol.15, pp.139-144, 1994.

ABSTRACT

Traveling-wave Electroabsorption Modulators

by

Shengzhong Zhang

The transmission bit rates in backbone telecommunication optical fibers are increasing rapidly, motivated by the explosive growth of Internet traffic. As the channel bit rate – distance product increases, external modulation of the laser light is necessary to avoid the unacceptably high chirping of directly modulated lasers and to overcome the dispersion of standard single mode fiber.

$LiNbO_3$ electro-optic modulators are currently widely used in low bit-rate applications. However, the high drive voltage requirement for these modulators becomes a big problem at high bit rates. On the other hand, electroabsorption (EA) modulators based on quantum confined Stark effect in multiple quantum wells (MQWs) are advantageous for their high speed, low drive voltage, high extinction ratio and integratibility with lasers. Currently, EA modulators use lumped electrode structures, which limit the device bandwidth by the RC time constant and require a short device length for high speed operation.

This thesis proposes a traveling-wave electrode structure for 1.55 μm EA modulators to overcome the RC limitation in lumped devices, and therefore makes it possible to achieve high bandwidths with longer device lengths and lower drive voltages. This structure has been demonstrated to improve the bandwidth of the device. An InGaAsP/InGaAsP MQW traveling-wave EA modulator with a bandwidth of 25 GHz and a drive voltage of 1.2 V for an extinction ratio of 20-dB has been demonstrated. Successful transmission experiments at 10 Gbit/s and 30 Gbit/s have for the first time shown promising system performance with these devices. This is also the first electrical time division multiplexing system ever been demonstrated by a university to operate over 20 Gbit/s. We present here the design, fabrication and characterization of these devices.

CONTENTS

CHAPTER 1

Introduction

1.1 External modulators for fiber-optic communications

In recent years, the optical fiber communication networks are experiencing a rapid growth, driven by the explosive growth of Internet data traffic and voice traffic. In order to best utilize the enormous capacity of the optical fiber, intensity modulation direct detection (IMDD) systems with time division multiplexing (TDM) and/or wavelength division multiplexing (WDM) are widely used. In TDM systems, the low bit-rate baseband signals are multiplexed in time to a single-wavelength high bit-rate signal; while in WDM systems, the signals are multiplexed in the wavelength domain such that there are more than one wavelength in a single fiber.

Currently, WDM systems with each channel bit rate of 2.5 Gbit/s are commercially available. For better frequency efficiency, dense wavelength division multiplexing (DWDM) are deployed, in which the channel spacing is reduced to 50 ~ 100 GHz. This will, however, still lose large amount of the optical bandwidth, and require ultra-stable wavelength control on lasers and optical filters that demultiplex the signal. On the other hand, TDM systems have much loose requirements on the wavelength stability of the laser and have higher bandwidth efficiency. One solution is to incorporate TDM into WDM channel by increasing the bit rate of each WDM channel. WDM systems with single channel bit rate of 10 Gbit/s are under commercial development, while systems with single channel bit rates even higher are attracting research interest. Over terabit per second transmission capacities have been demonstrated in the lab with multiple wavelengths at channel bit rates of 10Gbit/s [1], 20 Gbit/s [2-5], 160 GHz [6], 200 GHz [7]. Therefore, the development of high-speed TDM systems will be the basis for future WDM systems.

TDM systems with single channel bit rate of 400 Gbit/s [8] have been demonstrated. The multiplexing of these signals is done in the optical domain and it is called OTDM – optical time division multiplexing, which is achieved by

delaying each baseband optical channel and then combining them together. For optical multiplexing, mode-locked laser sources are used. This return-to-zero (RZ) signal has a drawback in that it will require double of the frequency bandwidth of the non-return-to-zero (NRZ) signal. It also has problems relating to mode-locked source generating, optical multiplexing and demultiplexing.

The counterpart of optical TDM is electrical TDM, in which the multiplexing of baseband signal is done in the electrical domain. In this case, the ultra-high speed electrical signals are directly applied onto the optical coding devices, such as lasers and modulators. This system has the advantage that it has the highest frequency efficiency, and can take the advantages of electronics. Electrical TDM systems have demonstrated operations at 40 Gbit/s [9-13]. The key elements for such an electrically multiplexed TDM system include the high-speed circuitry for signal generation, amplification, synchronization, and demultiplexing [14], and high-speed optical coding devices.

The laser light can either be directly modulated or externally modulated. For direction modulation, the modulation electrical signal is directly applied onto the laser; while for external modulation, the laser operates continuously and a modulator is used to modulate the light.

The highest 3-dB bandwidth of a directly modulated laser reported to date is 48 GHz [15] at a wavelength of 0.98 μm. The highest bandwidth of a 1.55-μm laser reported to date is 30 GHz [16]. These bandwidths are large enough for a system with channel speed as high as 40 Gbit/s; however, the biggest problem for a directly modulated laser is its frequency chirping, which represents itself as wavelength (frequency) variation between on and off states [17-20]. Due to this wavelength variation, the optical pulse will have an extra broadening effect when transmitting through a dispersive fiber, hence degrade the system performance.

Frequency chirping also exists in light modulated with external modulators [21] due to the Kramers-Kronig relations [22] between the real and the imaginary parts of the dielectric constant, which is also the reason for frequency chirping in lasers.

Fig. 1.1 shows the predicted transmission capacity for standard single mode fiber, defined as the bit rate (B) square and length (L) product, as a function of the

chirp parameter [23]. Here non-return to zero signal is assumed. The chirp parameter, α, also called linewidth enhancement factor, is defined as [21]

$$\alpha = \frac{\partial n}{\partial k},$$

where, n and k are, respectively, the real and imaginary parts of the modal index of the electroabsorption waveguide.

From Fig.1.1, we can see that the transmission capacity degrades rapidly as α increases for positive chirp [23]. A maximum capacity is predicted with a slightly negative chirp parameter, due to the constructive interplay between the negative chirp and the positive dispersion [24]. The chirp parameter is typically between 4-6 for semiconductor lasers [25], while it can be as low as zero or be negative for external modulators [21, 23, 26, 27]. Therefore, the transmission distance can be greatly increased with external modulators. This is the main reason for using external modulation rather than direct modulation in high-speed long-haul transmission systems.

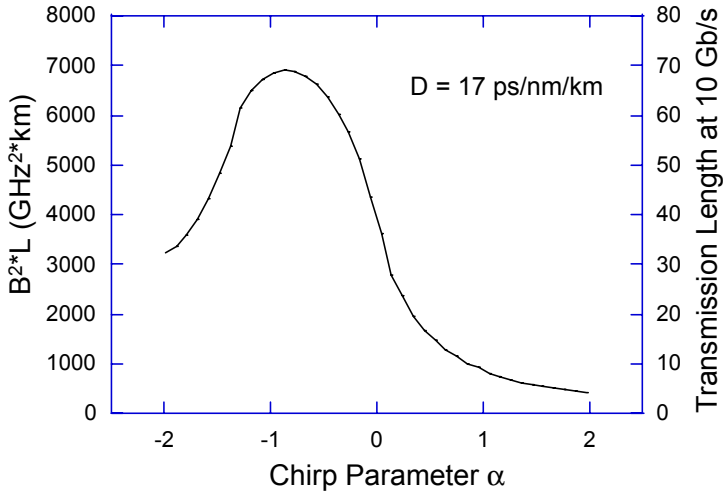

Fig. 1.1 Transmission capacity as a function of the chirp parameter. The right axis shows the possible transmission length at 10 Gb/s, after reference [23].

1.2 Electroabsorption vs. electro-optic modulators

In terms of operation mechanism, there are generally two types external modulators, electro-optic (EO) and electroabsorption (EA) modulators.

Electro-optic modulators are based on linear electro-optic effect, which is defined as the change of material refraction index under the presence of an electric field. By modulating the electric field, the optical phase is modulated, therefore making a phase modulator [28] or an intensity modulator in a Mach-Zehnder interferometer configuration. The latter is widely used for making electro-optic intensity modulators and they are usually made with traveling-wave electrode structures in order to achieve high-speed operation [29].

Electroabsorption modulators are based on electroabsorption effect, which is defined as the change of material absorption in the presence of an electric field. It is called the Franz-Keldysh effect in bulk materials [30, 31] and Quantum Confined Stark Effect (QCSE) in quantum-well materials [32, 33]. The QCSE type has much higher modulation efficiency and attracts much research and commercial interest.

In order to compare the performance of different modulators, we use a figure of merit similar to the one proposed by Walker [29] as

$$FOM = \frac{2Z_{in}}{50 + Z_{in}} \cdot \frac{f_{3dBe}}{V_{20dB}} \cdot \frac{\lambda}{\lambda_0}$$

where

Z_{in} is the characteristic impedance looking into the modulator (in Ω),

f_{3dBe} is the electrical 3-dB bandwidth of the modulator (in GHz),

V_{20dB} is the drive voltage for the electroabsorption modulators, and half wave phase shift voltage for electro-optic modulators (in V),

λ is the operation wavelength, and $\lambda_0 = 1.55$ μm.

Since we are mostly considering modulators operating around wavelength of 1.55 μm, the figure of merit is normalized to this wavelength.

Material systems that have been used for making traveling-wave electro-optic modulators include: $LiNbO_3$ [34-40], GaAs/AlGaAs [29, 41-44], InGaAsP/ InP [45-47], InGaAlAs/InAlAs [48], and polymer [49-53].

Table 1.1 summarizes the performance of these electro-optic modulators.

$LiNbO_3$ modulators are among all kinds of modulators the most widely commercialized modulators. Optical 3-dB bandwidth as high as 75 GHz has been demonstrated [38]; however, the highest electrical 3-dB bandwidth is 40 GHz [38, 40]. The lowest drive voltage is 2.9 V [39]. The drawback of this type of modulator is the bias point sensitivity to temperature and it is not suitable to integrate with driving circuitry or lasers. The drive voltage of $LiNbO_3$ modulator (2.9 ~ 5 V) is generally higher than that of the electroabsorption modulator (1.2 ~ 3.3 V).

GaAs/AlGaAs modulators have the advantages in possibility to integrate with driving circuitry or a laser source, and easier to obtain optical and electrical wave velocity match. These modulators usually use bulk materials and have thick intrinsic layer [54]. However, due to the small electro-optic coefficient, these modulators usually require long interaction region and the drive voltages for these modulators are very high, making it hard to use in communication systems.

Other than GaAs/AlGaAs modulators that operate at wavelength far away from the bandgap energy, InGaAsP/InP and InGaAlAs/InAlAs MQW Mach-Zehder electrooptic modulators have bandgap energies close to the photon energy. These modulators use multiple quantum well structures and have thin intrinsic layers, therefore have a larger electric field. Due to Kramers-Kronig relations [22], the electric field-induced index change is enhanced when close to bandgap. Also, quantum confined Stark effect will further reduce the drive voltage. These devices can be made with an order of magnitude shorter than the GaAs/AlGaAs devices, and have been demonstrated with reasonably low drive voltages. InGaAsP/InP MQW EO modulators have been integrated with long-wavelength lasers and transmission experiments have shown promising performance [47].

Material System	Ref.	V_π (V)	f_{3dBe} (GHz)	ER_{max} (dB)	FOM (GHz/V)	Comments
$LiNbO_3$						
Kawano, 1989	[34]	4.7	10		2.13	
Gopalakrishnan, 1992	[35]	5.0	15		3	
Dolfi, 1992	[36]	12.3	44		3.58	
Rangaraj, 1992	[37]	5.0	10		2.0	
Noguchi, 1994	[38]	5.0	40	22	8	f_{3dBo}=75 GHz
Noguchi, 1998	[39]	2.9	30		10.3	
Mitomi, 1998	[40]	3	40		13.3	
GaAs/AlGaAs						
Wang, 1988	[41]	11	16	13	1.22	λ=1.3 μm
Walker, 1991	[29]	4.25	22.5		3.93	λ=1.15 μm
Spickermann, 1996	[42]	14	>40		>2.86	
Spickermann, 1996	[43]				6.45	
Khazaei, 1998	[44]	20.5	22	9.5	1.07	
InGaAsP/InP, MQW						
Agrawal, 1995	[45]	6.8	14	19	2.1	(1)
Fetterman, 1996	[46]	6.0				L=300 μm
Rolland, 1998	[47]	~4.0	~10	16		(2)
Rolland, 1998	[47]	~2.6	~2.5			(3)
InGaAlAs/InAlAs, MQW						
Wakita, 1992	[48]	3.8	20	20	5.3	L=300 μm
Polymer						
Van Schooti, 1996	[49]	7.5	20	20	2.7	L=2 cm
Lee, 1997	[50]	4.85				L=1.5 cm
Ermer, 1997	[51]	3.5				L=2.6 cm
Chen, 1997	[52]					(4)
Chen, 1999	[53]	<10	f_{3dbo} 40			

Table 1.1 Summary of electro-optic Mach-Zehnder modulators. Unless specified, the operation wavelength is 1.55 μm.

Note: (1) 7.2 dB optical propagation loss, L=500 μm

(2) 10 Gb/s, L=500 μm, 105 km SMF transmission demonstrated with V_{pp}=4 V

(3) 2.5 Gb/s L=1200 μm, 825 km SMF transmission demonstrated with V_{pp}=2.6 V

(4) λ=1.3 μm, less than 3 dB (optical) drop within 75 ~ 113 GHz range.

Material System	Ref.	V_{20dB} (V)	f_{3dBe} (GHz)	L_{active} (μm)	ER_{max} (dB)	Electrode Structure	FOM (GHz/V)	Note
InGaAs/InAlAs								
Wakita, 1987	[55]	2.0		120-180	20	Lumped		
Kotaka, 1991	[56]	2.0	16.2	100	21	Lumped	8.1	
Devaux, 1995	[57]	2.4	42	75	30	Lumped	17.5	
Wakita, 1995	[58]	1.5	22	200	41	Lumped	14.7	
Yoshino, 1996	[59]	2.3	40	100	32	Lumped	17.4	
Satzke, 1995	[60]	2.5@ 16dB	42	120	16	Lumped		
Ido, 1996	[61]	3.3	50	63	25	Regrowth	15.15	
Ido, 1996	[61]	2.6	27	100	>22	Regrowth	10.38	
Ido, 1996	[61]	2.25	21	150	>32	Regrowth	9.33	
Heinzelmann, 1996	[62]	10@ 19dB	70	1.0 mm	21	TW	5.87	n-i-n λ=1.3μm
InGaAlAs/InAlAs								
Kotaka, 1989	[63]	6@19 dB	>20	100	18.6	Lumped	3.33	
Wakita, 1990	[64]	6.0	25	90-120	25	Lumped	4.17	
Kawano, 1997	[65]	2.1	13	200	35	TW	6.19	f_{3dBo} = 50 GHz
InGaAs/InGaAlAs								
Mihailidi, 1995	[66]					TW		(1)
Devaux, 1997	[67]	1.5	20	145	28	Lumped	13.33	Spiked QW
InAsP/InGaP								
Liao, 1997	[68]					TW		(2)
InGaAsP/ InGaAsP								
Devaux, 1993	[69]	1.7	27	100	26	Lumped	15.43	
This work, 1999	[70]	1.2	25	300	50	TW	17.2	Z_{in}=35 Ω

Table 1.2 Summary of quantum well electroabsorption modulators. Unless specified, the operation wavelength is 1.55 μm. TW: traveling-wave structure, ER_{max}: maximum extinction ratio.

Note: (1) No optical response was reported. Microwave loss was 7.3 $dBcm^{-1}$ $GHz^{-1/2}$ for a ridge width of 3.9 μm and an intrinsic layer thickness of 0.787 μm.

(2) λ=1.3μm, no optical response was reported, microwave loss was 5.6 dB/mm @ 40 GHz for a ridge width of 3.0 μm and an intrinsic layer thickness of 0.9 μm.

Polymer materials are attracting increasing interest for their low dispersion, fast electronic response, and suitability for large-scale product manufacturing. Modulators made of polymer have demonstrated less than 3-dB (optical) drop within the whole W band (75 ~ 110 GHz). However, these modulators usually require large drive voltage. The performance is still far from practical use for ultra-high speed fiber optic communications.

Material systems that have been used for making quantum well electroabsorption modulators include: InGaAs/InAlAs [55-62], InGaAlAs/InAlAs [63-65], InGaAs/InGaAlAs [66, 67], InAsP/InGaP [68], and InGaAsP/InGaAsP [69, 70].

Table 1.2 summarizes the performance of these quantum well electro-absorption modulators.

Compared to EO modulators, EA modulators have generally lower drive voltages (1.2 ~ 3.3 V), higher figure of merits and larger maximum extinction ratios. The highest 3-dBe bandwidth reported for EA modulators is 50 GHz. Furthermore, compared to $LiNbO_3$ modulators, III-V EA modulators have another freedom in that they can be monolithically integrated with driver circuitry and/or laser sources.

Most of the EA modulators reported are lumped devices. These devices are typically shorter than 200 μm. For ultra-high speed operation, the devices are as short as 63~75 μm to reduce capacitance [57, 61]. However it is difficult to fabricate such a short device, and cleaving length restricts the minimum device length and hence the modulation speed. Furthermore, such a short device is hard to package because microwave strip lines as well as the optical components must be assembled close to the device. In order to achieve this ultra-short length, passive waveguides were grown to make the whole device long enough to handle [61]. This therefore complicates the fabrication process. Another drawback for these short active region devices is that the maximum extinction ratio is lower and the drive voltage is higher compared to longer devices.

In order to achieve both high speed and low drive-voltage operation traveling-wave electrode structures have been attracting research interest. Among the four traveling-wave electroabsorption modulators (TEAMs) reported by other

groups, three of them were using thick intrinsic regions [62, 66, 68]. These modulators have very low electroabsorption efficiencies due to low electric field and only one of them reported EO response, but with a drive voltage as high as 10.0 V and a maximum extinction ratio of only 18.5 dB. Kawano et al [65] reported a 200-μm long traveling-wave device with thin active region. This device revealed an optical bandwidth of 50 GHz; however, the electrical bandwidth was only 13 GHz. In order to have longer device length for making the feed lines, passive waveguides were grown outside of the active region. This, however, complicates the fabrication process.

As will be shown throughout this thesis, we have successfully demonstrated traveling-wave EA modulators with both high speed (f_{3dBe}=25 GHz) and low drive voltages (V_{10dB}=0.8 V, V_{20dB}=1.2V), yielding to a figure of merit as high as the best ever reported. Transmission experiments were demonstrated at 10 Gbit/s and 30 Gbit/s for the first time for any traveling-wave EA modulators. This is also the first electrical TDM experiment over 20 Gb/s ever been demonstrated by a university (Table 1.3).

Fig. 1.2 shows the figure of merit for different types of modulators.

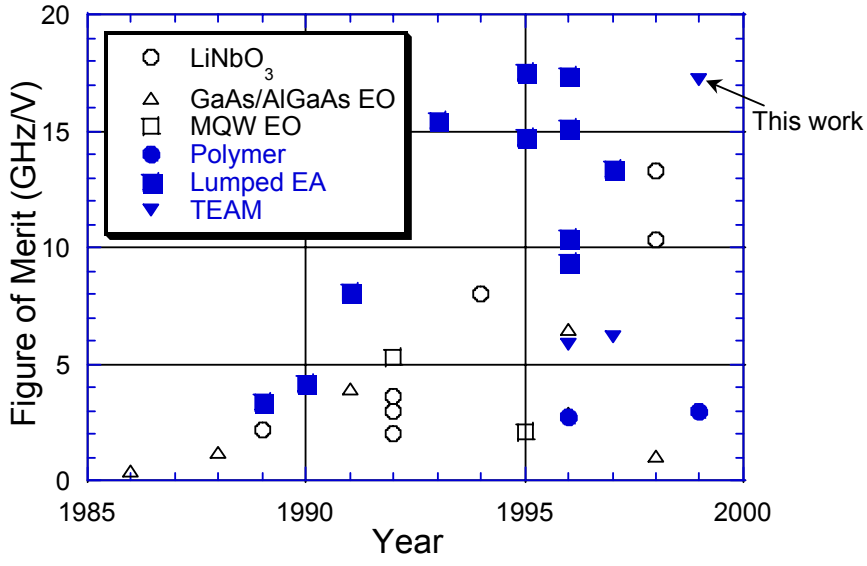

Fig. 1.2 Figure of merit of modulators. Data are listed in Tables 1.1 and 1.2.

Table 1.3 shows the electrical TDM transmission experiments ever demonstrated with single channel bit-rate over 20 Gbit/s. The highest single channel bit rate ever demonstrated is 40 Gbit/s. As we can see from the table, both electroabsorption and $LiNbO_3$ modulators have been demonstrated in the transmission experiments; however, $LiNbO_3$ modulators generally require higher driving voltages. This is the main reason for us to choose EA modulators for making low drive voltage, high speed intensity modulators.

Company	Single carrier bit-rate (Gb/s)	# of channels	Mod. type	Mod. f_{3dBe} (GHz)	Modulator drive V_{pp} (V)	Laser Source	Year
NTT[9]	40	4	EA	30	2.0	DFB-CW	1996
NTT[10]	40	1	LN			Mode-locked	1997
NTT[11]	40	1	EA		3.0	DFB+EA	1997
Siemens AG[12]	40	1	LN	20	7.0 (V_π = 5.0V)	DFB-CW	1997
NTT[13]	40	4	LN	30	5.0 (V_π = 3.9V)	DFB-CW	1998
This work [71]	30	1	EA	25	1.6	DFB-CW	1999

Table 1.3 Electrical TDM transmission experiments ever demonstrated with single carrier bit rate over 20 Gbit/s. EA: electroabsorption modulator; LN: $LiNbO_3$ modulator; DFB-CW: DFB laser CW operation, with external modulator; DFB+EA: DFB laser monolithic with EA modulator; Mode-locked: mode-locked laser.

1.3 Traveling-wave vs. lumped EA modulators

As a comparison, Fig. 1.3 shows the schematic device structures of lumped and traveling-wave electroabsorption modulators.

In the lumped electrode configuration, the microwave signal is applied from the center of the optical waveguide; therefore, the microwave signal will experience strong reflections from two ends of the waveguide. As a result of this, the device performs as a lumped element and the intrinsic speed of the device is limited by the total RC time constant. In practice, a parallel 50 Ω load is usually used to reduce microwave reflection back to the driver. The modulator itself can be modeled as a junction capacitance (C_i) series with a differential resistance (R_d). These are then

parallel with the contact pad capacitance (C_p). Fig. 1.4 (a) shows the circuit model of lumped EA modulators. Here the inductors from the bonding wires are also included. Because the speed of the device is limited by the total parasitics, the device has to be short in order to achieve high speed (Table 1.2). This will therefore make the device difficult to handle and package, potentially increase the drive voltage and reduce the saturation power.

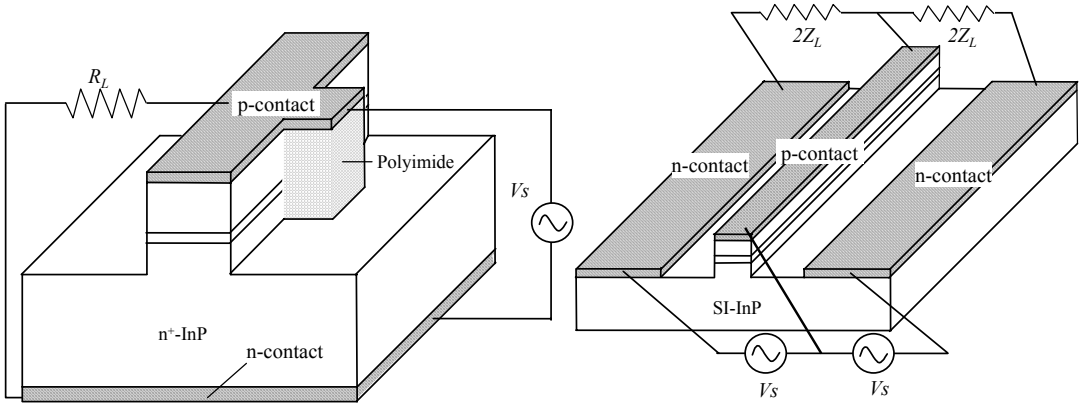

Fig. 1.3 Structures of (left) lumped and (right) traveling-wave electroabsorption modulators.

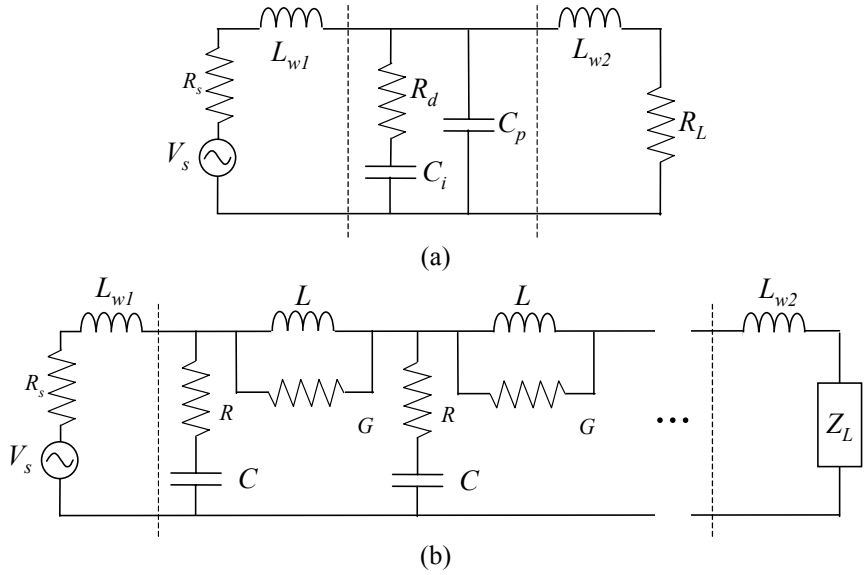

Fig. 1.4 Circuit models for (a) lumped (b) traveling-wave EA modulators.

On the other hand, in a traveling-wave electrode configuration, the microwave signal is applied from one end of the optical waveguide and it co-propagates with the optical signal. At the output end of the waveguide, the microwave signal is terminated with a matching load such that there is little reflection from this end. In this case, the microwave signal will only see distributed parasitics (Fig. 1.4 (b)); therefore overcome the RC limitation as exists in lumped devices and the device should have higher speed. We can also make the device longer yet still achieve the same speed requirement as for the lumped devices. This therefore will reduce the drive voltage. With longer device, we can increase the saturation power because the optical confinement factor can be smaller yet still achieve enough extinction ratio.

It will be discussed in chapter 3 that in our traveling-wave EA modulators, the velocity mismatch is not the speed-limiting factor because of the short interaction length. The central concept is to eliminate microwave reflection at the load end to overcome RC limitation. In these devices, the speed-limiting factor will be the microwave loss at high frequencies, which includes propagation loss and source port reflection loss. Because of waveguide dispersion, high frequency components will experience smaller characteristic impedance and hence higher reflection loss when launched from a 50 Ω driver.

1.4 Other applications

So far we have discussed the applications of EA modulators as high-speed transmitters for telecommunication systems [9, 11]. The devices are also suitable for other applications, such as short optical pulse generation [72-74], pulse encoding [74], pulse retiming [75], and optical demultiplexing in OTDM [75, 76] and/or soliton transmission systems [75]. Owing to their low drive voltage requirement and high modulation efficiency, they are also well suited for antenna remoting and active phase array applications [77, 78].

1.5 Outline of the thesis

The objective of this thesis is to make high-speed low drive voltage TEAMs for fiber optic communication applications.

In chapter 2, the design of the material and optical waveguide structures for achieving polarization insensitivity and low drive voltage operation will be discussed. The coupling efficiency to the single mode optical fiber will also be discussed.

In chapter 3, equivalent circuit model of TEAMs is presented. Based on the equivalent circuit model, design rules for achieving low microwave loss are giving. Optimum material and device structure parameters are determined based on the overall electrical-to-electrical and electrical-to-optical responses.

Chapter 4 discusses the fabrication and measurement results of the first generation devices, which were made of MBE grown InGaAs/InAlAs materials. A 3-dBe bandwidth of 12 GHz and a 20-dB extinction-ratio drive voltage of 2.7 V were achieved. The main reason for limiting the device speed is discussed.

Chapter 5 discusses the fabrication and measurement results of the second generation devices, which were made of MOCVD grown InGaAsP/InGaAsP materials. Polarization-insensitivity, a 20-dB extinction-ratio drive voltage of 1.2 V and a 3-dBe bandwidth of 24.7 GHz were achieved, yielding to a figure of merit among the best ever reported. Measurement results support the theory presented in Chapter 3. Traveling-wave electrode structure was verified to improve the device speed.

Chapter 6 presents 10 Gbit/s and 30 Gbit/s electrical TDM transmission experiments with the second generation devices.

Chapter 7 is the summary and future work.

Appendices A-F are arranged as follows:

Appendix A: resonant scattering method for quantum well level calculation

Appendix B: polarization-independent InGaAsP/InGaAsP quantum well design

Appendix C: coplanar waveguide circuit element calculation

Appendix D: transmission matrix calculation

Appendix E: measurement configurations

Appendix F: device fabrication processes

References

[1] T. Morioka, H. Takara, S. Kawanishi, O. Kamatani, K. Takiguchi, K. Uchiyama, M. Saruwatari, H. Takahashi, M. Yamada, T. Kanamori, and H. Ono, "100 Gbit/s*10 channel OTDM/WDM transmission using a single supercontinuum WDM source," *OSA OFC'96*, San Jose, CA, pp. 411-414, 1996.

[2] H. Onaka, H. Miyata, G. Ishikawa, K. Otsuka, H. Ooi, Y. Kai, S. Kinoshita, M. Seino, H. Nishimoto, and T. Chikama, "1.1 Tb/s WDM transmission over a 150 km 1.3 μm zero-dispersion single-mode fiber," *OSA OFC'96*, San Jose, CA, pp.403-406, 1996.

[3] A. R. Chraplyvy, A. H. Gnauck, R. W. Tkach, J. L. Zyskind, J. W. Sulhoff, A. J. Lucero, Y. Sun, R. M. Jopson, F. Forghieri, R. M. Derosier, C. Wolf, and A. R. McCormick, "1-Tb/s transmission experiment," *IEEE Photonics Technol. Lett.*, vol. 8, pp. 1264-1266, 1996.

[4] Y. Yano, T. Ono, K. Fukuchi, T. Ito, H. Yamazaki, M. Yamaguchi, and K. Emura, "2.6 terabit/s WDM transmission experiment using optical duobinary coding," *ECOC'96*, Oslo, Norway, pp. 3-6 vol. 5, 1996.

[5] S. Aisawa, T. Sakamoto, M. Fukui, J. Kani, M. Jinno, and K. Oguchi, "Ultra-wideband, long distance WDM demonstration of 1 Tbit/s (50*20 Gbit/s), 600 km transmission using 1550 and 1580 nm wavelength bands," *Electron. Lett.*, vol. 34, pp. 1127-1129, 1998.

[6] S. Kawanishi, H. Takara, K. Uchiyama, I. Shake, and K. Mori, "3 Tbit/s (160 Gbit/sx19 ch) OTDM/WDM transmission experiment," *OSA OFC'99*, San Diego, CA, Post deadline paper, PD1, 1999.

[7] S. Kawanishi, H. Takara, K. Uchiyama, I. Shake, O. Kamatani, and H. Takahashi, "1.4 Tbit/s (200 Gbit/s*7 ch), 50 km OTDM-WDM transmission experiment," *OECC'97*, Seoul, South Korea, 14-15 suppl., 1997.

[8] S. Kawanishi, H. Takara, T. Morioka, O. Kamatani, K. Takiguchi, T. Kitoh, and M. Saruwatari, "400 Gbit/s TDM transmission of 0.98 ps pulses over 40 km employing dispersion slope compensation," *OSA OFC'96*, San Jose, CA, pp. 423-426, 1996.

[9] S. Kuwano, N. Takachio, K. Iwashita, T. Otsuji, Y. Imai, T. Enoki, K. Yoshino, and K. Wakita, "160-Gbit/s (4-ch*40-Gbit/s electrically multiplexed data) WDM transmission over 320-km dispersion-shifted fiber," *OSA OFC'96*, San Jose, CA, pp. 427-430, 1996.

[10] K. Hagimoto, M. Yoneyama, A. Sano, A. Hirano, T. Kataoka, T. Otsuji, K. Sato, and K. Noguchi, "Limitations and challenges of single-carrier full 40-Gbit/s repeater system based on optical equalization and new circuit design," *OSA OFC'97*, Dallas, TX, pp. 242-243, 1997.

[11] H. Takeuchi, K. Tsuzuki, K. Sato, M. Yamamoto, Y. Itaya, A. Sano, M. Yoneyama, and T. Otsuji, "NRZ operation at 40 Gb/s of a compact module containing an MQW electroabsorption modulator integrated with a DFB laser," *IEEE Photonics Technol. Lett.*, vol. 9, pp. 572-574, 1997.

[12] W. Bogner, E. Gottwald, A. Schopflin, and C. J. Weiske, "40 Gbit/s unrepeatered optical transmission over 148 km by electrical time division multiplexing and demultiplexing," *Electron. Lett.*, vol. 33, pp. 2136-2137, 1997.

[13] K. Yonenaga, M. Yoneyama, Y. Miyamoto, K. Hagimoto, and K. Noguchi, "160 Gbit/s WDM transmission experiment using four 40 Gbit/s optical duobinary channels," *Electron. Lett.*, vol. 34, pp. 1506-1507, 1998.

[14] K. Runge, P. J. Zampardi, R. L. Pierson, P. B. Thomas, S. M. Beccue, R. Yu, and K. C. Wang, "High speed AlGaAs/GaAs HBT circuits for up to 40 Gb/s optical communication," *GaAs IC Symposium*, Anaheim, CA, pp.211-214, 1997.

[15] X. Zhang, A. Gutierrez-Aitken, D. Klotzkin, P. Bhattacharya, C. Caneau, and R. Bhat, "0.98- μm multiple-quantum-well tunneling injection laser with 98-GHz intrinsic modulation bandwidth," *IEEE J. Sel. Top. Quantum Electron. (USA)*, vol. 3, pp. 309-314, 1997.

[16] Y. Matsui, H. Murai, S. Arahira, S. Kutsuzawa, and Y. Ogawa, "30-GHz bandwidth 1.55-μm strain-compensated InGaAlAs-InGaAsP MQW laser," *IEEE Photonics Technol. Lett.*, vol. 9, pp. 25-27, 1997.

[17] C. H. Henry, "Theory of the linewidth of semiconductor lasers," *IEEE J. Quantum Electron.*, vol. QE-18, pp. 259-264, 1982.

[18] T. L. Koch and J. E. Bowers, "Nature of wavelength chirping in directly modulated semiconductor lasers," *Electron. Lett.*, vol. 20, pp. 1038-1040, 1984.

[19] T. L. Koch and R. A. Linke, "Effect of nonlinear gain reduction on semiconductor laser wavelength chirping," *Appl. Phys. Lett.*, vol. 48, pp. 613-615, 1986.

[20] M. Osinski and J. Buus, "Linewidth broadening factor in semiconductor lasers-an overview," *IEEE J. Quantum Electron.*, vol. QE-23, pp. 9-29, 1987.

[21] F. Koyama and K. Iga, "Frequency chirping in external modulators," *J. Lightwave Technol.*, vol. 6, pp. 87-93, 1988.

[22] D. C. Hutchings, M. Sheik-Bahae, D. J. Hagan, and E. W. van Stryland, "Kramers-Kronig relations in nonlinear optics," *Opt. Quantum Electron.*, vol. 24, pp. 1-30, 1992.

[23] F. Dorgeuille and F. Devaux, "On the transmission performances and the chirp parameter of a multiple-quantum-well electroabsorption modulator," *IEEE J. Quantum Electron.*, vol. 30, pp. 2565-2572, 1994.

[24] G. P. Agrawal, *Fiber-Optic Communication Systems*. Singapore: John Wiley & Sons, Inc., pp. 48-55, 1993.

[25] L. A. Coldren and S. W. Corzine, *Diode Lasers and Photonic Integrated Circuits*. New York: John Wiley & Sons, Inc., p. 209, 1995.

[26] K. Wakita, K. Yoshino, I. Kotaka, S. Kondo, and Y. Noguchi, "High speed, high efficiency modulator module with polarisation insensitivity and very low chirp," *Electron. Lett.*, vol. 31, pp. 2041-2042, 1995.

[27] K. Yamada, K. Nakamura, Y. Matsui, T. Kunii, and Y. Ogawa, "Negative-chirp electroabsorption modulator using low-wavelength detuning," *IEEE Photonics Technol. Lett.*, vol. 7, pp. 1157-1158, 1995.

[28] J. G. Mendoza-Alvarez, L. A. Coldren, A. Alping, R. H. Yan, T. Hausken, K. Lee, and K. Pedrotti, "Analysis of depletion edge translation lightwave modulators," *J. Lightwave Technol.*, vol. 6, pp. 793-808, 1988.

[29] R. G. Walker, "High-speed III-V semiconductor intensity modulators," *IEEE J. Quantum Electron.*, vol. 27, pp. 654-567, 1991.

[30] W. Franz, *Z. Naturforsch.*, vol. 13, pp. 484, 1958.

[31] L. V. Keldysh, *Sov. Phys.*, vol. JETP7, pp. 788, 1953.

[32] D. A. B. Miller, D. S. Chemla, T. C. Damen, A. C. Gossard, W. Wiegmann, T. H. Wood, and C. A. Burrus, "Electric field dependence of optical absorption near the band gap of quantum-well structures," *Phys. Rev. B, Condens. Matter*, vol. 32, pp. 1043-1060, 1985.

[33] D. A. B. Miller, D. S. Chemla, and S. Schmitt-Rink, "Relation between electroabsorption in bulk semiconductors and in quantum wells: the quantum-confined Franz-Keldysh effect," *Phys. Rev. B, Condens. Matter*, vol. 33, pp. 6976-6982, 1986.

[34] K. Kawano, T. Kitoh, H. Jumonji, T. Nozawa, and M. Yanagibashi, "New travelling-wave electrode Mach-Zehnder optical modulator with 20 GHz bandwidth and 4.7 V driving voltage at 1.52 μm wavelength," *Electron. Lett.*, vol. 25, pp. 1382-1383, 1989.

[35] G. K. Gopalakrishnan, C. H. Bulmer, W. K. Burns, R. W. McElhanon, and A. S. Greenblatt, "40 GHz, low half-wave voltage Ti:$LiNbO_3$ intensity modulator," *Electron. Lett.*, vol. 28, pp. 826-827, 1992.

[36] D. W. Dolfi and T. R. Ranganath, "50 GHz velocity-matched broad wavelength $LiNbO_3$ modulator with multimode active section," *Electron. Lett.*, vol. 28, pp. 1197-1198, 1992.

[37] M. Rangaraj, T. Hosoi, and M. Kondo, "A wide-band Ti:$LiNbO_3$ optical modulator with a conventional coplanar waveguide type electrode," *IEEE Photonics Technol. Lett.*, vol. 4, pp. 1020-1022, 1992.

[38] K. Noguchi, H. Miyazawa, and O. Mitomi, "75 GHz broadband Ti:$LiNbO_3$ optical modulator with ridge structure," *Electron. Lett.*, vol. 30, pp. 949-951, 1994.

[39] K. Noguchi, H. Miyazawa, and O. Mitomi, "40-Gbit/s Ti:$LiNbO_3$ optical modulator with a two-stage electrode," *IEICE Trans. Electron. (Japan)*, vol. E81-C, pp. 1316-1320, 1998.

[40] O. Mitomi, K. Noguchi, and H. Miyazawa, "Broadband and low driving-voltage $LiNbO_3$ optical modulators," *IEE Proc., Optoelectron.*, vol. 145, pp. 360-364, 1998.

[41] S. Y. Wang and S. H. Lin, "High speed III-V electrooptic waveguide modulators at λ=1.3 μm," *J. Lightwave Technol.*, vol. 6, pp. 758-771, 1988.

[42] R. Spickermann, S. R. Sakamoto, M. G. Peters, and N. Dagli, "GaAs/AlGaAs travelling wave electro-optic modulator with an electrical bandwidth >40 GHz," *Electron. Lett.*, vol. 32, pp. 1095-1096, 1996.

[43] R. Spickermann, "High speed Gallium Arsenide/Aluminum Gallium Arsenide traveling wave electrooptic modulators," University of California, Santa Barbara, CA, Ph.D. Dissertation, 1996.

[44] H. R. Khazaei, E. Berolo, and F. Ghannouchi, "High-speed slow-wave coplanar strip GaAs/AlGaAs electro-optic laser modulator," *Microw. Opt. Technol. Lett.*, vol. 19, pp. 184-186, 1998.

[45] N. Agrawal, C. M. Weinert, H. J. Ehrke, G. G. Mekonnen, D. Franke, C. Bornholdt, and R. Langenhorst, "Fast 2*2 Mach-Zehnder optical space switches using InGaAsP-InP multiquantum-well structures," *IEEE Photonics Technol. Lett.*, vol. 7, pp. 644-645, 1995.

[46] M. Fetterman, C. P. Chao, and S. R. Forrest, "Fabrication and analysis of high-contrast InGaAsP-InP Mach-Zehnder modulators for use at 1.55- μm wavelength," *IEEE Photonics Technol. Lett.*, vol. 8, pp. 69-71, 1996.

[47] C. Rolland, "InGaAsP-based Mach-Zehnder modulators for high-speed transmission systems," *OSA OFC'98*, San Jose, CA, pp. 283-284, 1998.

[48] K. Wakita, I. Kotaka, and H. Asai, "High-speed InGaAlAs/InAlAs multiple quantum well electrooptic phase modulators with bandwidth in excess of 20 GHz," *IEEE Photonics Technol. Lett.*, vol. 4, pp. 29-31, 1992.

[49] P. Van Schooti, V. Lambecki, M. J. Gilde, Y. P. Chan, J. P. Lecomte, G. Tapolsky, R. Meyrueix, S. V. Kershaw, and J. V. Collins, "Design and realisation of a MZI type polymer based high speed EO-modulator," *ECOC'96*, Oslo, Norway, pp. 281-284 vol. 3, 1996.

[50] H.-M. Lee, H. Wol-Yon, O. Min-Cheol, P. Heuk, Z. Taehyoung, and K. Jang-Joo, "High performance electro-optic polymer waveguide device," *Appl. Phys. Lett.*, vol. 71, pp. 3779-3781, 1997.

[51] S. Ermer, W. W. Anderson, T. E. Van Eck, D. G. Girton, S. M. Lovejoy, D. S. Leung, J. A. Marley, and A. Harwit, "Progress in optoelectronic polymers and devices," *SPIE'97*, San Jose, CA, pp. 397-404, 1997.

[52] D. Chen, H. R. Fetterman, C. Antao, W. H. Steier, L. R. Dalton, W. Wenshen, and S. Yongqiang, "Demonstration of 110 GHz electro-optic polymer modulators," *Appl. Phys. Lett.*, vol. 70, pp. 3335-3337, 1997.

[53] D. Chen, D. Bhattacharya, A. Udupa, B. Tsap, H. R. Fetterman, C. Antao, L. Sang-Shin, C. Jinghong, W. H. Steier, and L. R. Dalton, "High-frequency polymer modulators with integrated finline transitions and low V_{pi}," *IEEE Photonics Technol. Lett.*, vol. 11, pp. 54-56, 1999.

[54] R. Spickermann, M. G. Peters, and N. Dagli, "A polarization independent GaAs-AlGaAs electrooptic modulator," *IEEE J. Quantum Electron.*, vol. 32, pp. 764-769, 1996.

[55] K. Wakita, Y. Kawamura, M. Nakao, and H. Asahi, "Long wavelength waveguide multiple quantum well optical modulators," *IEEE J. Quantum Electron.*, vol. QE-23, pp. 2210-2215, 1987.

[56] I. Kotaka, K. Wakita, K. Kawano, M. Asai, and M. Naganuma, "High-speed and low-driving-voltage InGaAs/InAlAs multiquantum well optical modulators," *Electron. Lett.*, vol. 27, pp. 2162-2163, 1991.

[57] F. Devaux, S. Chelles, A. Ougazzaden, A. Mircea, and J. C. Harmand, "Electroabsorption modulators for high-bit-rate optical communications: a comparison of strained InGaAs/InAIAs and InGaAsP/InGaAsP MQW," *Semicond. Sci. Technol.*, vol. 10, pp. 887-901, 1995.

[58] K. Wakita, I. Kotaka, K. Yoshino, S. Kondo, and Y. Noguchi, "Polarization-independent electroabsorption modulators using strain-compensated InGaAs-InAlAs MQW structures," *IEEE Photonics Technol. Lett.*, vol. 7, pp. 1418-1420, 1995.

[59] K. Yoshino, K. Wakita, I. Kotaka, S. Kondo, Y. Noguchi, S. Kuwano, N. Takachio, T. Otsuji, Y. Imai, and T. Enoki, "40-Gbit/s operation of InGaAs/InAlAs MQW electroabsorption modulator module with very low driving-voltage," *ECOC'96*, Oslo, Norway, pp. 203-206 vol. 3, 1996.

[60] K. Satzke, D. Baums, U. Cebulla, H. Haisch, D. Kaiser, E. Lach, E. Kuhn, J. Weber, R. Weinmann, P. Wiedemann, and E. Zielinski, "Ultrahigh-bandwidth (42 GHz) polarisation-independent ridge waveguide electroabsorption modulator based on tensile strained InGaAsP MQW," *Electron. Lett.*, vol. 31, pp. 2030-2032, 1995.

[61] T. Ido, S. Tanaka, M. Suzuki, M. Koizumi, H. Sano, and H. Inoue, "Ultra-high-speed multiple-quantum-well electro-absorption optical modulators with integrated waveguides," *J. Lightwave Technol.*, vol. 14, pp. 2026-2034, 1996.

[62] R. Heinzelmann, A. Stohr, T. Alder, R. Buss, and D. Jager, "EMC measurements using electrooptic waveguide modulators," *IEEE International Topical Meeting on Microwave Photonics (MWP'96)*, Kyoto, Japan, pp. 177-180, 1996.

[63] I. Kotaka, K. Wakita, O. Mitomi, H. Asai, and Y. Kawamura, "High-speed InGaAlAs/InAlAs multiple quantum well optical modulators with bandwidths in excess of 20 GHz at 1.55 μm," *IEEE Photonics Technol. Lett.*, vol. 1, pp. 100-101, 1989.

[64] K. Wakita, I. Kotaka, O. Mitomi, H. Asai, Y. Kawamura, and M. Naganuma, "High-speed InGaAlAs/InAlAs multiple quantum well optical modulators," *J. Lightwave Technol.*, vol. 8, pp. 1027-1032, 1990.

[65] K. Kawano, M. Kohtoku, M. Ueki, T. Ito, S. Kondoh, Y. Noguchi, and Y. Hasumi, "Polarisation-insensitive travelling-wave electrode electroabsorption (TW-EA) modulator with bandwidth over 50 GHz and driving voltage less than 2 V," *Electron. Lett.*, vol. 33, pp. 1580-1581, 1997.

[66] M. M. Mihailidi, J. E. Zucker, M. D. Feuer, M. N. Khan, T. Y. Chang, and N. J. Sauer, "Microwave properties of traveling-wave InGaAs/InGaAlAs quantum-well optical waveguide modulators," *Microw. Opt. Technol. Lett.*, vol. 10, pp. 204-207, 1995.

[67] F. Devaux, J. C. Harmand, I. F. L. Dias, T. Guettler, O. Krebs, and P. Voisin, "High power saturation, polarisation insensitive electroabsorption modulator with spiked shallow wells," *Electron. Lett.*, vol. 33, pp. 161-163, 1997.

[68] H. H. Liao, X. B. Mei, K. K. Loi, C. W. Tu, P. M. Asbeck, and W. S. C. Chang, "Microwave structures for traveling-wave MQW electro-absorption modulators for wide band 1.3 μm photonic links," *SPIE'97*, San Jose, CA, pp. 291-300, 1997.

[69] F. Devaux, F. Dorgeuille, A. Ougazzaden, F. Huet, M. Carre, A. Carenco, M. Henry, Y. Sorel, J. F. Kerdiles, and E. Jeanney, "20 Gbit/s operation of a high-efficiency InGaAsP/InGaAsP MQW electroabsorption modulator with 1.2-V drive voltage," *IEEE Photonics Technol. Lett.*, vol. 5, pp. 1288-1290, 1993.

[70] S. Z. Zhang, C. Yi-Jen, P. Abraham, and J. E. Bowers, "25 GHz polarization-insensitive electroabsorption modulators with traveling-wave electrodes," *IEEE Photonics Technol. Lett.*, vol. 11, pp. 191-193, 1999.

[71] S. Z. Zhang, V. Kaman, A. Keating, Y. J. Chiu, P. Abraham, and J. E. Bowers, "30 Gbit/s operation of a traveling-wave electroabsorption modulator," *OSA OFC'99*, San Diego, CA, paper ThT3, 1999.

[72] M. Suzuki, H. Tanaka, N. Edagawa, K. Utaka, and Y. Matsushima, "Transform-limited optical pulse generation up to 20-GHz repetition rate by a sinusoidally driven InGaAsP electroabsorption modulator," *J. Lightwave Technol.*, vol. 11, pp. 468-473, 1993.

[73] D. G. Moodie, A. D. Ellis, and C. W. Ford, "Generation of 6.3 ps optical pulses at a 10 GHz repetition rate using a packaged electroabsorption modulator and dispersion compensating fibre," *Electron. Lett.*, vol. 30, pp. 1700-1701, 1994.

[74] N. Souli, F. Devaux, A. Ramdane, P. Krauz, A. Ougazzaden, F. Huet, M. Carre, Y. Sorel, J. F. Kerdiles, M. Henry, G. Aubin, E. Jeanney, T. Montallant, J. Moulu, B. Nortier, and J. B. Thomine, "20 Gbit/s high-performance integrated MQW TANDEM modulators and amplifier for soliton generation and coding," *IEEE Photonics Technol. Lett.*, vol. 7, pp. 629-631, 1995.

[75] G. Aubin, E. Jeanney, T. Montalant, J. Moulu, F. Pirio, J. B. Thomine, and F. Devaux, "20 Gbit/s soliton transmission over transoceanic distances with a 105 km amplifier span," *Electron. Lett.*, vol. 31, pp. 1079-1080, 1995.

[76] D. D. Marcenac, A. D. Ellis, and D. G. Moodie, "80 Gbit/s OTDM using electroabsorption modulators," *Electron. Lett.*, vol. 34, pp. 101-103, 1998.

[77] P. K. L. Yu, R. B. Welstand, G. L. Li, W. X. Chen, L. T. Zhu, P. S. A., C. K. Sun, R. Nguyen, and Y. Z. Liu, "Electroabsorption waveguide modulators for high performance analog fiber links," *IEEE Microwave Photonics (MWP'98)*, Princeton, New Jersey, pp. 29-32, paper MC1, 1998.

[78] K. K. Loi, X. B. Mei, J. H. Hodiak, C. W. Tu, and W. S. C. Chang, "38 GHz bandwidth 1.3 um MQW electroabsorption modulators for RF photonic links," *Electron. Lett.*, vol. 34, pp. 1018-1019, 1998.

CHAPTER 2

Optical Waveguide Design

For most applications, there are a couple of criteria for modulators, which include (1) a high extinction ratio (*ER*), (2) a small insertion loss, (3) a low drive voltage (V_{20dB}), (4) a large bandwidth (f_{3dBe}), and (5) a low chirp (α). Based on these requirements, different optimization design schemes have been proposed [1-4]. Nojima *et al.* [1] first proposed $\Delta\alpha/\alpha_0$ where $\Delta\alpha$ is the absorption change and α_0 is the residual absorption at the photon wavelength, as the electroabsorption figure of merit. Later Bigan *et al*. [2] proposed to use $\Gamma\Delta\alpha/F$ as the figure of merit, where Γ is the optical confinement factor and F is the applied electric field. However, none of these two approaches considers the bandwidth of the device. This Chapter will discuss the design of the optical waveguide material structure for achieving low driving voltage, polarization insensitivity and high coupling efficiency. The high speed design issues will be discussed in Chapter 3.

In this chapter, we will show that the quantum confined Stark shift can be increased by using wider quantum wells, and hence will reduce the drive voltage. By utilizing tensile strained quantum well, polarization insensitivity has been achieved. Section 5 of this chapter will discuss the waveguide design rules for achieving high coupling efficiency with single mode optical fibers based on the optical mode calculation.

2.1 Quantum Confined Stark Effect (QCSE)

The electroabsorption (EA) effect is a fundamental effect for the operation of electroabsorption modulators. It is defined as the change of material absorption in the presence of an electric field. This effect was first studied by Franz [5] and Keldysh [6] in bulk semiconductors and was called the Franz-Keldysh effect. Franz-Keldysh electroabsorption effect can be described as the below-band-gap photon-assisted tunneling of electrons from the valence to the conduction band in the presence of the electric field. A full description of such an interband optical absorption should include the effects of the Coulomb interaction of the electron and hole [7, 8]. This results in exciton (electron-hole pair) resonances and enhancement

of the optical absorption above the optical band gap with no applied field. However, these exciton resonances are quickly broadened and diminished with external electric field due to the ionization of the exciton.

Qualitatively different electroabsorption behavior is observed in multiple quantum well (MQW) materials. Electric fields applied perpendicular to the MQW layers result in large shifts in the optical absorption to lower photon energies, with the exciton resonances remaining well resolved even at high electric field [9, 10]. The excitons are not as easily field-ionized because (1) there is a relatively long time period for the electrons and the holes to tunnel out of the quantum well, and (2) the Coulomb attraction is strong since the electrons and holes are confined to the very thin quantum well region. This electroabsorption effect in quantum well materials is called Quantum Confined Stark Effect. In the case of QCSE, the absorption edge is much sharper and moves faster with reverse biased electric field as a result of this room temperature exciton resonance in MQW materials. This feature makes the MQW devices favorable in achieving low drive voltage, low insertion loss and high extinction ratio.

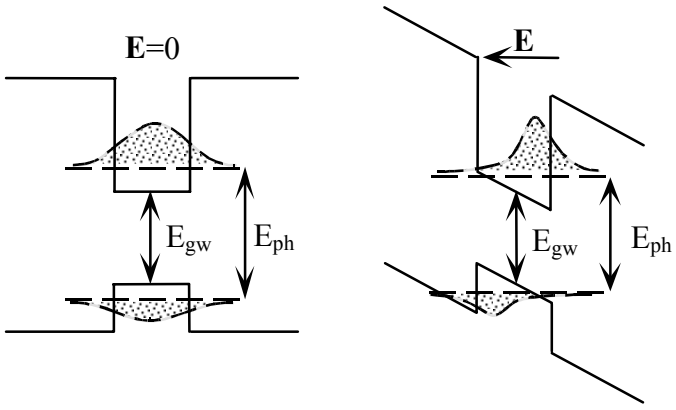

Fig 2.1 Band diagram under zero and finite electric field. The electron and hole wave functions are spatially superimposed on the band diagram.

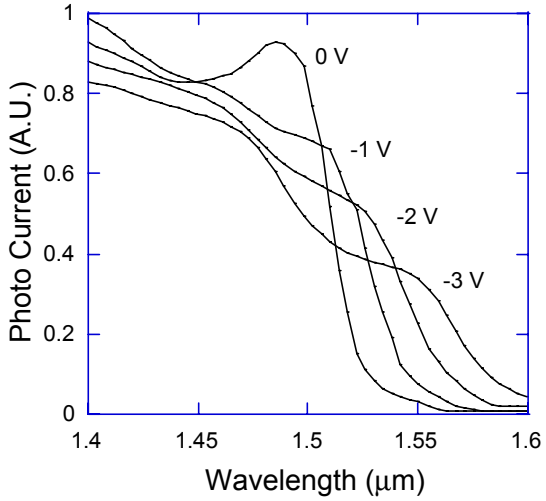

Fig 2.2 Typical photocurrent spectra under different biases [11].

Fig 2.1 shows the band diagram under zero and finite electric field. As a result of the reverse biased electric field in a p-i-n structure, several features are observed in the absorption spectra (Fig 2.2) [9]. First, the excitonic absorption edge shifts to longer wavelengths due to the reduction of effective electron and hole energy levels. Second, a reduction in the peak excitonic absorption is observed due to the spatial separation of the electron and hole wave functions. Because of the reduction of the binding energy, the exciton lifetime is reduced and the absorption spectra are broadened.

The excitonic absorption energy can be expressed as

$$E_{ph} = E_{gw} + E_e + E_h - E_x , \qquad (2.1)$$

where E_{ph} is the photon energy, E_{gw} is the quantum-well bandgap energy, E_e is the electron subband energy, E_h is the hole subband energy, and E_x is the exciton binding energy. The estimated experimental binding energy is about 6 meV for GaInAs/AlInAs quantum-wells [12].

The exact solution for a particle in a finite well in the presence of a uniform static field can be solved by the variational method [13]. In the presence of a weak field, the field-induced energy shift (Quantum-Confined-Stark-Shift, QCSS) was

found to be quadratic to the electric field and proportional to the 4th power of the quantum well thickness [13]

$$\Delta E = -\frac{\Omega^2}{8}\frac{m^* e^2 F^2 L^4}{\hbar^2}, \tag{2.2}$$

where Ω is a constant depends on the barrier height and the well thickness, m^* is the electron effective mass, e is the electron charge, F is the electric field, L is the well thickness, and $\hbar$ is the reduced Planck constant.

To reduce the driving voltage of the modulator, it is essential to optimize the parameters, such as the bandgap and well thickness of the MQW absorption layer. Due to the quadratic relation of the energy shift to the electric field, we need to make the unintentionally doped region thinner so as to increase the electric field. On the other hand, the reduction in the intrinsic layer thickness will reduce the bandwidth for a lumped device in the same proportion. The bandwidth-to-drive-voltage ratio is thus independent of the intrinsic region thickness [14].

It was verified both theoretically [13] and experimentally [15, 16] that increasing the well thickness leads to a larger QCSS and a lower driving voltage, while decreasing in the oscillation strength of the electroabsorption. There is thus an optimum well thickness for high modulation efficiency. Simulation has shown that the optimum well thickness is around 8-9 nm to achieve the highest contrast ratio [1].

2.2 Spiked Vs. non-spiked quantum wells

With the resonant scattering method given in Appendix A, we can calculate the bound state of the quantum wells under external electric field.

Currently lattice matched and strained InGaAs/InAlAs, InGaAlAs/InAlAs and InGaAsP/InGaAsP quantum wells have been used to fabricate electroabsorption modulators operating at 1.55 μm. In order to achieve this wavelength operation, the quantum well has to be designed to have an absorption edge wavelength just slightly shorter than 1550 nm. The optimum photoluminescence wavelength is around 1490 nm. Choosing a longer wavelength will cause higher residual absorption at 1550 nm when no bias is applied, while

choosing too short wavelengths will require a larger bias voltage and will have a smaller modulation efficiency.

With lattice matched InGaAs/InAlAs, a quantum well with width of about 7.2 nm has to be used. A tensile strained well will be preferred for achieving larger Stark shift. With tensile strain the well bandgap is wider and this allows wider quantum wells yet still achieving 1550 nm operation. One way to achieve wider quantum well with lattice matched InGaAs/InAlAs is to add a very thin layer of InAlAs into the InGaAs well [17].

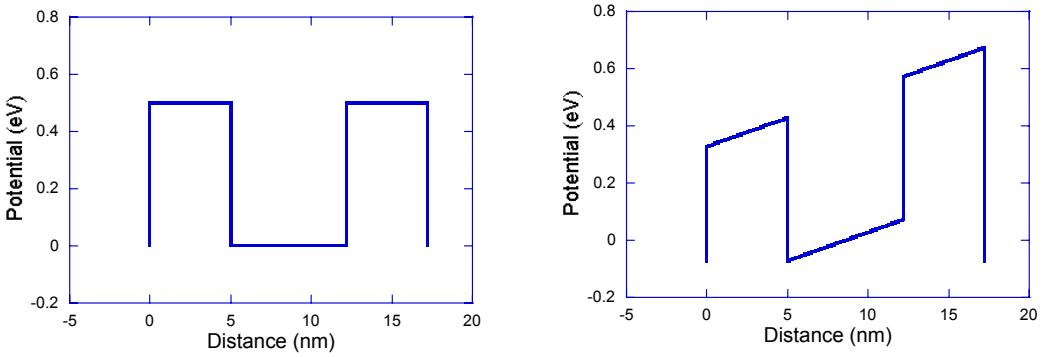

(a) (b)

Fig. 2.3 Conduction band potential profile of an $In_{0.53}Ga_{0.47}As/In_{0.52}Al_{0.48}As$ quantum-well under (a) 0, and (b) 200 kV/cm electric field. The well thickness is 7.2 nm, and the barrier thickness is 5 nm.

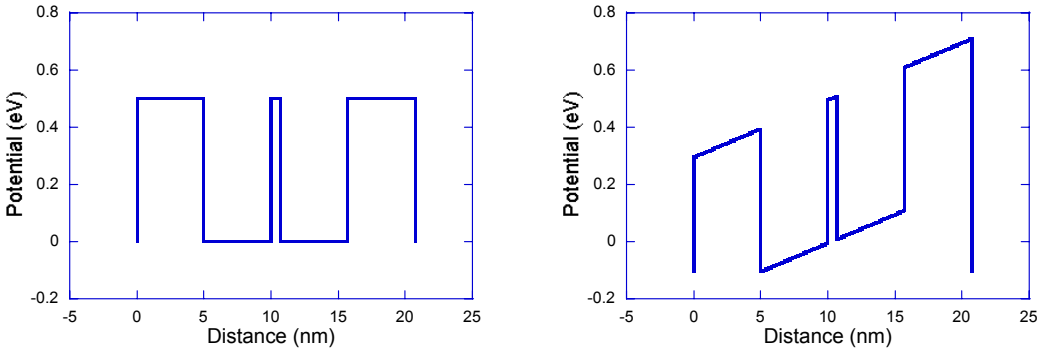

(a) (b)

Fig. 2.4 Conduction band potential profile of a spiked $In_{0.53}Ga_{0.47}As/In_{0.52}Al_{0.48}As$ quantum-well under (a) 0, and (b) 200 kV/cm electric field. The well thickness is 5 nm on both halves with a 0.7 nm $In_{0.52}Al_{0.48}As$ spike in between, and the barrier thickness is 5 nm.

We have studied both the conventional non-spiked quantum well and the spiked quantum well. Fig. 2.3 shows the conduction band diagram of a conventional $In_{0.53}Ga_{0.47}As$/ $In_{0.52}Al_{0.48}As$ quantum well under two different electric field intensities, while Fig. 2.4 shows the case for a spiked quantum well. For successful numerical calculation, the potentials at the two ends are set to equal to the lowest energy value of the overall potential profile. The ramped potential regions are divided to multiple small sections with each of 0.1 nm wide. The potential is treated as constant within each section.

	$In_{0.532}Ga_{0.468}As$	$In_{0.523}Al_{0.477}As$	InP
m_c^* / m_e	0.041[(a)]	0.075[(a)]	0.077[(b)]
m_{hh}^* / m_e	0.46[(a)]	0.41[(a)]	0.61[(b)]
m_{lh}^* / m_e	0.051[(a)]	0.096[(a)]	0.12[(b)]
ΔE_c (eV)	0	0.516[(c)]	…
ΔE_v (eV)	0	0.199[(c)]	…
E_g (eV)	0.741[(c)]	1.44[(c)]	1.351[(b)]

Table 2.1: Material parameters used in calculations for InGaAs/InAlAs lattice matched to InP.

[(a)] M. Ilegems, "InP-based lattice-matched heterostructures," in *Properties of Lattice-Matched and Strained Indium Gallium Arsenide,* Edited by Pallab Bhattacharya, INSPEC, p. 23, 1993.

[(b)] L. A. Coldren and S. W. Corzine, *Diode Lasers and Photonic Integrated Circuits*, John Wiley & Sons, New York, p. 12, 1995.

[(c)] D. J. Moss, T. Ido, and H. Sano, "Photo generated carrier sweep-out times in strained $In_xGa_{1-x}As$/ $In_yAl_{1-y}As$ quantum well modulators," *Electron. Lett.,* vol. 30, pp. 405-406, 1994.

Table 2.1 summarizes the material parameters of InGaAs/InAlAs/InP system. The absorption edge will correspond to the transition between the first electron level to first heavy hole level for a lattice non-strained quantum well. The room temperature photoluminescence energy of the material corresponding to this transition is

$$E_{PL} = E_g + E_{e1} + E_{hh1} - E_x, \tag{2.3}$$

where E_g is the bandgap energy of the well, E_{e1} is the first electron subband energy, E_{hh1} is the first heavy hole subband energy. The exciton binding energy E_x is about 6 meV [12].

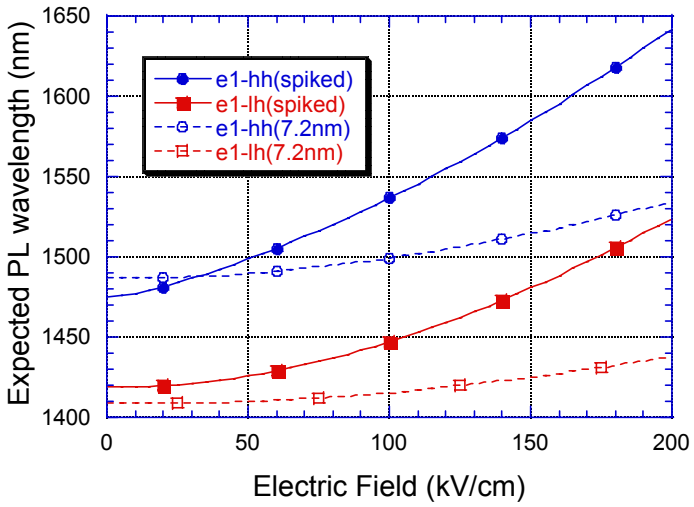

Fig. 2.5 Simulated photoluminescence wavelengths for heavy hole (e_1-hh_1) and light hole (e_1-lh_1) transitions for spiked and non-spiked quantum wells under external electric field.

Fig. 2.5 shows the calculated room temperature photoluminescence wavelengths corresponding to heavy hole (e_1-hh_1) and light hole (e_1-lh_1) transitions for spiked and non-spiked quantum wells. As shown in the figure, the heavy hole transition has a much longer wavelength than that of light hole transition, which suggests that the absorption edge will be dominated by the heavy hole transition. Since the heavy hole transition will only absorb TE polarized light the device is polarization sensitive [18].

Fig. 2.6 shows the calculated photoluminescence wavelength shift for heavy hole transitions as a function of the applied electric field. In comparison, Fig. 2.7 shows the measured absorption edge shift for different MBE samples. It was verified by simulation and measurement that a wider quantum will generate larger absorption edge shift, and hence will reduce the drive voltage of the modulator.

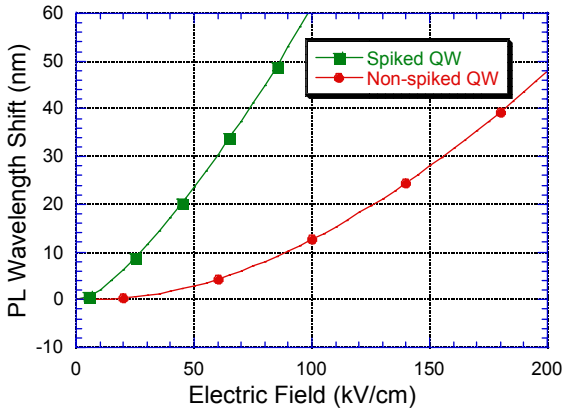

Fig. 2.6 Simulated photoluminescence wavelength shift for heavy hole (e_1-hh_1) transitions for spiked and non-spiked quantum wells under external electric field.

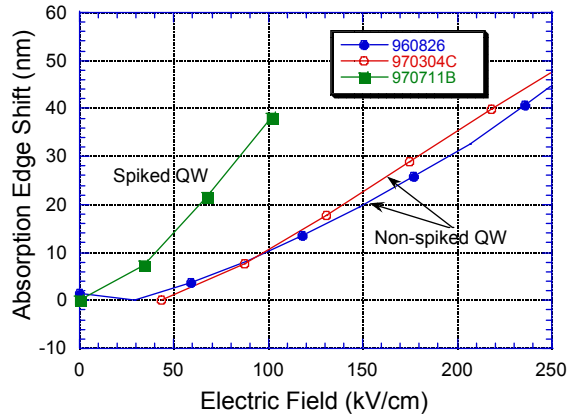

Fig. 2.7 Measured absorption edge shift for spiked and non-spiked quantum wells under external electric field.

2.3 Polarization insensitive quantum well design

Polarization-independent operation is an important feature for many optoelectronic devices used in telecommunication systems. Since local strains in the fiber will induce birefringence, the polarization-state of light is randomized after propagating through even limited spans. Polarization dependence of electroabsorption MQW material has been studied extensively [18-20]. The polarization dependence is a result of a number of factors including the waveguide

geometry, the optical selection rule, the transition strength and the nature of electroabsorption effect.

The absorption can be thought of the sum of the absorption due to heavy-hole (HH) and light-hole (LH) transitions. Due to the nature of the electroabsorption effect, the HH transition mostly contributes to the absorption in TE polarization (or in-plane polarization) light whereas the LH transition is the only contribution to the absorption in the TM polarization (or axial polarization) light. The absorption for light propagating in a waveguide device with either TE or TM polarization is given by [21]

$$\begin{aligned} \alpha_{TE} &= \frac{1}{4}\alpha_{LH} + \frac{3}{4}\alpha_{HH}, \\ \alpha_{TM} &= \alpha_{LH} \end{aligned} \tag{2.4}$$

where α_{TE} and α_{TM} are the absorption for the TE and TM light, respectively. The weighting factors are related to the dipole matrix elements. It is not difficult to conclude from Equation (2.4) that the absorption in TE and TM can be equal only if the absorption associated with the heavy holes and the light holes are equal. For a device with a length of L and a optical confinement factor of Γ(defined as the ratio of optical power in the active material and the total guided optical power), the optical transmission coefficient through the device is

$$T(V) = \gamma(1-R)^2 \exp[-\Gamma\alpha_{QW}(V)L], \tag{2.5}$$

where γ is the coupling coefficient between the incident optical mode and the waveguide, R is the power reflection coefficient of each facet, $\alpha_{QW}(V)$ is the quantum well absorption coefficient and is dependent on the applied voltage.

Equation (2.5) suggests that in order to achieve polarization independent operation, the coupling coefficient γ, the facet reflection R, and the modal absorption $\Gamma\alpha_{QW}(V)$ need to be the same for TE and TM modes. Practically, TE and TM modes have similar coupling and facet reflection coefficients. Therefore, the absorption difference is dominated by the modal absorption coefficient. The extinction ratio ER, defined as the on-state and off-state power transmission ratio is

$$ER = 4.343 \cdot \Gamma \cdot [\alpha_{QW}(V_{off}) - \alpha_{QW}(V_{on})] \cdot L \qquad \text{[dB]. (2.6)}$$

Roughly, the heavy- and light-hole bandgap should be identical in order to achieve the same absorption coefficient $\alpha_{QW}(V)$. This is obviously not the case when holes are confined in unstrained quantum wells since the quantum confinement energy depends on the carrier effective mass, which results in narrower bandgap for heavy-hole transition in both InGaAsP/InGaAsP and InGaAs/InAlAs quantum wells. The use of tensile strained material allows one to lower the bulk material light-hole bandgap with respect to the heavy-hole one. The combination of the material bandgap and quantum confinement energy can then be approximately equal.

From Eqs (2.5) and (2.6), we see that valence band degeneracy is not sufficient to obtain polarization independence. When applying an electric field, the heavy- and light-hole absorption edges should shift the same way. The modal absorption change with applied electric field depends on the exciton shift, its oscillator strength, line width and the optical confinement factor. Even though these parameters depend on the type of carrier and light, they happen to compensate each other over a useful range of electric field [18, 20]. For realistic modulator structure parameters, heavy- and light-hole degeneracy is sufficient to ensure the polarization insensitivity of the optical absorption for multiple-quantum-well materials using the quantum-confined Stark Effect [18].

In the following we present the design of InGaAsP/InGaAsP multiple quantum wells grown on InP for polarization insensitive modulators. Appendix A describes the calculation of bandgap energy and band offset for InGaAsP/InP material.

Besides polarization independence, another highly desired feature is high power saturation, i.e., the incident light power value from which the absorption of the modulator deviates from linearity and leads to degradation of performances. The limiting factor for the power saturation is the accumulation of photo-generated holes in the wells, which screens the applied field [22]. To overcome this problem shallow barriers for holes are necessary to decrease their escape time. In InGaAs/InAlAs/InP material system the valance band discontinuity is intrinsically

low, with about 70% of the bandgap discontinuity on the conduction band. On the other hand, about 60% of the bandgap discontinuity is on the valance band for InGaAsP/InGaAsP/InP material systems. Consequently the composition range for quaternary material which satisfies both polarization insensitivity and high power saturation is very narrow.

Fig. 2.8 shows the strain and photoluminescence wavelength for bulk InGaAsP as functions of Ga and As composition. In order to achieve successful growth with thick strain layers, strain compensation technique was used. The quantum well material was chosen to have a PL wavelength of 1584 nm, and a tensile strain of –0.37%. This corresponds to Ga and As compositions of about 0.515 and 0.979, respectively. The barrier material was chosen to have a PL wavelength of 1150 nm, and a compressive strain of +0.5%. This corresponds to Ga and As compositions of about 0.077 and 0.325, respectively. The well and barrier are designed to 10.4 nm and 7.6 nm thick, respectively. The measured PL wavelength of the quantum well material was 1495 nm.

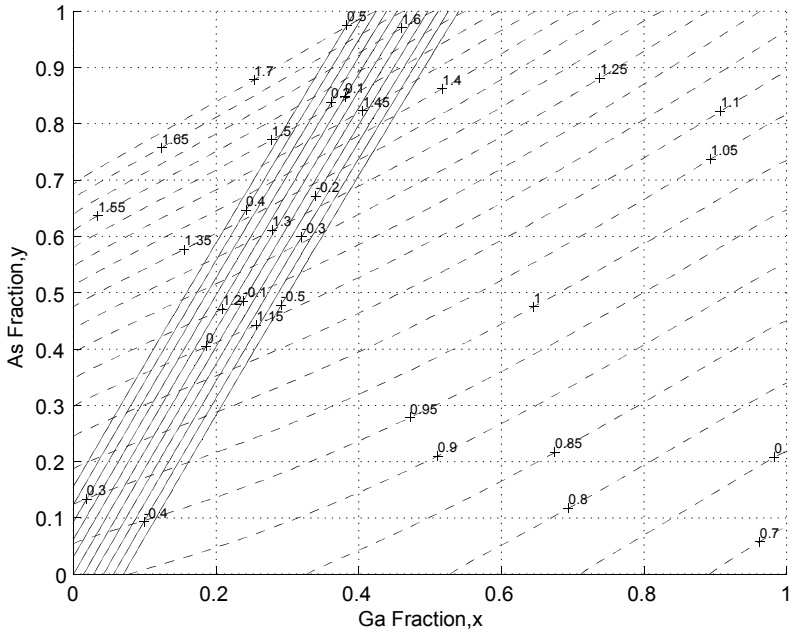

Fig. 2.8 Calculated room temperature photoluminescence wavelength (dashed) and strain (solid) as functions of Ga and As mole fractions for InGaAsP on (001) InP.

Fig. 2.9 shows the predicted PL wavelengths for heavy- and light-hole transitions for this material under external electric field. It should be noted that due to p-i-n junction build-in voltage, electric field exists even under zero external bias voltage. This is part of the reason that causes discrepancy between measured QW PL wavelength and predicted zero field PL wavelengths. In contrast to the lattice matched QW as shown in Fig. 2.5, the heavy- and the light-hole transitions have very little difference in PL wavelength for the practical electric field range. Polarization insensitive modulators were fabricated based on this design rule and the result will be giving in Chapter 4. Table 2.2 shows the material parameters used in the calculation.

	λ_{PL} (nm)	Strain ε	Thickness (Å)	x	y	ΔE_c (meV)	ΔE_{hh} (meV)	ΔE_{lh} (meV)
Well	1584	-0.37%	104	0.515	0.979			
Barrier	1150	+0.5%	76	0.077	0.325	130	164	240
QW	1495							

Table 2.2: Material parameters for the $In_{1-x}Ga_xAs_yP_{1-y}/In_{1-x}Ga_xAs_yP_{1-y}$ multiple quantum wells used in this thesis.

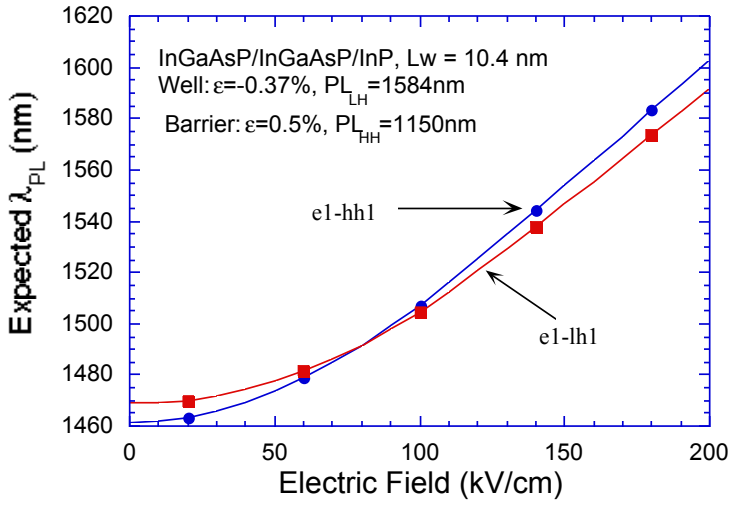

Fig. 2.9 Calculated room temperature photoluminescence wavelengths for HH and LH transitions under external electric field.

2.4 InGaAs/InAlAs vs. InGaAsP/InGaAsP quantum wells

The search for the best materials for fabricating 1.55-μm electroabsorption modulators was first started with InGaAs/InAlAs material [23] for the reason of the large conduction band discontinuity and small valence band discontinuity in this material system. Large conduction band offset provides better electron confinement and a stronger exciton effect, while smaller valence band discontinuity increases the saturation power, because of the reduction of the hole sweep out time. Due to much larger effective mass compared to electrons, hole (heavy-hole) pile-up at heterointerface was found to be the dominant limiting factor for the saturation power [24, 25]. Because of the large valence band offset in the InGaAs/InP material system, the power handling capability was poor [24]. The saturation power was increased with InGaAlAs as barrier and InGaAs as quantum well [22]. By utilizing InGaAsP as well and InGaAsP as barrier, the valence band discontinuity was reduced and yielded a larger power saturation [26].

Table 2.3 shows the comparison of lattice-matched and strained InGaAs/InAlAs and InGaAsP/InGaAsP QW devices. Here we focus on MBE grown InGaAs/InAlAs and MOCVD grown InGaAsP/InGaAsP MWQ modulators.

The InGaAs/InAlAs quantum well has 70% of the bandgap discontinuity on the conduction band. This provides a good confinement to the electrons, which enhances the exciton effect. Smaller valence band offset also reduces the valence band offset and the hole sweep out time, which improves the saturation power.

In order to achieve 1.55-μm operation, the quantum well has to be very thin. This reduces the absorption edge shift rate and the modulation efficiency. By using tensile strained quantum well, the well can be thicker to increase absorption efficiency.

In terms of electrical characteristics, p-InAlAs has very low hole mobility, and this makes the InAlAs-cladded InGaAs/InAlAs material system disadvantageous over the InP-cladded InGaAsP/ InGaAsP material system for high-speed operation. The InAlAs cladded material system is also difficult to get a good straight side wall and makes it disadvantageous for high-speed operation.

	InGaAs/InAlAs lattice-matched	**InGaAs/InAlAs strained**	**InGaAs/InP lattice-matched**	**InGaAsP/InGaAsP strained**
Well	InGaAs, ε=0	InGaAs, ε=-0.35%	InGaAs, ε=0	InGaAsP,ε=-.3%
Barrier	InAlAs, ε=0	InAlAs, ε=0	InP, ε=0	InGaAsP, ε=+.5%
Cladding	InAlAs	InAlAs	InP	InP
$\Delta E_c/\Delta E_g$	~70%		~40%	
$\Delta E_c/\Delta E_{hh}/\Delta E_{lh}$	500/200/200 meV	452/199/226 meV	220/**390**/**390** meV	130/164/240meV
Well thickness	**~7.2 nm**	~12 nm	**~6.5 nm**	~11 nm
Growth	MBE		MOCVD	
Growth quality	Good uniformity, hard to grow strain free thick p-cladding (~1.8μm)		Poor uniformity; cladding strain free	
p-cladding hole mobility	**25** cm^2/v.s		**130** cm^2/v.s	
Absorption	strong excitonic peak, sharp edge		weak excitonic peak, broad edge	
Processing	Cl_2 RIE, angled side-wall, 67^O		CH_4:H_2:Ar RIE, 90^O side-wall	
Saturation power	High	High	**Low**	Very high

Table 2.3: Comparison of latticed-matched and strained InGaAs/InAlAs, InGaAsP/InGaAsP quantum wells.

2.5 Optical Waveguide Design

The goal of the optical waveguide design is to achieve high coupling efficiency with optical fibers and good optical confinement for the largest electroabsorption efficiency. However, it may not be able to satisfy these two goals simultaneously. Also, the waveguide design has to be considered together with the requirements for high-speed operation.

The butt coupling efficiency from a fiber to a waveguide is

$$\eta = \frac{\left|\iint U_{fb}^{*} \cdot U_{WG}\, dxdy\right|^2}{\iint \left|U_{fb}\right|^2 dxdy \cdot \iint \left|U_{WG}\right|^2 dxdy}, \tag{2.7}$$

where U_{fb} and U_{WG} are mode profiles in the fiber and in the waveguide, respectively.

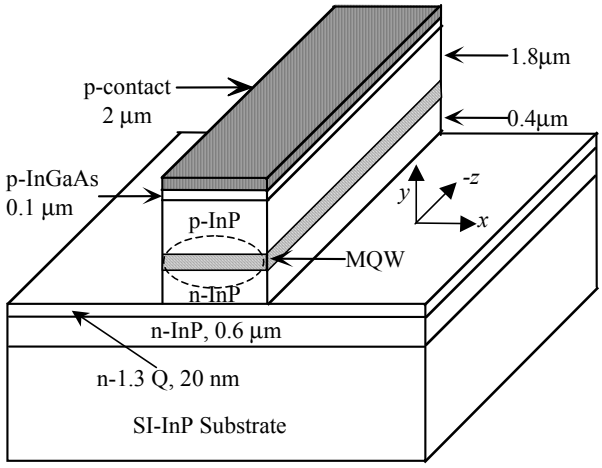

Fig. 2.11 Schematic structure of an InGaAsP/InGaAsP MQW electroabsorption modulator fabricated on semi-insulating InP substrate. The oval on the waveguide represents the mode profile.

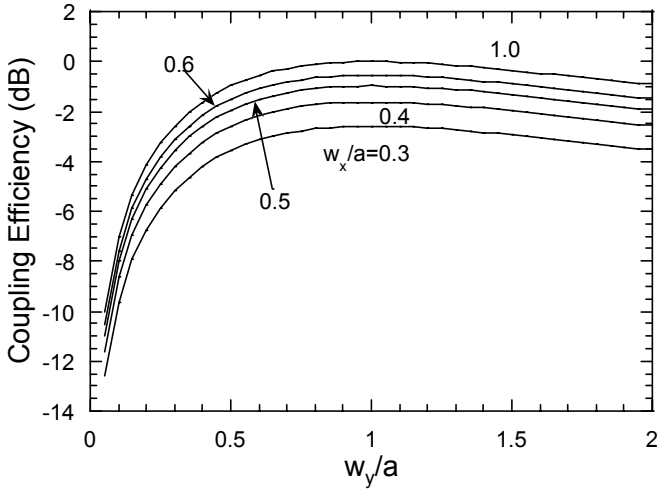

Fig. 2.12 Calculated coupling efficiency as a function of the lateral and the transverse mode sizes, assuming Gaussian mode profiles.

Equation (2.7) gives the coupling efficiency for arbitrary fiber and waveguide mode profiles. However, this will require the full understanding of the mode profiles of the fiber and the waveguide, and the calculation is rather

complicated. By approximating the fiber mode and the fundamental waveguide modes with Gaussian functions, the coupling efficiency for the fundamental waveguide mode is given approximately by [27, 28]

$$\eta = \frac{4}{(\frac{w_x}{a} + \frac{a}{w_x})(\frac{w_y}{a} + \frac{a}{w_y})}, \tag{2.8}$$

where w_x and w_y are the half full-width-at-half-maximum (FWHM) mode sizes of the waveguide in the lateral and transverse directions, respectively, and a is the mode radius of the fiber. Here the loss due to misalignment and the reflection at end facets are excluded. Equation (2.8) is plotted in Fig. 2.12.

The optical confinement factor Γ is defined as the ratio of optical power in the waveguide (here the MQW region) and the total optical power. It can be calculated from

$$\Gamma = \frac{\iint_{WG} |U_{WG}|^2 \, dxdy}{\iint_{All\ space} |U_{WG}|^2 \, dxdy} \tag{2.9}$$

As shown in Equation (2.6), the extinction ratio is highly depending on the confinement factor Γ. Larger Γ will increase the extinction ratio, however, it will sometimes require a thicker active region, which will increase the intrinsic region thickness, decrease the electric field and increase the drive voltage. On the other hand, a thinner active region will increase electric field, but it will reduce confinement factor, increase device capacitance and reduce the operation speed. An optimum design has to take into account all the parameters, instead of only optimized for specific parameter(s).

The Gaussian approximation (Equation 2.8) is accurate for large waveguide modes; however, it becomes inaccurate for small core thickness [4]. Also, actual devices with complicated waveguide structures like the one shown in Fig. 11 usually don't have an ideal Gaussian mode profile, especially at the transverse direction (y-direction as in the figure). Therefore a full calculation of the mode

profile will be necessary. The Beam Propagation Method (BPM) is one of the effective methods to calculate this 3-D structure. A commercial BPM program was employed to calculate the fundamental mode of the waveguide [29].

Waveguide simulation programs take the refractive indexes of each layer as their input. The refractive index of lattice matched quaternary alloy $In_{1-x}Ga_xAs_yP_{1-y}$ can be characterized by its photoluminescence wavelength λ_{PL} under low intensity optical excitation. The index of this quaternary alloy is given by [30]

$$n(E,E_{PL})=\left(1+\frac{A_1}{1-\left(\frac{E}{E_{PL}+E_1}\right)^2}+\frac{A_2}{1-\left(\frac{E}{E_{PL}+E_{21}}\right)^2}\right)^{\frac{1}{2}}, \qquad (2.10)$$

where $E=1.2398/\lambda$ and $E_{PL}=1.2398/\lambda_{PL}$ are respectively the incident photon energy and photoluminescence peak photon energy for wavelengths in μm. $A_1(E_{PL})$, $A_2(E_{PL})$, E_1, and E_2 are fitted parameters given by

$$\begin{aligned} A_1 &= 13.3510-5.4554\cdot E_{PL}+1.2332\cdot E_{PL}^2 \\ A_2 &= 0.7140-0.3606\cdot E_{PL} \\ E_1 &= 2.5048\,eV \\ E_2 &= 0.1638\,eV \end{aligned} \qquad (2.11)$$

For InP, the photoluminescence peak wavelength is 0.939 μm.

Fig. 2.13 shows the waveguide structure and the parameters. The material consists of, from bottom to top, 0.6 μm n-InP conducting layer, 20 nm 1.3 quaternary etch stop and n-contacting layer, 0.4 μm n-InP n-cladding layer, multiple quantum well region, 1.85 μm p-InP p-cladding layer, 0.1 μm p^+-InGaAs cap layer, and 2 μm Au.

A 3-D BPM simulation was performed to calculate fundamental mode. Since the width of the waveguide will greatly affect the circularity of the fundamental mode, it is a sensitive parameter for coupling efficiency. On the other

hand, the number of QW periods, which sets the total guiding layer thickness, will highly affect the optical confinement factor and the mode shape. The other structural parameters such as cladding layer thickness and cap layer thickness, are not sensitive parameters for the mode shapes and they are pretty much fixed. Based on these reasons, the simulation was focused on studying the effect of the number of quantum wells and waveguide width.

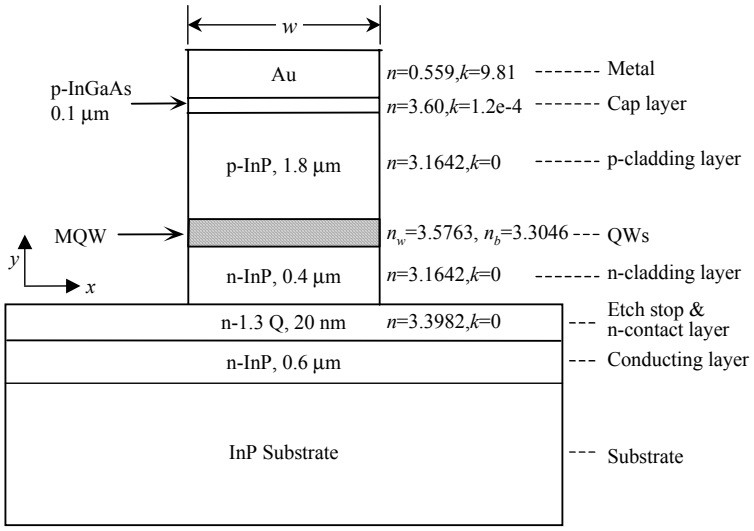

Fig. 2.13 Waveguide structure for the beam propagation calculation. $k = \frac{\alpha}{4\pi} \cdot \lambda$

For simplicity, the quantum well region was considered as a bulk material with an index of [4]

$$n_{QW} = \sqrt{(t_w \cdot n_w^2 + t_b \cdot n_b^2)/(t_w + t_b)}, \qquad (2.12)$$

where t_w=10.36 nm is the well thickness, t_b=7.59 nm is the barrier thickness, n_w and n_b are refractive indexes for well and barrier materials calculated from Equation (2.10). The effective index of the quantum well region is thus n_{QW}=3.4640.

In the following BPM simulation, a circular Gaussian beam with a beam width of 4 μm was used to launch to the waveguide.

Fig. 2.14 shows the calculated optical field contour plot for a waveguide with a 2-μm ridge, and 10 quantum wells. The quantum well region has an optical confinement factor of 0.4086, a lateral FWHM of 1.078 μm, and a transverse FWHM of 0.365 μm. The circles correspond to the intensity of, from inside to outside, 75%, 50%, 25%, and 10% of the peak intensity.

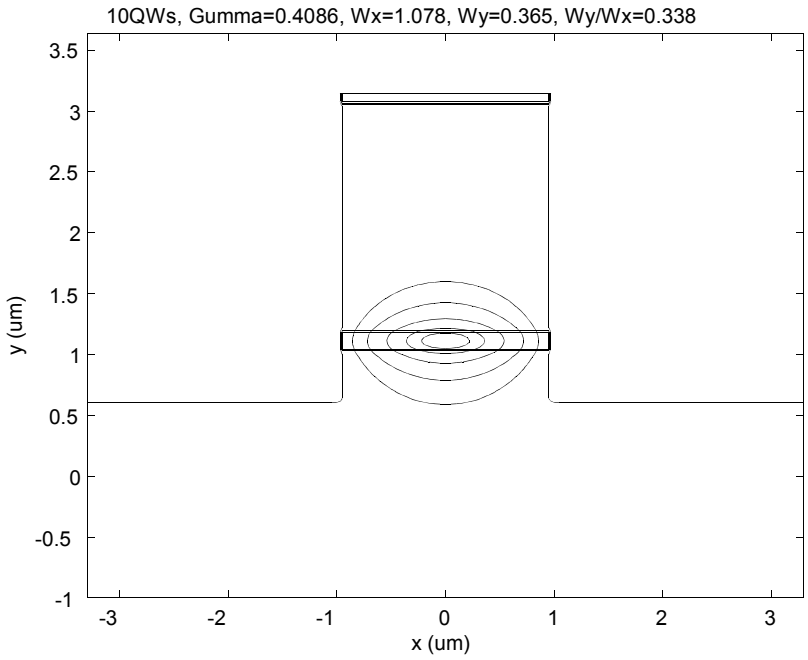

Fig. 2.14 Calculated fundamental-mode field contour for a 2-μm wide, 10-quantum-well waveguide. The input Gaussian beam has a FWHM of 4 μm. The circles correspond to optical intensities of, from inside to outside, 90%, 75%, 50%, 25%, and 10% of the peak intensity.

Fig. 2.15 shows the calculated effective index for fundamental modes for TE polarization and different ridge widths. The dots represent 3-D BPM simulation result, where the device was considered as a 3-D ridge waveguide structure [29], and the two lines represent 2-D simulation result, where the waveguide was treated as a slab waveguide structure [31]. Also shown in the graph is the refractive index of InP. Any mode with effective index smaller than that of InP is not a guiding mode. As can be seen from the figure, the minimum numbers

of quantum wells required for supporting any guiding mode are 10, 4, and 2 for waveguide ridge widths of 1-, 2-, and 3-μm, respectively. It is also noticed that slab waveguide model becomes fairly accurate for device width close to or larger than 3 μm.

Fig. 2.16 shows the optical confinement factor calculated both with 3-D and 2-D structures. It should be noted that the confinement factor here is defined as for the whole quantum well region (including barriers), instead of simply the wells.

Fig. 2.17 shows the calculated mode spot size in the lateral (x-) and transverse (y-) directions. For modes far away from cut-off, the mode FWHM at the lateral direction is independent of the number of quantum wells and has a linear relation with the waveguide width as

$$w_x = 0.076993 + 0.49802 \cdot w, \qquad [\mu m] \tag{2.13}$$

where w is the ridge width with unit in μm.

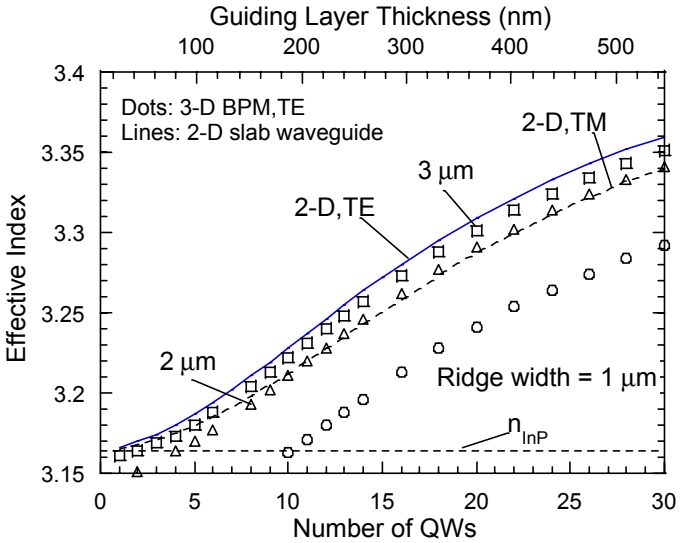

Fig. 2.15 Calculated effective index for fundamental modes. Lines: calculated with 2-D slab waveguide structure; dots: TE polarization, calculated with 3-D BPM program.

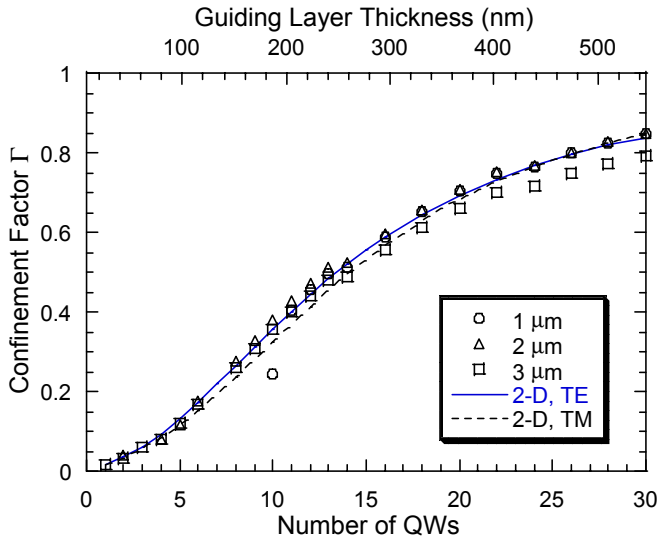

Fig. 2.16 Optical confinement factor for fundamental modes calculated with 2-D and 3-D simulation programs. All 3-D data are for TE polarization.

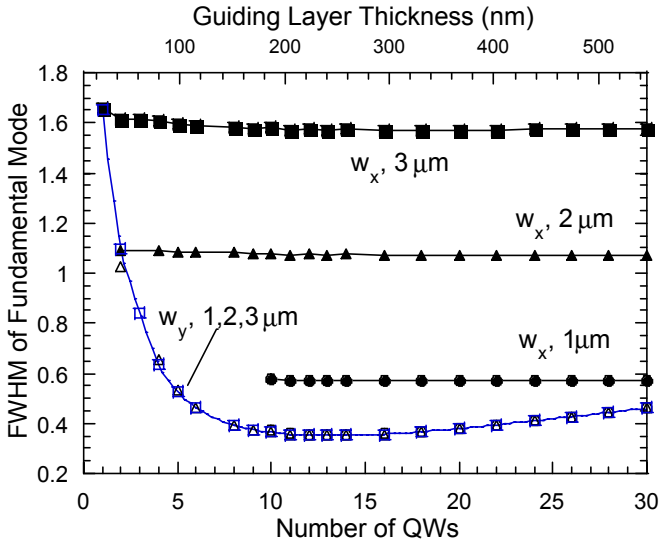

Fig. 2.17 Mode size for fundamental modes calculated with 3-D BPM for TE polarization and different ridge widths.

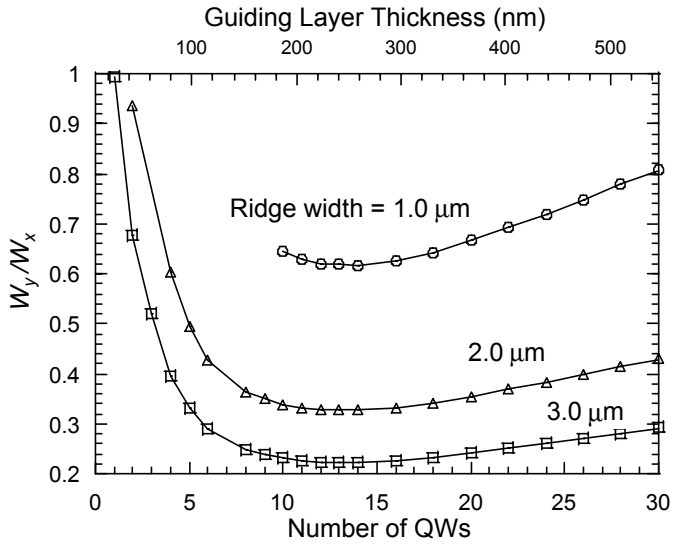

Fig. 2.18 Mode ellipticity (w_y / w_x) for fundamental modes calculated with 3-D BPM for TE polarization and different ridge widths.

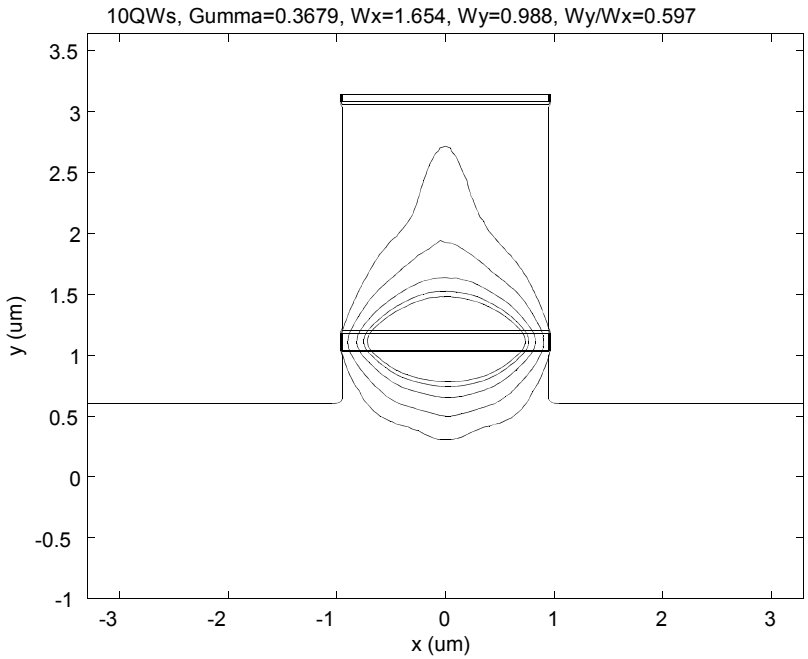

Fig. 2.19 Calculated field contour after propagating through a 400-μm long, 2-μm wide, 10-quantum-well waveguide. The input Gaussian beam has a FWHM of 4 μm. The circles correspond to optical intensities of, from inside to outside, 90%, 75%, 50%, 25%, and 10% of the peak intensity.

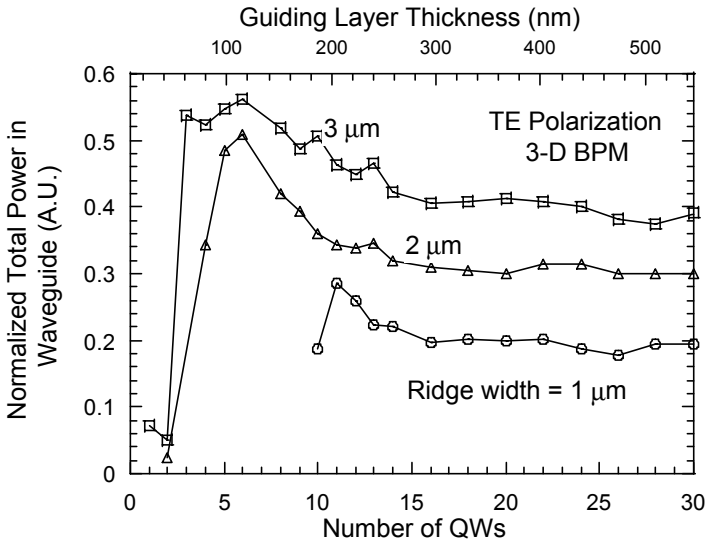

Fig. 2.20 Total optical power after propagating through 400-μm long waveguide calculated with 3-D BPM for TE polarization and different ridge widths. The input optical power is normalized to unity.

The spot size in the transverse direction is sensitive to the thickness of the guiding layer but not to the ridge width. For a thin guiding layer, the spot size is large due to less confinement to the mode. The spot size decreases quickly with the increase of guiding layer thickness and reaches minimum with a quantum well number in the range of 11~13. Further increase in the number of quantum wells increases the core thickness and the spot size, however the increase is not quite dramatic. For practical quantum well numbers (about 8~13), the optical mode shape is highly elliptical, with ellipticities in the ranges of 0.62~0.65, 0.33~0.36, 0.22~0.25 for ridge widths of 1, 2, and 3 μm, respectively (Fig. 2.18).

For a structure with 10 quantum wells and a 2 μm wide ridge, the mode sizes are w_x = 1.08 μm, w_y =0.36 μm. According to the Gaussian approximation (Equation 2.8) the coupling loss will be 10.46 dB for a fiber mode size of 4 μm. This value is far away from what practically obtained values of about 5~6-dB insertion loss per facet with anti-reflection coating. Besides the fact that the mode is not an ideal Gaussian, one important reason is that since the waveguide is usually very short, the optical mode does not fully convert to the fundamental mode before it exits the output facet. Also, the waveguide is actually multi-mode in lateral

direction, which can have some optical power coupled into the higher order modes. Fig. 19 shows the output field contour of the optical signal after propagating through a 400-μm long, 2-μm wide, 10-quantum-well waveguide. The total optical power after propagating through 400-μm long waveguide with different ridge width and number of QWs are shown in Fig. 2.20. Here the QWs are assumed to be lossless. As shown in the figure, the largest coupling efficiency could be achieved with a quantum well number of 6 for a ridge width of 2 μm. However, the optical confinement factor becomes quite small, which will cause the extinction ratio to reduce to about half of that for a 10 QW one provided with the same electric field (Equation 2.13). From Fig. 2.20, the coupling loss is about 4.43 dB/per-facet for a 2-μm wide, 10-quantum-well waveguide, which is close to the actual measurement.

The p-cladding thickness is an important parameter in waveguide design because if this layer is too thin, the cap layer (lattice matched InGaAs has an absorption wavelength of 1.67 μm) will cause large optical loss, while a too thick cap layer will cause deeper Beryllium diffusion into the intrinsic region. Fig. 2.21 shows the optical confinement factor for the 0.1-μm-thick cap layer as a function of the p-cladding layer thickness in a waveguide structure with 2-μm-wide ridge and 10-QW active region. Also shown is the optical confinement factor of the quantum well region. By numerical fitting (solid line in the plot), the cap layer optical confinement factor is related to the p-cladding layer thickness by

$$\Gamma_{cap} = 0.11657 \cdot \exp(-5.2887 \cdot t_{pclad}), \tag{2.14}$$

where t_{pclad} is the thickness of the p-cladding layer in unit of μm.

Assuming an absorption coefficient of 10000 cm^{-1} for lattice matched InGaAs at 1.55 μm, the modal absorption coefficient of the cap layer is shown on the right vertical scale. Assuming the same absorption coefficient for the well, then the active region modal-absorption-coefficient should multiply this 10000 cm^{-1} by the active region confinement factor and $t_w/(t_w + t_b)$, where the latter takes into account the well thickness in the QW region.

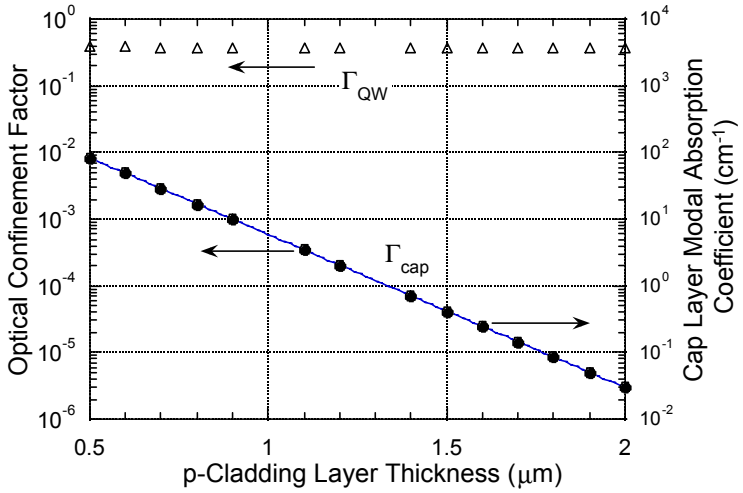

Fig. 2.21 Optical confinement factor as a function of the p-cladding layer thickness calculated with 3-D BPM program (left vertical scale). The waveguide is assumed to be 2-μm-wide and with 10 QWs. The right vertical scale shows the modal absorption coefficient of the 0.1-μm cap layer. The solid line is an exponential fit to the cap layer confinement factor.

2.6 Summary

This chapter has discussed the design of the optical waveguide material structure for achieving low drive voltage, polarization insensitivity and high coupling efficiency with single mode optical fibers.

It has been shown both theoretically and experimentally that the quantum confined Stark shift can be increased by using spiked InGaAs/InAlAs quantum wells due to the increase of effective quantum well width. By utilizing tensile strained quantum well, polarization insensitivity has been achieved. Based on 3-D beam propagation simulation and 2-D mode matching simulation, design rules for achieving high coupling efficiency with single mode optical fibers have been presented.

References

[1] S. Nojima and K. Wakita, "Optimization of quantum well materials and structures for excitonic electroabsorption effects," *Appl. Phys. Lett.*, vol. 53, pp. 1958-1960, 1988.

[2] E. Bigan, M. Allovon, M. Carre, C. Braud, A. Carenco, and P. Voisin, "Optimization of optical waveguide modulators based on Wannier-Stark localization: an experimental study," *IEEE J. Quantum Electron.*, vol. 28, pp. 214-223, 1992.

[3] M. K. Chin, P. K. L. Yu, and W. S. C. Chang, "Optimization of multiple quantum well structures for waveguide electroabsorption modulators," *IEEE J. Quantum Electron.*, vol. 27, pp. 696-701, 1991.

[4] K. Kawano, K. Wakita, O. Mitomi, I. Kotaka, and M. Naganuma, "Design of InGaAs-InAlAs multiple-quantum-well (MQW) optical modulators," *IEEE J. Quantum Electron.*, vol. 28, pp. 224-230, 1992.

[5] W. Franz, *Z. Naturforsch.*, vol. 13, pp. 484, 1958.

[6] L. V. Keldysh, *Sov. Phys.*, vol. JETP7, pp. 788, 1953.

[7] J. D. Dow and D. Redfield, "Electroabsorption in semiconductors: The excitonic absorption edge," *Phys. Rev. B, Solid State*, vol. 1, pp. 3358-3371, 1970.

[8] I. A. Merkulov and V. I. Perel, "Effects of electron-hole interaction on electroabsorption in semiconductors," *Phys. Lett. A*, vol. 45A, pp. 83-84, 1973.

[9] D. A. B. Miller, D. S. Chemla, T. C. Damen, A. C. Gossard, W. Wiegmann, T. H. Wood, and C. A. Burrus, "Electric field dependence of optical absorption near the band gap of quantum-well structures," *Phys. Rev. B, Condens. Matter*, vol. 32, pp. 1043-1060, 1985.

[10] D. A. B. Miller, D. S. Chemla, and S. Schmitt-Rink, "Relation between electroabsorption in bulk semiconductors and in quantum wells: the quantum-confined Franz-Keldysh effect," *Phys. Rev. B, Condens. Matter*, vol. 33, pp. 6976-6982, 1986.

[11] I. Kotaka, K. Sato, K. Wakita, M. Yamamoto, and T. Kataoka, "High-speed (20 Gb/s), low-drive voltage (2 V/sub p-p/) strained InGaAsP MQW modulator/DFB laser light source," *Electron. Commun. Jpn. 2, Electron.* , vol. 78, pp. 1-9, 1995.

[12] J. S. Weiner, D. S. Chemla, D. A. B. Miller, T. H. Wood, D. Sivco, and A. Y. Cho, "Room-temperature excitons in 1.6- μm band-gap GaInAs/AlInAs quantum wells," *Appl. Phys. Lett.*, vol. 46, pp. 619-621, 1985.

[13] G. Bastard, E. E. Mendez, L. L. Chang, and L. Esaki, "Variational calculations on a quantum well in an electric field," *Phys. Rev. B, Condens. Matter*, vol. 28, pp. 3241-3245, 1983.

[14] F. Devaux, P. Bordes, A. Ougazzaden, M. Carre, and F. Huet, "Experimental optimisation of MQW electroabsorption modulators with up to 40 GHz bandwidths," *Electron. Lett.*, vol. 30, pp. 1347-1348, 1994.

[15] S. Nojima, Y. Kawaguchi, K. Nakashima, and K. Wakita, "Field-induced energy shift of excitonic absorption in InGaAs/InP multiquantum wells grown by metalorganic molecular beam epitaxy," *Jpn. J. Appl. Phys. 2, Lett.*, vol. 26, pp. 1927-1928, 1987.

[16] S. Nojima, Y. Kawamura, K. Wakita, and O. Mikami, "Electric field effects in excitonic absorption for high-quality InGaAs/InAlAs multiple-quantum-well structures," *J. Appl. Phys.*, vol. 64, pp. 2795-2797, 1988.

[17] F. Devaux, J. C. Harmand, I. F. L. Dias, T. Guettler, O. Krebs, and P. Voisin, "High power saturation, polarisation insensitive electroabsorption modulator with spiked shallow wells," *Electron. Lett.*, vol. 33, pp. 161-163, 1997.

[18] S. Chelles, R. Ferreira, and P. Voisin, "On the design of polarization-insensitive optoelectronic devices," *Semicond. Sci. Technol.*, vol. 10, pp. 105-109, 1995.

[19] M. Suzuki, H. Tanaka, and Y. Matsushima, "InGaAsP electroabsorption modulator for high-bit-rate EDFA system," *IEEE Photonics Technol. Lett.*, vol. 4, pp. 586-588, 1992.

[20] T. Aizawa, K. G. Ravikumar, S. Suzaki, T. Watanabe, and R. Yamauchi, "Polarization-independent quantum-confined Stark effect in an InGaAs/InP tensile-strained quantum well," *IEEE J. Quantum Electron.*, vol. 30, pp. 585-592, 1994.

[21] G. Bastard, *Wave Mechanics Applied to Semiconductor Heterostructures*: Les Ulis: Editions de Physique, 1988.

[22] T. H. Wood, T. Y. Chang, J. Z. Pastalan, C. A. J. Burrus, N. J. Sauer, and B. C. Johnson, "Increased optical saturation intensities in GaInAs multiple quantum wells by the use of AlGaInAs barriers," *Electron. Lett.*, vol. 27, pp. 257-259, 1991.

[23] K. Wakita, Y. Kawamura, M. Nakao, and H. Asahi, "Long wavelength waveguide multiple quantum well optical modulators," *IEEE J. Quantum Electron.*, vol. QE-23, pp. 2210-2215, 1987.

[24] T. H. Wood, J. Z. Pastalan, C. A. Burrus, Jr., B. C. Johnson, B. I. Miller, J. L. deMiguel, U. Koren, and M. G. Young, "Electric field screening by photogenerated holes in multiple quantum wells: A new mechanism for absorption saturation," *Appl. Phys. Lett.*, vol. 57, pp. 1081-1083, 1990.

[25] M. Suzuki, H. Tanaka, and S. Akiba, "Effect of hole pile-up at heterointerface on modulation voltage in GaInAsP electroabsorption modulators," *Electron. Lett.*, vol. 25, pp. 88-89, 1989.

[26] F. Devaux, E. Bigan, A. Ougazzaden, F. Huet, M. Carre, and A. Carenco, "High-speed InGaAsP/InGaAsP MQW electroabsorption modulator with high optical power handling capacity," *Electron. Lett.*, vol. 28, pp. 2157-2159, 1992.

[27] S. Y. Wang and S. H. Lin, "High speed III-V electrooptic waveguide modulators at λ=1.3 μm," *J. Lightwave Technol.*, vol. 6, pp. 758-771, 1988.

[28] T. Tanaka and Y. Suematsu, "An exact analysis of cylindrical fiber with index distribution by matrix method and its application to focusing fiber," *Trans. Inst. Electron. Commun. Eng. Jpn. E, Engl.*, vol. E59, pp. 1-8, 1976.

[29] BeamProp, software by RSoft, Inc., Ossining, NY.

[30] C. H. Henry, L. F. Johnson, R. A. Logan, and D. P. Clarke, "Determination of the refractive index of InGaAsP epitaxial layers by mode line luminescence spectroscopy," *IEEE J. Quantum Electron.*, vol. QE-21, pp. 1887-1892, 1985.

[31] A computer program written by Zuon-Min Chuang that calculates wave function and mode effective index of GaAs/AlGaAs/GaAs, InGaAs/InAlAs/InP and InGaAsP /InGaAsP/InP slab waveguides.

CHAPTER 3

Traveling-Wave Electrode Design

The previous chapter discusses the design of quantum-well and optical waveguide for achieving low drive voltage, polarization insensitive, low insertion-loss electroabsorption modulators. However, these designs only consider the static response of the modulator. This chapter will focus on the design issues in achieving high-speed operation using traveling-wave electrode structures.

In a traveling-wave electroabsorption modulator, the electrical signal co-propagates with the optical signal. The speed limiting factors in a traveling-wave electroabsorption modulator will include carrier sweep out time [1], microwave loss at high frequencies, and optical-electrical group velocity mismatch [2].

Large electron or hole sweep out times are related to the conduction or valence band discontinuities, and will limit the device performance at high input optical power levels. Bandgap engineering can solve this problem as discussed in Chapter 2. A further discussion will be given in Chapter 5 on power saturation characteristics.

As will be shown in Section 3.3 of this chapter, group velocity mismatch is not the main speed-limiting factor for TEAM as well because of the very short interaction length.

In this chapter, we will show that the most important issue for TEAM design is to reduce microwave propagation and reflection losses. The higher propagation loss at high frequencies is because of the larger conductor loss due to the thinner skin depth, and larger shunt current through the resistive layers at high frequencies. The larger reflection loss at high frequencies is because of the smaller characteristic impedance, which is again related to the skin effect in metal.

3.1 Transmission Line Structures

The first step in electrode design is to choose proper transmission line structure. Considering the very small size of the modulator waveguide (usually several hundred micrometers in length), proper microwave transmission feed lines and contact pads are necessary for practical application. The need for integrated

circuit interconnections has driven the study of different planar microwave transmission lines. Fig. 3.1 shows four most possible candidates for TEAMs [3]. Microstrip was evolved from stripline, which has upper and bottom ground planes and dielectric slab to fully cover the center conductor. Other than stripline that supports true transverse electromagnetic (TEM) mode, microstrip can not support a true TEM mode due to the inhomogeneous dielectric. In order to match electric and magnetic fields at the air-dielectric interface, the total fields must be described in terms of infinite series of coupled TE- and TM-modes. As frequency increases, the currents on the conductors develop transverse components because the fields have longitudinal components. Nevertheless, at least at lower frequencies, the microstrip appears to have characteristics much like a TEM line. This has led to the concept of quasi-TEM approximation up to some upper frequency limit.

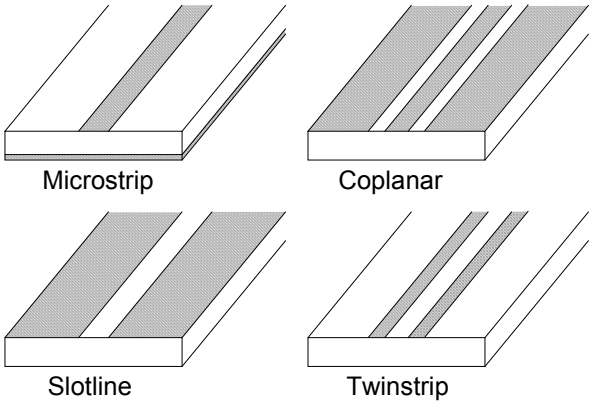

Fig. 3.1 Planar microwave transmission lines.

Microstrip has several practical problems arising from its structure. Firstly, the structure must be fabricated on a highly conducting substrate, which will induce large microwave loss. For an n^+-InP substrate with a resistivity of 2.0×10^{-3} Ω cm, the skin depth will be 11.2 μm at 40 GHz (Fig. 3.9). Penetrated fields will induce current flows in the 'resistive' substrate and contribute to microwave loss. Secondly, direct dependence of the characteristic impedance on the thickness of the substrate makes it difficult to achieve repeatability from batch to batch. Third,

even with lossless substrate, the inductance will be large due to the thick substrate, and contribute to large microwave loss. To achieve very thin substrate, special semiconductor device processing techniques so as to transfer the thin epilayer to a new highly conductive substrate, such as gold, need to be developed [4]. Fourth, at higher frequencies the substrate must be very thin to prevent higher order mode propagation. Fifth, practical problem in utilizing microstrip line structure in electroabsorption modulator is the difficulty in fabricating input and output contact pads on the conductive substrate. Based on these reasons, microstrip was not a proper structure for traveling-wave electroabsorption modulators.

For integrated circuit application, it's very important that both the signal and ground lines are accessible easily. For microstrip the ground plane is inaccessible without making a hole in the substrate and passing or plating a conductor through. Coplanar waveguide (CPW) was proposed by moving the ground plane to the same side of the substrate as the center conductor [5]. In CPW structure, the substrate does not necessarily conduct current – it can be made of semi-insulating substrate. So the microwave loss from the substrate can be avoided, and big contact pads can be fabricated without introducing extra loss or capacitance. The substrate can be thick and the ground plane is at hand for connecting other elements – suitable for packaging with high-speed connectors (such as K- or V-connectors). These, together with other important features make CPW the best configuration for traveling-wave EA modulators.

Besides microstrip and CPW, twin-strip and slot-line are also possible structures for TEAM. It can be seen from Fig. 3.1 that twinstrip and CPW are geometrically the same, except that they have complementary metal structures; where one has metal, the other has none, and vice versa. These structures are electromagnetic duals, or complementary structures. CPW is unbalanced electrically with respect to ground, while twinstrip is balanced. This makes CPW suitable for connecting with standard high-speed connectors such as K- and V-connectors, which are also unbalanced transmission lines. When the twinstrip conductors are expanded to infinity, a slot-line is obtained. The slot-line is not a quasi-TEM line. Just like twinstrip, slot-line is a balanced line and will also have difficulty in connecting to unbalanced coaxial cables. Twinstrip and slot-lines are

special cases of asymmetric double-strip coplanar waveguide (CPS), whose conductor widths can be unequal [6].

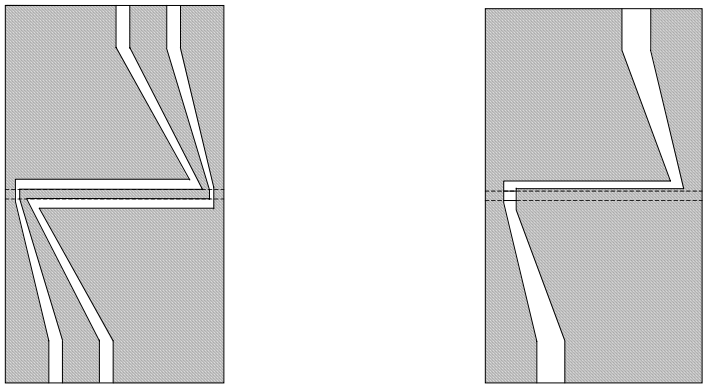

(a) Coplanar waveguide (CPW) (b) Double-strip coplanar waveguide (CPS)

Fig. 3.2 Schematic diagrams of possible electrode structures for traveling-wave EA modulators using coplanar waveguide and double-strip coplanar waveguide structures. The optical waveguides are represented as dashed lines in the center of the devices. The CPS structure is ruled out due to its balanced transmission line feature and the very narrow gap width to achieve 50 Ω.

Even though CPS is a balanced transmission line, it could still be a good candidate because suitable high-speed probes are available. Fig. 3.2 shows the TEAM schematic diagrams of electrode structures using coplanar waveguide and double-strip coplanar waveguide structures. One important issue is to design the transmission feed lines such that they match the driver/load impedances. Fig. 3.3 shows the required gap width for achieving different target characteristic impedance values using double-strip coplanar waveguide [6]. Here the metal was considered to have zero thickness and the substrate was 100 μm thick. The result will not differ much with finite metal thickness. As can be seen, very small gap widths (e.g. 0.8 μm for 10-μm signal width, 1.7 μm for 20-μm signal width) are required to achieve a characteristic impedance of 50 Ω. These small gap widths make it impractical for making feed lines on InP substrate.

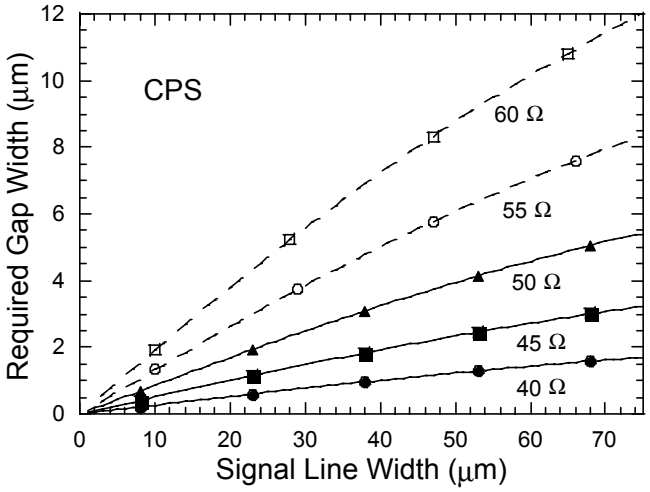

Fig. 3.3 Calculated gap width as a function of signal line width for different target characteristic impedance values for double-strip coplanar waveguide, assuming equal signal line widths for the two conductors, ε_r=12.4, substrate thickness = 100 μm. Calculation was done with the model discussed in reference [6].

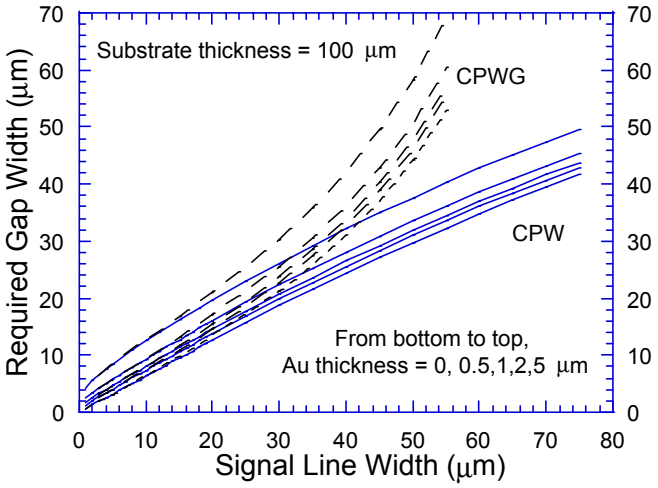

Fig. 3.4 Gap width for 50 Ω coplanar waveguide as a function of signal line width for different metal thickness values. Calculation was done with LineCalc, ε_r=12.4, substrate thickness = 100 μm.

Fig. 3.4 shows the required gap width calculated with LineCalc [7] for 50 Ω coplanar waveguide with different metal thickness values. Together shown is the case of coplanar waveguide with ground plane located at the bottom of the substrate (CPWG). Due to the increased capacitance associated with the thicker

metal, the gap width is slightly increased with the increase of metal thickness. In a package, the device is usually mounted on top of metal for good heat sinking and ground connection. The introduction of a ground plane at the bottom of the substrate increases the capacitance. This effect becomes prominent for wide signal lines. A ground plane will pull the impedance of a 48 Ω coplanar waveguide with signal/gap/substrate thickness of 55/33.2/100 μm down to 44 Ω. Fig. 3.5 shows the characteristic impedance as a function of substrate thickness for two signal-line /gap width configurations. For a usual substrate thickness in the range of 70 ~ 100 μm, the change in impedance due to the ground plane can be as large as 20% for a 55/33.2/70 μm line and should be taken into account in the design. On the other hand, the impedance variation can be less than 7% with signal and gap widths of 10 and 9.3 μm. Fortunately ground-plane effect is small for small signal line widths. The optical waveguide and most of the feed line regions are not affected by this extra grounding effect.

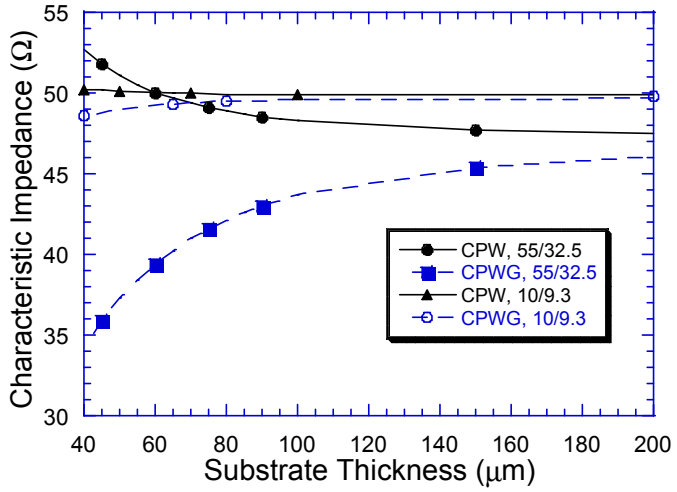

Fig. 3.5 Characteristic impedance as a function of substrate thickness.

3.2 Equivalent Circuit Model

The study of microwave transmission lines on multi-layered semiconductor structures was first done with metal-insulator-semiconductor (MIS) microstrip

structures for integrated circuit interconnects and Schottky contact transmission line [8-11]. The understanding of the properties of this structure can help us understand that of a CPW line. Fig. 3.6 shows a schematic diagram of such an MIS structure for integrated interconnects.

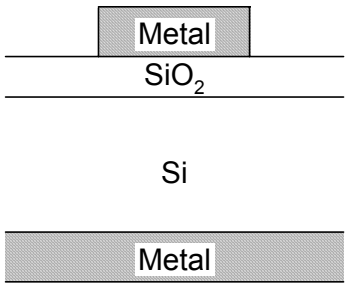

Fig. 3.6 Metal-insulator-semiconductor (MIS) microstrip line for integrated circuit interconnects.

There are three fundamental modes that exist in the microstrip, i.e., "dielectric quasi-TEM mode", "skin-effect mode", and "slow-wave mode", depending on the resistivity of the substrate and the frequency range [10].

1) When the product of the frequency and the resistivity of the Si substrate is large enough to produce a small dielectric loss angle, the substrate acts like a dielectric. The fundamental mode would closely resemble to the TEM mode, as long as the wavelength is much larger than the thickness of the double layer. In the dielectric quasi-TEM mode the line can be regarded as a microstrip line loaded with a double layer dielectric consisting of silicon and silicon dioxide.
2) When the frequency and substrate conductivity is large enough to yield a small depth of penetration into silicon, the substrate would behave like a lossy conductor wall. In the skin-effect mode, the line may be treated as a microstrip line on the imperfect ground plane made of silicon. Microstrip EA modulators fabricated on n^+-InP substrate ($\rho \sim 2\times10^{-3}$ Ω-cm) will have a strong skin-effect mode within the tens of gigaherz frequency range, where the skin depth is in the range of a couple of micrometers to tens of micrometers and is usually smaller than the substrate thickness.
3) When the frequency-resistivity product is moderate, the waveguide fundamental mode is a "slow-wave" mode, whose phase velocity is slower than

expected simply from the permittivity and permeability of the media. The "slow-wave" mode is of special interest because it appears within the resistivity and frequency ranges suited for the monolithic circuit technology.

Generally a "full-wave" solution will be needed to analyze the "slow-wave" mode of the microstrip line as well as other transmission lines, either by two-dimensional mode matching method [8-11], or by much complicated three-dimensional full-wave analysis [12-19]. These 3-D full-wave treatments have been based on either the classical mode-matching (MM) method [12, 13, 15], the spectral-domain analysis (SDA) method [16-19], or the finite-element method (FEM) [14]. These "full-wave" solutions typically involve considerable numerical computation. Fortunately, a quasi-TEM analysis, which includes metal losses, has been seen to satisfactorily describe the properties of transmission lines operating at "slow-wave" modes [20-26].

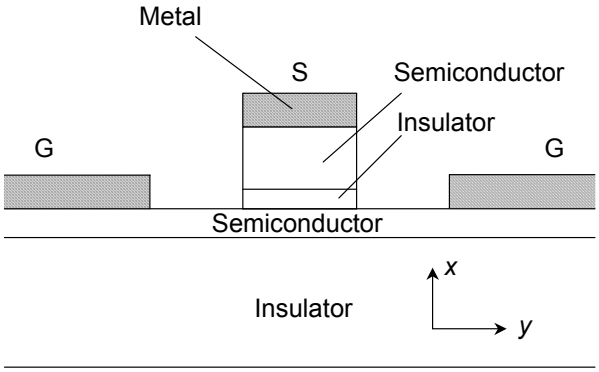

Fig. 3.7 Schematic cross-section of a hybrid-coplanar waveguide structure.

The device geometry chosen for fabrication is a hybrid-coplanar waveguide structure as shown in Fig. 3.7. It's a hybrid structure of coplanar waveguide and microstrip – its propagating mode has characteristics of both microstrip and CPW modes. The currents are primary carried in the metal conductors and nearly all of the voltage drops across the insulator layer. Thus, the magnetic field distribution is nearly that of CPW, while the electric field pattern is similar to that of a microstrip structure. This hybrid-coplanar structure has been successfully used in fabricating ultra-high speed traveling-wave photodetectors [27, 28]. Equivalent-circuit models

have been developed to describe the propagation characteristics of metal-insulator-semiconductor (MIS) coplanar structures (figure 3.6) and hybrid-coplanar structures (figure 3.7). Good agreement has been obtained between measurements and full-wave simulations [14, 20-26].

Fig. 3.8 (a) defines the structural dimensions and material properties that lead to the equivalent-circuit of Fig. 3.8 (c). Here we only consider the case with semi-insulating substrate, where ρ_{sub} can be as large as 2e7 ~ 1e8 Ω-cm and can be treated as insulator. In order to simulate cases when the side wall of the waveguide is not 90^o, a variable angle is assumed. The bottom ground plane is optional; it exists when the device is mounted onto a conductive metal mount. Since most of the capacitance is from the intrinsic layer, the bottom ground plane will mainly affect the inductance.

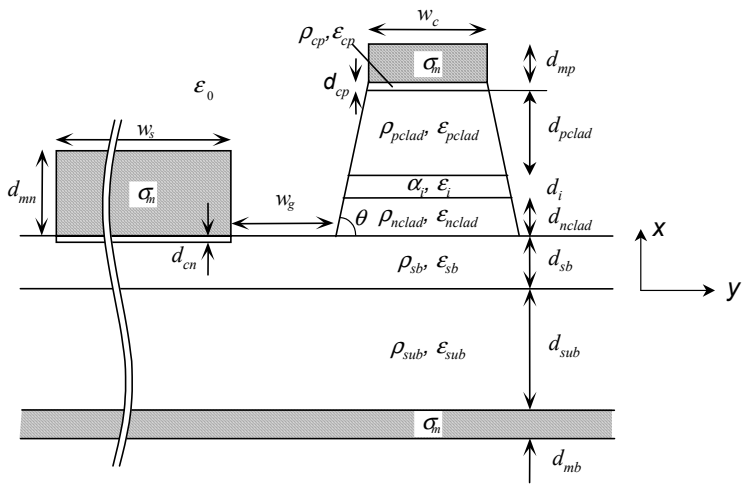

(a)

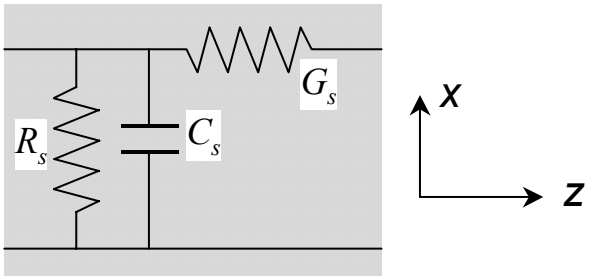

(b)

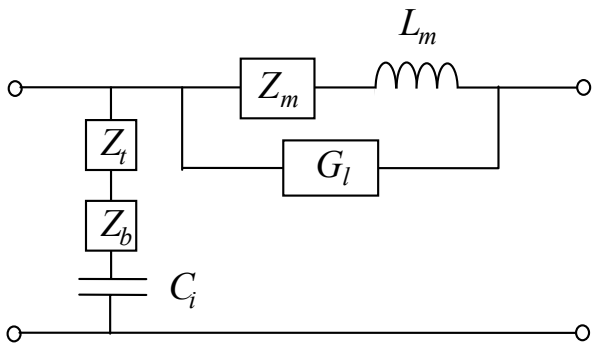

(c)

Fig. 3.8 (a) Hybrid-coplanar TEAM structural dimensions and material properties; (b) Equivalent circuit of each cladding layer; (c) Equivalent-circuit model for transmission line characteristics. Element values are listed in Table 3.1.

$Z_m = \dfrac{\eta_{xm0t}}{w_c}$	$L_m = L_{CPW}$	$w_1 = w_c$
$Z_{cp} = \dfrac{\rho_{cp}}{1 + j\omega\rho_{cp}\varepsilon_{cp}} \cdot \dfrac{1}{2\cot\theta} \cdot \ln\left(\dfrac{w_2}{w_1}\right)$		$w_2 = w_1 + 2d_{cp}\cot\theta$
$Z_{pclad} = \dfrac{\rho_{pclad}}{1 + j\omega\rho_{pclad}\varepsilon_{pclad}} \cdot \dfrac{1}{2\cot\theta} \cdot \ln\left(\dfrac{w_3}{w_2}\right)$		$w_3 = w_2 + 2d_{pclad}\cot\theta$
$C_i = \dfrac{2\varepsilon_i \cot\theta}{\ln(w_4 / w_3)}$		$w_4 = w_3 + 2d_i \cot\theta$
$Z_{nclad} = \dfrac{\rho_{nclad}}{1 + j\omega\rho_{nclad}\varepsilon_{nclad}} \cdot \dfrac{1}{2\cot\theta} \cdot \ln\left(\dfrac{w_5}{w_4}\right)$		$w_5 = w_4 + 2d_{nclad}\cot\theta$
$Z_b = \dfrac{\rho_{sb}}{1 + j\omega\rho_{sb}\varepsilon_{sb}} \cdot \dfrac{(w_5/6 + w_g + w_T)}{2d_{sb}} \cdot$		$w_T = \sqrt{\dfrac{\rho_{cn}}{\rho_{sb}} \cdot \dfrac{1 + j\omega\rho_{sb}\varepsilon_{sb}}{1 + j\omega\rho_{cn}\varepsilon_{cn}} d_{cn} d_{sb}}$
$G_{cp} = \dfrac{(w_1 + w_2)d_{cp}}{6\rho_{cp}}$		$G_{pclad} = \dfrac{(w_2 + w_3)d_{pclad}}{6\rho_{pclad}}$
$G_{nclad} = \dfrac{(w_4 + w_5)d_{nclad}}{6\rho_{nclad}}$		
$Z_t = Z_{cp} + Z_{pclad} + Z_{nclad}$		$G_l = G_{cp} + G_{pclad} + G_{nclad}$

Table 3.1 Hybrid-coplanar TEAM element values for the equivalent circuit model in Fig. 3.8 with $\theta \neq 90^o$. ρ is the resistivity and σ=1/ρ is conductivity; ε and μ are permittivity and permeability.

Table 3.1 shows the hybrid-coplanar TEAM element values for the equivalent-circuit mode [26]. The two cladding layers are modeled as a resistor parallel with a capacitor in the transverse direction, and a conductance in the longitudinal direction (Fig. 3.8(b)). In the case of non-90^o angle, the transverse capacitance and resistance are intermixed and are calculated by integration. Thin contact layers are modeled to account for the contact resistance. The metal impedance of the two ground planes is ignored because the impedance of the signal line metal is much larger. Similarly the conductance of the bottom semiconductor layer is neglected because the conductance of the p-cladding and n-cladding layers is much less.

η_{xm0t} is the transverse wave impedance of the metal-air layers and is given by [11, 26]

$$\eta_{xm0t} = \eta_m \coth\left[(1+j)\frac{d_{mp}}{\delta_{sm}}\right] \tag{3.1}$$

where $\eta_m = \sqrt{j\omega\mu_0/\sigma_m}$ is the wave impedance in metal, $\delta_{sm} = \sqrt{2/\omega\mu_0\sigma_m}$ is the skin depth in metal. η_{xm0t} reaches $1/\sigma_m d_m$ at low frequencies, and η_m at high frequencies.

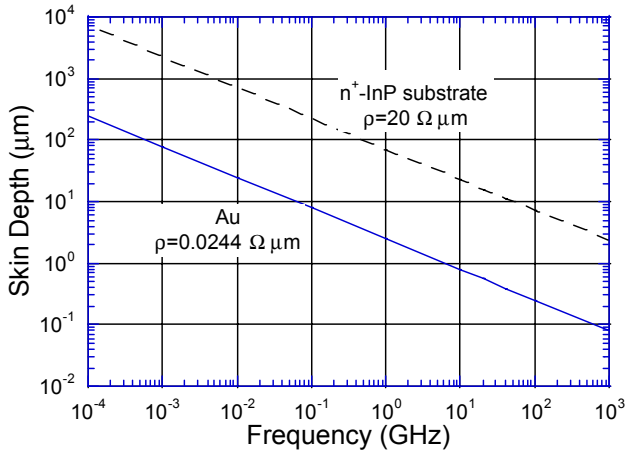

Fig. 3.9 Skin depth as a function of microwave frequency for gold and n$^+$-InP substrate.

Fig. 3.9 shows the skin depth for gold and n$^+$-InP substrate as a function of the microwave frequency. The n$^+$-InP resistivity is 20 Ω–μm [29]. As can be seen,

at a frequency of 40 GHz, the skin depth is less than 0.4 μm in gold, while in n^+-InP substrate it is about 11 μm, a value thicker than the epilayers but thinner than the substrate.

The inductance, L_m, is equal to that of CPW with identical metal pattern, and can be found from a commercial program such as LineCalc [7]. However, an analytical form will sometimes be much desired and is given in Appendix B. This analytical form is used to calculate tapered feed line regions.

The transverse impedance, Z_t, is composed of the transverse impedance from the p-contact layer, p-cladding layer and n-cladding layer. The impedance of the bottom n-conducting layer, Z_b, is composed of terms for the spreading resistance under the ridge, the bulk resistance of the gap, and the resistance of the ground contact. The spreading resistance includes a factor of 1/2 for the structural symmetry and a factor of 1/3 that results from the current distribution. The bottom contact resistance is proportional to the transfer length, w_T. The whole impedance is multiplied with 1/2 because of the double ground lines.

The conductance at the longitudinal direction, G_l, is composed of the longitudinal conductance from the p-contact layer, the p-cladding layer, and the n-cladding layer. The conductance from the contact layer is usually much smaller than the contribution from the other two layers because it is very thin.

Table 3.2 shows the equivalent-circuit elements when the angle is 90^o.

$$Z_m = \frac{\eta_{xm0t}}{w_c} \qquad L_m = L_{CPW} \qquad C_i = \varepsilon_i \frac{w_c}{d_i}$$

$$Z_b = \frac{\rho_{sb}}{1 + j\omega\rho_{sb}\varepsilon_{sb}} \cdot \frac{(w_c/6 + w_g + w_T)}{2d_{sb}} \cdot \quad w_T = \sqrt{\frac{\rho_{cn}}{\rho_{sb}} \cdot \frac{1 + j\omega\rho_{sb}\varepsilon_{sb}}{1 + j\omega\rho_{cn}\varepsilon_{cn}} d_{cn} d_{sb}}$$

$$Z_t = \left(\frac{\rho_{cp} d_{cp}}{1 + j\omega\rho_{cp}\varepsilon_{cp}} + \frac{\rho_{pclad} d_{pclad}}{1 + j\omega\rho_{pclad}\varepsilon_{pclad}} + \frac{\rho_{nclad} d_{nclad}}{1 + j\omega\rho_{nclad}\varepsilon_{nclad}} \right) / w_c$$

$$G_l = \frac{w_c d_{cp}}{3\rho_{cp}} + \frac{w_c d_{pclad}}{3\rho_{pclad}} + \frac{w_c d_{nclad}}{3\rho_{nclad}}$$

Table 3.2 Hybrid-coplanar TEAM element values for the equivalent circuit model in Fig. 3.8 with $\theta = 90^o$. ρ is the resistivity and σ=1/ρ is conductivity; ε and μ are permittivity and permeability.

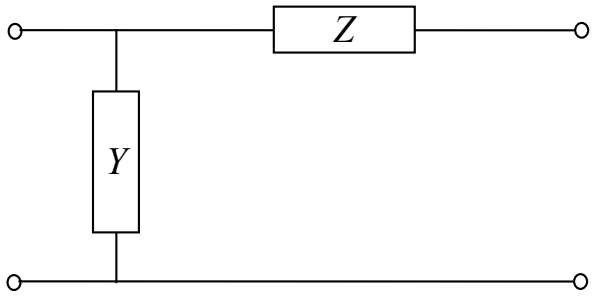

Fig. 3.10 General transmission equivalent-circuit model.

The transmission line propagation characteristics may be found by comparing the equivalent-circuit model of Fig. 3.8 to the general transmission line equivalent-circuit model of Fig. 3.10. The general equivalent-circuit model is composed of series impedance, Z, and shunt admittance Y, per unit length. The coupled differential equations for voltage and current waves are

$$\frac{dV}{dz} = -IZ \tag{3.2a}$$

$$\frac{dI}{dz} = -VY \tag{3.2b}$$

These equations lead to the wave equation,

$$\frac{d^2V}{dz^2} = \gamma^2 V \tag{3.3}$$

And the general solution is

$$V(z) = V_0^+ e^{-\gamma z} + V_0^- e^{\gamma z}, \tag{3.4}$$

where

$$\gamma = \sqrt{YZ} = \alpha_e + j\beta, \tag{3.5}$$

is the propagation constant. Microwave loss and propagation velocity are found directly from the field attenuation constant, α_e, and the propagation phase constant, β. The characteristic impedance of the transmission line is

$$Z_0 = \sqrt{Z/Y}, \tag{3.6}$$

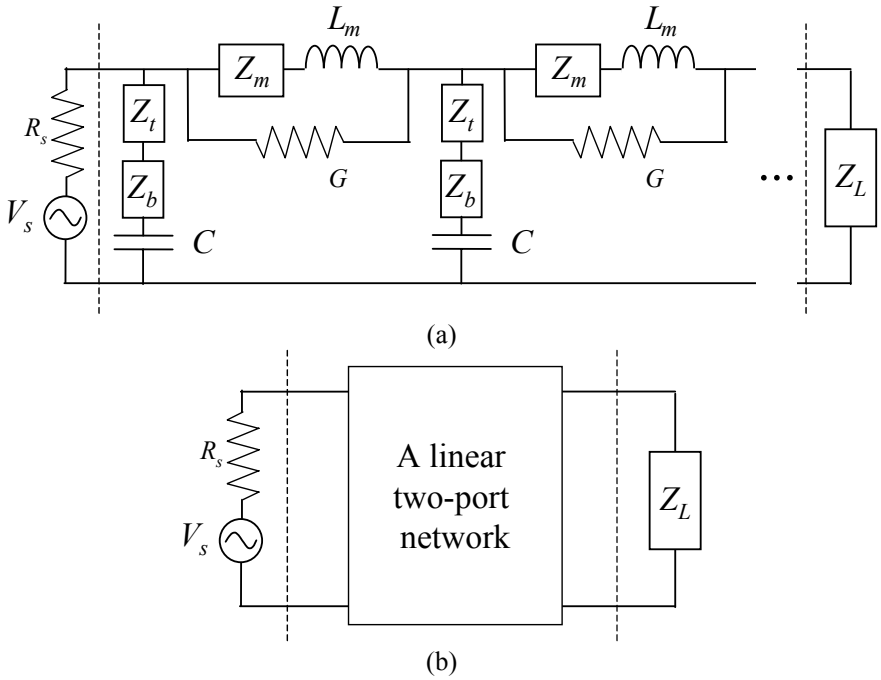

Fig. 3.11 Equivalent circuit diagram of TEAM with input source and load and its two-port network representation.

Fig. 3.11 shows the equivalent circuit diagram of TEAM with source and load connections. The electrical response of the TEAM can be described by its linear two-port network parameters, such as S-parameters [30]. The S parameters are related to the characteristic impedance and the propagation constant by

$$S_{11} = S_{22} = \frac{(\overline{Z}_0^2 - 1)\sinh \gamma l}{2\overline{Z}_0 \cosh \gamma l + (\overline{Z}_0^2 + 1)\sinh \gamma l}, \tag{3.7}$$

$$S_{21} = S_{12} = \frac{\overline{Z}_0}{2\overline{Z}_0 \cosh \gamma l + (\overline{Z}_0^2 + 1)\sinh \gamma l}, \tag{3.8}$$

where $\overline{Z}_0 = Z_0 / Z_{0R}$ is the normalized impedance, Z_{0R} is the reference impedance of the measurement system and is equal to 50 Ω in our case, and l is the length of the waveguide.

S_{21} represents the transmission coefficient through the TEAM. It includes both the microwave propagation loss in the waveguide section and the reflection

loss due to the impedance mismatch. As will be shown later, the propagation loss and the reflection loss often have opposite dependence on device parameters, S_{21} represents the overall performance, and is the ultimate parameter to be optimized.

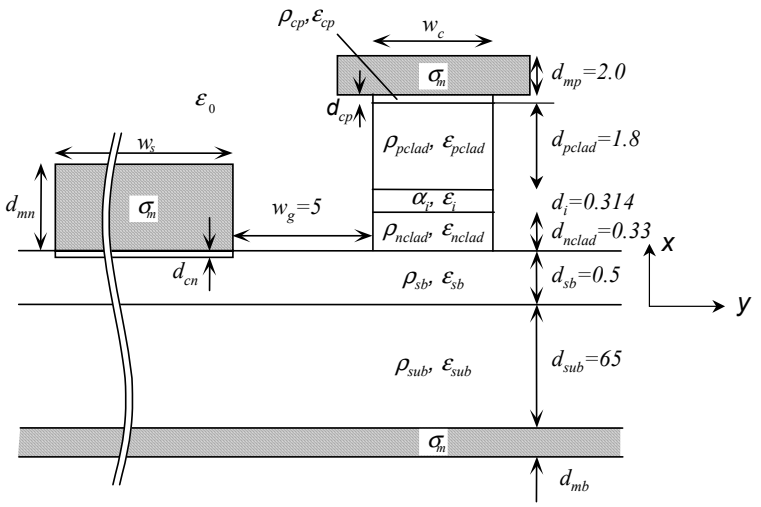

Fig. 3.11 Waveguide structure parameter for the simulation.

Layer	Width (μm)	Thickness (μm)	ρ (Ω-cm)	ε_r
p-metal	6.0	2.0	2.3e-6	
p-contact	2.0	0.01	1.0	12.4
p-cladding	2.0	1.8	0.03	12.4
i	2.0	0.314		12.4
n-cladding	2.0	0.33	4.5e-3	12.4
n-conducting	w_g=5.0	0.5	0.01	12.4
n-contact	20	0.01	1.0	12.4
substrate		65	2e7~1.2e8	12.4

Table 3.3 Parameters for the structure in Fig. 3.11.

By using the equivalent-circuit model, the propagation constants and the characteristic impedance can be readily obtained. It will be of great interest to understand the effect of the circuit elements to the transmission line characteristic parameters. Fig. 3.11 shows the cross-section structure of a device and the parameters are listed in Table 3.3. In order to get a thick metal on top of the ridge a

second metal evaporation is used. This leads to a wider metal width than the ridge width.

In order to study the effect of each circuit element (Fig. 3.8(c)) on the characteristics of the transmission line, Fig. 3.12-3.13 plot the dependence of these elements to frequency.

Fig. 3.12 shows that the longitudinal conductance G_l is much smaller than the one from the conductor, and can be treated as a perturbation throughout the frequency range from DC to 1 THz, $\omega L_m << 1/G_l$ and $Z_m << 1/G_l$. At low frequencies (f<<1 GHz), the metal-air transverse wave impedance dominates the inductance, $\omega L_m << Z_m$, while for high frequencies (f >>40 GHz), the inductance dominates, $\omega L_m > Z_m$. At the medium frequency regime, which is of great interest since the device bandwidth falls in this region, the contribution from the inductance and the metal-air transverse impedance are at the same range.

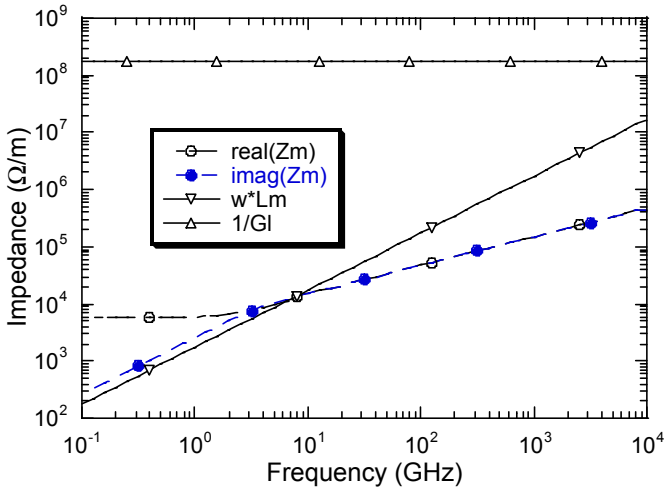

Fig.3.12 Comparison of metal-air transverse wave impedance, Z_m, inductance, *Lm,* and semiconductor longitudinal conductance, G_l.

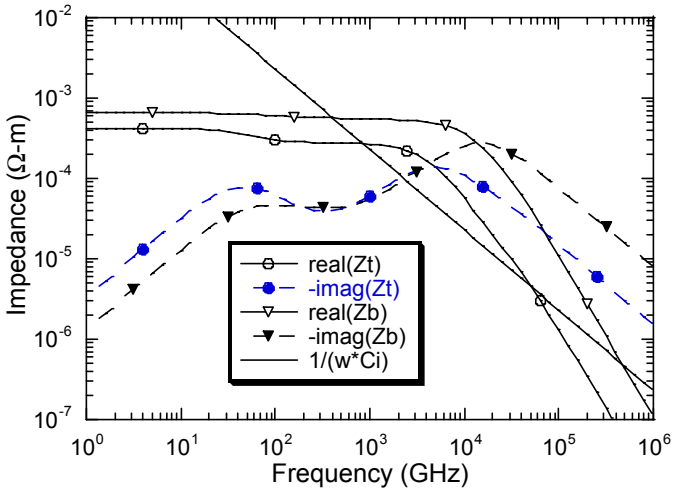

Fig.3.13 Comparison of transverse impedance, Z_t, n-conducting layer impedance, Z_b, and intrinsic layer capacitance, C_i.

From Fig. 3.13, the semiconductor layers are more resistive than capacitive up to 1 THz. The intrinsic layer capacitance dominates up to hundreds of gigaherz. So for the frequency range we are interested in (DC to 50 GHz), we can represent the impedance of all semiconductor layers with a single resistance, $R = R_t + R_b$, where $R_t = R_{cp} + R_{pclad} + R_{nclad}$, and we have $R << 1/\omega C_i$. The n-conducting layer resistance is larger than the p-cladding layer resistance and might be the dominant loss source. For frequencies as high as a few tens of THz, the frequency reaches the dielectric relaxation frequencies of the semiconductor layers and the semiconductor acts as a dielectric, the mode is a dielectric quasi-TEM mode.

Before getting into the specific simulations, an extreme case analysis will help us get into the general behavior of the propagation constant and the characteristic impedance.

At very low frequencies, $R << 1/\omega C_i$, $\omega L_m << Z_m$, and $\omega L_m << 1/G_l$, the elements R, L_m, and G, can be neglected. The complex propagation constant and characteristic impedance are given by

$$\gamma \approx \sqrt{j\omega Z_m C_i} = \sqrt{\frac{\omega Z_m C_i}{2}}(1+j), \tag{3.9}$$

$$Z_0 \approx \sqrt{\frac{Z_m}{j\omega C_i}} = \sqrt{\frac{Z_m}{2\omega C_i}}(1-j), \tag{3.10}$$

At this low frequency regime, the field attenuation coefficient is proportional to the square root of frequency (at very low frequencies Z_m is not much dependent on frequency as shown in Fig. 3.12).

At mid-frequency range ($R << 1/\omega C_i$, $Z_m << \omega L_m$, and $\omega L_m << 1/G_l$) the complex propagation constant and characteristic impedance can be written as

$$\gamma \approx \frac{\omega^2}{2v_e}(RC_i + G_l L_m) + j\frac{\omega}{v_e}, \tag{3.11}$$

$$Z_0 \approx R_0\left[1 + j\frac{\omega}{2}(RC_i - G_l L_m)\right], \tag{3.12}$$

where $v_e \equiv \omega/\beta = 1/\sqrt{L_m C_i}$ and $R_0 \equiv \sqrt{L_m / C_i}$ are phase velocity and characteristic impedance for a transmission line with pure L_m and C_i. At this frequency the loss is proportional to the square of the frequency. The real part of the impedance is equal to that of a lossless line, while the imaginary part is proportional to the frequency.

3.3 Velocity Mismatch

Before getting into the process of optimizing the microwave loss due to impedance mismatch-induced reflection loss and propagation loss, let's first take a look at the velocity mismatch effect in TEAM.

With the structure given in Fig. 3.11 and parameters in Table 3.3, the phase velocity of the microwave is readily calculated using Eq.3.5. Fig. 3.14 shows the calculated phase velocity of microwave for different ridge widths. Together shown is the optical phase velocity calculated from BPM simulation. As shown in the figure, the microwave phase velocity is close to or higher than 50% of that of the

optical wave. Considering a device length of 300 μm, the velocity mismatch-length product is 0.15%-cm. The time difference for the two waves to pass the device will be about 3ps. Also, considering the exponential absorption characteristics, the velocity mismatch limited bandwidth should be over 100 GHz [31]. Even though the group velocities can be a little bit different from the phase velocities, we can still conclude that the group velocity mismatch limited bandwidth will be much higher than the range we are considering (DC to 50 GHz). Based on this reason, the design will mostly focus on reducing the microwave loss at high frequencies, either by reducing the reflection loss, or by reducing the propagation loss.

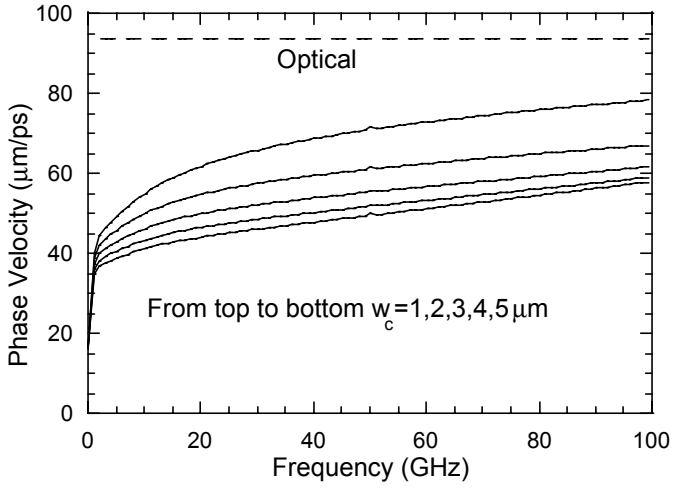

Fig. 3.14 Phase velocity calculated as a function of frequency for different ridge widths. Except for the ridge width, the other structure parameters are listed in Table 3.3.

3.4 Microwave loss sources

Considering the general equivalent-circuit model Fig. 3.8 (c) and Eq. 3.5, neglecting the conductance G_l, the propagation constant can be written as

$$\gamma \approx \sqrt{j\omega Z_{mr} C_i - \omega Z_{mi} C_i - \omega^2 L_m C_i} \cdot \left(1 - \frac{1}{2} j\omega R_t C_i - \frac{1}{2} j\omega R_b C_i\right), \qquad (3.13)$$

The propagation loss comes from three resistive elements in the equivalent circuit, 1) real part of metal-air transverse impedance, Z_{mr}, 2) resistance from the p-contact, p-cladding layer, and n-cladding layer, R_t, 3) resistance from the n-conducting layer, R_b. The first two are inversely proportional to the ridge width, w_c, while R_b is linearly dependent on w_c.

By artificially setting the real part of Z_m, Z_b, Z_t, to zero (yet still leave the imaginary part untouched), we can separate each contribution within the total loss. Fig. 3.15 shows the calculated field attenuation constant. As can be seen, the metal loss contributes to most of the loss at the frequency range we are interested in, while the n-conduction layer second, and the p- and n-cladding layers third. When all these three resistive components are taken off, the loss virtually reduced to zero even with G_l still included in the calculation. This also verifies that the parallel conductance, G_l, is negligible.

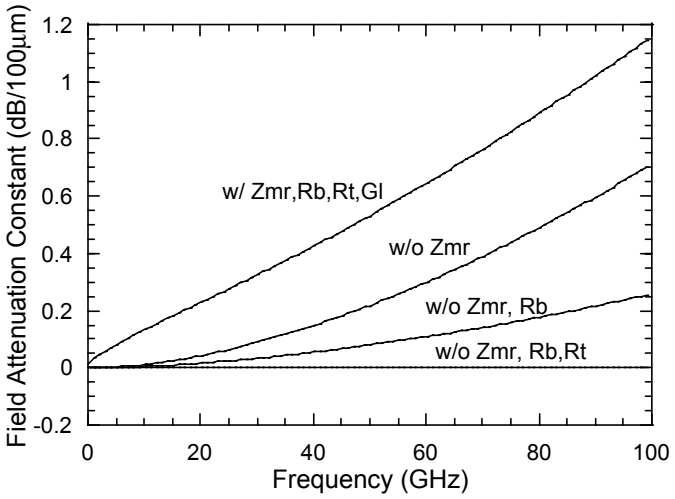

Fig.3 15 Field attenuation constant under the condition when the resistive components are artificially taken away from the calculation. The structure parameters are listed in Table 3.3.

3.5 Microwave characteristics vs. device parameters

This section will focus on the effect of device structure and material parameters on the characteristic impedance, Z_0, the microwave attenuation constant,

α_e, and S_{21} of the transmission line. These parameters include ridge width, w_c, intrinsic layer thickness, d_i, metal thickness, d_m, metal width, w_m, gap width, w_g, n-conducting layer thickness, d_{sb}, n-conducting layer resistivity, ρ_{sb}, p-cladding layer resistivity, ρ_{pclad}, and the side wall angle, θ. The dependence of characteristic impedance and attenuation constant on some of these parameters may be opposite and only the S_{21} is the overall figure of merit.

Reducing the ridge width will have effects both on the resistive elements and the capacitive and inductive elements. Fig. 3.16 shows the dependence of Z_0, α_e, and S_{21} on ridge width. Reducing the ridge width will reduce the intrinsic layer capacitance, even though it will also increase the metal impedance and line inductance, However, the first effect dominates and causes the increase in characteristic impedance and reduction in propagation loss. The S_{21} is significantly dependent on the ridge width. This suggests that a smaller the ridge width is better. However, too small ridge width will cause large optical coupling loss (Fig. 2.19) and large optical scattering loss. We chose 2 μm as our smallest ridge width for the devices.

Changing the thickness of the intrinsic layer will change its capacitance, C_i, and will change both the impedance and the attenuation constant. Fig. 3.17 shows the dependence of Z_0, α_e, and S_{21} on the thickness of the intrinsic layer. Increasing the thickness of the intrinsic layer will only reduce the intrinsic layer capacitance and will not affect any other circuit elements; hence it will increase the characteristic impedance and reduce the propagation loss. However, a thin intrinsic layer is preferred in order to achieve high electric field so as to achieve large wavelength shift. An active region composed of 10 quantum wells and 0.15-μm p-doping-offset layer is chosen for the InGaAsP/InGaAsP device. The doping offset is used to avoid Be diffusion into MQW region during MOCVD growth.

To reduce the metal loss, thicker metal will be needed. Fig. 3.18 shows the dependence of Z_0, α_e, and S_{21} on the p-metal thickness. Changing the p-metal thickness will only affect the metal-air transverse impedance, Z_m. The characteristic impedance is not sensitive to the change in metal thickness. As shown in Fig. 3.18(b), a metal thickness over 1 μm is sufficient.

Fig. 3.19 shows the dependence of Z_0, α_e, and S_{21} on the p-metal width. Because two-layer metal process technique is usually used to obtain thick metal, the p-metal width can be wider than that of the ridge underneath. Wider p-metal will slightly reduce the metal impedance, however it will reduce the inductance and will require wider gap width to achieve the same inductance. Since the characteristic impedance is proportional to $\sqrt{L_m / C_i}$ at medium frequencies (Eq. 3.10), a larger inductance will increase the characteristic impedance. It will also change the field attenuation coefficient. The overall performance (S_{21}) suggests that a metal width equal to the ridge width have better performance than the one with 4 μm wider (Fig.3.19(c)). A one-step thick-p-metal evaporation will be needed to achieve this goal.

The n-conducting layer loss can be reduced by reducing the gap width (Fig. 3.20), using thicker conducting layer (Fig. 3.21), or reducing the resistivity (Fig. 3.22).

Fig. 3.20 shows the dependence of Z_0, α_e, and S_{21} on the thickness of the gap width of the CPW line. In this calculation, the p-metal width was chosen to be the same as the ridge width. Increasing the gap width will increase the inductance, and hence increase the characteristic impedance. However, this will also increase the resistive loss coming from the n-conducting layer. The overall S_{21} performance was not changed much. A gap width of 5 μm and a metal width of 4 μm were chosen for the device.

Fig. 3.21 shows the dependence of Z_0, α_e, and S_{21} on the thickness of the n-conducting layer. A thicker n-conducting layer will reduce the loss due to this layer. As shown in Figs. 3.21 (b, c), an n-conducting layer thicker than 0.5 μm will be needed to achieve negligible loss.

Fig. 3.22 shows the dependence of Z_0, α_e, and S_{21} on the resistivity of the n-conducting layer. A resistivity of 100 Ω–μm was evaluated for the n-conducting layer, which was higher than the resistivity of ρ~10 Ω–μm as reported for bulk n-InP with doping level of n=3e18 cm^{-3} [32]. The diffusion of Fe to the first 0.5-μm n-InP layer might be the reason for the high resistivity level of the actual device. Fig. 3.21 (b, c) suggests that a resistivity of better than 100 Ω–μm will be needed for achieving good conductivity.

Higher doping can reduce the resistivity of the p-InP-cladding layer and hence reduce the loss. Fig. 3.23 shows the dependence of Z_0, α_e, and S_{21} on the resistivity of the p-cladding layer. Due to the low hole-mobility of p-InP, the p-cladding layer has very high resistivity compared to n-InP. As shown, a resistivity higher than 300 Ω–μm is preferred. A high p-doping will be needed.

Fig. 3.24 shows the dependence of Z_0, α_e, and S_{21} on the angle of the side wall. As will be discussed in Chapter 4, an angle of 67.6° was shown up on the InGaAs/InAlAs ridges etched with Cl_2/Ar Reactive Ion Etching. Due to this non-90° side wall, the actual intrinsic layer width was increased, resulting in a much larger junction capacitance, a smaller characteristic impedance and a larger microwave propagation loss. This results in a much smaller 3-dB bandwidth on the S_{21} curve, which is one of the main reasons why we switch from InGaAs/InAlAs/ InP system to InGaAsP/InGaAsP/InP system.

Table 3.4 summarizes the relations between the circuit characteristics and the device parameters.

	Z_o	α_e	S_{21} 3dB-bandwidth	Comments
Decrease w_c	+	-	+	Increase optical loss
Increase d_i	+	-	+	Increase drive voltage
Increase d_m	~	-	+	$d_m > 1$ μm needed
Decrease w_m	+	+	+	One-step metal process
Increase w_g	+	+	~	$w_g = 5$ μm chosen
Increase d_{sb}	-	-	+	$d_{sb} > 0.5$ μm needed
Decrease ρ_{sb}	-	-	+	$\rho_{sb} < 100$ Ω–μm needed
Decrease ρ_{pclad}	-	-	+	$\rho_{pclad} < 300$ Ω–μm needed
Increase θ to 90°	+	-	+	Need 90° side wall

Table 3.4 Summary of the relations between the transmission line characteristics and the device parameters. +: increase; -: decrease; ~: small change.

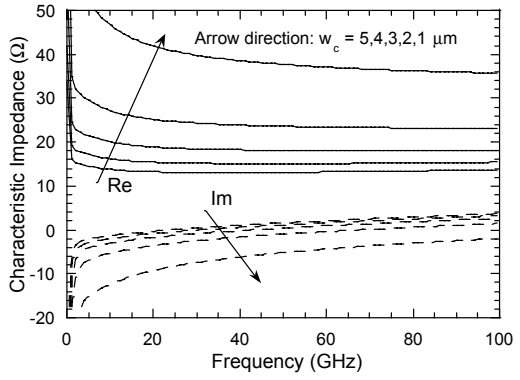

(a)

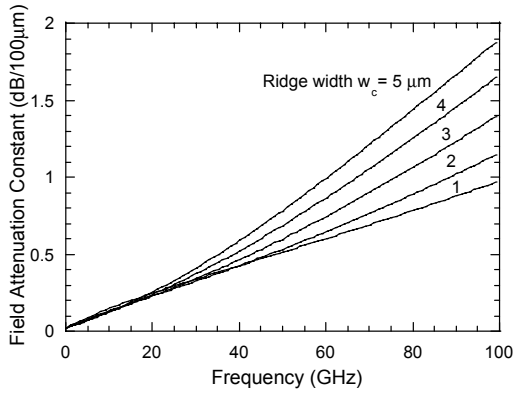

(b)

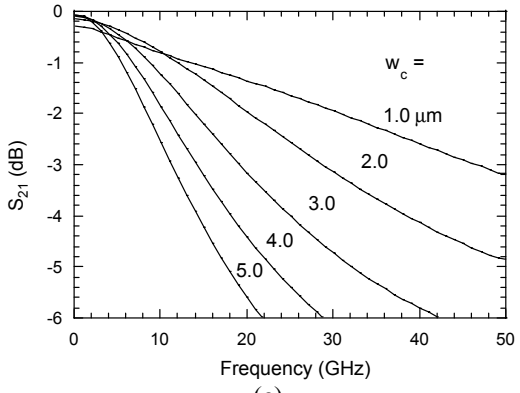

(c)

Fig. 3.16 Transmission line characteristics as a function of frequency for different ridge widths. Except for the ridge width, the other structure parameters are listed in Table 3.3.

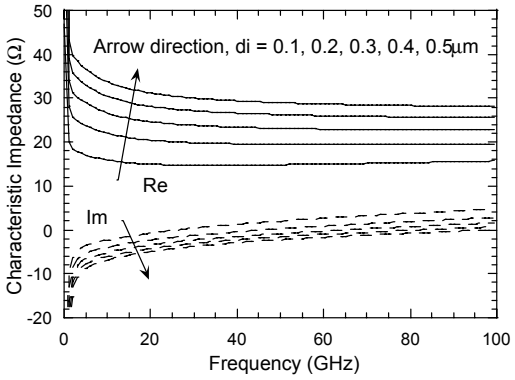

(a)

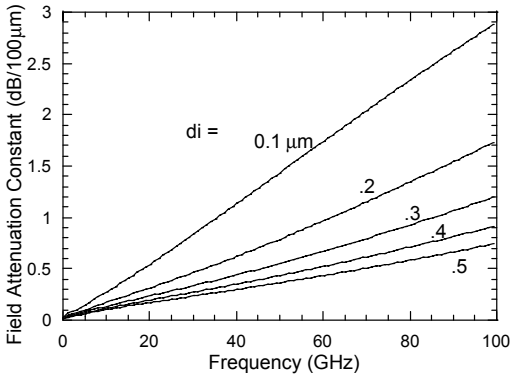

(b)

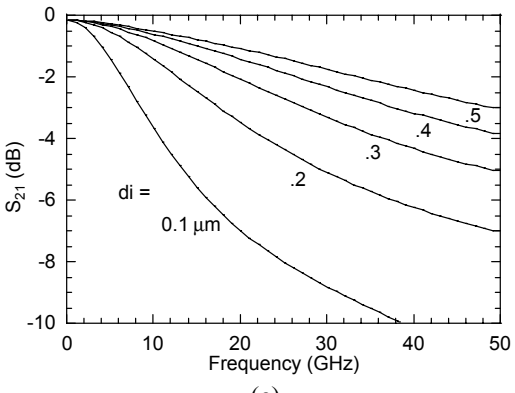

(c)

Fig. 3.17 Transmission line characteristics as a function of frequency for different intrinsic region thickness values. Except for the intrinsic region thickness, the other structure parameters are listed in Table 3.3.

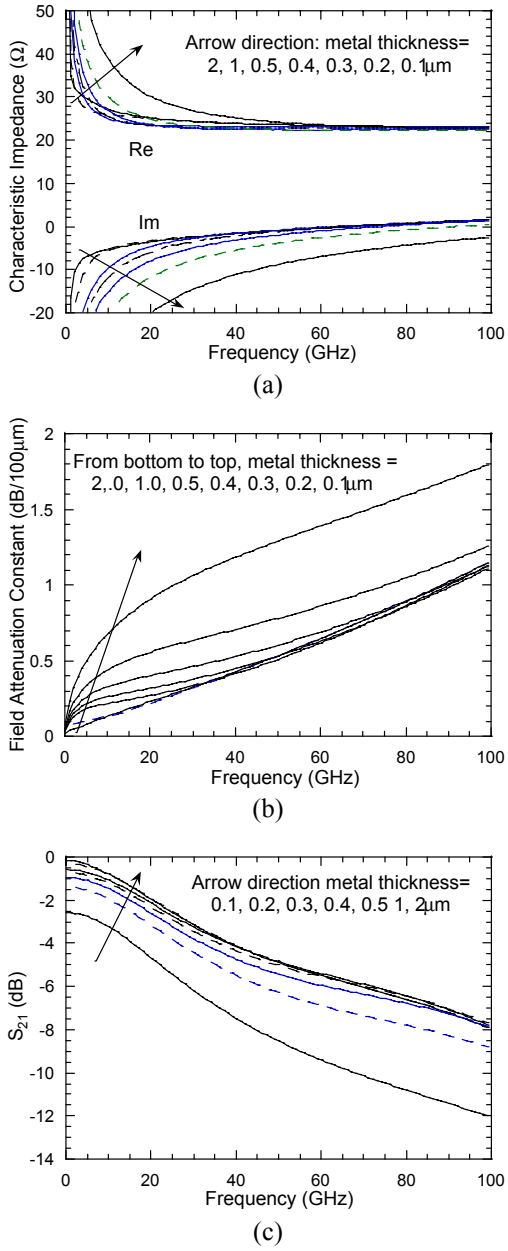

Fig. 3.18 Transmission line characteristics as a function of frequency for different metal thickness values. Except for the metal thickness, the other structure parameters are listed in Table 3.3.

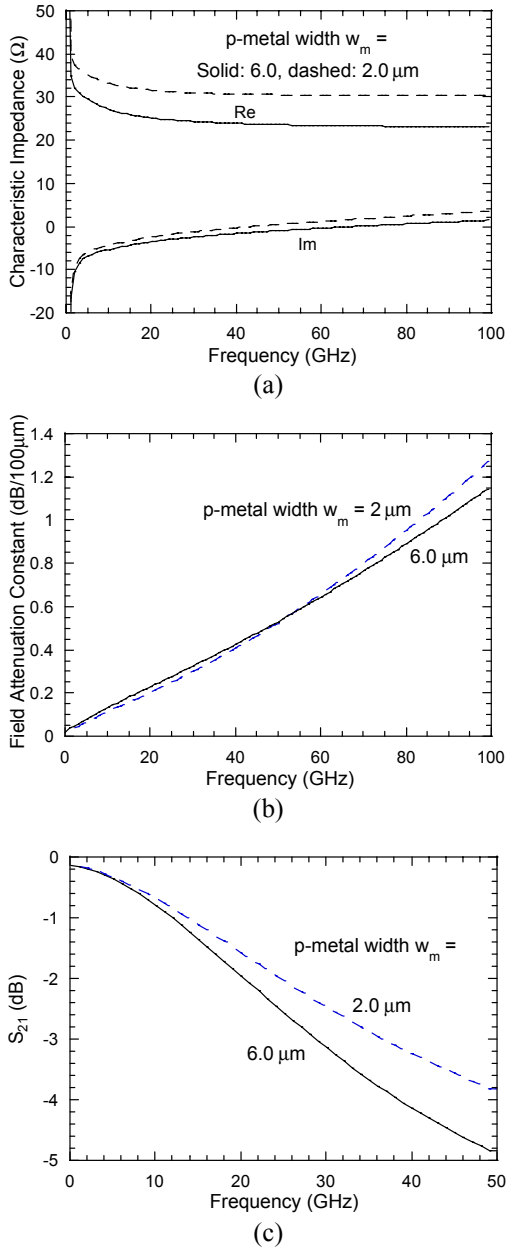

Fig. 3.19 Transmission line characteristics as a function of frequency for different p-metal widths. Except for the p-metal width, the other structure parameters are listed in Table 3.3.

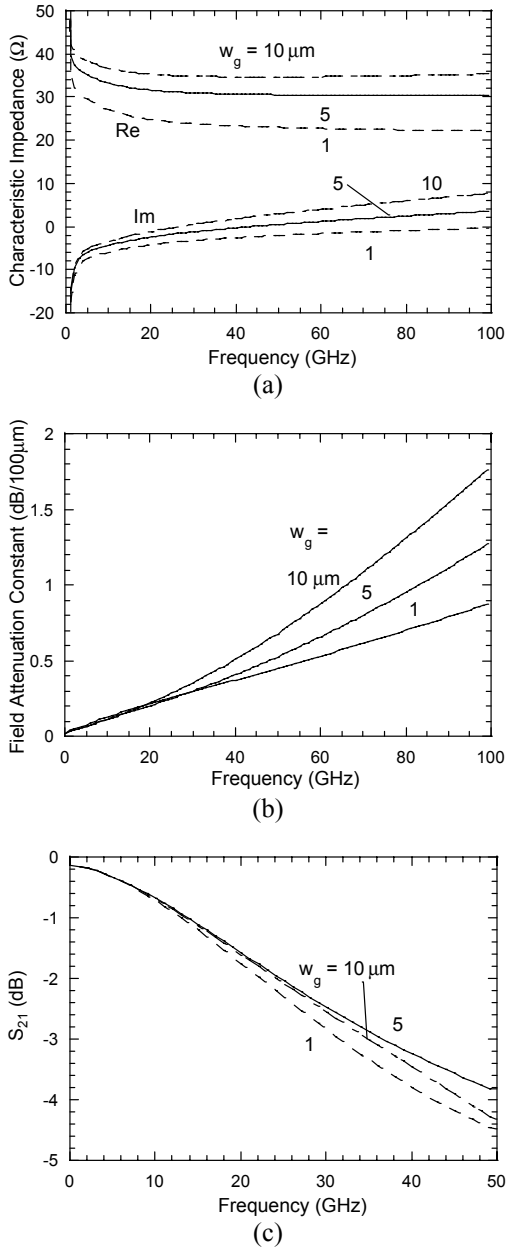

Fig. 3.20 Transmission line characteristics as a function of frequency for different gap widths. Except for the gap width, the other structure parameters are listed in Table 3.3.

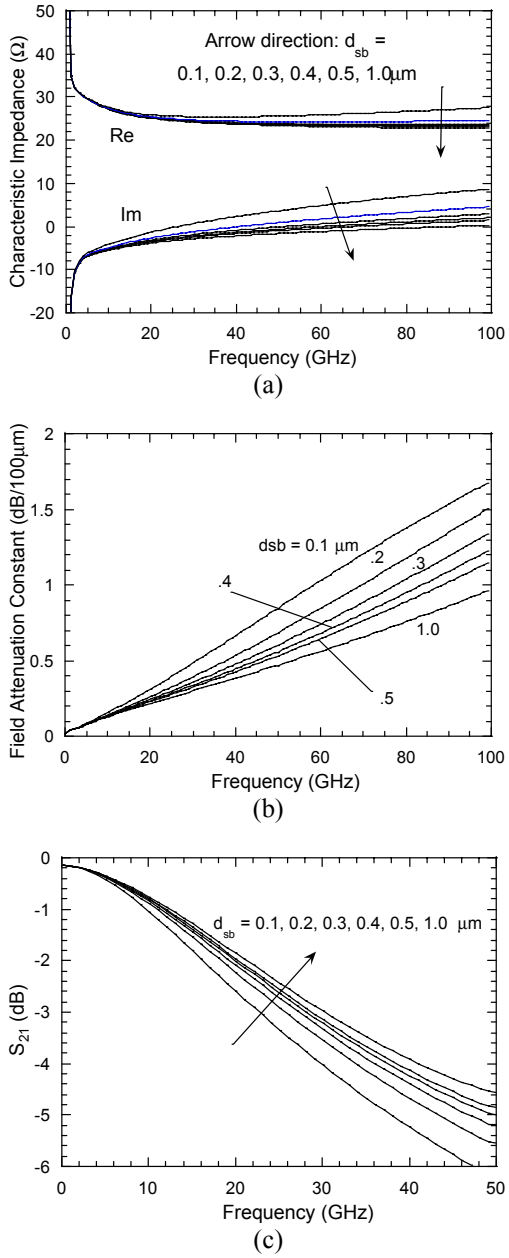

Fig. 3.21 Transmission line characteristics as a function of frequency for different n-conducting layer thickness values. Except for the n-conducting layer thickness, the other structure parameters are listed in Table 3.3.

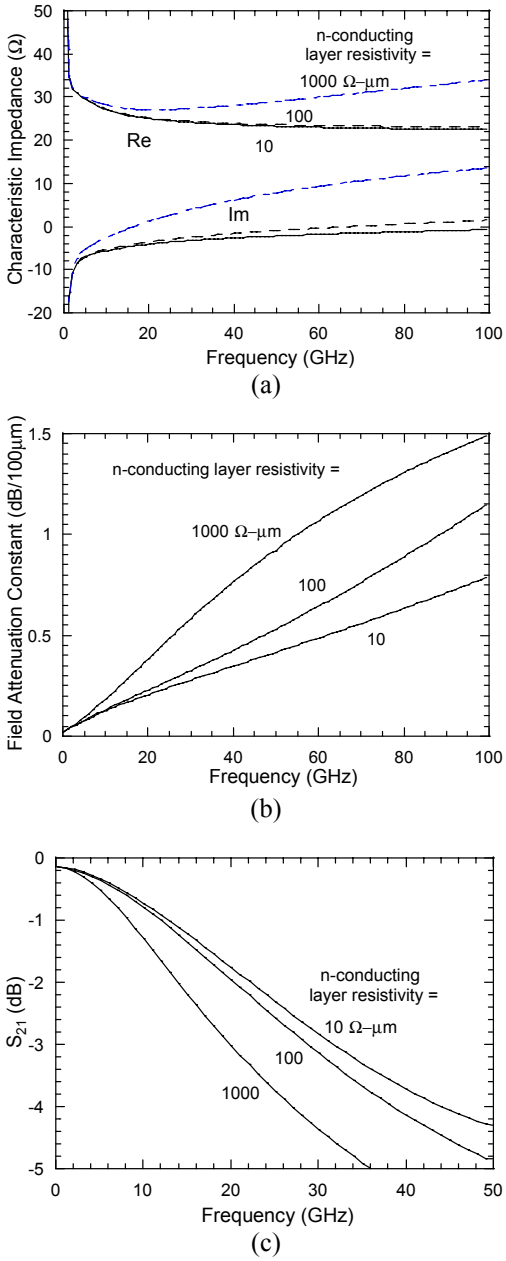

Fig. 3.22 Transmission line characteristics as a function of frequency for different n-conducting layer resistivity values. Except for the n-conducting layer resistivity, the other structure parameters are listed in Table 3.3.

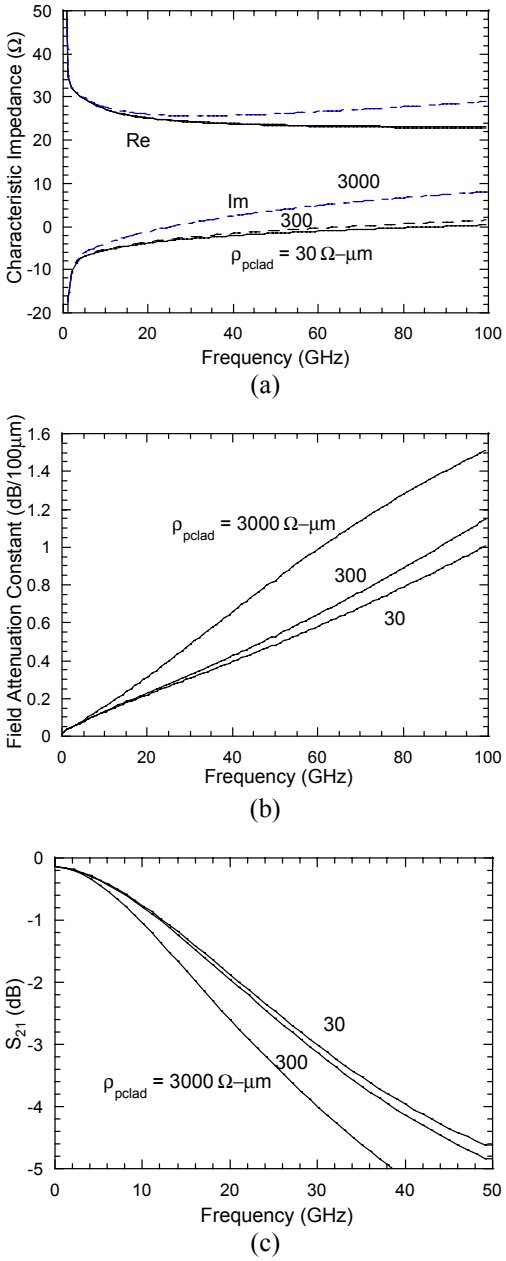

Fig. 3.23 Transmission line characteristics as a function of frequency for different p-cladding layer resistivity values. Except for the p-cladding layer resistivity, the other structure parameters are listed in Table 3.3.

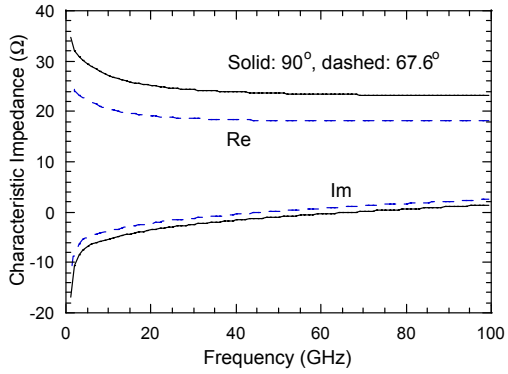

(a)

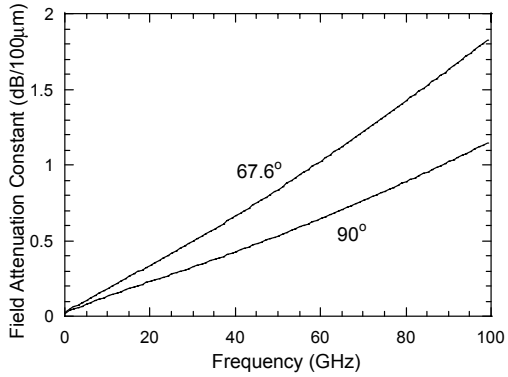

(b)

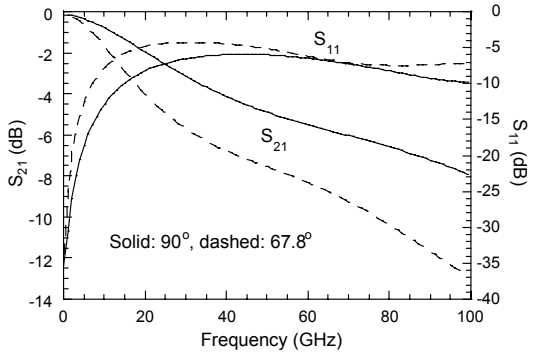

(c)

Fig. 3.24 Transmission line characteristics as a function of frequency for different side wall angles. Except for the side wall angle, the other structure parameters are listed in Table 3.3.

3.6 E-O Response

Previous discussions are all limited to a pure straight coplanar waveguide structure and to electrical domain. In a real device, the feedline as well as load responses should be included. The final parameter that represents the performance of the device will be the electrical-to-optical (EO) response S_{21}. This section focuses on optimizing the overall electrical-to-optical response, including the design of feed lines and the choice of load.

Including the tapered feed lines, the schematic diagram and the linear two-port representation of the device is shown in Fig. 3.25.

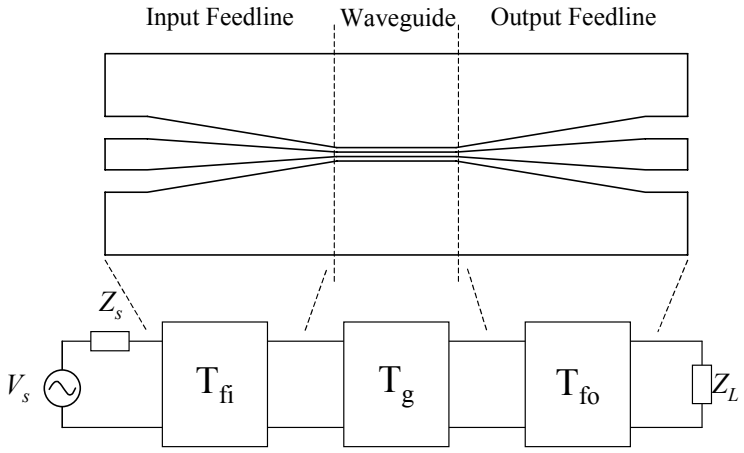

Fig. 3.25 Schematic diagram of transmission line and linear two-port representation of a TEAM. In the case when wire bonding is used to connect the load, an inductance corresponding to the gold wire is included in the load impedance. The inductance of a gold wire/ribbon can be calculated with a commercial software called libra [33].

The whole device is composed of an input transmission feed line, an optical waveguide section, and an output transmission line. Each section is represented with a linear two-port transmission matrix. Appendix D discusses the calculation of any voltages in the waveguide.

With the voltage signal known in every position throughout the waveguide, the output optical waveform can be obtained through the calculation of electroabsorption effect. The transfer function of an electroabsorption modulator can usually fit as [21]

$$\frac{P}{P_o} = \exp(-(V/V_o)^n), \tag{3.14}$$

where P/P_o is the normalized output optical power, V is the applied external voltage, V_o and n are fitting parameters.

Even though actual device transfer function may be quite different from the form of equation (3.14), this equation should still give us enough precision for small signal modulations.

As discussed in the previous section, the characteristic impedance of the waveguide section is usually far smaller than 50 Ω. With the designed structure as shown in Table 3.3, the impedance is about 20 Ω. Therefore, there will be a strong reflection back to the modulator driver. It will be ideal to design the load impedance and the transmission feed lines such that the impedance looking from the input port of the device can be a 50 Ω. Impedance tapering in the feedline region might help improve the performance.

Fig. 3.26 shows the impedance schematic diagram of a general tapered transmission line section. Tapering is usually used to match two transmission lines with different characteristic impedances. In calculation, arbitrarily tapering impedance profile can be simulated with multiple discrete steps, with each step considered as a simple transmission line [34].

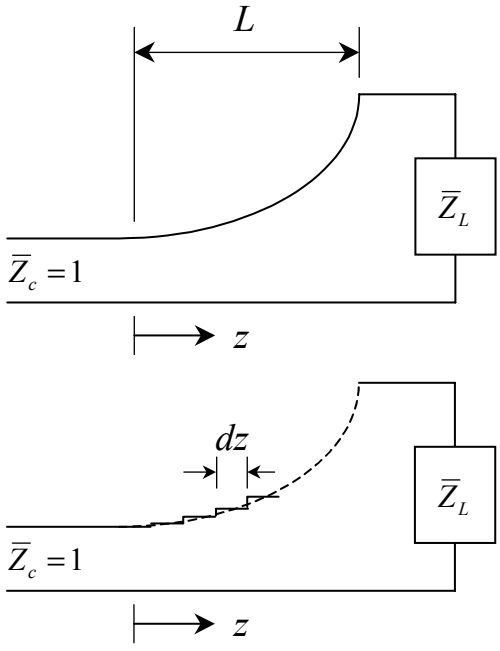

Fig. 3.26 Tapered transmission line section

Three different tapered structures are studied numerically. The first one is called exponential taper, in which $\ln \overline{Z}$ varies linearly with distance, and hence the normalized $\overline{Z} = Z / Z_c$ varies exponentially, from unity to $\ln \overline{Z}_L$. That is

$$\ln \overline{Z} = \frac{z}{L} \ln \overline{Z}_L , \tag{3.15a}$$

$$\overline{Z} = \exp(\frac{z}{L} \ln \overline{Z}_L) , \tag{3.15b}$$

The second tapered structure is called triangular distribution, in which $d(\ln \overline{Z}) / dz$ is chosen as a triangular function of the form

$$\frac{\ln \overline{Z}}{dz} = \begin{cases} \dfrac{4z}{L^2} \ln \overline{Z}_L & 0 \le z \le L/2 \\ \dfrac{4}{L^2}(L - z) \ln \overline{Z}_L & L/2 \le z \le L \end{cases} , \tag{3.16}$$

The third structure is a linear width tapering, in which the signal line width, w, and the gap width, g, are linearly tapered from one end (w_L, g_L) to the other(w_c, g_c), with each-end impedance matched to the impedance at that end. That is

$$w = \frac{z}{L}(w_L - w_c) + w_c , \tag{3.17a}$$

$$g = \frac{z}{L}(g_L - g_c) + g_c \tag{3.17b}$$

In order to calculate small signal electrical-to-optical (EO) response, a Gaussian-shaped electrical pulse with a full-width-at-half-maximum (FWHM) width of $10\sqrt{\ln 2}$ ps and an amplitude of 0.07 V is launched into the input port of the device. Fig. 3.27 shows the real part of the characteristic impedance (the imaginary part is much smaller and is not shown for clarity) at 40 GHz for the three tapered structures. The x-axis is the distance starting from the input port to the output port. The flat region in the center is the 300-μm long optical waveguide, and the two flat ends are 100-μm contact pads.

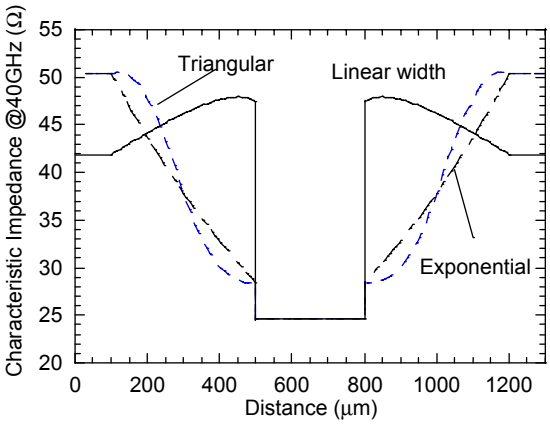

Fig. 3.27 Characteristic impedance distribution for three tapered structures. The center flat region is the 300-μm optical waveguide. There are 100-μm contact pads on both input and output ports.

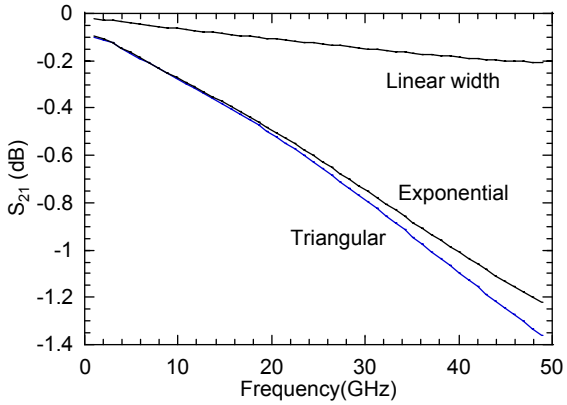

Fig. 3.28 S_{21} response of the pure tapered input transmission feed line section.

Fig. 3.28 shows the S_{21} response of the tapered input transmission feed line section. As can be seen, both the exponential and triangular tapered structures have significant loss, due to the impedance tapering induced reflection.

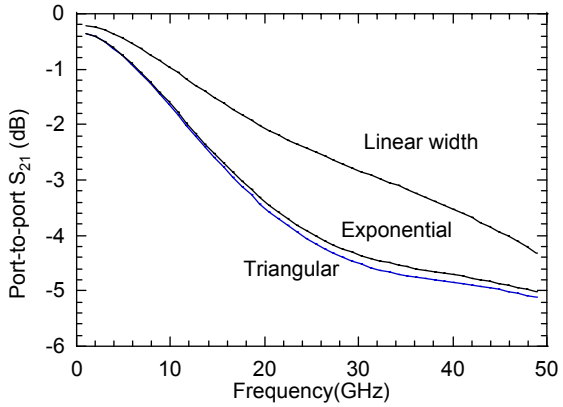

Fig. 3.29 Input-port-to-output-port S_{21} response of the whole device with different tapered transmission feed line sections.

Fig. 3.29 shows the input-port-to-output-port S_{21} response of the whole device with tapered transmission feed line sections. Surprisingly, the best result is obtained with linear tapering. Two reasons may explain this effect. Since the tapered section is very short (500 μm) compared to the wavelength of the microwave signal (~1250 μm at 40 GHz), the length is not long enough to achieve a phase shift for a null reflection [34]. In the linear-width-tapered structure, the impedance first slightly increases at the feedline region. This will introduce a positive reflection and can cancel with the negative reflection from the optical waveguide. This positive reflection can be observed in the simulated output optical pulse as shown in Fig. 3.30 on the slightly overshoot on the linearly tapered case.

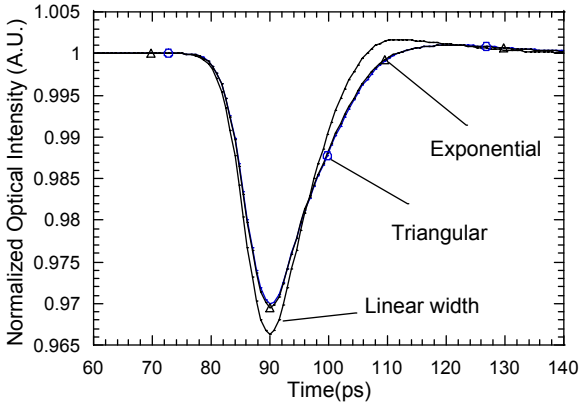

Fig. 3.30 Simulated output optical pulse under modulation of a Gaussian pulse.

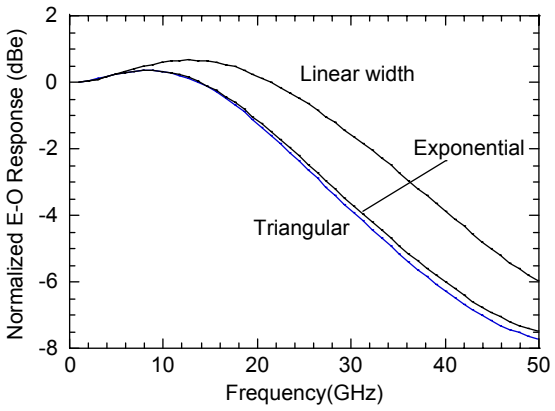

Fig. 3.31 Normalized EO response for different taper structures.

Fig. 3.31 shows the simulated overall EO response for different taper structures. As shown, the linear-width tapering is the best choice for the device.

3.7 Summary

This chapter discusses the equivalent circuit model for traveling-wave electroabsorption modulators. Material and device structural parameters are studied on their effects on the characteristic impedance, microwave propagation attenuation constant and finally on the S_{21} performance of the waveguide. Table 3.4 lists the design rules for achieving low loss microwave waveguide. The last section of the chapter discusses optimization of the whole device based on the overall port-to-port S_{21} parameter and EO response. Tapering of the transmission feed lines are studied and linear width tapered structure is found to be better than triangular and exponential tapered structures.

References

[1] F. Devaux, S. Chelles, A. Ougazzaden, A. Mircea, and J. C. Harmand, "Electroabsorption modulators for high-bit-rate optical communications: a comparison of strained InGaAs/InAIAs and InGaAsP/InGaAsP MQW," *Semicond. Sci. Technol.*, vol. 10, pp. 887-901, 1995.

[2] R. Spickermann, S. R. Sakamoto, and N. Dagli, “In traveling wave modulators which velocity to match?,” *IEEE LEOS'96*, Boston, MA, pp.97-98 vol.2, 1996.

[3] W. J. Getsinger, “An introduction to microwave transmission lines,” *Midwest Symposium on Circuits and Systems*, Washington, DC, pp.1016-1019 vol.2, 1992.

[4] D. Tauber, M. Horita, J. Piprek, P. Abraham, A. L. Holmes, Jr., and J. E. Bowers, “The microstrip laser,” *IEEE Photonics Technol. Lett.*, vol. 10, pp. 478-80, 1998.

[5] C. P. Wen, “Coplanar waveguide: a surface strip transmission line suitable for nonreciprocal gyromagnetic device applications,” *IEEE Trans. Microw. Theory Tech.* , vol. 17, pp. 1087-1069, 1969.

[6] R. K. Hoffmann, *Handbook of Microwave Integrated Circuits*. Boston: Artech House, Inc., 1987.

[7] LineCalc, distibuted by Hewlett Packard Company, Westlake Village, CA, 1996.

[8] H. A. Wheeler, “Transmission-line properties of parallel strips separated by a dielectic sheet,” *IEEE Trans. Microw. Theory Tech.* , vol. 13, pp. 172-185, 1964.

[9] H. Guckel, P. A. Brennan, and I. Palocz, “A parallel-plate waveguide approach to microminiaturized, planar transmission lines for integrated circuits,” *IEEE Trans. Microw. Theory Tech.* , vol. 15, pp. 468-476, 1967.

[10] H. Hasegawa, M. Furukawa, and H. Yanai, “Properties of microstrip line on Si-SiO/sub 2/ system,” *IEEE Trans. Microw. Theory Tech.* , vol. MTT-19, pp. 869-881, 1971.

[11] D. Jager, “Slow-wave propagation along variable Schottky-contact microstrip line (SCML),” *IEEE Trans. Microw. Theory Tech.* , vol. MTT-24, pp. 566-573, 1976.

[12] Y. Fukuoka and T. Itoh, “Analysis of slow-wave phenomena in coplanar waveguide on a semiconductor substrate,” *Electron. Lett.*, vol. 18, pp. 589-590, 1982.

[13] R. Sorrentino, G. Leuzzi, and A. Silbermann, “Characteristics of metal-insulator-semiconductor coplanar waveguides for monolithic microwave circuits,” *IEEE Trans. Microw. Theory Tech.* , vol. MTT-32, pp. 410-416, 1984.

[14] C. K. Tzuang and T. Itoh, “Finite-element analysis of slow-wave Schottky contact printed lines,” , pp. 1483-1489, 1986.

[15] T. G. Livernois and P. B. Katehi, “A generalized method for deriving the space-domain Green's function in a shielded, multilayer substrate structure with applications to MIS slow-wave transmission lines,” *IEEE Trans. Microw. Theory Tech.* , vol. 37, pp. 1761-1767, 1989.

[16] J. C. Liou and K. M. Lau, “A solution to characteristics of planar transmission lines made of finite-thickness metal on multi-layer media,” *IEEE MTT-S International Microwave Symposium*, Dallas, TX, pp.179-182 vol.1, 1990.

[17] K. Wu and R. Vahldieck, “Hybrid-mode analysis of homogeneously and inhomogeneously doped low-loss slow-wave coplanar transmission lines,” *IEEE Trans. Microw. Theory Tech.* , vol. 39, pp. 1348-1360, 1991.

[18] J. P. K. Gilb and C. A. Balanis, “MIS slow-wave structures over a wide range of parameters,” *IEEE Trans. Microw. Theory Tech.* , vol. 40, pp. 2148-2154, 1992.

[19] J. C. Liou and K. M. Lau, "Analysis of slow-wave transmission lines on multi-layered semiconductor structures including conductor loss," *IEEE Trans. Microw. Theory Tech.* , vol. 41, pp. 824-829, 1993.

[20] C. Seguinot, P. Kennis, P. Pribetich, and J. F. Legier, "Analytical model of the Schottky contact coplanar line," *European Microwave Conference*, Liege, Belgium, pp.160-165, 1984.

[21] K. Kawano, K. Wakita, O. Mitomi, I. Kotaka, and M. Naganuma, "Design of InGaAs-InAlAs multiple-quantum-well (MQW) optical modulators," *IEEE J. Quantum Electron.*, vol. 28, pp. 224-230, 1992.

[22] V. M. Hietala and K. S. Champlin, "Measurement of the microwave properties of micron-sized coplanar transmission lines," *J. Electromagn. Waves Appl.* , vol. 5, pp. 439-452, 1991.

[23] E. Tuncer and D. P. Neikirk, "Highly accurate quasi-static modeling of microstrip lines over lossy substrates," *IEEE Microw. Guid. Wave Lett.*, vol. 2, pp. 409-411, 1992.

[24] K. S. Giboney, M. J. W. Rodwell, and J. E. Bowers, "Traveling-wave photodetector design and measurements," *IEEE J. Sel. Top. Quantum Electron.* , vol. 2, pp. 622-629, 1996.

[25] K. S. Giboney, J. W. Rodwell, and J. E. Bowers, "Traveling-wave photodetector theory," *IEEE Trans. Microw. Theory Tech.* , vol. 45, pp. 1310-1319, 1997.

[26] K. S. Giboney, "Travelling-wave photodetectors," University of California, Santa Barbara, CA, Ph.D. Dissertation, 1995.

[27] K. S. Giboney, R. L. Nagarajan, T. E. Reynolds, S. T. Allen, R. P. Mirin, M. J. W. Rodwell, and J. E. Bowers, "Travelling-wave photodetectors with 172-GHz bandwidth and 76-GHz bandwidth-efficiency product," *IEEE Photonics Technol. Lett.*, vol. 7, pp. 412-414, 1995.

[28] Y.-J. Chiu, S. B. Fleischer, D. Lasaosa, and J. E. Bowers, "Ultrafast (370 GHz bandwidth) p-i-n traveling wave photodetector using low-temperature-grown GaAs," *Appl. Phys. Lett.*, vol. 71, pp. 2508-2510, 1997.

[29] MCP Wafer Technology, Sn doped InP substrate product spec sheet, resistivity $\rho = 1.5\text{x}10^{-3} \sim 2.1\text{x}10^{-3}$ Ω-cm.

[30] P. A. Rizzi, *Microwave Engineering Passive Circuits*: Prentice Hall, Appendix C and D, 1988.

[31] R. Spickermann, "High speed Gallium Arsenide/Aluminum Gallium Arsenide traveling wave electrooptic modulators," University of California, Santa Barbara, CA, Ph.D. Dissertation, 1996.

[32] G. W. Iseler, "Resistivity of bulk InP," in *Properties of Indium Phosphide*, S. Adachi, Ed.: INSPEC, the Institution of Electrical Engineers, London and New York, 1991, pp. 25-32.

[33] Libra, distibuted by Hewlett Packard Company, Westlake Village, CA, 1996.

[34] R. E. Collin, *Foundations for Microwave Engineering*: McGraw-Hill Book Company, pp. 237-254, pp. 237-254, 1966.

CHAPTER 4

InGaAs/InAlAs Device Fabrication and Characterization

In the previous two chapters we have discussed the design issues of achieving low drive voltage, high coupling efficiency, and high-speed traveling-wave electroabsorption modulators. The design examples are mostly based on the InGaAsP/InGaAsP material system; however, our first generation device is with InGaAs/InAlAs material system. As discussed in Chapter 2, InGaAs/InAlAs was first recognized as an excellent material system for fabricating 1.55-μm EA modulators because of its strong exciton effect and natural band structure good for high saturation power operation. Ultra-high-speed and low drive voltage EA modulators have been reported with this material system [1-4]; however, all of these devices are lumped structures. This chapter will describe the fabrication and characteristics of TEAMs fabricated with InGaAs/InAlAs. Similar design procedures for high-speed operation as those discussed in Chapter 2 have been performed for InGaAs/InAlAs material system and will not be discussed specially.

Epilayer structures were designed and compared experimentally for achieving low drive voltage. The devices were fabricated using a self-aligned ridge waveguide process. PMGI [5] was used to passivate, planarize, and bridge the ridge for its good properties and ease to process. High-speed measurements on these devices revealed that the side wall's non-90^{o} angle was the main limiting factor for the bandwidth of the devices.

4.1 Material structure and characterization

4.1.1 Growth structure

The material was grown on a semi-insulating InP substrate for high-speed operation. The epilayers were lattice matched to the substrate. As discussed in Chapter 2, the thickness of an unstrained quantum well that operates at 1.55 μm will be very thin and the energy shift with external electric field will be small. This

will cause an increase in the driving voltage. It has been demonstrated that by inserting a thin InGaAlAs layer into the InGaAs quantum well the effective quantum well bandgap is larger, therefore we can use a wider shallow quantum well [6].

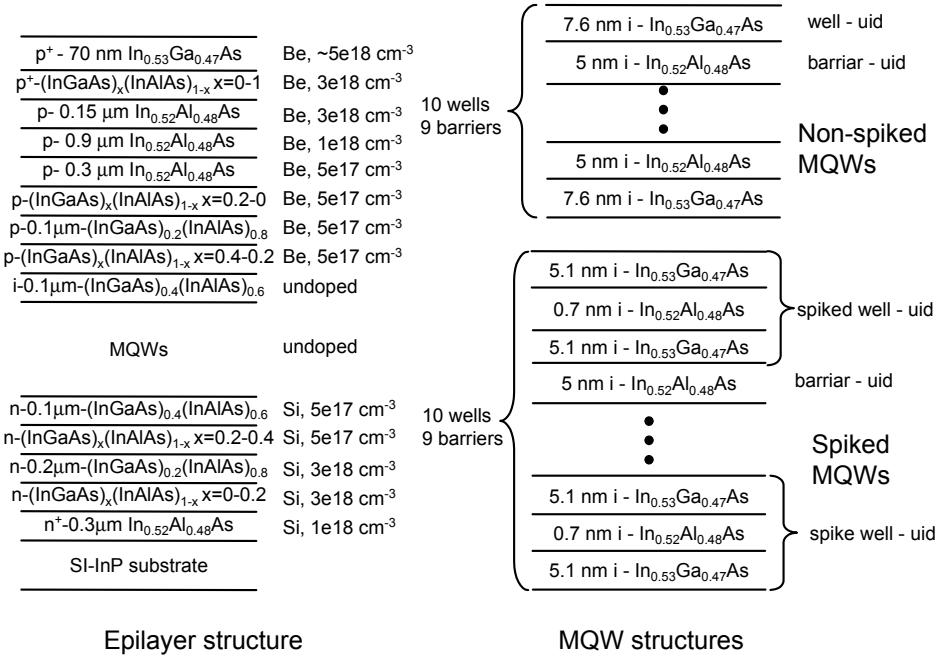

Fig. 4.1 Material structure of InGaAs/InAlAs TEAMs.

Two different quantum well structures were grown; one with standard quantum well without spiked InAlAs layer, and the other with a spiked InAlAs layer. Fig. 4.1 shows the whole epilayer structure together with these two quantum well structures. The device structure consists of 10 lattice matched InGaAs/InAlAs quantum wells sandwiched by p-InAlAs cladding and n-InAlAs cladding layers. Prior to the other layers, a 0.3-μm n^+-InAlAs layer was grown on the semi-insulating InP substrate for the n-conducting layer.

In order to reduce carrier trapping effect at heterointerfaces, digital-alloy-grading layers were grown at the interfaces between quantum well region and p- and n- cladding layers, and between p-contact layer and p-cladding layer [7, 8]. The InGaAs/InAlAs superlattice can also help smooth the growth surface and

improve the quality of the quantum well region [9] and has been used for fabricating InGaAlAs lasers [10, 11]. As will be shown later in Fig. 4.2, these superlattice layers do improve the photoluminescence efficiency.

Since Be is highly diffusive in InP [12], a p-doping offset layer of 0.1 μm was grown to prevent Be from diffusing into the active region. This will, however, increase the total intrinsic layer thickness, reduce the electric field intensity and increase the drive voltage.

The epilayers were grown at 530^{o}C, with a V-III flux ratio of 20:1. Since there is a total thickness of over 2.0-μm InAlAs, it is very important to precisely control the strain of the material. A calibration growth was performed before growing the actual device structure. X-ray double crystal measurement was used to characterize the lattice constant of the material while room temperature photoluminescence (PL) was used to calibrate the PL wavelength and to evaluate the quality of the material.

4.1.2 Photoluminescence characteristics

The as-grown material was first characterized with room temperature PL measurement. Fig. 4.2 shows photoluminescence spectra of four different wafers; two of them were grown without digital grading layers, while the other two were grown with digital grading layers. Among these samples, only one of them was calibrated with X-ray during the calibration growth. As can be seen, for samples without X-ray calibration, the sample with digital-alloy-grading layers has a PL intensity of about 50% more than the ones without; for the samples with digital-alloy-grading layers, the sample with X-ray calibration has a PL intensity of about 100% more than the one without. This suggests that digital-alloy-grading layers do help improve the quality of the quantum wells and X-ray calibration prior to growth is crucial for achieving high quality material.

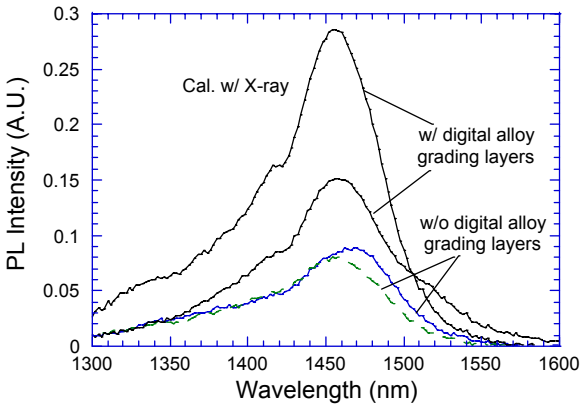

Fig. 4.2 PL spectra of four different wafers.

The PL intensity was observed to have a dramatic improvement after post growth Rapid Thermal Annealing (RTA). Fig.4.3 shows a comparison of PL spectra with and without post annealing. In this case, the sample was grown without digital-alloy-grading layers and no X-ray calibration was performed during the calibration growth. Close to an order of magnitude improvement was observed. The best annealing condition was found to be at a temperature of 850~900^{o}C for about 60 seconds. A peak wavelength shift was observed; however, multiple tests showed that the shift direction was randomly distributed, which could partially be due to the non-uniformity of the wafer and the limited accuracy of the monochromator.

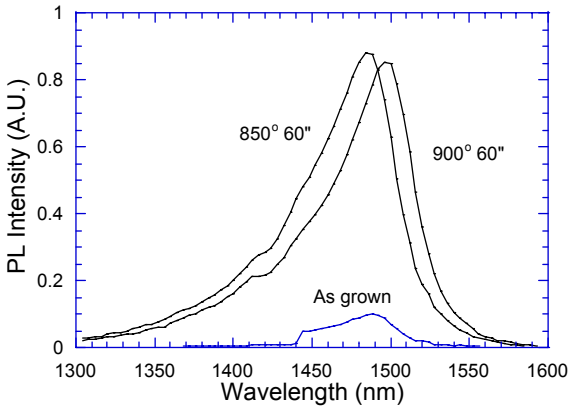

Fig. 4.3 PL spectra with and without post growth rapid thermal annealing. The sharp jump on the curve of the as grown sample is due to the locking amplifier's sensitivity range switch.

The improvement of PL efficiency after post annealing can be understood as the removal of defects in InAlAs layers that were formed during the relatively low temperature growth. Due to the high desorption rate of Indium atoms at high temperatures the growth temperature was only about 530^{o}C, much lower than the optimum growth temperature for AlGaAs.

Even though post annealing has been successfully used in achieving record low threshold current density InGaAlAs-AlGaAs lasers [13], it does not help much in the absorption characteristic of the material. Actually, a slight reduction of wavelength shift under the same bias was observed from photo current measurement due to the fact that high temperature annealing will disorder the heterointerfaces and reduce the quantum confinement effect.

4.1.3 Photocurrent measurement

Besides PL measurement, photocurrent measurement was also performed to characterize the material quality. In a photocurrent measurement, the modulator is used as a detector to convert light to current; thus the photocurrent spectrum reveals the absorption characteristics of the material.

Broad area structure devices were fabricated specially for photocurrent measurement prior to the fabrication of the high-speed devices. The detailed measurement configuration is given in Appendix E.

Fig. 4.4 shows the photocurrent spectra of a device with non-spiked quantum wells and Fig. 4.5 shows that of a device with spiked quantum wells. As can be seen, the absorption edge shifted much faster for the device with spiked quantum wells, in agreement with the theoretical prediction given in Chapter 2. Also, as expected, the absorption edge became less sharp for the spiked quantum wells due to larger exciton radius and hence lower confinement.

A comparison of the absorption edge shift for different samples is shown as a function of electric field in Fig. 2.7. The theorectical prediction is shown in Fig. 2.6.

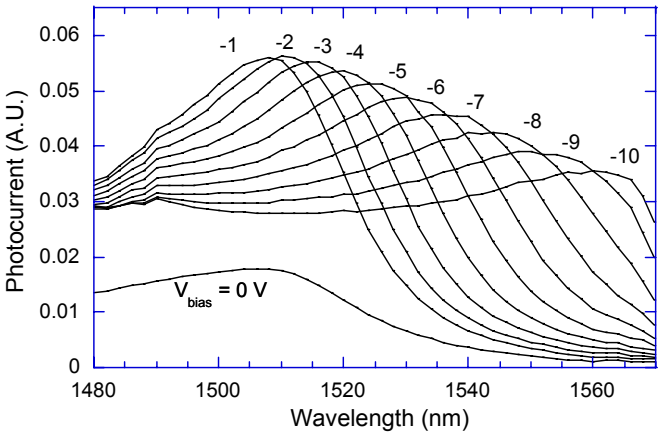

Fig. 4.4 Photocurrent spectra of a device with non-spiked quantum wells.

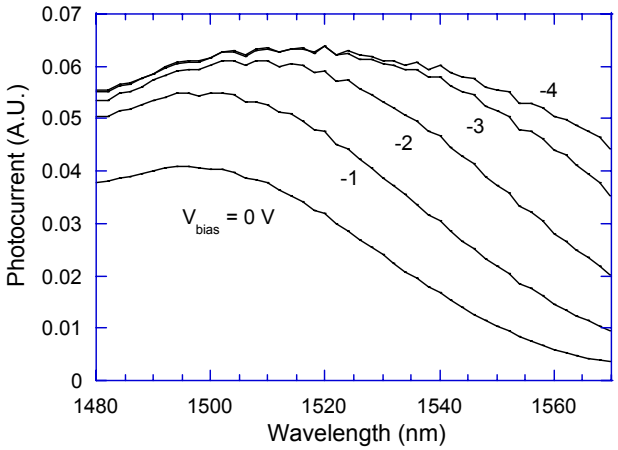

Fig. 4.5 Photocurrent spectra of a device with spiked quantum wells.

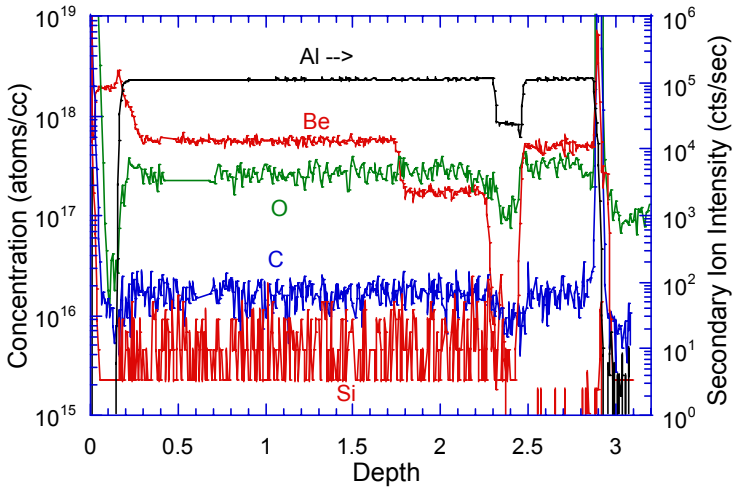

Fig. 4.6 Secondary Ion Mass Spectroscopy measurement result.

4.1.4 SIMs measurement

Residual unintentional doping in the active region can cause electric field non-uniformity and could severely reduce the sharpness of the absorption edge as well as the absorption coefficient. Unintentional doping level below 10^{16} cm^{-3} is important for achieving high device performance [14]. Oxygen is the most common unintentional dopant in InGaAs/InAlAs QWs due to the aluminum compound. Secondary Ion Mass Spectroscopy (SIMs) measurement was performed to study the residual doping level. Fig. 4.6 shows the SIMs measurement result. We can see that the oxygen level was about 10^{17} cm^{-3}, a level that could severely affect the electroabsorption efficiency.

4.2 Device fabrication

Before getting into the details of the fabrication process, let's examine the structure of the final device.

Fig. 4.7 shows a Scanning Electron Microscope (SEM) picture of the fabricated devices prior to cleaving, while Fig. 4.8 shows the SEM pictures of a single device and the waveguide to feed line connection region. Fig. 4.7 shows the meshed cleaving lines. These cleaving lines were 10 μm wide. For better ground

connection from one side of the waveguide to the other side, a PMGI-bridge was fabricated as shown in Fig. 4.8 and in the facet view of the waveguide in Fig. 4.9. As we will discuss later, there is a side wall angle of 68^{o} on the ridge due to Reactive Ion Etching (RIE).

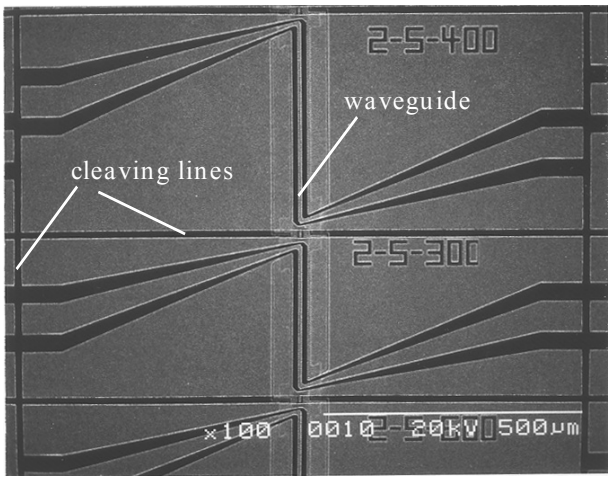

Fig. 4.7 SEM picture of fabricated devices prior to cleaving to single devices.

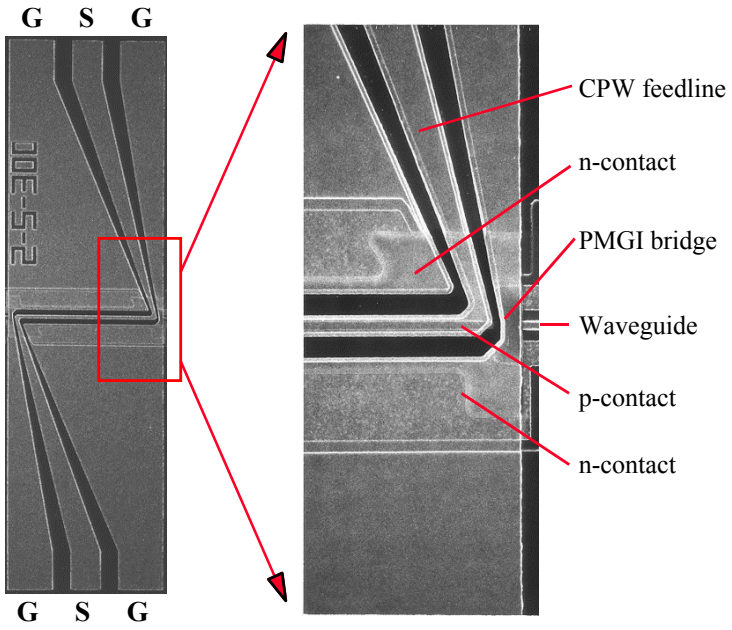

Fig. 4.8 Close-up SEM pictures of a single device and the waveguide to feed line connection region.

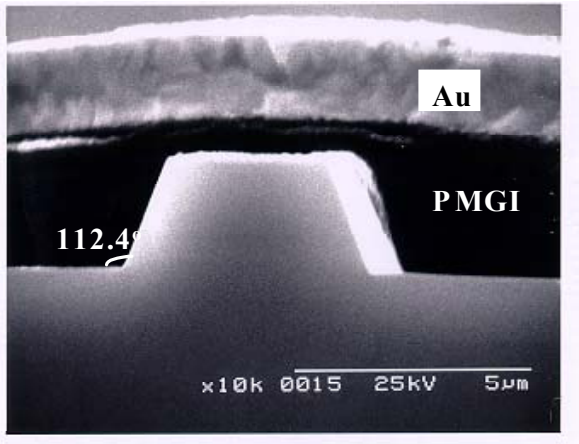

Fig. 4.9 Facet view SEM picture of a 3-μm ridge device.

The processing steps for traveling-wave EA modulators are shown in Fig. 4.10. These steps include 1) p-contact evaporation; 2) ridge formation; 3) n-contact evaporation and contact annealing; 4) mesa etch, PMGI passivation/bridging/ planarization; and, 5) final metalization, cleaving line formation, wafer lapping and device cleaving.

Itemized processing steps are listed in Appendix F; here we only give an outlined description.

The first mask process was p-contact evaporation and RIE mask evaporation, to make a self-aligned mask for optical waveguide etch (Fig. 4.10 step 1). The evaporated layers included Cr/Au/Zn/Au = 5/5/19/400 nm, evaporated with the thermal evaporator, and Ti/SiO_2 = 20/650 nm, evaporated with the electron beam evaporator. SiO_2 served as the mask for subsequent RIE etching while Ti was used to improve the adhesion of SiO_2 to the surface.

Following p-metal/mask evaporation, Cl_2/Ar RIE etching was performed to form the optical waveguide (Fig. 4.10 step 2). In order to accurately control the etch depth, a He-Ne laser was used to monitor the surface reflection intensity during RIE etching [15]. Prior to the real device etch, a test etch was performed to record the surface reflection curve. Fig. 4.11 shows such a curve recorded during the RIE test etch. The stop etch point was chosen right before the $(InGaAs)_x(InAlAs)_{1-x}$ grading layers as shown in the figure.

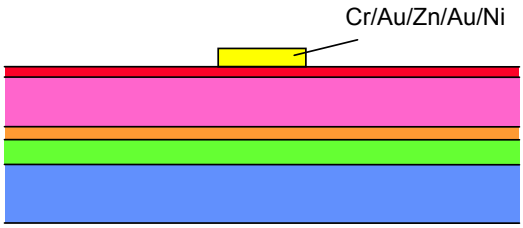

Step 1: p-contact evaporation

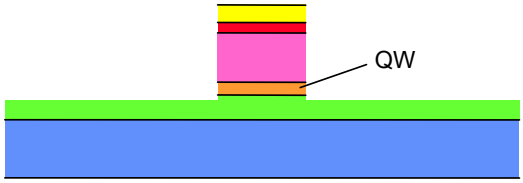

Step 2: Ridge formation

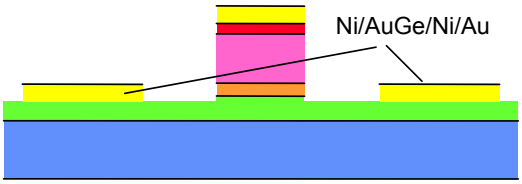

Step 3: n-contact evaporation

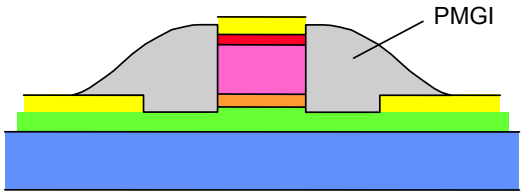

Step 4: Mesa etch, PMGI passivation/bridging/planarization

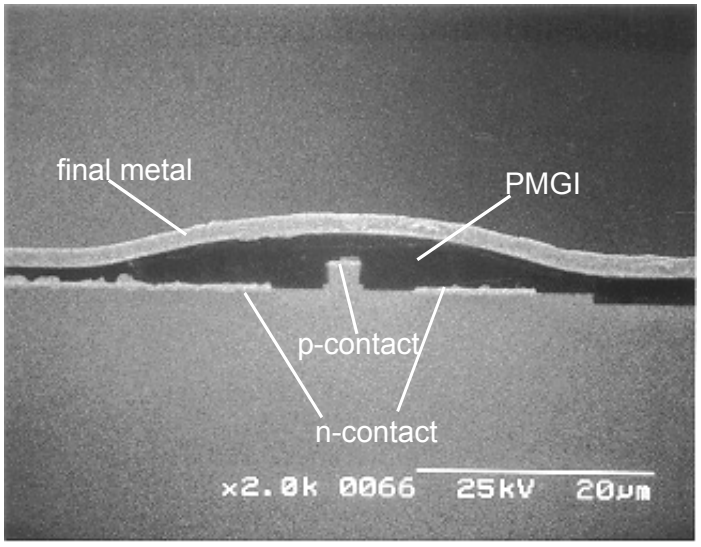

Step 5: Final metalization, cleaving line etch, wafer lapping, device cleaving. This picture was taken from an InGaAsP/InGaAsP device, which had a 90° side wall.

Fig. 4.10 Processing steps for traveling-wave EA modulators.

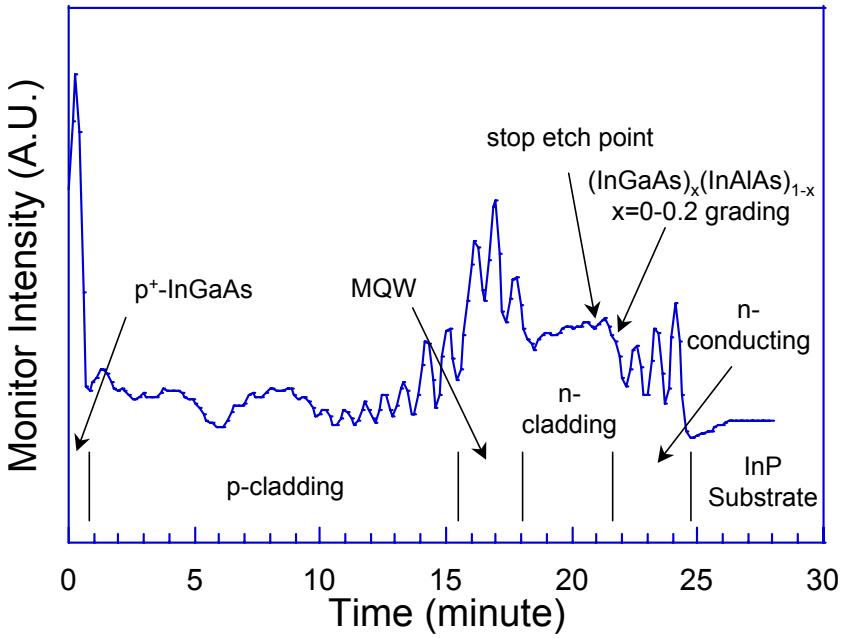

Fig. 4.11 He-Ne laser monitored surface reflection intensity during RIE etching.

Due to the non-volatile property of $InCl_3$, it was not fully removed from the etching surface, which at the end resulted in a side wall angle of about 67.6^o (Fig. 4.9). Many methods have been used to overcome this problem. These include raising the substrate temperature [16], increasing the etch bias voltage with mixture Ar/Cl_2 gasses [17], and using reactive ion beam etching (RIBE) followed with a slight wet etching [2].

After dry etching, residual SiO_2 was removed with a buffered HF dip. This process also took away the adhesion Ti layer.

The second mask process was n-contact evaporation (Fig. 4.10 step 3). An n-contact metal consisting of Ni/Ge/Au/Ni/Au = 5/17/30/20/400 nm was evaporated.

The third mask process was the mesa etch (Fig. 4.10 step 4). This step was to remove residual conductive layers and etch down to the SI-InP substrate at the

feed line region. Photo resist was used as etch mask and the etching was done with Cl_2/Ar RIE etching. Again, He-Ne laser was used to monitor the etching depth.

After mesa etching, the contacts were alloyed using rapid thermal annealing.

The fourth and the fifth mask processes were for PMGI [5] passivation, bridge formation, and planarization (Fig. 4.10 step 4). PMGI was first spun onto the wafer and then cured in the oven. Thick photoresist was used to define the bridge area (fourth mask), and planarization etch was done with O_2 RIE etching. After the planarization etch, the fifth mask was used to protect PMGI at the waveguide region. Then the residual PMGI at the feed line region was removed with SAL 101 develop after deep UV exposure.

After PMGI was defined, it was re-flowed in an oven to smooth the surface steps (Fig. 4.10 step 4).

The sixth mask process was the final metal evaporation. The metal was thick for better microwave conductivity. It was composed of a 25/2000 nm-thick Ti/Au layer.

The seventh mask process was to etch cleaving lines and to remove PMGI in the cleaving lines. This was for easier cleaving.

After these steps, the wafer was lapped down to about 70 μm thick. Devices were cleaved, mounted onto copper bars with silver epoxy, and were ready for testing.

4.3 Device characterization

A lens pair was used to couple light from the fiber to the waveguide and vice versa. The lens pair was composed of two lenses, one with a numerical aperture matched to the single mode fiber, while the other one with a numerical aperture of 0.55. Two Cascade probes [18] were used to connect to the input and output ports of the device. Both open and with 50 Ω terminations were tested. In the case of 50 Ω termination, the output probe was terminated with a standard 50 Ω load. High-frequency measurements were performed with an HP Lightwave Component Network Analyzer, which can measure electrical to electrical, electrical

to optical, optical to electrical, and optical to optical responses. Detailed measurement configurations are described in Appendix E.

4.3.1 Static characteristics

Fig. 4.12 shows the fiber-to-fiber optical transmission versus reverse bias voltage for several wavelengths and for TE and TM polarization states. The device length was 300 μm, and the ridge width was 2 μm. The quantum well region composed of ten spiked-quantum wells. These curves were taken without anti-reflection coating on the facets. With AR coating, a 3-dB improvement in coupling efficiency was typically observed. With TE polarization, the drive voltage for a 10-dB extinction ratio was 2.0 V and it was 2.7 V for a 20-dB extinction ratio at 1530 nm. A quite large polarization dependence was observed because the quantum wells were unstrained.

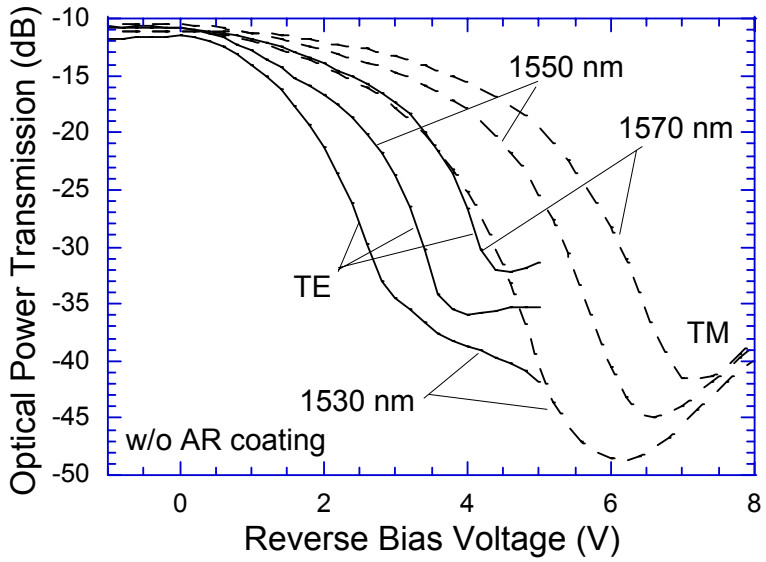

Fig. 4.12 Fiber-to-fiber transmission versus reverse bias voltage for several wavelengths and for TE and TM polarization states. The facets were not anti-reflection coated.

The optical propagation loss can be measured using the resonance property of the Fabry-Perot resonator. Due to resonance, the transmission of the waveguide

fluctuates with wavelength. Assuming that the incident angle is 0^o, then the optical transmission (output power divided by input power) is

$$T = \frac{P_{out}}{P_{in}} = \frac{(1-R)^2 e^{-\alpha l}}{(1-R\,e^{-\alpha l})^2 + 4R\,e^{-\alpha l}\sin^2\beta l}, \tag{4.1}$$

where l is the optical waveguide length, α is the power attenuation constant, β is the propagation constant, and R is the power reflectance at the facet. Here we assume both facets have the same reflectivity.

$$R = \left(\frac{n_{eff}-1}{n_{eff}+1}\right)^2 \tag{4.2}$$

It's not difficult to relate the propagation loss with the transmission minimum to maximum ratio by

$$Ratio = \frac{T_{\min}}{T_{\max}} = \left(\frac{1-R\,e^{-\alpha l/2}}{1+R\,e^{-\alpha l/2}}\right)^2 \tag{4.3}$$

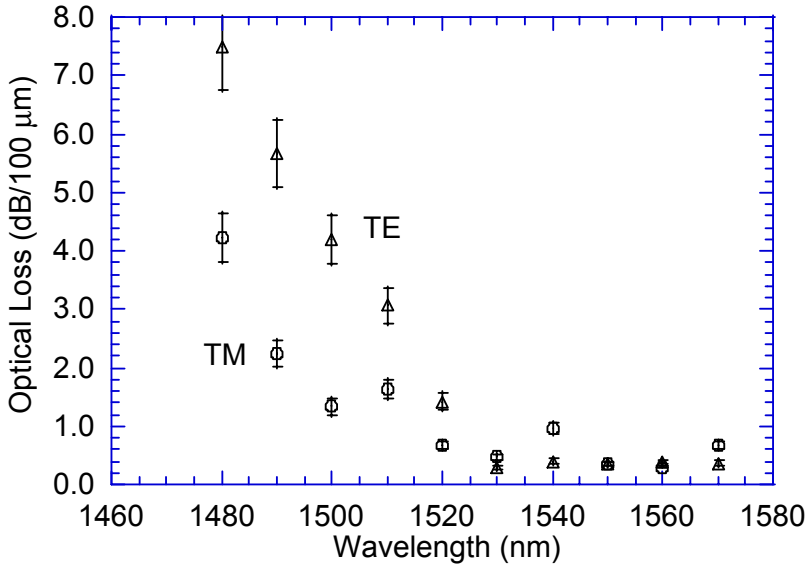

Fig. 4.13 Waveguide optical propagation loss measured by Fabry-Perot resonance method. The bias voltage was 0 V.

Figure 4.13 shows the measured optical power transmission loss at different wavelengths and for TE and TM polarization states. We can see that the propagation loss was about 1.0 dB for a 300-μm long device at a wavelength of 1.55 μm, which according to Fig. 4.12 suggests that the coupling loss is about 5 dB per facet.

4.3.2 Dynamic performance

Microwave port-to-port S parameter measurements were first made to understand the electrical wave propagation characteristics. Fig. 4.14 and Fig. 4.15 show the S_{21} and S_{11} responses of two 500-μm long, 2.5-μm wide devices. Also shown are simulation results for both the transmission line model and the lumped RC model. As we can see from both figures, the transmission line model had better agreement with measurements, especially at high frequencies. The device had lower loss than what the lumped model predicted at high frequencies. This suggests that the transmission line structure does help improve the performance at high frequencies.

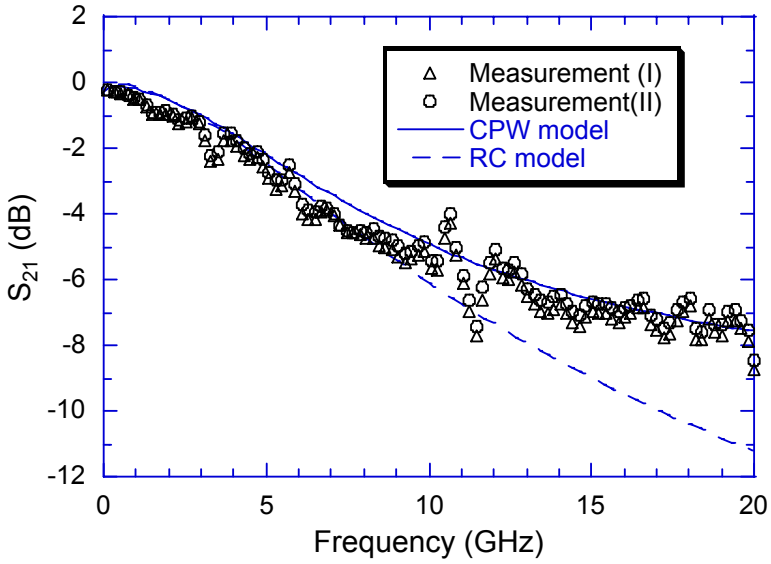

Fig. 4.14 Port-to-port S21 response of two 500-μm long, 2.5-μm wide devices (dots). Also shown are simulation results both with the CPW model and the lumped RC model (lines).

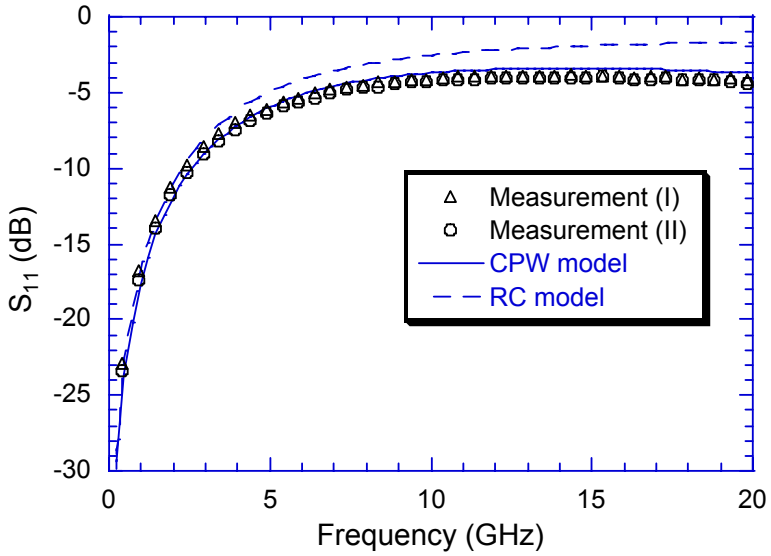

Fig. 4.15 Port-to-port S_{11} response of two 500-µm long, 2.5-µm wide devices (dots). Also shown are simulation results both with the CPW model and the lumped RC model (lines).

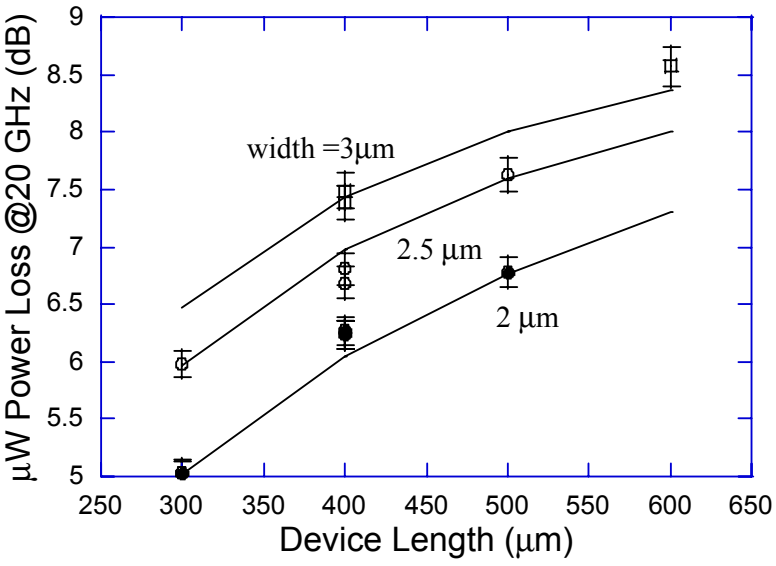

Fig. 4.16 Measured microwave port-to-port loss at 20 GHz for different device lengths and widths (dots). Together shown are simulated results with transmission line model (lines).

Nominal width (μm)	Actual top width(μm)	Active region width(μm)
2	1.78	3.85
2.5	2.66	4.59
3	3.16	5.03

Table 4.1 Actual device widths for different nominal width values.

Devices with different lengths and widths were measured and the microwave loss at 20 GHz is shown in Fig. 4.16. Theoretical simulations with the transmission line model are shown as lines. In the simulation, the actual device width values were used instead of the nominal values (Table 4.1). Due to the angled side wall, the widths at the active region were about two micrometers wider than their corresponding top widths. This extra width caused an increase in microwave propagation loss and reduced the characteristic impedance, and both effects cause the increase of the microwave loss. Simulations suggested that the microwave power propagation loss was about 0.68 dB per 100 μm at 20 GHz; however, the S_{21} loss was about 5 dB for a 300-μm long device (Fig.4.16). This suggested that there was a loss of about 3 dB from other sources, most of which were from the characteristic impedance induced reflection loss. So it is crucial to reduce reflection loss.

Fig. 4.17 shows the normalized overall electrical-to-optical responses for a 300-μm long, 2-μm wide device under different terminations. Without any load termination, the 3-dBe bandwidth was about 5.5 GHz. It increased to 12 GHz with a 50 Ω termination from the output cascade probe. This bandwidth was highly affected by the angled side wall as shown in the simulation result in Fig. 3.24.

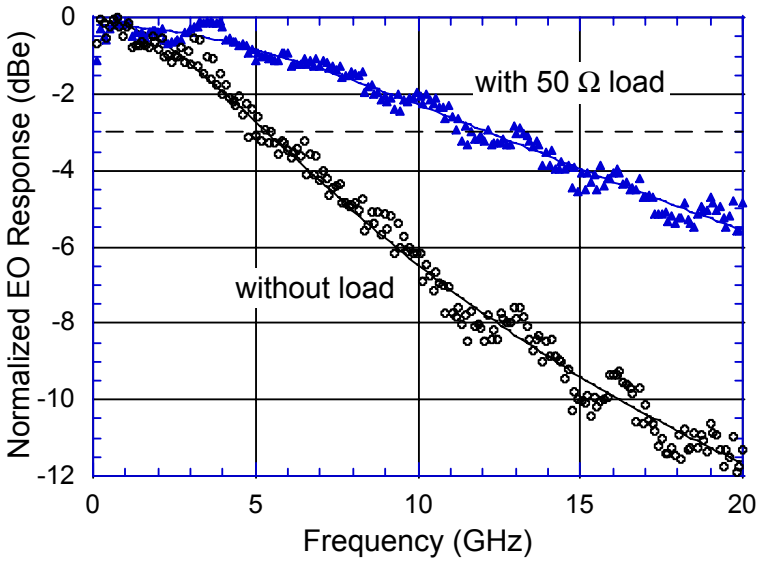

Fig. 4.17 Normalized electrical-to-optical response under different terminations.

4.4 Discussion and Summary

The first generation of traveling-wave electroabsorption modulators were designed and fabricated with MBE grown InGaAs/InAlAs material on a semi-insulating InP substrate. It was verified that the use of spiked quantum wells can reduce the drive voltage for the same absorption wavelength shift. With spiked quantum wells, drive voltages of 2.0 V and 2.7 V have been achieved for extinction ratios of 10 dB and 20 dB.

High speed measurements revealed that there was a large amount of loss associated with the impedance-mismatch induced microwave loss. A 3-dB bandwidth was limited to only 12 GHz with a 50 Ω load. The angled side wall was the main reason for limiting the bandwidth of the device. Also, as discussed in Section 2.5, the very low p-InAlAs hole mobility also contributes to larger microwave propagation loss in p-cladding layer compared to devices with an InP-cladding layer.

Based on these reasons, MOCVD grown InGaAsP/InGaAsP/InP material that used InP as cladding layer was chosen as our second-generation device material.

References

[1] K. Wakita, K. Yoshino, I. Kotaka, S. Kondo, and Y. Noguchi, "High speed, high efficiency modulator module with polarisation insensitivity and very low chirp," *Electron. Lett.*, vol. 31, pp. 2041-2, 1995.

[2] K. Wakita, I. Kotaka, K. Yoshino, S. Kondo, and Y. Noguchi, "Polarization-independent electroabsorption modulators using strain-compensated InGaAs-InAlAs MQW structures," *IEEE Photonics Technol. Lett.*, vol. 7, pp. 1418-20, 1995.

[3] T. Ido, S. Tanaka, M. Suzuki, M. Koizumi, H. Sano, and H. Inoue, "Ultra-high-speed multiple-quantum-well electro-absorption optical modulators with integrated waveguides," *J. Lightwave Technol.*, vol. 14, pp. 2026-34, 1996.

[4] F. Devaux, S. Chelles, A. Ougazzaden, A. Mircea, and J. C. Harmand, "Electroabsorption modulators for high-bit-rate optical communications: a comparison of strained InGaAs/InAIAs and InGaAsP/InGaAsP MQW," *Semicond. Sci. Technol.*, vol. 10, pp. 887-901, 1995.

[5] PMGI SF15, manufactured by Micro Chem Corp., Newton, MA.

[6] F. Devaux, J. C. Harmand, I. F. L. Dias, T. Guettler, O. Krebs, and P. Voisin, "High power saturation, polarisation insensitive electroabsorption modulator with spiked shallow wells," *Electron. Lett.*, vol. 33, pp. 161-163, 1997.

[7] Y.-G. Wey, "High-speed double heterostructure GaInAs/InP p-i-n photodiodes: theory, fabrication and measurement," University of California, Santa Barbara, CA, Ph.D. Dissertation, 1993.

[8] K. S. Giboney, "Travelling-wave photodetectors," University of California, Santa Barbara, CA, Ph.D. Dissertation, 1995.

[9] Y.-J. Chiu, personal communication.

[10] M. J. Mondry, Z. M. Chuang, M. G. Peters, and L. A. Coldren, "Low threshold current density 1.5 μm (In, Ga, Al)As quantum well lasers grown by MBE," *Electron. Lett.*, vol. 28, pp. 1471-2, 1992.

[11] M. J. Mondry, E. J. Tarsa, and L. A. Coldren, "Molecular beam epitaxial growth of strained AlGaInAs multi-quantum well lasers on InP," *J. Electron. Mater.*, vol. 25, pp. 948-54, 1996.

[12] B. L. Sharma, "Diffusion data for semiconductors," in *CRC Handbook of Chemistry and Physics*, D. R. Lide, Ed., 74 ed. Boca Raton, FL: CRC Press, 1993, pp. 12-89-12-99.

[13] J. Ko, M. J. Mondry, D. B. Young, S. Y. Hu, L. A. Coldren, and A. C. Gossard, "Threshold reduction by rapid thermal annealing in MBE-grown AlInGaAs multiquantum well lasers on GaAs," *Electron. Lett.*, vol. 32, pp. 351-2, 1996.

[14] K. Wakita, personal communication.

[15] R. L. Nagarajan, “Carrier transport effects in high speed quantum well lasers,” University of California, Santa Barbara, CA, Ph.D. Dissertation, 1992.

[16] D. G. Yu, E. L. Hu, and G. Hasnain, “Radical beam ion-beam etching of InAlAs/InP using Cl_2,” *J. Vac. Sci. Technol. B*, vol. 12, pp. 3378-3381, 1994.

[17] R. Germann, S. Hausser, and J.-P. Reithmaier, “Reactive ion etching of InAlAs with Ar/Cl_2 mixtures for ridge waveguide lasers,” *Microelectronic Engineering*, vol. 22, pp. 345-348, 1993.

[18] ACP40-GSG Cascade probe with 100 micron contact pitch, manufactured by Cascade Microtech, Inc., Beaverton, Oregon.

CHAPTER 5

InGaAsP/InGaAsP Device Fabrication and Characterization

As discussed in the previous chapter, compared to InAlAs-cladded devices, InP-cladded devices have smaller microwave loss due to the possibility of making 90^{o}-side wall waveguide and the higher conductivity of InP cladding layers. InGaAsP/InGaAsP devices have been demonstrated with high speed, low drive voltage, polarization independent and high power saturation [1-4]. So InGaAsP/InGaAsP material system is both good for achieving high static performance, such as low drive voltage, polarization independent and high power saturation, and for high-speed traveling-wave operation. Based on these reasons, we used it as our second-generation device material.

A device processing procedure similar to that for the MBE grown InGaAs/InAlAs device was deployed. A dry etch combined with wet etch were used to form the optical waveguide. Better etch depth control was achieved with the use of etching stop layer for wet etchant. A 90^{o}-side wall was easily achieved with these devices. The MOCVD grown InGaAsP/InGaAsP devices yielded polarization insensitivity, lower drive voltages, and higher bandwidths. High figure of merit was achieved with these modulators.

5.1 Material structure and characterization

5.1.1 Growth structure

The material was grown on 3^{o}-off (001) semi-insulating InP substrates. Fig. 5.1 shows the epilayer structure. The quantum well was designed for polarization insensitive operation as discussed in Section 2.4. We used tensile strained quantum well for polarization independence as discussed in Chapter 2. In order to avoid misfit dislocation, a compressively strained barrier was used to compensate the strain. The quantum wells were composed of 10.4-nm thick tensile strained InGaAsP wells with strain of –0.37% and a bulk photoluminescence wavelength of 1580 nm, and 7.6-nm thick compressively strained InGaAsP barriers with strain of

+0.5% and a bulk photoluminescence wavelength of 1150 nm. The overall photoluminescence wavelength of the quantum well region was about 1495 nm. Table 2.2 shows the detailed structure of the quantum well region.

0.1 μm p^+-InGaAs	p-contact/cap
0.5 μm InP p = 1e18	p-cladding
1.0 μm InP p = 5e17	
~0.15 μm InP nid	p-doping offset
10 QW 11 Barrier	MQWs
30 nm InP nid	n-doping offset
0.3 μm InP n = 5e17	n-cladding
20 nm InGaAsP n = 3e18	n-contact/etching stop
0.5 μm InP n = 3e18	n-conducting
SI - InP	Substrate

Fig. 5.1 Material structure of MOCVD grown InGaAsP/InGaAsP TEAMs. The quantum well structure is shown in Table 2.2.

Similar to the InGaAs/InAlAs devices, the device structure consisted of 10 wells and 11 barriers. This structure used p- and n-InP as cladding layers, and a 0.5-μm n^+-InP layer as n-conducting layer. A 20-nm thick 1.3Q InGaAsP was inserted between n-cladding and n-conducting layers to serve as wet etching stop layer and as n-contact layer. The layers were grown on semi-insulating InP substrate for high-speed operation.

Since Zn is highly diffusive in InP [5], a p-doping offset layer of 0.15 μm was grown to prevent Zn from diffusing into the active region. A much thinner doping-offset was used in the n-side because the diffusion coefficient of Si is much smaller than that of Zn.

The epilayers were grown with low pressure MOCVD at 615^{o}C. The pressure was 350 Torr and the V-III flux ratio ranged from 10 to 50. Calibration

growths were carried on before the growth of the actual device structure. Double crystal X-ray measurements were used to characterize the lattice constant of the material and room temperature photoluminescence (PL) were used to calibrate the PL wavelength and to evaluate the quality of the material.

5.1.2 Photoluminescence characteristics

The as grown material was first characterized with room temperature PL measurement and X-ray double crystal measurement. Fig. 5.2 shows photoluminescence spectra of two different positions on the same wafer; one at the center of the wafer, while the other at the very edge. The edge had weaker PL intensity; however, the peak wavelength position was close to that at the center. This suggested that the wavelength uniformity was good enough for precise wavelength operation.

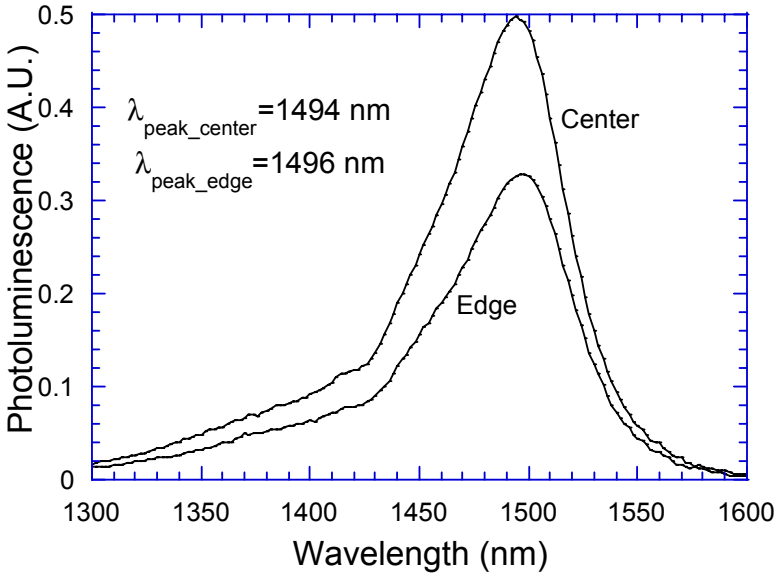

Fig. 5.2 PL spectra at two different positions on the same wafer.

5.1.3 X-ray diffraction characteristics

Fig. 5.3 shows the (400) double crystal rocking curve of the as grown wafer. The zero-order peak was almost at the same position as the InP peak, suggesting that the strain in the quantum well region was well compensated. The period of the quantum well can be obtained with [6]

$$\Lambda = \frac{\lambda}{2(\cos\theta)\cdot\delta\theta}, \tag{5.1}$$

where λ =0.15405 nm is the X-ray wavelength, θ = 31.669^{o} is the X-ray incident angle, and $\delta\theta$ is the angle separation between the zero and the first order peaks. With these values substituted into Eq. 5.1, the period is

$$\Lambda = 1.8667\times10^{4} / \delta\theta(arc\,\mathrm{sec}) \qquad [\mathrm{nm}], \tag{5.2}$$

where $\delta\theta$ is with a unit in arcsec, and the period is with a unit in nm.

From the rocking curve, the period of the quantum well was calculated to be 17.95 nm. According to the thickness ratio between the well and the barrier, the quantum well was 10.36 nm, and the barrier was 7.59 nm.

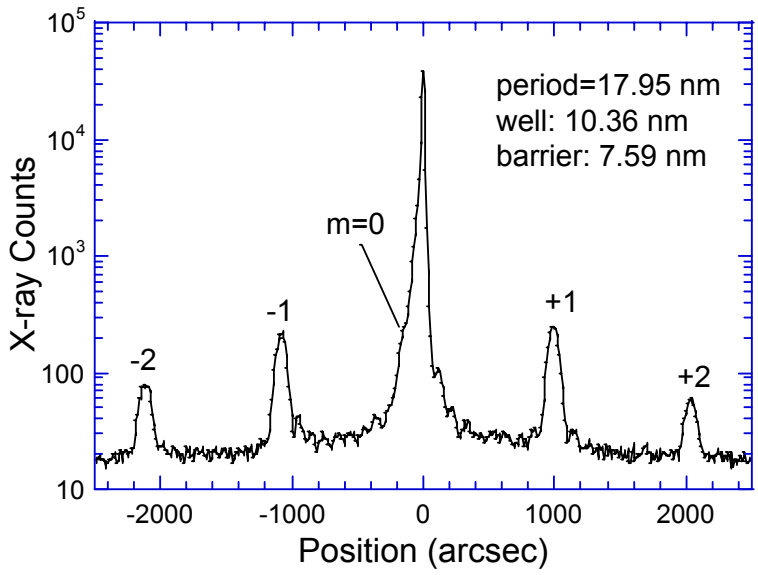

Fig. 5.3 X-ray double crystal rocking curve of the (400) reflection using CuKα radiation.

5.1.4 Photocurrent measurement

A photocurrent measurement system slightly different from the one used for the MBE material characterization was used. In the previous set-up, a tunable diode laser was used to scan the wavelength, which limited the wavelength range to 1480 ~ 1570 nm. In order to obtain the information at a wider wavelength range, a halogen white light source plus a monochromator were used to generate wide wavelength range source. The detailed measurement set-up is given in Appendix E.

Broad area structure devices were fabricated specially for photocurrent measurement prior to the fabrication of the real devices. Fig. 5.4 shows the photocurrent spectra of a sample under the illumination of TM polarization light. Compared to the photocurrent spectra of the MBE samples (Figs. 4.5-4.6), the absorption edge of the MOCVD sample shifted faster than the non-spiked quantum well. But it shifted at about the same speed as the spiked quantum well, which is expected since they had about the same quantum well thickness.

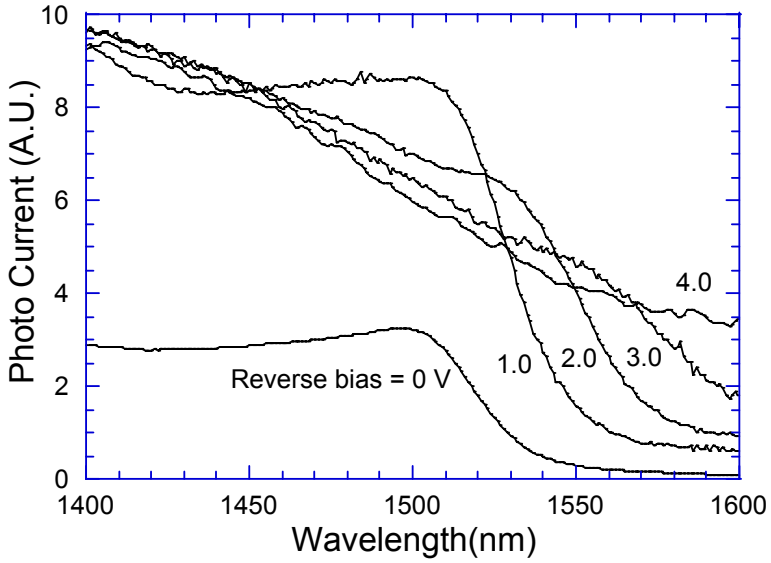

Fig. 5.4 Photocurrent spectra of a device under different reverse bias voltages.

5.2 Fabrication processes

The device fabrication process was similar to that for the MBE devices. The only differences were the p-contact metals, RIE dry etching, and the wet etching used for the post RIE etching surface clean and for the mesa etching. Better etch depth control was achieved with the use of etching stop layer for wet etchant.

The device electrode structure is the same as the MBE one, and is shown in Figs. 4.7-4.8. The processing steps are schematically shown in Fig. 4.10.

Itemized processing steps are listed in Appendix F; here we only give an outlined description of the steps that are different from that for the MBE devices. At the end of this section, the process for making thin-film resistors and for anti-reflection facet coating are also discussed.

5.2.1 Device fabrication

The first mask process was p-contact evaporation and RIE/wet etch self-aligned mask evaporation (Fig. 4.10 step 1). The evaporations included Ti/Pt/Au/Si = 20/50/500/200 nm evaporated with electron beam evaporator. Si served as the mask for subsequent RIE etching.

Following p-metal/mask evaporation, CH_4/H_2/Ar RIE etching was performed to form the optical waveguide (Fig. 4.10 step 2). In order to accurately control the etch depth, a He-Ne laser was used to monitor the surface reflection intensity during RIE etching [7]. Fig. 5.5 shows a curve recorded during the real sample etch. The stop etch point was chosen two cycles after the quantum well and one cycle before the etching stop layer. The monitor beam was shining on the edge of the sample. Due to non-uniformity of the plasma, the etching rate at the edge was higher than that at the center. Extending the four edges with InP substrate will improve etching uniformity [8].

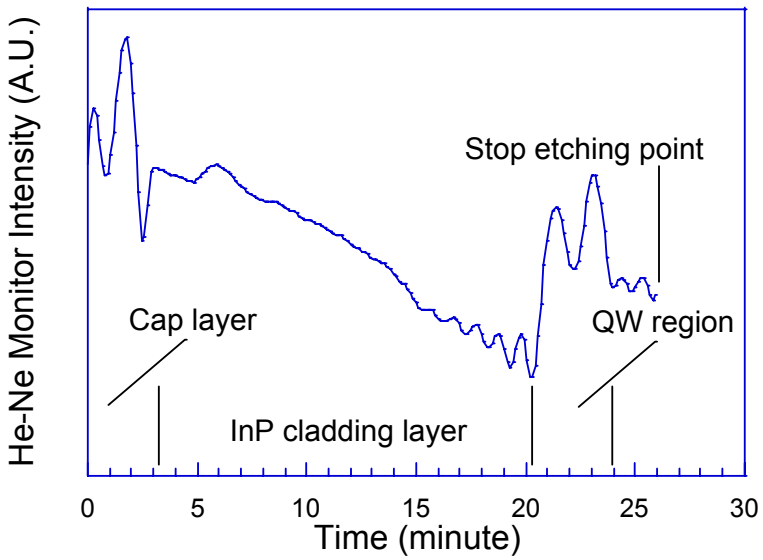

Fig. 5.5 He-Ne laser monitored surface reflection intensity during RIE etching.

After dry etching, residual Si was removed with CF_4/O_2 RIE etching. Then wet etchant H_3PO_4:HCl=3:1 was used to smooth the side wall and to etch to the n-contact and etch stop layer (1.3 Q InGaAsP). SEM was used to watch the side wall after wet etching. The CH_4/H_2/Ar RIE and subsequent wet etching form a 90^o-side wall on $(0\bar{1}\bar{1})$ oriented ridges. Fig. 5.6 shows the facet view SEM picture of a finished 2-μm wide device. The wider width at the bottom of the ridge was due to the post-RIE wet etching, which will not etch the quaternary material.

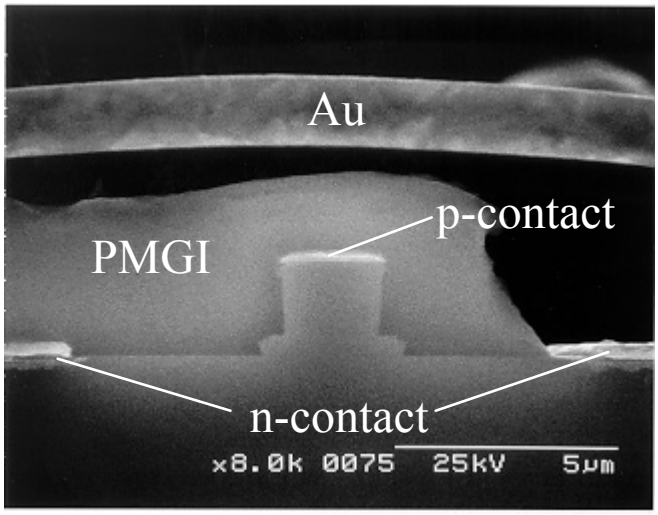

Fig. 5.6 Facet view SEM picture of a finished InGaAsP/InGaAsP TEAM.

The second mask process was n-contact evaporation (Fig. 4.10 step 3). Same as for the MBE devices, an n-contact metal consisting of Ni/Ge/Au/Ni/Au = 5/17/30/20/400 nm was evaporated.

The third mask process was mesa etching (Fig. 4.10 step 4). This step was to remove residual conductive layers and etch down to the SI-InP substrate at the feed line region. Photo resist was used as etch mask. The etching was done with H_3PO_4:HCl=3:1 etch to remove the residual n-InP cladding layer, followed by H_3PO_4:H_2O_2:H_2O=1:1:30 etch to break through the etching stop layer, and finally H_3PO_4:HCl=3:1 etch through the n-conducting layer.

After the mesa etch, the contacts were alloyed via rapid thermal annealing.

The fourth and the fifth masks processes were for PMGI passivation, bridge formation, and planarization (Fig. 4.10 step 4). These processes are the same as those for MBE devices.

The sixth mask process was final metal evaporation. It composed of Ti/Au layer of 25/2000 nm thick.

The seventh mask process was to etch cleaving lines and to remove PMGI in the cleaving lines. Gold etchant and deep UV exposure followed by SAL 101 [9] developing formed the cleaving lines.

After these steps, the wafer was lapped down to about 70 μm thick. Devices were cleaved, mounted onto copper bars with silver epoxy. Thin film resistors were fabricated as load termination. For the devices loaded with thin film resistors, the resistors were also mounted on the copper bars, and were connected to the modulator output ports with ribbon bonding.

5.2.2 Thin film resistor fabrication

The thin film resistors were made on aluminum nitride substrates [10]. Resistive material TeN was pre-deposited by the AlN substrate manufacturer. The left part of Fig. 5.7 shows the material structure of the AlN substrate. The resistivity of the TeN layer was 50 Ω/square.

The resistor was designed to have 50 Ω transmission feed lines. The thin film region was designed to be large (200 μm wide, 200 ~ 330 μm long) in order to handle high bias DC current.

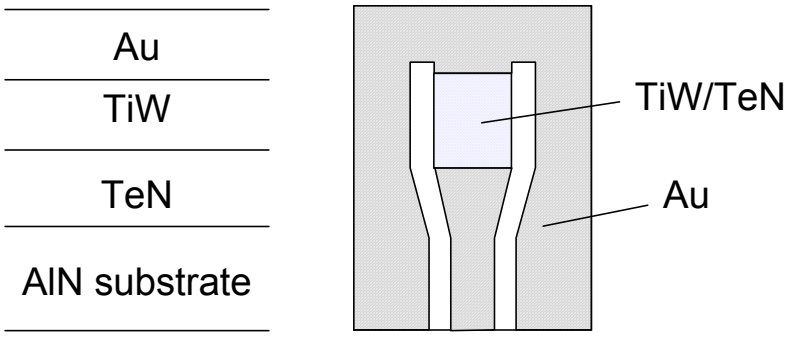

Fig. 5.7 Material structure of AlN substrate used for making thin film resistors and the top view structure of the resistor.

There were two mask layers for the thin film resistor. The first layer etched away the isolation region and the second defined the thin film region.

The top gold layer was etched with Technic Strip Cyanide gold etchant (lethal when mixed with acid, avoid any acid!). TiW was etched with 40^{o}C straight H_2O_2, while TeN was etched with H_3NO_4:HF = 3:1 solution. Testing structures on the mask were used to determine whether specific layer was etched through by measuring the resistance during the etching process.

The thin film region was designed to have partial TiW left on, in order to reduce the resistivity of the film. This will allow a bigger film size for the same resistance. Resistance measurements were performed between TiW etch steps to ensure the resistance end up with the designed value.

5.2.3 Anti-reflection coating

For some devices, anti-reflection coating was done in order to reduce the facet optical reflection. The film was a single layer quarter-wavelength SiO. The refractive index of evaporated SiO film was about 1.8~2, resulting in a quarter wavelength of about 200 nm for operation wavelength near 1.55 μm.

It was found that the devices typically had about 3-dB insertion loss reduction from fiber to fiber after being AR coated.

5.3 Device characterization

The device measurement setup was described in Appendix E. Here we only present the results.

5.3.1 Transmission-voltage characteristics

Fig. 5.8 shows the fiber-to-fiber optical transmission versus reverse bias voltage for several wavelengths and for TE and TM polarization states. The device length was 300 μm, and the ridge width was 2 μm. These curves were taken without anti-reflection coating on the facets. With TE polarization, the drive voltage for 10-dB extinction ratio was 0.8 V and it was 1.2 V for a 20-dB extinction ratio at 1550 nm. The device showed little dependence on polarization due to the strained quantum well design as described in Chapter 2 Section 2.4. The drive voltage for 20-dB extinction ratio was 1.28 V for TM polarization.

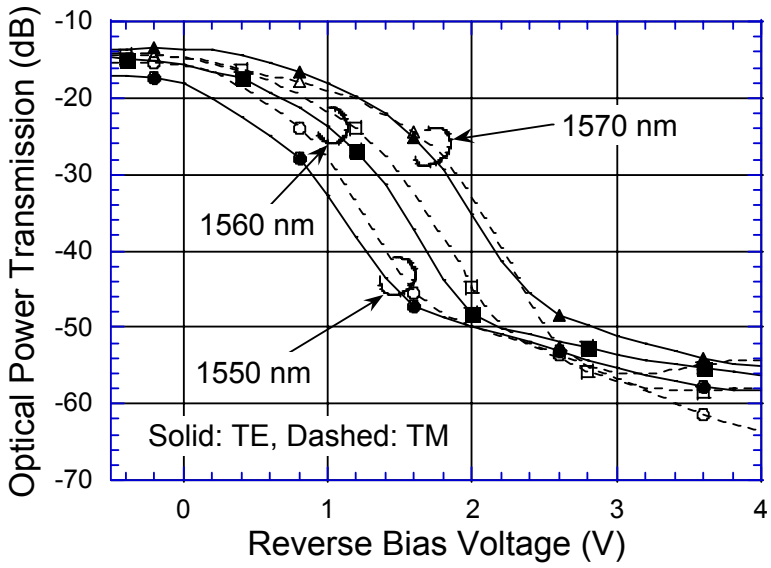

Fig. 5.8 Fiber-to-fiber transmission versus reverse bias voltage for several wavelengths and for TE and TM polarization states. The facet was without anti-reflection coating.

5.3.2 Straight waveguide microwave characteristics

Microwave port-to-port S parameter measurement was first made to understand the electrical wave propagation characteristics.

Straight waveguide section was measured to study the characteristics of the device without feed lines. Pico probes were used to probe the two ends of the straight waveguide. A 50 GHz HP network analyzer was used to accurately measure the response up to 50 GHz. The bias voltage was 0 V (no bias).

S parameters were measured with the network analyzer. Following is the derivation showing how to obtain the characteristic impedance and the propagation constant from the S parameters [11, 12].

The ABCD matrix can be related to the S parameters by [11, 12]

$$\begin{bmatrix} A & B \\ C & D \end{bmatrix} = \begin{bmatrix} \dfrac{(1+S_{11})(1-S_{22})+S_{12}S_{21}}{2S_{21}} & Z_{0R}\dfrac{(1+S_{11})(1+S_{22})-S_{12}S_{21}}{2S_{21}} \\ \dfrac{1}{Z_{0R}}\dfrac{(1-S_{11})(1-S_{22})-S_{12}S_{21}}{2S_{21}} & \dfrac{(1-S_{11})(1+S_{22})+S_{12}S_{21}}{2S_{21}} \end{bmatrix}, \quad (5.3)$$

where Z_{0R} is reference impedance of the measurement system which is 50 Ω in this work.

On the other hand, the ABCD matrix of a lossy transmission line is

$$\begin{bmatrix} A & B \\ C & D \end{bmatrix} = \begin{bmatrix} \cosh(\gamma l) & Z_0 \sinh(\gamma l) \\ \dfrac{\sinh(\gamma l)}{Z_0} & \cosh(\gamma l) \end{bmatrix}, \quad (5.4)$$

where Z_0 is the characteristic impedance of the line, $\gamma=\alpha+j\beta$ is the propagation constant, and l is the length of the waveguide.

Therefore the characteristic impedance and the propagation constant are

$$Z_0 = \sqrt{\frac{B}{C}}, \quad (5.5)$$

$$\gamma = \frac{1}{l} a\cosh\left(\frac{A+D}{2}\right) = \frac{1}{l}\ln\left(\frac{A+D}{2} \pm \sqrt{\left(\frac{A+D}{2}\right)^2 - 1}\right), \quad (5.6)$$

where Eq. 5.6 has double values, the physical meaningful value of γ is the one with positive α.

The phase velocity of the microwave is

$$v_{ph} = \frac{\omega}{\beta}. \quad (5.7)$$

Fig. 5.9 shows the characteristic impedance as a function of frequency for device ridge widths of 2.0 and 3.3 μm. Solid lines are for the measurement and dashed lines are for the simulation. The characteristic impedance of a 2.0 μm device was about 20 Ω for the frequency range of 10~40 GHz, while it was about 17 Ω for the 3.3 μm ridge device.

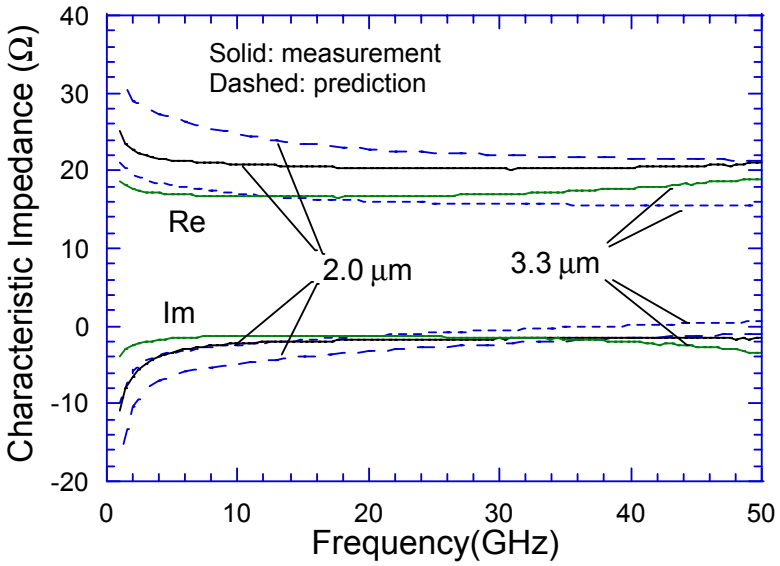

Fig. 5.9 Characteristic impedance of straight waveguides with different ridge widths. Solid curves: measurement, dashed curves: simulation.

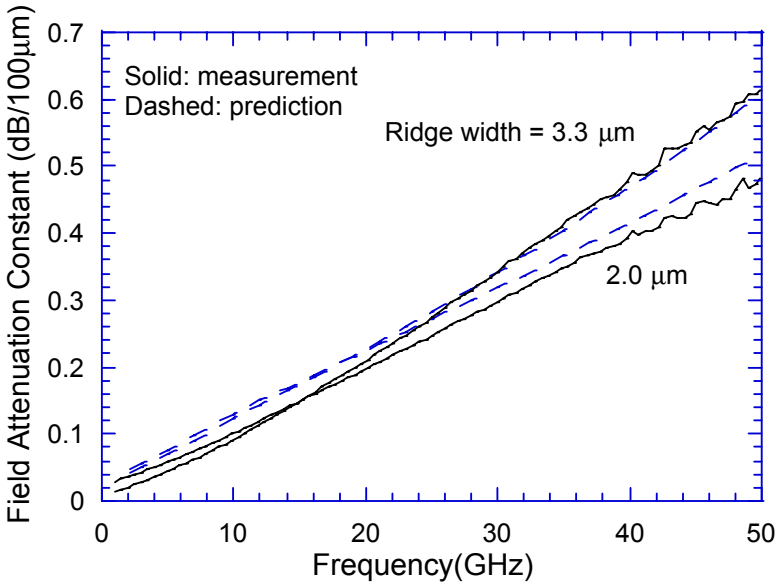

Fig. 5.10 Microwave field attenuation constant of straight waveguides with different ridge widths. Solid curves: measurement, dashed curves: simulation.

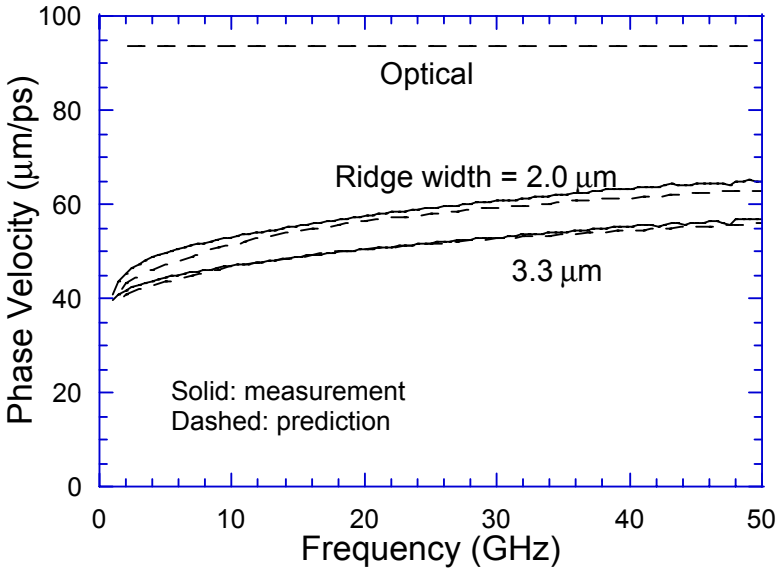

Fig. 5.11 Phase velocity of straight waveguides with different ridge widths. Solid curves: measurement, dashed curves: simulation, top dashed straight line: predicted optical phase velocity.

Fig. 5.10 shows the field attenuation constant as a function of frequency for device ridge widths of 2.0 and 3.3 μm. As we can see from the figure, the theory agrees reasonably well with the measurement. The discrepancy at low frequencies could be from the inaccuracy in modeling the actual metal impedance, because the quality of the evaporated gold may not be perfect in terms of conductivity, roughness and width variation. The measurement shows that the field attenuation at 20 GHz is about 0.2-dB/100 μm for both ridge-width devices. This means that the microwave power propagation loss through a 300-μm long device will be only 1.2 dB. At 50 GHz, the microwave power propagation loss through a 300-μm long device will be 3.0 dB for the 2.0-μm device, which means that 50 GHz device might be possible if there is no other loss sources, especially, the reflection loss.

At 40 GHz, the field attenuation was 0.4 dB/100 μm, close to the value of 0.43 dB/100 μm reported by Chiu et al [13]. Tauber et al reported a much higher field attenuation of 2.5 dB/100 μm, which could possibly come from a thinner intrinsic layer and a wider gap width [14].

Fig. 5.11 shows the phase velocity of the microwave. Together shown is the optical phase velocity predicted from the beam propagation method simulation, which suggested an optical effective index of 3.21 (Fig.2.15). For the 2.0-μm device, the microwave phase velocity is 56~67% of that of the optical wave for the frequency range of 10~40 GHz.

Straight-line waveguide measurements (Figs. 5.9-5.11) show that the equivalent circuit model is accurate for predicting the characteristics of the waveguide.

5.3.3 Port-to-port device microwave response

Microwave characterization was also performed with the full device with the input and the output feed lines.

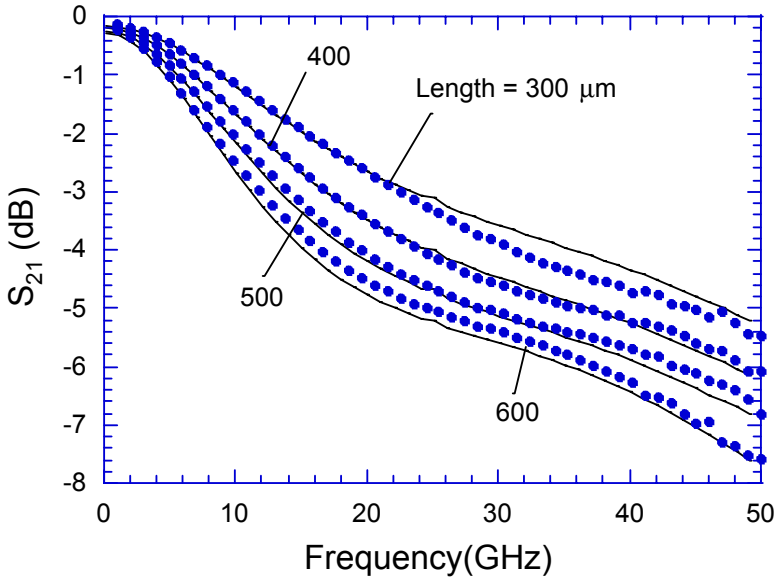

Fig. 5.12 Microwave port-to-port S_{21} responses for 2.0-μm wide devices with different lengths. Dots: measurement, curves: prediction.

Fig. 5.12 shows the microwave port-to-port S_{21} responses for devices with 2.0-μm wide ridges but with different waveguide lengths. The dots in the figure represent the measurement while the curves are simulations.

Devices with different lengths and widths were measured and the microwave loss at 20 GHz is shown in Fig. 5.13. The microwave port-to-port loss at 20 GHz is about 2.7 dB for a 300-μm long device. From Fig. 5.10 we know the propagation loss is about 1.2 dB. So there is an extra loss of 1.5 dB coming from other sources.

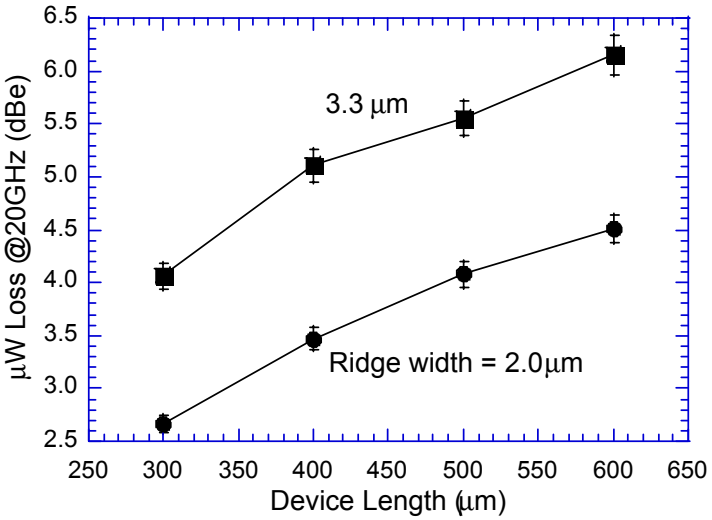

Fig. 5.13 Measured microwave port-to-port loss at 20 GHz for different device lengths and widths.

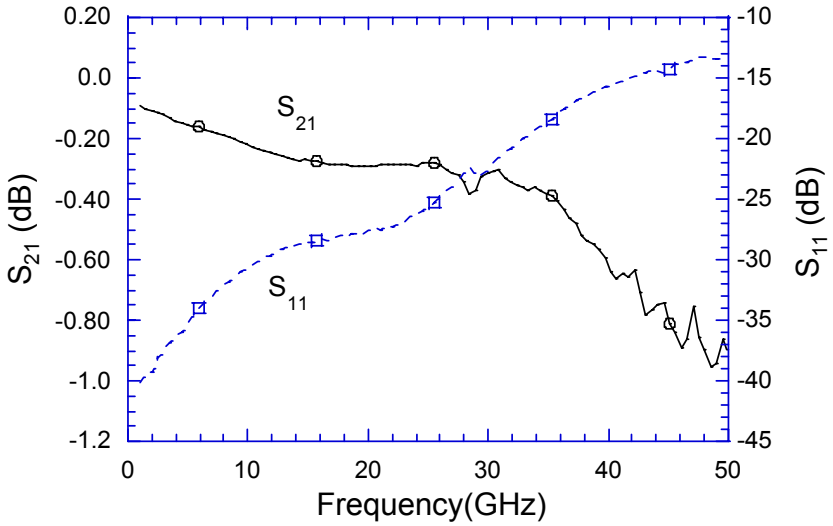

Fig. 5.14 Measured S_{21} and S_{11} responses of a comparison sample that has the same electrode structure as the 2-μm wide, 300-μm long device, except that it was fabricated all on semi-insulating InP substrate.

In order to verify if the feed lines could contribute to a large microwave loss comparison structures were fabricated together with the real devices. These test structures had the same electrode structure as for the real device except that it was made all on top of semi-insulating substrate. Fig. 5.14 shows the S_{21} and S_{11} of such a test structure that had the same electrode structure as the 2- μm wide, 300- μm long devices. A transmission loss of about 0.3 dB was observed at 20 GHz. This is the total loss of the feed lines and the waveguide region. Therefore the impedance mismatch induced reflection loss in the real device could be as large as 1.2 dB. This is a rather large loss compared to the propagation loss of 1.2 dB. This suggests that impedance matching is equally or even more important than reducing propagation loss in the waveguide region.

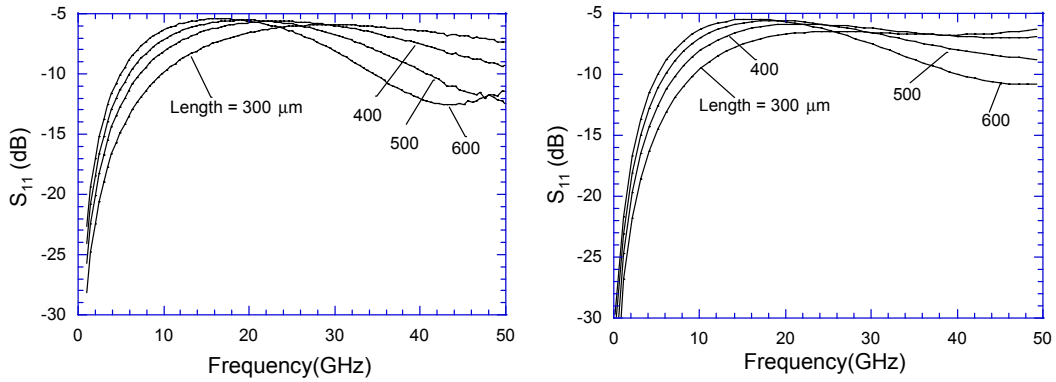

Fig. 5.15 Port-to-port S_{11} responses for 2.0-μm wide devices with different lengths. Left: measurement; right: simulation

Fig. 5.15 shows the port-to-port electrical S_{11} responses for 2- μm wide devices with different lengths. We can clearly see reflection reduction at some high frequencies. As verified by simple calculation, this was due to the cancellation of reflections from the input port and from the waveguide to the output feed line junction. As shown in Fig. 3.27, since the input contact pad has an impedance smaller than 50 Ω, there will be a negative reflection from this point; on the other hand, there will be a positive reflection from the waveguide to the output feed line junction. At frequencies when the round trip phase shift is 2π, these two reflections will cancel each other. The right part of Fig. 5.15 shows the simulation result based on the theory discussed in Chapter 3. A fairly good agreement is seen,

especially at low frequencies. The reason why the simulated resonant frequency is higher could be because the effective feed line length is longer than the straight distance from the contact pad to the waveguide (Fig. 4.8), which is used in the simulation. It should be noted that this reflection cancellation effect is a proof of distributed effect in the structure.

5.3.4 E-O response

Fig. 5.16 shows the normalized overall electrical-to-optical responses for a 300-μm long, 2-μm wide device under different terminations. The dots are for the measurements and the curves are for the theoretical calculations. Without any load termination, the 3-dBe bandwidth was about 10.7 GHz. It increased to 18 GHz with a 50 Ω termination from the output cascade probe. When a thin film resistor with impedance of 35 Ω was used to terminate the output port via a ribbon bond, the bandwidth exceeded 20 GHz, the range of the HP Lightwave component network analyzer used. An extrapolated bandwidth from the theoretical prediction was 24.7 GHz, yielding to a figure of merit of 17.2 GHz/V for this device.

The key feature on the response curve with 35-Ω termination was the resonance peak, which was mainly caused by the microwave reflections at the load and the source ends and at the interfaces between the optical waveguide and the feed lines. Because of the negative reflection at the load, the response at some frequencies was enhanced. This effect was also observed in traveling-wave electro-optic modulators [15].

The load impedance effect can be seen in Fig. 5.17, which shows the simulated optical signal output under small signal modulation with three different terminations. Here, a Gaussian-shaped pulse with $T_{FWHM} = 10\sqrt{\ln 2}$ ps and an amplitude of 0.07 V was used as the modulation signal that superimposes on a dc bias level.

Without any load termination, the output optical pulse profile showed multiple reflection structures that come from the interfaces between the optical waveguide and the feed line; and between the feed lines and the source/load. These reflections had the same sign as the output signal because both the source and the load had higher impedance than the waveguide (characteristic impedance ~ 20 Ω)

and the feed line (characteristic impedance ~ 40-50 Ω, Fig. 3.27). The reflections became much weaker when a 50-Ω termination was used. The reflection changes the sign when the load impedance was reduced to 35 Ω and canceled the reflection at the connections between the optical waveguide and the feed lines. This cancellation in reflection caused a frequency response enhancement at high frequencies.

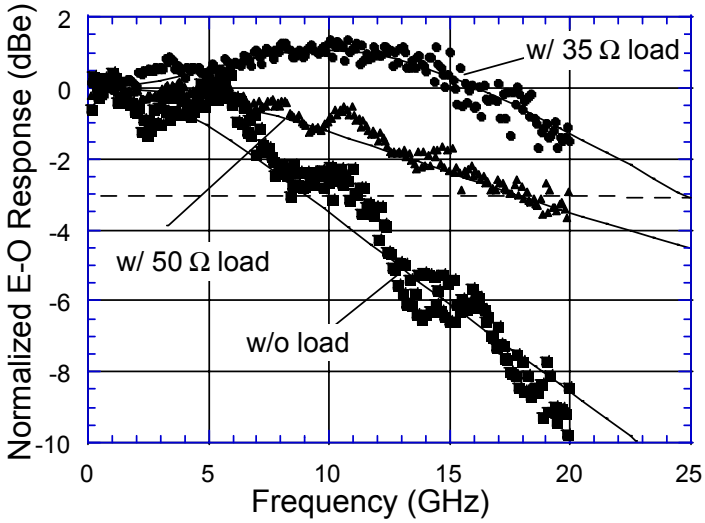

Fig. 5.16 Normalized electrical-to-optical response under different terminations. Dots: measurement, curves: prediction.

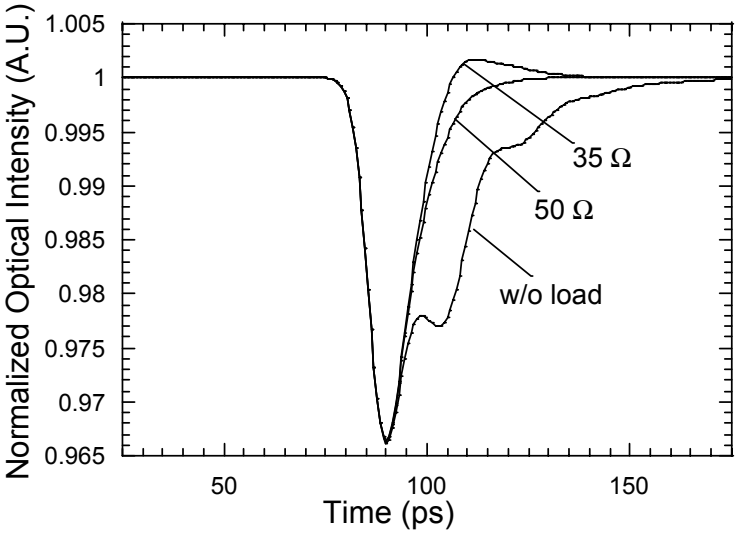

Fig. 5.17 Simulated output optical pulses with different load impedances under small signal modulation.

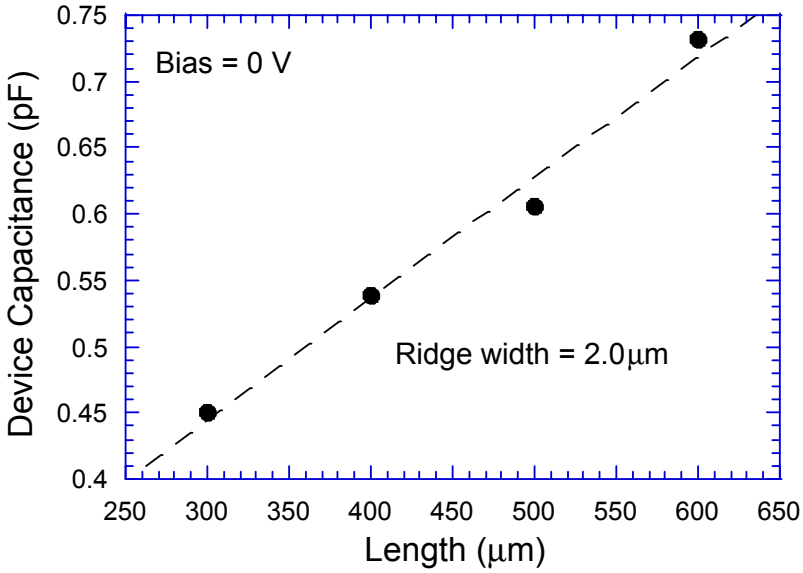

Fig. 5.18 Measured device capacitance for different ridge widths and lengths.

5.3.5 Traveling-wave vs. lumped

In order to verify if the traveling-wave electrode design improves the performance of the device, we measured the capacitance of the device. The output feed line was cleaved off to avoid reflection from the output port. HP network analyzer was used to measure the S_{11} parameter of the device. The capacitance at low frequencies (e.g. < 10 GHz) was obtained by fitting the S_{11} parameter with lumped circuit model. At low frequencies, the wavelength is much longer than the device length and the device can well be treated as a lumped element. Fig. 5.18 shows the capacitance as a function of device length for different device widths at zero bias. A capacitance of 0.40 pF and a series resistance of 4.6 Ω were obtained for a 2.0 μm-wide and 300-μm long device under –1.7 V bias. These values infer RC limited bandwidths of 7.3, 13.4 and 15.8 GHz for output termination with open, 50 Ω and 32 Ω. All of these RC-limited bandwidths are smaller than the actual measured bandwidths of 10.7, 18.0, and 24.7 GHz. This suggests that the traveling wave electrode does improve the bandwidth of the device.

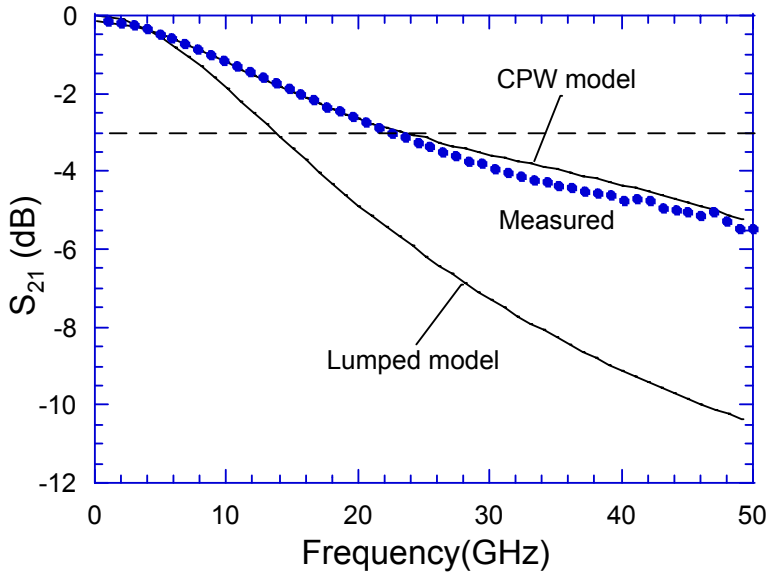

Fig. 5.19 Microwave port-to-port S_{21} response for a 2.0-μm wide, 300-μm long device. Dots: measured, curves: simulations.

Fig. 5.19 shows the microwave port-to-port S_{21} response for a 2.0-μm wide, 300 –μm long device. The dots are for the measurement, while the two curves are for predictions with traveling model and lumped model. Here a series resistance of 4.6 Ω and a junction capacitance of 0.4 pF are used for the lumped model calculation. The lumped device is imaginary put under a two-port test condition to evaluate the S_{21} response. We can see that the hybrid-coplanar waveguide model agrees well with the measurement. The measurement shows a significant improvement over the lumped case. The 3 dB bandwidths are 13.7, 22.6, and 23.3 GHz for lumped model prediction, for measurement, and for CPW model prediction. This corresponds to a 3-dB bandwidth improvement of 66% for the actual device compared to its lumped equivalent. This is a proof that the traveling-wave electrode does have significant improvement for the bandwidth of the device.

5.3.6. Power saturation

The absorption of modulator depends on the input optical power. With a small input optical signal excitation, the output optical power is linearly dependent on the input power. The output power to input power ratio is a constant. On the

other hand, if the input optical power is big enough such that it is close to or higher than the saturation power of the modulator, the absorption will most likely decrease with increased optical power, leading to nonlinear optical transmission. Power saturation will result in a decrease of modulation efficiency and a degraded switching speed.

Power saturation arises from the fact that at high input power levels the photo-generated electron or hole will build up in the quantum well, causing hole pile-up [16, 17], band filling [18, 19] and electric field screening [3, 20]. Hole pile-up is due to the large number of photogenerated holes trapped at the valence band discontinuity of the heterointerfaces in the depletion region. The accumulation of trapped holes induces a large potential drop at the heterointerface, thus reduces the electric field of the other region and causes the waveguide to become more transparent. Band filling effect is specifically for MQW devices and it happens when all the exciton states, or the bottom of the conduction band are filled, therefore prevents further photon absorption. The field screening effect is due to the large amount of space charge generated in the waveguide by the electroabsorption process, which instantly produces an internal electric field that screens out the applied bias. This field screening can be due to purely hole accumulation [20] or the accumulation of both electrons and holes [3, 21].

Fig. 5.20 shows the output optical power as a function of the input optical power under different bias voltages for a 2-μm wide, 300-μm long device.

For an ideal modulator with infinite saturation power, the curve should be a straight line with a slope of unity. Fig. 5.20 shows that TE and TM polarization lights have different saturation performance, with TM polarization light having a higher saturation power. This is in agreement with the prediction, since only light hole participates in the absorption of TM light, while heavy hole dominates in the absorption of TE polarization light. The larger effective mass for the heavy hole causes a more significant hole accumulation in the depletion region. Both figures reveal a linearity improvement at high biases due to the reduction of carrier sweep out time, hence the reduction of the accumulated carrier density.

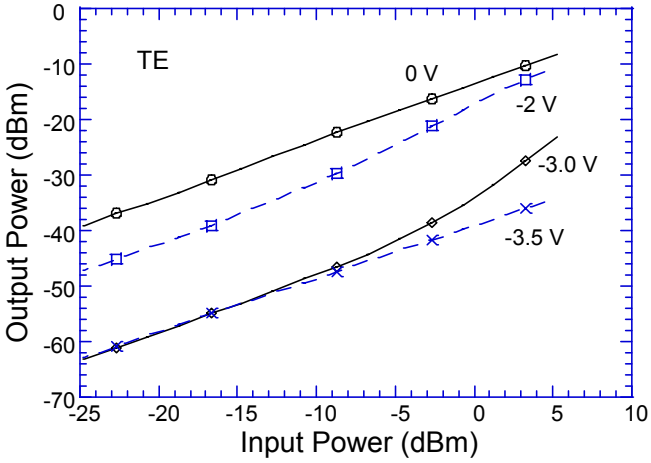

(a)

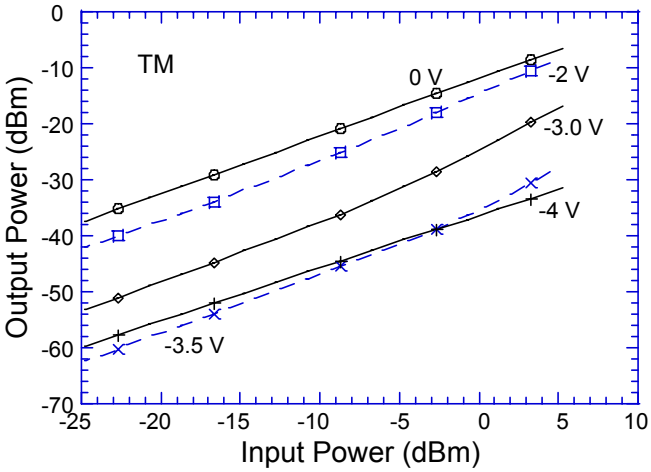

(b)

Fig. 5.20 Optical power in the output fiber versus optical power in the input fiber for several bias voltages for (a) TE and (b) TM polarization states. The light wavelength was 1542 nm.

Fig. 5.21 shows the frequency response of such a device under different input power levels. Power saturation does not seem to affect the response at high frequencies, however, we start to see a response tail at low frequencies, which was partially due to the saturation of the photodetector of the network analyzer. Here the bias voltages were adjusted for maximum E-O response corresponding to the input power.

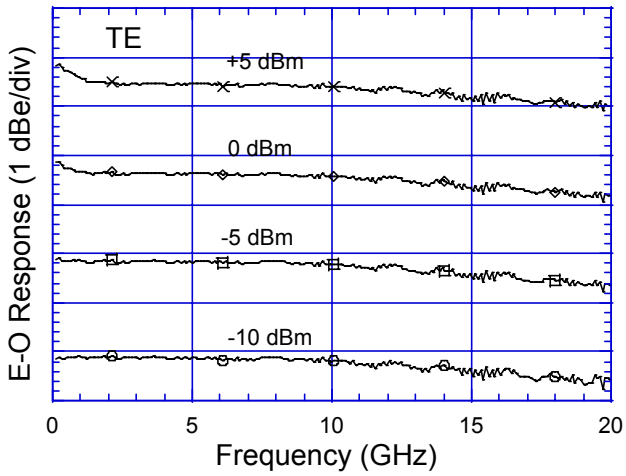

Fig. 5.21 E-O response for TE polarization light under different input optical power levels. The optical wavelength was 1542 nm.

Based on calculation, the valence bandgap offset for the heavy hole is about 164 meV between the well and the barrier, while it is about 147 meV between the barrier and the InP-cladding layer. Both interfaces could cause carrier-trapping effect and reduce the saturation power. Similar situation exists for the electron and the light hole. A graded interface between the cladding layer and the barriers should improve the power saturation.

5.4 Discussion and Summary

In this chapter, the design and fabrication of traveling-wave electroabsorption modulators with MOCVD grown InGaAsP/InGaAsP MQWs are discussed. Polarization insensitive operation has been achieved with bandgap engineering. For a 2-μm wide, 300-μm long device, drive voltages of 0.8 V and 1.2 V have been obtained for extinction ratios of 10 dB and 20 dB.

Significant bandwidth improvement is observed over the MBE grown devices due to the reduction of capacitance and more favorable material property. The speed of the device is limited by the microwave loss at high frequencies. As verified experimentally, microwave propagation and reflection losses are both important and should be taken into account in the design. Electrical-to-optical response is demonstrated to depend on the termination at the output port. A 3-dB

bandwidth of 24.7 GHz has been obtained by terminating the device with a 35-Ω thin film resistor, resulting in a bandwidth-voltage efficiency of 17.2 GHz/V.

There are at least three evidences of the distributed effect with these devices. Firstly, reflection cancellation effect was observed on the port-to-port S_{11} response. Secondly, with a 35 Ω thin-film resistor termination, an enhancement of EO response at high frequencies was observed. It was verified numerically that constructive reflection between the device and the load was the reason for the response improvement at high frequencies. Thirdly, compared to the lumped device with the same total capacitance, the traveling-wave device showed an S_{21} bandwidth improvement of over 60%. It should also be noted that for these three effects, the measurement results were all in agreement with the simulation based on transmission line model.

References

[1] F. Devaux, F. Dorgeuille, A. Ougazzaden, F. Huet, M. Carre, A. Carenco, M. Henry, Y. Sorel, J. F. Kerdiles, and E. Jeanney, "20 Gbit/s operation of a high-efficiency InGaAsP/InGaAsP MQW electroabsorption modulator with 1.2-V drive voltage," *IEEE Photonics Technol. Lett.*, vol. 5, pp. 1288-90, 1993.

[2] K. Satzke, D. Baums, U. Cebulla, H. Haisch, D. Kaiser, E. Lach, E. Kuhn, J. Weber, R. Weinmann, P. Wiedemann, and E. Zielinski, "Ultrahigh-bandwidth (42 GHz) polarisation-independent ridge waveguide electroabsorption modulator based on tensile strained InGaAsP MQW," *Electron. Lett.*, vol. 31, pp. 2030-2, 1995.

[3] F. Devaux, S. Chelles, A. Ougazzaden, A. Mircea, and J. C. Harmand, "Electroabsorption modulators for high-bit-rate optical communications: a comparison of strained InGaAs/InAIAs and InGaAsP/InGaAsP MQW," *Semicond. Sci. Technol.*, vol. 10, pp. 887-901, 1995.

[4] F. Devaux, J. C. Harmand, I. F. L. Dias, T. Guettler, O. Krebs, and P. Voisin, "High power saturation, polarisation insensitive electroabsorption modulator with spiked shallow wells," *Electron. Lett.*, vol. 33, pp. 161-163, 1997.

[5] B. L. Sharma, "Diffusion data for semiconductors," in *CRC Handbook of Chemistry and Physics*, D. R. Lide, Ed., 74 ed. Boca Raton, FL: CRC Press, 1993, pp. 12-89-12-99.

[6] V. Swaminathan and A. T. Macrander, *Materials aspects of GaAs and InP based structures*. Englewood Cliffs, New Jersey: Prentice Hall, 1991.

[7] R. L. Nagarajan, "Carrier transport effects in high speed quantum well lasers," University of California, Santa Barbara, CA, Ph.D. Dissertation, 1992.

[8] G. Fish, personal communication.

[9] Microposit SAL-101, manufactured by Shipley, Marlborough, MA.

[10] Aluminum nitride substrate, manufactured by Steller Industris, Leominster, MA.

[11] P. A. Rizzi, *Microwave Engineering Passive Circuits*: Prentice Hall, Appendix C and D, 1988.

[12] K. Kiziloglu, N. Dagli, G. L. Matthaei, and S. I. Long, "Experimental analysis of transmission line parameters in high-speed GaAs digital circuit interconnects," *IEEE Trans. Microw. Theory Tech.* , vol. 39, pp. 1361-7, 1991.

[13] Y.-J. Chiu, S. B. Fleischer, and J. E. Bowers, "High-speed low-temperature-grown GaAs p-i-n traveling-wave photodetector," *IEEE Photonics Technol. Lett.*, vol. 10, pp. 1012-1014, 1998.

[14] D. A. Tauber, R. Spickermann, R. Nagarajan, T. Reynolds, A. L. Holmes, Jr., and J. E. Bowers, "Inherent bandwidth limits in semiconductor lasers due to distributed microwave effects," *Appl. Phys. Lett.*, vol. 64, pp. 1610-12, 1994.

[15] S. Y. Wang and S. H. Lin, "High speed III-V electrooptic waveguide modulators at λ=1.3 μm," *J. Lightwave Technol.*, vol. 6, pp. 758-771, 1988.

[16] M. Suzuki, H. Tanaka, and S. Akiba, "Effect of hole pile-up at heterointerface on modulation voltage in GaInAsP electroabsorption modulators," *Electron. Lett.*, vol. 25, pp. 88-89, 1989.

[17] M. Suzuki, H. Tanaka, and S. Akiba, "High-speed characteristics at high input optical power of GaInAsP electroabsorption modulators," *Electron. Lett.*, vol. 24, pp. 1272-3, 1988.

[18] A. M. Fox, D. A. B. Miller, G. Livescu, J. E. Cunningham, and W. Y. Jan, "Quantum well carrier sweep out: relation to electroabsorption and exciton saturation," *IEEE J. Quantum Electron.*, vol. 27, pp. 2281-95, 1991.

[19] S. H. Park, J. F. Morhange, A. D. Jeffery, R. A. Morgan, A. Chavez-Pirson, H. M. Gibbs, S. W. Koch, N. Peyghambarian, M. Derstine, A. C. Gossard, J. H. English, and W. Weigmann, "Measurements of room-temperature band-gap-resonant optical nonlinearities of GaAs/AlGaAs multiple quantum wells and bulk GaAs," *Appl. Phys. Lett.*, vol. 52, pp. 1201-3, 1988.

[20] T. H. Wood, J. Z. Pastalan, C. A. Burrus, Jr., B. C. Johnson, B. I. Miller, J. L. deMiguel, U. Koren, and M. G. Young, "Electric field screening by photogenerated holes in multiple quantum wells: A new mechanism for absorption saturation," *Appl. Phys. Lett.*, vol. 57, pp. 1081-1083, 1990.

[21] J. E. Bowers and C. A. Burrus, Jr., "Ultrawide-band long-wavelength p-i-n photodetectors," *J. Lightwave Technol.*, vol. LT-5, pp. 1339-50, 1987.

CHAPTER 6

Transmission Experiments

The previous two chapters have emphasized on the performance of the device itself. We have demonstrated that by utilizing traveling-wave electrode structures, the bandwidth of the modulator can be improved. Hence it is possible to achieve both high speed and low drive voltage operation. However, the ultimate evaluation of the performance is the actual application on real fiber-optic transmission systems. In this chapter, I will emphasis on the system performance using these traveling wave electroabsorption modulators. Issues such as insertion loss, modulation bandwidth, extinction ratio, and chirping will be examined on their effect on the system performance.

All of the transmission experiments discussed here are done with MOCVD grown InGaAsP/InGaAsP modulators [1-3].

The devices were all mounted on copper bars, terminated with thin film resistors that had DC resistances of about 35 Ω. The devices were all 2.0-μm wide, 300-μm long. Cascade probe [4] was used to apply microwave signal.

6.1 Device characteristics

The device described in Fig. 5.8 had a fairly large on-state propagation loss at 1542 nm, which was the wavelength we used in our transmission experiments. In order to reduce the insertion loss, the device used for the transmission experiment was from a different batch of MOCVD wafer, which had a shorter QW PL wavelength (1476 ~ 1480 nm). This larger wavelength detuning led to a wider flat transmission region compared to the one shown in Fig. 5.9. Fig. 6.1 shows the fiber-to-fiber transmission characteristics measured with an input optical power of 2.2 mW. The device was anti-reflection coated with SiO.

The device had similar frequency response as Fig. 5.16. Fig. 6.2 shows the electrical-to-optical frequency response of the modulator for the transmission experiment. At low bias voltages, the bandwidth was smaller because the active

region was not fully depleted and contributed to a larger capacitance. Oscillation was seen at low biases, due to the resonance between the load and the probe.

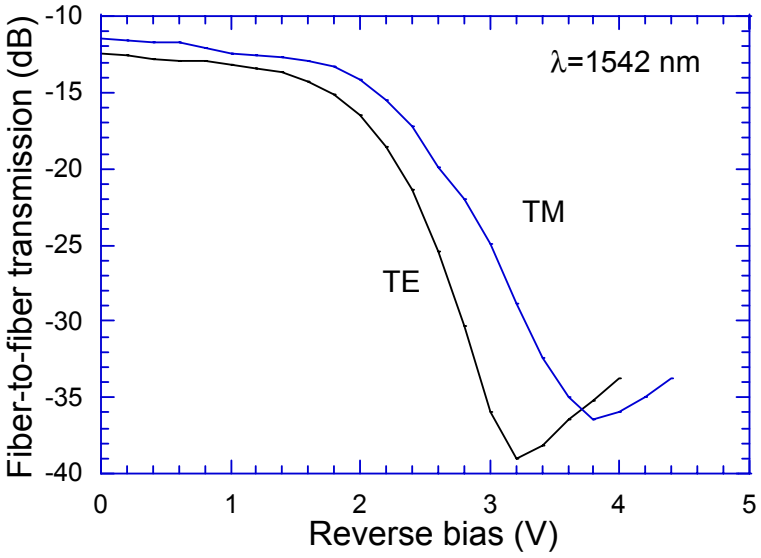

Fig. 6.1 Fiber-to-fiber transmission versus reverse bias voltage for TE and TM polarization states. The input optical power during the measurement was 2.2 mW.

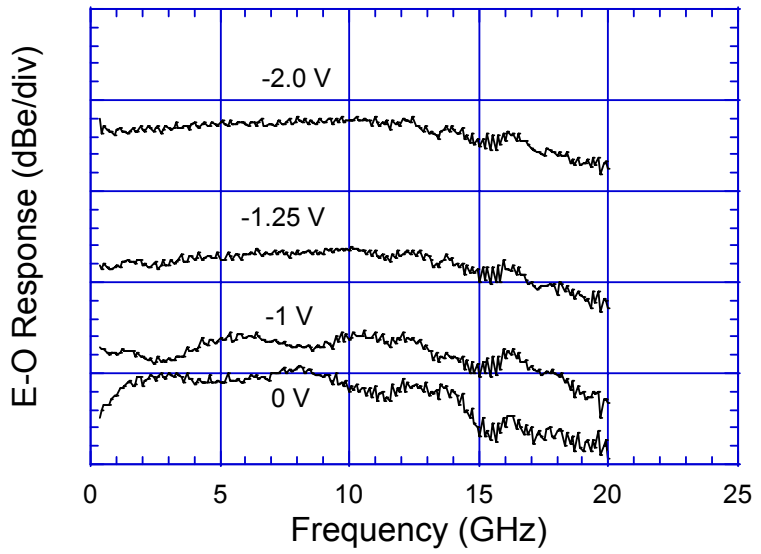

Fig. 6.2 E-O responses under different biases.

6.2 Transmission experiments at 10 Gbit/s

The transmission experiment was first carried out at 10 Gbit/s. Fig. 6.3 shows the schematic diagram of the experiment set-up. 10 Gbit/s pseudo-random bit sequence (PRBS) with a pattern length of 2^{31}-1 was generated from a pattern generator. This signal was amplified using a broadband amplifier. An output amplitude of about 1.6 V_{p-p} was applied onto the modulator. A DFB laser operating at 1542 nm followed by a polarization controller was used as the light source into the modulator. The input power to the modulator was 2.2 mW. The modulator had an insertion loss of about 16 dB at the bias point of –2.0 V.

An erbium-doped fiber amplifier (EDFA) increased the modulated optical signal before launching into 150 km of dispersion-shifted fiber (DSF) with a mean dispersion parameter of –0.93 ps/(nm-km).

At the receiver end, an optical attenuator was used to adjust the received optical power. An EDFA (with a noise figure of 7 dB) followed by a 0.6 nm optical filter was used as an optical preamplifier into the packaged receiver with a commercial 10 GHz-bandwidth receiver [5]. The receiver output signal was amplified by an electrical amplifier and then filtered by a low-pass baseband filter to reduce the noise. The bit error rate tester evaluated the error of the signal. Eye diagram was displayed after the baseband filter.

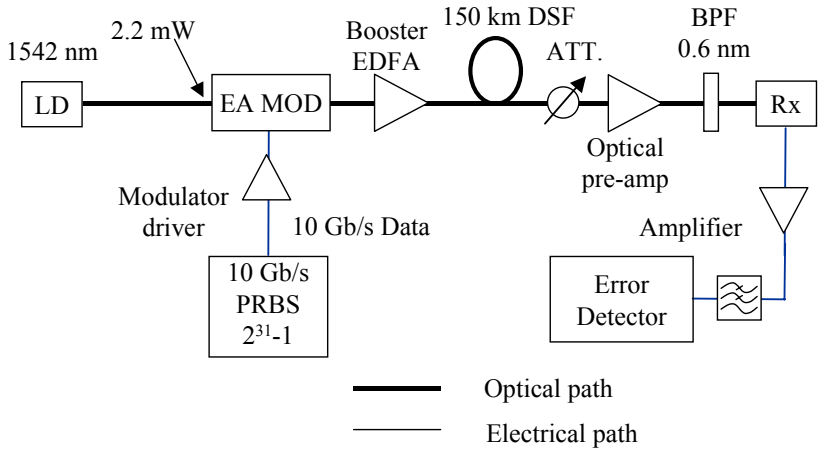

Fig. 6.3 Schematic diagram of 10 Gbit/s transmission experiment set-up.

Fig. 6.4 shows the eye diagrams at back-to-back transmission (0 km) and after transmitting through 150-km dispersion shifted fiber. Clean open eyes were obtained at both cases. An improvement was seen in the eyes after 150-km transmission due to the constructive interplay between the positive chirp of the modulator and the slightly negative dispersion of the fiber.

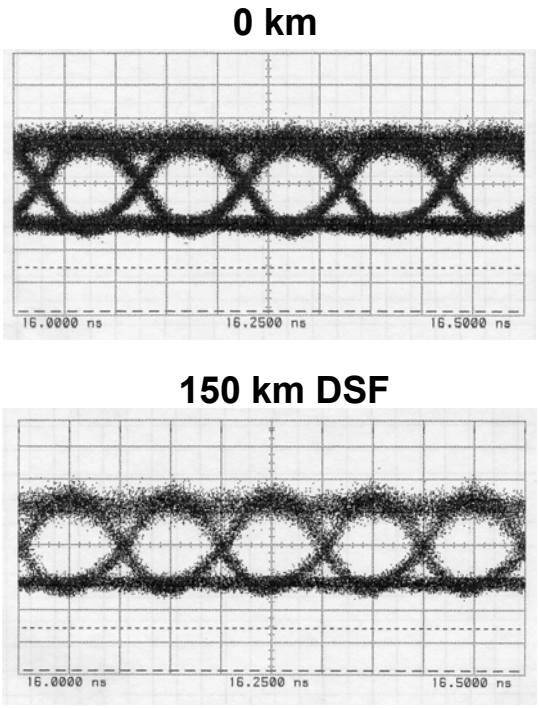

Fig. 6.4 Eye diagrams for (top) back-to-back and (bottom) 150-km DSF transmissions.

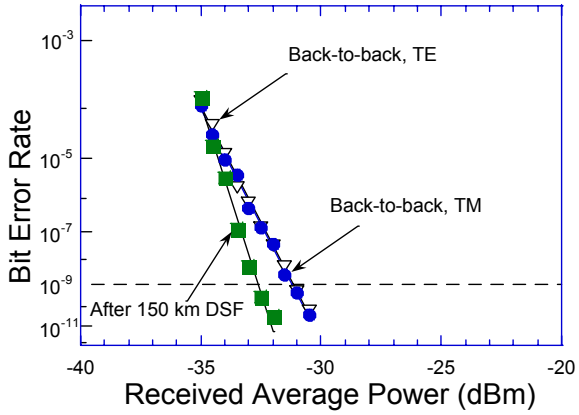

Fig. 6.5 Bit error rate versus received average power for 10 Gbit/s transmissions.

Fig. 6.5 shows the bit error rate (BER) performance of the system for back-to-back and over 150 km of dispersion shifted fiber. In the back-to-back measurements, error free operation and a sensitivity of –31.2 dBm for bit error rate of 10^{-9} was achieved for both the TM and the TE polarization states without changing the operation conditions of the modulator. This clearly indicated that the EA modulator is a polarization-insensitive device. An improved sensitivity of –32.8 dBm was achieved after 150 km DSF transmission, in agreement with the eye diagram improvement.

Transmission experiments over non-dispersion shifted fiber were also performed. Fig. 6.6 shows the eye diagram after transmission over 25-km standard single mode fiber. As can be seen, the eye was degraded by the dispersion of the fiber.

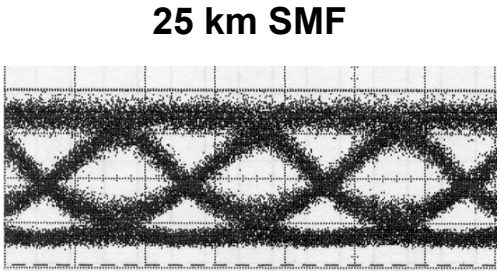

Fig. 6.6 Eye diagram after transmission over 25 km of standard single mode fiber.

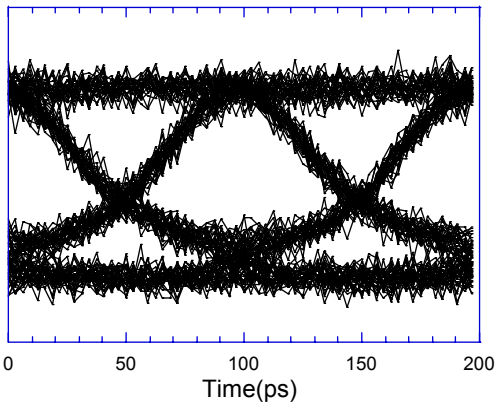

Fig. 6.7 Simulated eye diagram after transmission over 25 km of standard single-mode fiber [6].

A computer program was written to numerically simulate the system performance [6, 7]. Fig. 6.7 shows the simulated eye diagram when a linewidth enhancement factor of 1.2 was used for the modulator. As we can see, the simulation agreed well with the measurement, suggesting that the linewidth enhancement factor of the modulator was around 1.2. Further study of the chirping effect of the modulator will be shown in Section 6.3.

The error free operation at the pattern length of 2^{31}-1 suggested that the modulator had no low frequency problem.

6.3 Transmission experiments at 30 Gbit/s

Fig. 6.8 shows the schematic diagram of the 30 Gbit/s experiment set-up. The 30 Gbit/s NRZ electrical signal was generated by multiplexing four 7.5 Gbit/s 2^7-1 PRBS using a 4:1 multiplexer (MUX) [8]. The pattern length was limited by the receiver electronics. An output amplitude of 1.6 V_{p-p} (on the modulator), generated using a broadband amplifier, was applied to the EA modulator via a high-speed probe.

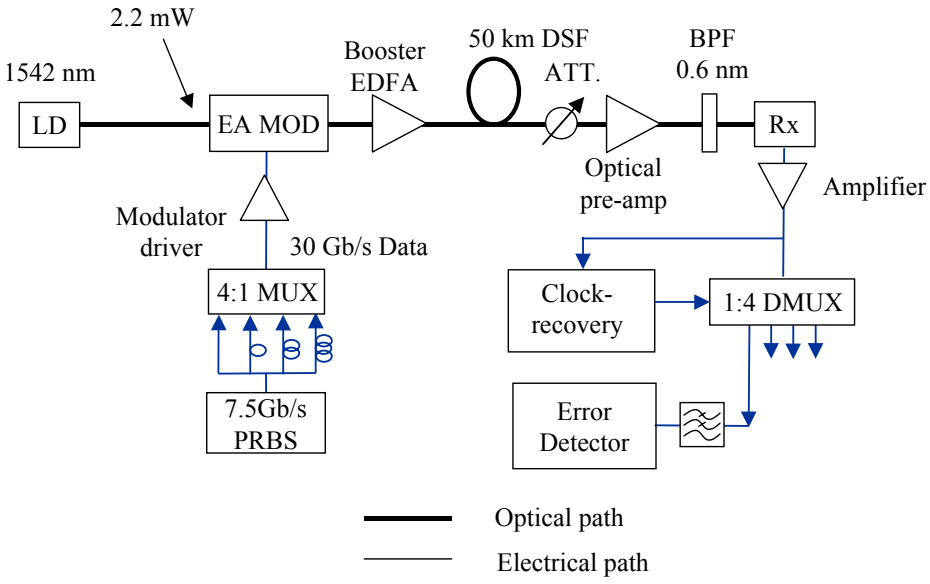

Fig. 6.8 Schematic diagram of the 30 Gbit/s transmission experiment set-up.

At the receiver end, a packaged receiver with 30 GHz bandwidth [9] followed by an amplifier was used to convert the signal. The amplified signal was electrically demultiplexed. The high-speed signal was fed into a 30 Gbit/s 1:4 demultiplexer (DMUX) and a clock recovery circuit (CRC) [8]. A 15 GHz voltage-controlled oscillator was phase locked to the 30 Gbit/s data. The output voltage swing of 300 mV_{p-p} at 7.5 Gbit/s from the DMUX was fed into the bit-error rate tester. Bit-error rate (BER) measurements in a back-to-back measurement showed that there was only 0.3 dB receiver sensitivity degradation with the CRC operating compared to using a clock signal directly from a synthesizer (Fig. 6.10).

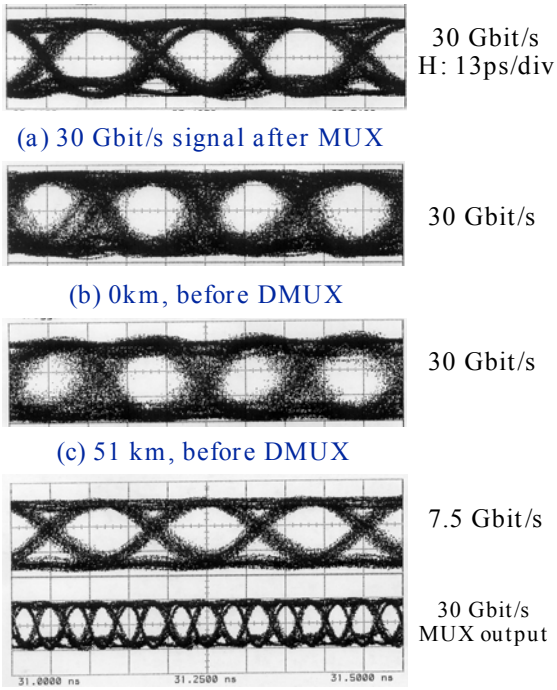

Fig. 6.9 30 Gbit/s eye diagrams of (a) the output signal from the 4:1 MUX, the received signal after transmission through (b) 0 km and (c) 51 km dispersion shifted fiber. The top half of Fig. (d) is the DMUX output after 51-km transmission, and the bottom half is the MUX output.

Fig. 6.9 shows (a) the 30 Gbit/s output of the 4:1 MUX, (b) the received 30 Gbit/s signal after back-to-back transmission, and (c) after transmission over 51 km

of DSF fiber (mean dispersion parameter of 0.16 ps/(nm-km)). In the case of back-to-back transmission, the booster EDFA was not used. The extra noise on the eye diagram after the transmission is due to the booster EDFA (with a noise figure of 9 dB). No pulse shape degradation is observed after the transmission. The top half of Fig. 6.9 (d) shows the DMUX output at 7.5 Gbit/s after 50 km of transmission.

Fig. 6.10 shows the BER performance of the tranmissions. An optical sensitivity of –20.2 dBm and –16.5 dBm were achieved for back-to-back and over 51-km DSF transmission, respectively. In the back-to-back measurement, the booster EDFA was not used and error-free operation was achieved. However, a 3.7 dB power penalty and an error-floor were observed in the fiber transmission using the booster EDFA (the input power to the booster EDFA was –18.3 dBm). In a separate back-to-back measurement including the booster EDFA, the same power penalty and the error floor were observed (Fig. 6.10). It was experimentally verified that the penalty and the error floor are due to the high noise-figure and the low input power into the booster EDFA. The EA modulator insertion loss was approximately 16 dB at the bias point including the fiber coupling losses. This was the major contributor to the low input power into the booster EDFA, and hence the lower system sensitivity. This was verified that when devices without AR coating were used in the transmission experiment, the bit error rate performance could not be better than 10^{-9}, even with back-to-back transmission.

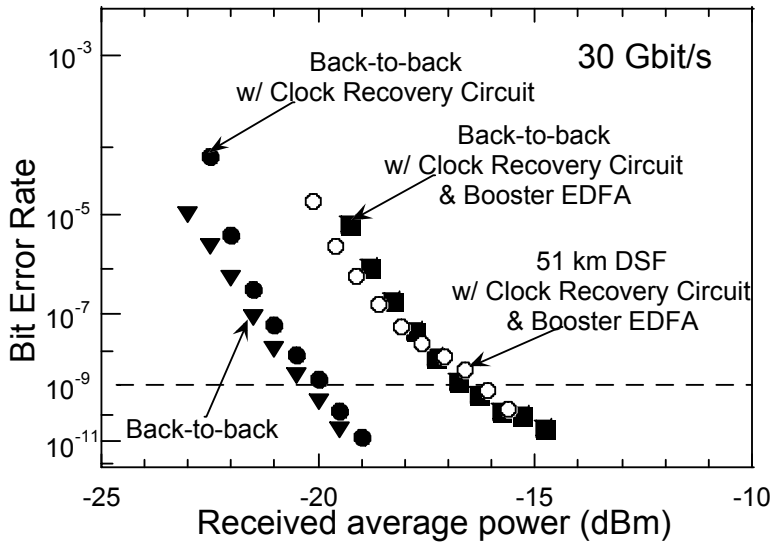

Fig. 6.10 Bit error rate performance at 30 Gbit/s.

No system degradation was observed when a device with slightly smaller bandwidth was used. This confirms that the bandwidth was not the limiting factor.

6.4 Chirp characteristics

The chirp parameter, also called linewidth enhancement factor in lasers, α, is defined as [10]

$$\alpha = \frac{\partial n}{\partial k}, \tag{6.1}$$

where, n and k are, respectively, the real and imaginary parts of the modal index of the electroabsorption waveguide.

In lasers, it is given by [11]

$$\alpha = -\frac{\dfrac{\partial n}{\partial N}}{\dfrac{\partial g}{\partial N}}, \tag{6.2}$$

where, g is the modal gain and N is the carrier density.

In the 10 Gbit/s transmission experiment, a chirp parameter of about 1.2 was obtained by comparing the eye diagram with numerical simulation. It will be desirable to measure the chirp factor directly.

We investigated the chirp parameter using the fiber response peak method proposed by Devaux [12]. This is based on the fact that the response of the fiber will have zeros, whose frequencies relate to the chirp of the light source.

The frequency response of the fiber can be expressed as

$$I_f = I_0 m\sqrt{1+\alpha^2}\left|\cos\left(\frac{\pi\lambda^2 DLf^2}{c} + \arctan(\alpha)\right)\right|, \tag{6.3}$$

where

I_0 is the average optical power,

m is the modulation depth,

D is the dispersion of the fiber,

L is the length of the fiber,

c is the speed of light in vacuum.

There are resonance frequencies at which the response goes to zero. Each resonance frequency *fu* corresponds to the uth-zeros of the response curve.

$$f_u^2 L = \frac{c}{2D\lambda^2}\left(1 + 2u - \frac{2}{\pi}\arctan(\alpha)\right), \tag{6.4}$$

where u=0,1,2, … is the order of the resonance frequency.

The experiment was done using HP 8703 Lightwave Component Network Analyzer. To cancel the response of the modulator, a calibration measurement was first performed by recording the frequency response curve of the whole link without the dispersive fiber. Then an 87.563-km standard single mode fiber (dispersion zero wavelength at 1.31 μm) frequency response was measured and then divided by the reference curve. An EDFA was insert before the fiber to amplify the signal.

Fig. 6.11 shows a typical frequency response of the fiber. The resonance frequencies were then obtained from this curve. Then $f_u^2 L$ was plotted as a function of *2u*. A linear fit allows us to find the chirp parameter and the dispersion of the fiber.

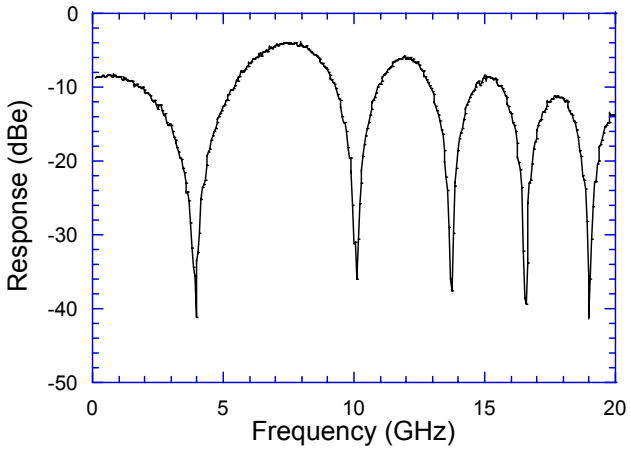

Fig. 6.11 Typical frequency response of an 87.563-km standard single mode fiber.

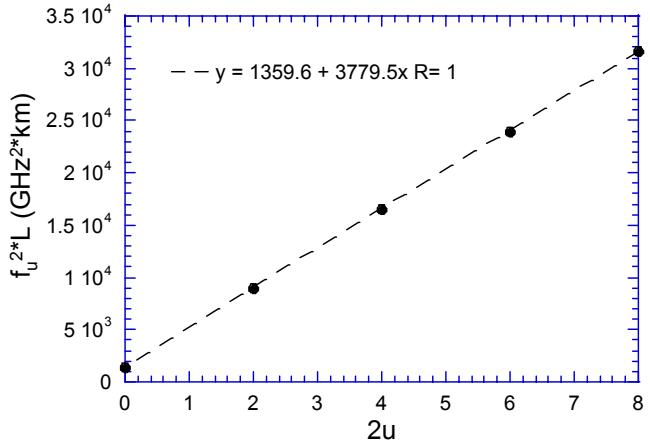

Fig. 6.12 Resonance frequencies squared (from Fig. 6.11) times fiber length versus two times the order of the resonance. Linear interpolation allows finding the chirp parameter and the dispersion from Eq. 6.2. The light wavelength was 1548 nm, and the modulator bias voltage was -2.0 V

Fig. 6.13 shows the chirp parameter of the modulator versus reverse bias at a wavelength of 1542 nm. Generally, the linewidth enhancement factor drops as the bias increases, because increase in bias will cause the absorption to shift to longer wavelength. A chirp factor of 1.2 was obtained from the curve at a bias of 2.0 V, in agreement with the eye diagram simulation.

Fig. 6.14 shows the chirp parameter and fiber dispersion versus wavelength for a bias voltage of –2.0 V. The chirp parameter decreases as the light wavelength decreases.

Both Figs. 6.13 and 6.14 show that when the pre-bias insertion loss gets larger, the chirp parameter gets smaller (ignoring the spike in Fig. 6.13). This can be understood with the help of Fig. 6.15 (a-c). Figure (a) shows the typical absorption spectra of the quantum well for on state, bias state, and off state. Here we assume the modulator is pre-biased at V_b and the voltage swing will generate the absorption curves for on and off states as shown in the figure. Figure (b) schematically plots the absorption change relative to the on state. Based on the

Kramers-Kronig relationship, the index change relative to the on state is plotted in figure (c) [13].

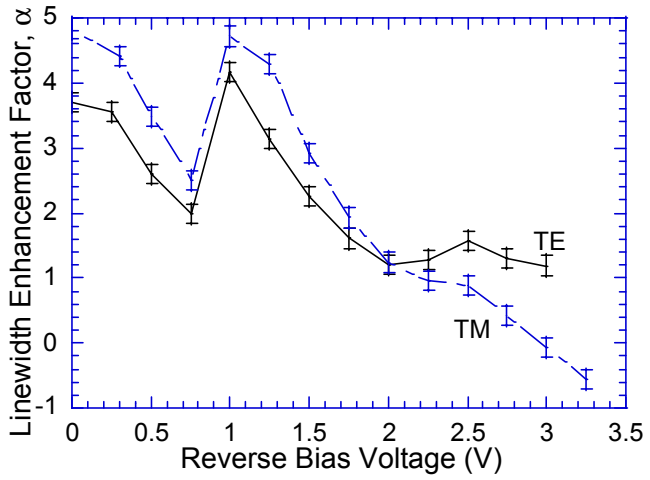

Fig. 6.13 Chirp factor as a function of reverse bias at a wavelength of 1542 nm.

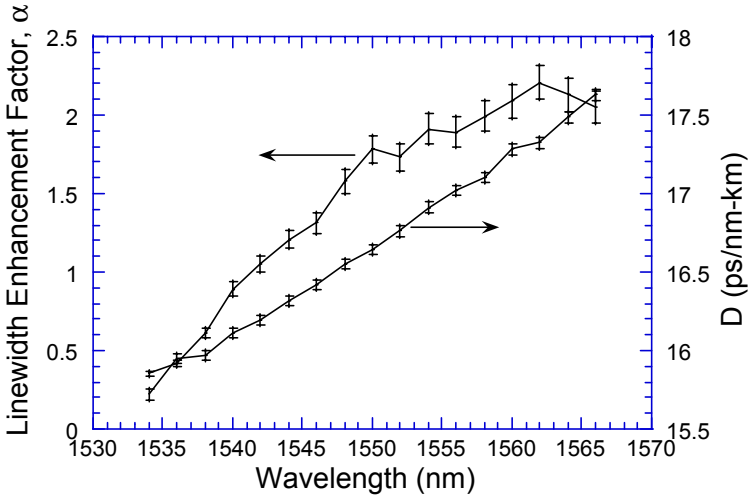

Fig. 6.14 Linewidth enhancement factor and fiber dispersion versus wavelength. The bias voltage to the modulator was -2.0 V.

To simplify, let's assume the transition from on state to off state is infinitely short in time, then there is only two states, on state and off state. The chirp can be

fully defined by only considering the refractive index change for the off state. There are three different chirp behavior regions as shown in the figure.

In region I, the decrease of wavelength will cause the increase of chirp in the off state, because the refractive index difference of the off state increases. As the wavelength keeps decreasing in region II, the chirp decreases to zero. This is the region that most of the modulators operate. At the boundary between region I and region II, the chirp reaches a maximum. When wavelength decreases to region III, the chirp becomes negative.

When the operation wavelength gets shorter, the loss becomes larger. This is equivalent to the increase of bias voltage. In the latter case, the operation wavelength is set, but the absorption curves move to longer wavelengths as bias increases. These therefore explain the reason for chirp increase at some voltage region and then decrease at higher voltage region as voltage increases (Fig. 6.13).

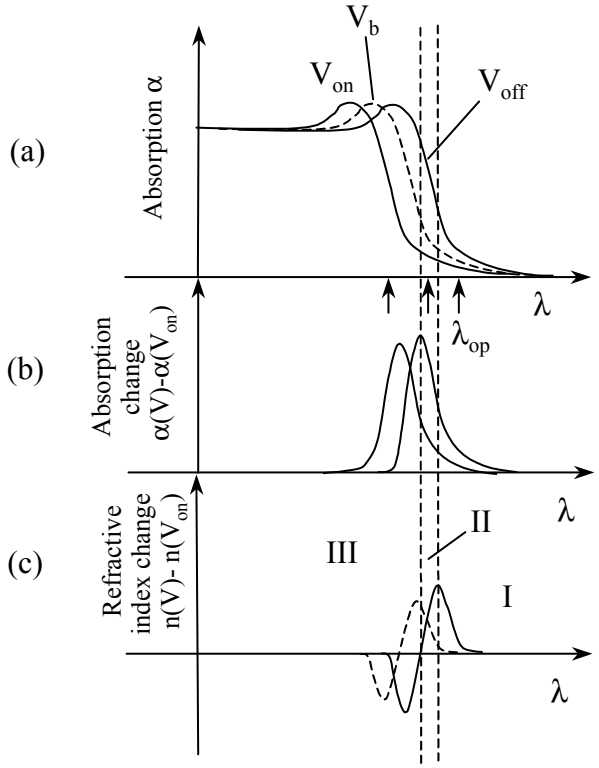

Fig. 6.15 (a) electroabsorption spectra for several applied biases; (b) absorption change relative to the on state; (c) refractive index change governed by Kramers-Kronig

relationship for two different drive biases. The arrows represent the position of the operation wavelength λ_{op}.

The previous argument is based on the assumption that there are only two states; however, the actual signal will always have a finite rise and fall time therefore intermediate states exist. In this case, the chirp behavior will be more complicated. Let's consider when the operation wavelength decreases from long wavelength and consider a voltage swing from off state to on state (leading edge). In region I, the chirp monotonically decreases from positive (off-state, high bias) to the intermediate state, and then to zero (on state, zero bias). In region II, it starts with positive, first increases then decreases back to zero. In region III, it increases from negative chirp to positive chirp and then back to zero. An effective chirp parameter is needed [14] to consider the overall chirp effect.

Even though the existance of intermediate states makes the chirp complicated, it is still true that a smaller wavelength detuning will reduce the chirp at the operation wavelength as long as the operation wavelength falls in region II; however, this is at the expense of increasing loss.

Based on these arguments, we conclude that the detuning of the current device is too large, which causes the chirp to have a peaking region on the chirp ~ voltage plot.

6.5 Discussion

The successful operation of the modulator at 10 Gbit/s and 30 Gbit/s demonstrates the advantage of TEAMs in high speed and low drive voltage applications. However, several issues still need to be solved in order for real system application.

As mentioned in the 30 Gbit/s experiment, the optical insertion loss for the current device is the biggest problem that needs to be solved. Because of the large insertion loss (about 16 dB at the bias point), the output optical signal is rather weak, which causes power penalty after EDFA amplification. An improved coupling scheme such as employing higher numerical lens or coupling-efficient lensed fiber should be developed. Another possible solution is to re-design the

waveguide structure such that the lateral mode size is larger. However this will usually reduce the optical confinement factor and increase the drive voltage.

Another possible limiting factor is the on-off ratio at high frequency modulation. From Fig. 6.1, the on-off ratio was 18 dB with a DC swing of 1.6 V at a bias of –2.0 V. The extinction ratio will cause a power penalty of [15]

$$\delta_{ex} = 10\log_{10}\left(\frac{1+ER}{1-ER}\right)$$

The extinction ratio ER is defined as the ratio of low level optical power to high level optical power. Based on this, an 18-dB extinction ratio will cause a power penalty of 0.14 dB.

However, the modulation efficiency will be smaller because of the microwave reflection and propagation loss. Assume a microwave power reduction of 3 dB at high frequencies, then the V_{pp} becomes 1.13 V. The extinction ratio will then be 10.5 dB, corresponding to a power penalty of 0.77 dB. From this, we conclude that the extinction penalty should not be the dominant factor.

One way to increase the output optical power is to increase the power saturation such that larger optical power can be launched into the device. As mentioned in Chapter 5, bandgap grading so as to reduce carrier blocking effect at the interfaces between the cladding layers and the quantum well region will improve the power handling.

The chirp parameter is still high for long distance standard single-mode fiber transmission. Both reducing the wavelength detuning and increasing the quantum well thickness will help reduce the chirp parameter.

6.6 Summary

In summary, first successful fiber optic transmission using traveling-wave electroabsorption modulator has been demonstrated at 10 Gbit/s and 30 Gbit/s. For the 10 Gbit/s transmission, error free operation was achieved with a 10^{-9} BER sensitivity of –32.8 dBm after 150-km dispersion shift fiber transmission. For the 30 Gbit/s transmission experiment BER better than 10^{-9} was achieved with a

receiver sensitivity of –16.5 dBm after 51-km dispersion shift fiber transmission. Chirp performance and mechanism are discussed.

Reference

[1] S. Z. Zhang, V. Kaman, A. Keating, Y. J. Chiu, P. Abraham, and J. E. Bowers, "30 Gbit/s operation of a traveling-wave electroabsorption modulator," *OSA OFC'99*, San Diego, CA, paper ThT3, 1999.

[2] J. E. Bowers, S. Z. Zhang, P. Abraham, Y.-J. Chiu, and V. Kaman, "Low drive voltage, high speed traveling-wave electroabsorption modulators," *The Ninth Annual DARPA Symposium on Photonic Systems for Antenna Applications*, Monterey, CA, 1999.

[3] V. Kaman, S. Z. Zhang, A. J. Keating, and J. E. Bowers, "High-speed operation of a traveling-wave electroabsorption modulator," *submitted to Electronics Letters*.

[4] ACP40-GSG Cascade probe with 100 micron contact pitch, manufactured by Cascade Microtech, Inc., Beaverton, Oregon.

[5] 10 Gb/s optical receiver model PP-10G, Northen Telecom Inc., Brampton, Ontario, Canada.

[6] LinkSim^{TM}, software developed from the author and co-workers' original program - Fiber Optic Demonstration Program (FOLD), distributed by RSoft, Inc., Ossining, NY.

[7] S. Zhang, R. Nagarajan, A. Petersen, and J. Bowers, "40 Gbit/s fiber optic transmission systems: are solitons needed?," *SPIE'96 High-Speed Semiconductor Laser Sources*, San Jose, CA, 182-185, 1996.

[8] K. Runge, P. J. Zampardi, R. L. Pierson, P. B. Thomas, S. M. Beccue, R. Yu, and K. C. Wang, "High speed AlGaAs/GaAs HBT circuits for up to 40 Gb/s optical communication," *GaAs IC Symposium*, Anaheim, CA, pp.211-214, 1997.

[9] A. K. Petersen, R. Reynolds, R. Nagarajan, Y. G. Wey, J. E. Bowers, and M. Rodwell, "3-MHz-30-GHz traveling-wave optical front-end receiver," *OSA OFC'95*, San Diego, CA, pp.157-158, 1995.

[10] F. Koyama and K. Iga, "Frequency chirping in external modulators," *J. Lightwave Technol.*, vol. 6, pp. 87-93, 1988.

[11] T. L. Koch and J. E. Bowers, "Nature of wavelength chirping in directly modulated semiconductor lasers," *Electron. Lett.*, vol. 20, pp. 1038-40, 1984.

[12] F. Devaux, Y. Sorel, and J. F. Kerdiles, "Simple measurement of fiber dispersion and of chirp parameter of intensity modulated light emitter," *J. Lightwave Technol.*, vol. 11, pp. 1937-40, 1993.

[13] D. C. Hutchings, M. Sheik-Bahae, D. J. Hagan, and E. W. van Stryland, "Kramers-Kronig relations in nonlinear optics," *Optical and Quantum Electronics*, vol. 24, pp. 1-30, 1992.

[14] F. Dorgeuille and F. Devaux, "On the transmission performances and the chirp parameter of a multiple-quantum-well electroabsorption modulator," *IEEE J. Quantum Electron.*, vol. 30, pp. 2565-72, 1994.

[15] G. P. Agrawal, *Fiber-Optic Communication Systems*. Singapore: John Wiley & Sons, Inc., 1993.

CHAPTER 7

Summary and Future Work

7.1 Summary

The motivation for developing a distributed electroabsorption modulator arises from the limitations on conventional lumped-element EA modulators, in which, the total RC time constant limits the maximum device length for achieving high speed operation. The proposed traveling-wave electrode configuration is designed to support microwave propagation on the device structure with characteristic impedance matched to the load, therefore minimize the reflection within the device and overcome the lumped RC bandwidth limitation. The following is a brief summary of the results reported in Chapters 2 through 6.

Chapter 2 presented the design of the material and optical waveguide structures focusing on achieving polarization insensitivity and low drive voltage operation. Wider quantum wells were found to improve the quantum confined Stark shift rate and to reduce the drive voltage of the device. Polarization independent design with tensile strained quantum wells was discussed. This chapter also discussed the optical waveguide design using simulation software based on 3-D beam propagation method and 2-D slab waveguide mode calculation. The coupling efficiency to the single mode optical fiber was investigated.

In chapter 3, an equivalent circuit model for TEAMs was presented. Based on the equivalent circuit model, the effects of structure parameters on the characteristic impedance, microwave attenuation constant and electrical-to-electrical transmission (S_{21}) were predicted. Design rules for achieving low microwave loss are given. Optimum material and device structure parameters are determined based on the overall electrical-to-electrical and electrical-to-optical responses. These material and device structure parameters include waveguide ridge width, intrinsic layer thickness, metal thickness, metal width, coplanar waveguide gap width, n-conducting layer thickness/resistivity, p-conducting layer resistivity, and side wall angle. The linear width tapering was found to be better than the triangular and exponential tapering for the feed lines.

Chapter 4 discussed the fabrication and measurement results of devices made of MBE grown InGaAs/InAlAs materials. A 3-dBe bandwidth of 12 GHz and a 20-dB extinction-ratio drive voltage of 2.7 V were achieved. Microwave measurements were found to agree well with the transmission line model. The angled side wall was found to be the main reason for limiting the device speed.

Chapter 5 discussed the fabrication and measurement results of devices made of MOCVD grown InGaAsP/InGaAsP materials. Polarization-insensitivity, a 20-dB extinction-ratio drive voltage of 1.2 V and a 3-dBe bandwidth of 25 GHz were achieved, yielding to a figure of merit among the best ever reported. Measurements on both the straight waveguides and the full devices supported the theory presented in Chapter 3. The traveling-wave electrode structure was verified to improve the device speed.

Chapter 6 presented the first successful fiber optic transmission using traveling-wave electroabsorption modulators at 10 Gbit/s and 30 Gbit/s. A transmission distance over 50-km dispersion shifted fiber was demonstrated. The large insertion loss, which caused the signal-to-noise-ratio reduction, was found to be the main limiting factor for the power penalty. The chirp characteristic and the method to improve it were also discussed.

7.2 Suggestions for future work

The future work can be summarized as to improve device performance and to study new applications using the unique characteristics of the modulator. The improvement on the performance can be considered from these four aspects: bandwidth, insertion loss, chirp and power saturation.

7.2.1 Improved bandwidth

The bandwidth of the device is limited by the microwave loss from the propagation loss and impedance mismatch induced reflection loss. Chapter 3 suggests that the most efficient method to increase the bandwidth is to use a narrower ridge and to increase the intrinsic layer thickness. However, the first will increase the insertion loss while the second will increase the drive voltage. None of them should be changed much from their current values.

Currently, the p-metal is made with two evaporation steps for greater thickness. This process caused a wider metal width than the ridge width (Fig. 3.11), which could reduce the bandwidth of the device by about 8 GHz according to Fig. 3.19 (c). A self-aligned single step evaporation should therefore improve the bandwidth of the device.

Besides this, however, there are at least two more efficient ways to improve the bandwidth of the device: by waveguide ion-implantation and load matching.

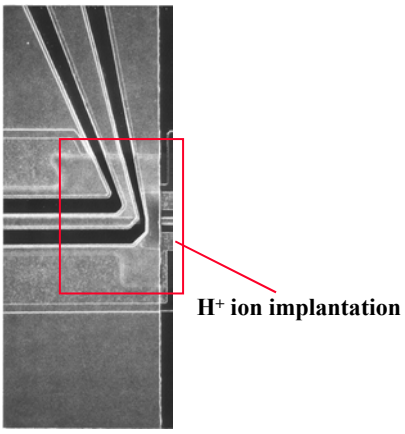

Fig. 7.1 Ion implantation to reduce extra capacitance at the feed-line-to-waveguide junction.

Fig. 7.1 shows the close-up SEM picture of the feed-line-to-waveguide junction region. As it can be seen, there is a 20~30 μm long waveguide section protruding outside of the coplanar waveguide region. This will serve as a lumped capacitor loading on the CPW line. Considering that the other end of the waveguide will also have a 'lumped' waveguide section, the total length of the lumped section is 40-50 μm. Up to date, lumped element electroabsorption modulators have been demonstrated to have a bandwidth of 38-50 GHz with a waveguide length of 63-120 μm [1-4]. Therefore, the lumped waveguide section could significantly limit the bandwidth of the device. Also, the sharp angle at the connection region will cause extra capacitance. By ion-implantation of this region to render the p-cladding layer to semi-insulating, these extra capacitances can be reduced greatly.

The minimum device length is now limited by the contact pad size. Ion implantation can effectively reduce the active region length and should improve the

bandwidth of the device [3, 5]; however, this is at the price of reducing the extinction ratio.

The second method is to match the waveguide with an optimized load to reduce the reflection from the load. Fig. 7.2 shows the measured electrical S_{11} response of the device used for the transmission experiment. We can see that the reflection is rather high at frequencies around 20 GHz. At higher frequencies, the reflection is lower due to the reflection cancellation as discussed in Chapter 5 Section 5.3.3. Compared to Fig. 5.10, we can observe an improvement in S_{11} response at high frequencies, but not quite much at low frequencies. Fig. 7.3 shows the impedance of the thin-film resistor. It's not a pure resistor at high frequencies. It is inductive for frequencies lower than 36 GHz, while it becomes capacitive at higher frequencies.

The bandwidth should be able to be improved with a proper load design, e.g., by using RLC or transmission line matching circuits. The measured two port S parameters of the devices (Figs. 5.12 and 5.15) should be used in the design to find the optimum load.

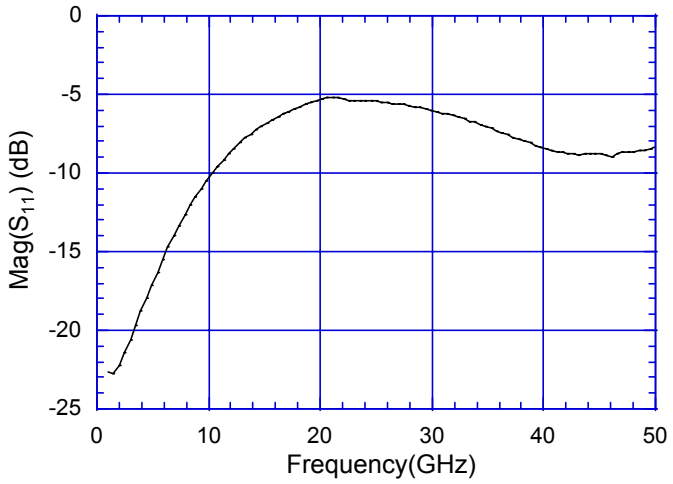

Fig. 7.2 Measured S_{11} response of a device loaded with a 35 Ω thin-film resistor. Device length: 300 μm, width 2 μm.

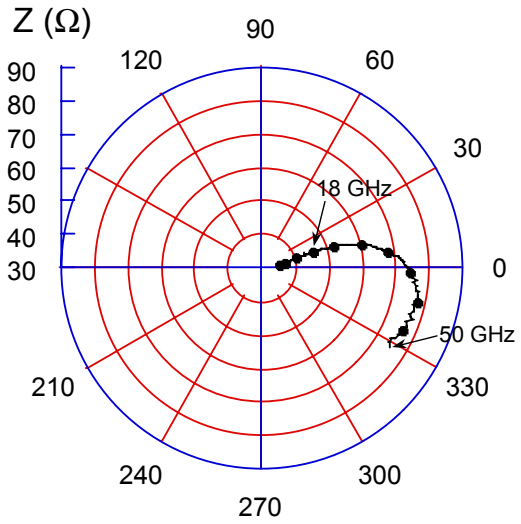

Fig. 7.3 Impedance of a fabricated thin-film resistor. The frequency separation between adjacent two dots is 5 GHz.

7.2.2 Improved insertion loss

As discussed in Chapter 6, it was found that the high insertion loss was one of the main reasons for causing the large power penalty in the 30 Gbit/s transmission experiment. Therefore improving the insertion loss is the most important task.

As discussed in Chapter 2, using either a wider waveguide or a thinner guiding layer will improve the coupling efficiency (Fig. 2.20). However, the first one will cause the reduction of bandwidth, while the second will reduce the optical confinement factor and hence increase the drive voltage.

One way to solve this dilemma is to integrate the modulators with semiconductor optical amplifiers (SOAs) [6]. Fig. 7.4 shows two different configurations, one with a single modulator section, and the other with two modulator sections. Both of these structures can use the identical active layer that makes the fabrication simple [6].

The advantage for the single modulator configuration is that the microwave application will be simple, while the disadvantage is that the extinction ratio could

be degraded by the output SOA if it is pumped too hard. The input SOA can not be pumped too hard either since the modulator could be saturated.

The double-modulator configuration solves the problem that exists in the single-modulator configuration, however, it requires two modulation signals. This can be obtained by electrically delaying the input microwave signal.

Even though the double-modulator configuration requires a more complicated driving circuitry, it nevertheless can improve the bandwidth and overcome the velocity mismatch limitation for long devices. On the other hand, special functionalities can be achieved by driving the modulator differently. As an example, we can use the first modulator as a pulse generator and the second as the encoder [7].

Since there are three SOAs, the two at the ends can be made shorter. Incorporating these two SOAs can expand the space for the ground pads of the modulators as well as providing optical gain.

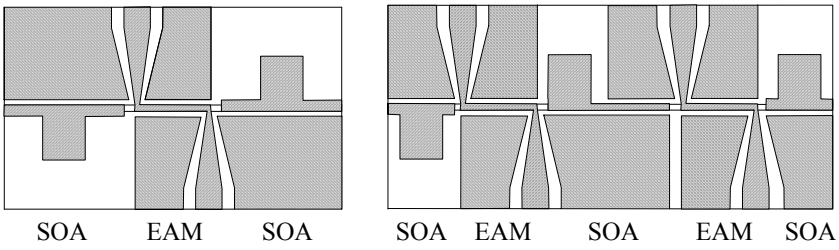

Fig. 7.4 Tandem of TEAMs and semiconductor optical amplifiers (SOA). Left: with single TEAM, right: with two TEAMs.

Another efficient way to reduce the insertion loss is to integrate the modulator with a DFB laser. Special functionalities can also be achieved by integrating more than one modulator.

7.2.3 Improved chirp characteristics

As discussed in Chapters 1 and 6 (Figs. 1.1, 6.13 and 6.14), the chirp parameter needs to be reduced for applications in long haul, high speed transmissions over standard single mode fibers.

As it has been discussed in Chapter 6 Section 6.4, a smaller wavelength detuning will reduce the chirp parameter. Another way to reduce the chirp is to use

a wider quantum well because the refractive index change associated with the absorption coefficient change is smaller based on Kramers-Kronig relations [8]. Furthermore, a thick quantum well can have effective absorption coefficient change even at small applied voltages as discussed in Chapter 2.

7.2.4 Improved power saturation

The power saturation is dominated by the carrier trapping at the heterointerfaces, especially by the heavy-hole pile-up because of its much smaller mobility. As mentioned in Chapter 5 Section 5.3.6, there is a rather high bandgap offset between the barrier and the InP cladding layer. Using digital alloy grading layers at these interfaces will improve the evacuation rate and hence improve the power saturation. Using a new material composition configuration to decrease the band offset between the well and the barrier will also improve the power saturation. However, the offset can not be too small because the quantum confined effect could be too weak.

7.2.5 Packaging

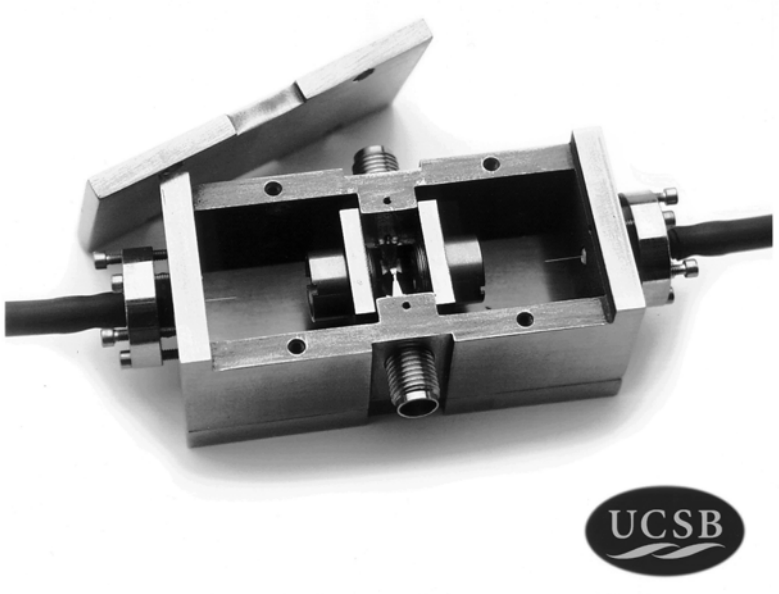

Fig. 7.5 A prototype package for the modulators [9].

Packaging is at many times even more important than fabricating the device itself. A modulator can never be practically usable unless it is packaged. Both the electrical connection and the optical connection need to be designed well to yield robust, high speed and low optical insertion loss operation. A prototype package has been designed and fabricated (Fig. 7.5) [9]. This package was designed to have two K-connectors for microwave input and output. Two pairs of optical lenses were used to couple light between the fibers and the modulator. Coplanar transmission lines made on quartz are used to electrically connect the K-connectors and the device input/output ports [10].

This package was designed to have the load termination outside of the package, which could have the problem that the long connection line would complicate the design. A new package design needs to move the load as close as possible to the device. Also, a DC block will be preferred so that there is minimum temperature heat up. An easier packaged optical coupling scheme, e.g., using conical shaped lensed fiber, should also be investigated.

7.2.6 New applications

Other than being used as the external encoder for CW or mode-locked laser light, EA modulators can also be used in many other applications. An interesting application is to use the modulator both as a photodetector and as a wavelength converter. When the modulator is operating at saturation, the information-encoded high power optical signal will cause the change of absorption according to the signal waveform. Therefore, a DC signal of another wavelength will see the loss variation corresponding to the patterned signal and hence be modulated. Simultaneously, photocurrent corresponding to the modulation signal is generated and can be used for clock recovery. Optical regeneration for return-to-zero optical signal was demonstrated using these features [11].

It should be noted that the second signal does not necessarily need to be a different wavelength from the information-bearing signal. We can launch them from opposite directions and separate them by an isolator. This therefore makes the modulator an optically controlled switch. The logic it represents is different

from that of semiconductor optical amplifiers. Operating at a saturation state, the SOAs will invert the converted signal.

For the applications utilizing the saturation effect, we need low-saturation power for the modulators. Special design for increasing hole trapping effect will be needed.

7.3 Outlook

Within this decade, the transmission systems are experiencing an explosive growth. The transmission data rate doubles itself every sixteen months. A total capacity of 3 Tbit/s [12] and a single channel data rate of 400 Gbit/s [13] have been demonstrated. In order to efficiently utilize the bandwidth of the optical fiber and the EDFA, dense WDM systems with a single channel data rate of 10 Gbit/s are under commercial development. In the near future, systems with single channel data rates of 40 Gbit/s are likely to happen. Compared to the other types of modulators, EA modulators are most suitable for the high bit rate operations for their low drive voltage, high speed and integratibility with lasers. The future direction outlined in this chapter should allow for better performance. Once the insertion loss and chirp problems are solved, these traveling-wave devices should demonstrate superior performance over other types of modulators and can be the best choice as the transmitter for the future ultra high speed communication systems.

References

[1] K. Satzke, D. Baums, U. Cebulla, H. Haisch, D. Kaiser, E. Lach, E. Kuhn, J. Weber, R. Weinmann, P. Wiedemann, and E. Zielinski, "Ultrahigh-bandwidth (42 GHz) polarisation-independent ridge waveguide electroabsorption modulator based on tensile strained InGaAsP MQW," *Electron. Lett.*, vol. 31, pp. 2030-2, 1995.

[2] F. Devaux, S. Chelles, A. Ougazzaden, A. Mircea, and J. C. Harmand, "Electroabsorption modulators for high-bit-rate optical communications: a comparison of strained InGaAs/InAIAs and InGaAsP/InGaAsP MQW," *Semicond. Sci. Technol.*, vol. 10, pp. 887-901, 1995.

[3] T. Ido, S. Tanaka, M. Suzuki, M. Koizumi, H. Sano, and H. Inoue, "Ultra-high-speed multiple-quantum-well electro-absorption optical modulators with integrated waveguides," *J. Lightwave Technol.*, vol. 14, pp. 2026-34, 1996.

[4] K. K. Loi, X. B. Mei, J. H. Hodiak, C. W. Tu, and W. S. C. Chang, "38 GHz bandwidth 1.3 μm MQW electroabsorption modulators for RF photonic links," *Electron. Lett.*, vol. 34, pp. 1018-1019, 1998.

[5] K. Kawano, M. Kohtoku, M. Ueki, T. Ito, S. Kondoh, Y. Noguchi, and Y. Hasumi, "Polarisation-insensitive travelling-wave electrode electroabsorption (TW-EA) modulator with bandwidth over 50 GHz and driving voltage less than 2 V," *Electron. Lett.*, vol. 33, pp. 1580-1, 1997.

[6] F. Devaux, N. Souli, A. Ougazzaden, F. Huet, and M. Carre, "High-speed tandem of MQW modulators for coded pulse generation with 14-dB fiber-to-fiber gain," *IEEE Photonics Technol. Lett.*, vol. 8, pp. 218-220, 1996.

[7] N. Souli, F. Devaux, A. Ramdane, P. Krauz, A. Ougazzaden, F. Huet, M. Carre, Y. Sorel, J. F. Kerdiles, M. Henry, G. Aubin, E. Jeanney, T. Montallant, J. Moulu, B. Nortier, and J. B. Thomine, "20 Gbit/s high-performance integrated MQW TANDEM modulators and amplifier for soliton generation and coding," *IEEE Photonics Technol. Lett.*, vol. 7, pp. 629-631, 1995.

[8] K. Wakita, K. Yoshino, I. Kotaka, S. Kondo, and Y. Noguchi, "Blue-chirp electroabsorption modulators with very thick quantum wells," *IEEE Photonics Technol. Lett.*, vol. 8, pp. 1169-1171, 1996.

[9] Prototype package, designed by Mike Anzlowar.

[10] Designed and fabricated by Volkan Kaman.

[11] T. Miyazaki, N. Edagawa, M. Suzuki, and S. Yamamoto, "Novel optical-regenerator using electroabsorption modulators," *OSA OFC'99*, San Diego, CA, paper WM53, 1999.

[12] S. Kawanishi, H. Takara, K. Uchiyama, I. Shake, and K. Mori, "3 Tbit/s (160 Gbit/sx19 ch) OTDM/WDM transmission experiment," *OSA OFC'99*, San Diego, CA, Post deadline paper, PD1, 1999.

[13] S. Kawanishi, H. Takara, T. Morioka, O. Kamatani, K. Takiguchi, T. Kitoh, and M. Saruwatari, "400 Gbit/s TDM transmission of 0.98 ps pulses over 40 km employing dispersion slope compensation," *OSA OFC'96*, San Jose, CA, pp. 423-426, 1996.

APPENDIX A

Resonant Scattering Method for QW Level Calculation

This appendix discusses the calculation of quantum well levels under and electric field.

The quantum confined Stark shift can be calculated with variational method [1] only for an extreme case, which is either weak field or strong field. However, the exact values of the energy shift can be numerically calculated under an arbitrary electric field with the resonant scattering theory [2-4].

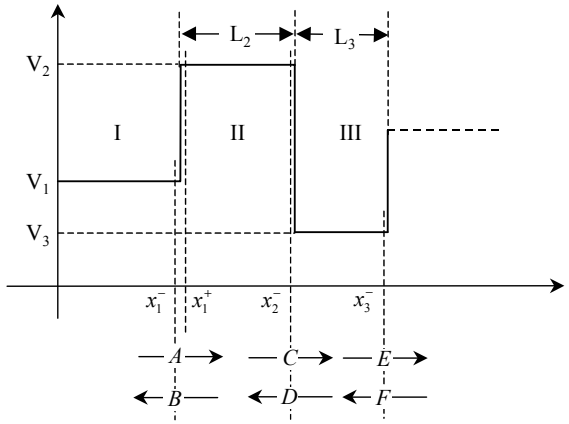

Fig. A.1 Scattering at an arbitrary potential profile. The global propagation matrix can be described as the product of the two potential-step propagation matrices of and a free space propagation matrix.

Following Kroemer's derivation [4], we derive the solutions of the Schroedinger equations that correspond to particles coming from infinity and being scattered by a non-constant potential. The wave functions at the three regions can be expressed as superpositions of plane waves, which may always be written as

$$\psi_1(x) = \frac{1}{\sqrt{k_1}}[A \cdot e^{ik_1(x-x_1^-)} + B \cdot e^{-ik_1(x-x_1^-)}] \tag{A.1a}$$

$$\psi_2(x) = \frac{1}{\sqrt{k_2}}[C \cdot e^{ik_2(x-x_2^-)} + D \cdot e^{-ik_2(x-x_2^-)}] \tag{A.1b}$$

$$\psi_3(x) = \frac{1}{\sqrt{k_3}}[E \cdot e^{ik_3(x-x_3^-)} + F \cdot e^{-ik_3(x-x_3^-)}], \qquad \text{(A.1c)}$$

where k_1, k_2 and k_3 are the local wave numbers at the three constant potential regions.

$$k_j = \sqrt{\frac{2m_j^*}{\hbar^2}(\varepsilon - V_j)}, \qquad \text{(A.2)}$$

where j = 1,2,3, …, ε is the incident energy, m_j^* is the electron effective mass at the jth potential constant region. When $\varepsilon - V_j > 0$, k_j is real and the wave is propagating, while when $\varepsilon - V_j < 0$, k_j becomes imaginary and the wave becomes evanescent.

The propagation matrix $\hat{P}$ is defined as

$$\begin{pmatrix} A \\ B \end{pmatrix} = \begin{pmatrix} P_{11} & P_{12} \\ P_{21} & P_{22} \end{pmatrix} \begin{pmatrix} C \\ D \end{pmatrix} = \hat{P} \begin{pmatrix} C \\ D \end{pmatrix}. \qquad \text{(A.3)}$$

It is not difficult to find out that the propagation matrix for a potential step from region I to region II (Fig. A.1) is

$$\hat{P}_{x_1^- - x_1^+} = \frac{1}{2\sqrt{k_1 k_1}} \begin{pmatrix} k_1 + k_2 & k_1 - k_2 \\ k_1 - k_2 & k_1 + k_2 \end{pmatrix}. \qquad \text{(A.4)}$$

The free space propagation matrix from x_1^+ to x_2^- is

$$\hat{P}_{\Delta 2} = \begin{pmatrix} e^{-ik_2 L_2} & 0 \\ 0 & e^{+ik_2 L_2} \end{pmatrix}. \qquad \text{(A.5)}$$

Therefore the overall propagation matrix from x_1^- to x_2^- is

$$\hat{P}_{x_1^- - x_2^-} = \hat{P}_{x_1^- - x_1^+} \cdot \hat{P}_{\Delta 2}. \qquad \text{(A.6)}$$

Notice that the step-potential propagation matrix (A.4) is valid both for an upward step and a downward step. So we can easily expand (A.6) to multiple potential steps by iteratively multiplying a step-potential propagation matrix and a free-space propagation matrix.

Once the overall propagation matrix has been obtained, the overall transmission probability of the composite potential profile, defined as the ratio of the transmitted current density to the incident current density in the absence of any current incidence from the out-going side, is

$$T = \frac{1}{\left|P_{11}\right|^2}. \tag{A.7}$$

A bound state is found when $P_{11} = 0$ or $T \to \infty$.

References

[1] G. Bastard, E. E. Mendez, L. L. Chang, and L. Esaki, "Variational calculations on a quantum well in an electric field," *Phys. Rev. B.*, vol. 28, no. 6, pp. 3241-3245, 1983.

[2] D. A. B. Miller, D. S. Chemla, T. C. Damen, A. C. Gossard, W. Wiegmann, T. H. Wood, and C. A. Burrus, "Electric field dependence of optical absorption near the band gap of quantum-well structures," *Phys. Rev. B*, vol. 32, no. 2, pp. 1043-1060, 1985.

[3] E. J. Austin and M. Jaros, "Electronic structure of an isolated GaAs-GaAlAs quantum well in a strong electric field," *Phys. Rev. B.,* vol. 31, pp. 5569-5572, 1985.

[4] H. Kroemer, *Quantum Mechanics: For Engineering, Materials Science, and Applied Physics*, Prentice Hall (1994), chapter 5.

APPENDIX B

Polarization Independent InGaAsP/InGaAsP Quantum Well Design

The design of polarization independent InGaAsP/InGaAsP quantum-well grown on (001) InP involves the calculation of bandgap energies of heavy- and light-holes for strained materials. Detail derivation of the bandgap energies in strained quantum wells can be found in reference [1].

For an unstrained bulk material, the heavy-hole (HH) and light-hole (LH) valence bands are degenerated. This two bands split when strain exist. For compressive strained material, the hydrostatic strain component shifts HH and LH bands equally while the shear strain component pushes the HH band up and pulls the LH band down, resulting in a smaller HH bandgap than the LH one. On the contrary, a tensile strain will result in a larger HH bandgap than the LH one.

For a strained material, the strain is defined as

$$\varepsilon \equiv \frac{a_{native} - a_{sub}}{a_{native}}, \tag{B.1}$$

where a_{native} is the native unstrained lattice constant of the strained material and a_{sub} is the lattice constant of the substrate. For compressive strain ε>0 while for tensile strain ε<0.

The hydrostatic deformation potential induced bandgap change is

$$H = (-a) \cdot 2\frac{C_{11} - C_{12}}{C_{11}}\varepsilon, \tag{B.2}$$

where C_{11} and C_{12} are referred to as the elastic stiffness coefficients or the elastic moduli, a is the hydrostatic deformation potential.

The shear strain energy is

$$S = (-b) \cdot 2\frac{C_{11} + 2C_{12}}{C_{11}}\varepsilon, \tag{B.2}$$

where b is the shear deformation energy.

The changes in the HH, LH, and split-off (SO) bandgaps are

$$\begin{aligned} \Delta E_{HH} &= H - S, \\ \Delta E_{LH} &= H + S - \delta, \\ \Delta E_{SO} &= H + \Delta + \delta, \end{aligned} \tag{B.3}$$

where Δ is the spin-orbit energy,

$$\delta = \frac{1}{2}\Delta\{[1 - 2(S/\Delta) + 9(S/\Delta)^2]^{1/2} - (1 - S/\Delta)\}, \tag{B.4}$$

represents additional energy change due to LH-SO band coupling.

Following we only consider properties of $In_{1-x}Ga_xAs_yP_{1-y}$ material on InP.

The lattice constants of quaternaries can be calculated from Vegard's law, which gives a value equal to the weighted average of all of the four possible constituent binaries.

$$a(In_{1-x}Ga_xAs_yP_{1-y}) = xya_{GaAs} + x(1-y)a_{GaP} + (1-x)ya_{InAs} + (1-x)(1-y)a_{InP} \tag{B.5}$$

For lattice-matched material (x~0.47y), E_g can be expressed accurately by Moon's equation as [2]

$$E_g(295K) = 1.35 - 0.755y + 0.149y^2 \text{ eV}. \tag{B.6}$$

In order to calculate lattice-mismatched InGaAsP, a modified Moon's equation is used [3]

$$\begin{aligned} E_g(295K) = {} & 1.35 + 1.09x - y + 0.33x(1-y) - (0.73 - 0.28y)x(1-x) \\ & - (0.101 + 0.109x)y(1-y) + 0.05\sqrt{xy(1-x)(1-y)} \end{aligned}. \tag{B.7}$$

Table B.1 shows the binary parameters that are used in the calculation. The conduction band discontinuity for InGaAsP/InGaAsP/InP quantum well is about 40% of the total bandgap difference [4]. Table B.1 also lists the valance band offset relative to that of AlAs for binary materials. This can also be used to calculate the band offset [5]

$$\begin{aligned} & dEv(In_{1-x}Ga_xAs_yP_{1-y}) = \\ & \quad xydEv_{GaAs} + x(1-y)dEv_{GaP} + (1-x)ydEv_{InAs} + (1-x)(1-y)dEv_{InP} - dEv_{InP} \end{aligned} \tag{B.8}$$

By utilizing Vegard's law, equation (B.1), the elastic moduli, deformation potentials, spin-orbit energy and effective masses for $In_{1-x}Ga_xAs_yP_{1-y}$ can be calculated.

In practice, the room temperature photoluminescence (PL) wavelength of bulk strained quaternary material is a measurable parameter in determining material compositions. The PL energy for bulk material is

$$E_{PL} = E_g + (\Delta HH + \Delta LH)/2 + K_B T/2, \quad \text{for HH and LH close to each other} \tag{B.9}$$

$$E_{PL} = E_g + \min(\Delta HH, \Delta LH) + K_B T/2. \quad \text{for HH and LH far apart} \tag{B.10}$$

Table B.1: Binary material parameters

Material	a_{native} (Å) [1]	Elastic Moduli ($x10^{11}$ dyn/cm^2) C_{11} [1]	C_{12} [1]	Deformation potentials (eV) [1] a	b	Δ (eV) [1]	dE_v (eV) [5]	Effective masses (m_0) [6] m_e	m_{hh}	m_{lh}
AlP	5.4635	13.2	6.3		-0.48					
GaP	5.4512	14.12	6.253	-9.76	0.29	0.10	0.10	0.254	0.67	0.17
AlAs	5.6611	12.02	5.70		0					
GaAs	5.6533	11.88	5.38	-8.68	0.48	0.34	0.34	0.067	0.38	0.09
InP	5.8688	10.22	5.76	-8.0	0.20	0.10	0.10	0.077	0.61	0.12
InAs	6.0584	8.329	4.526	-5.79	0.65	0.371	0.371	0.027	0.34	0.027

References

[1] L. A. Coldren and S. W. Corzine, *"Diode lasers and photonic integrated circuits,"* John Wiley & Sons, Inc., New York, pp. 527-536, 1995.

[2] M. Ilegems, "InP-based lattice-matched heterostructures," in *Properties of lattice-matched and strained Indium Gallium Arsenide*, edited by Pallab Bhattacharya, INSPEC, IEE, p. 19, 1993.

[3] A. Ichii, Y. Tsou, and E. Garmire, "An empirical rule for band offsets between III-V alloy compounds," *J. Appl. Phys.,* vol. 74, pp. 2112-2113, 1993.

[4] S. R. Forrest, P. H. Schmidt, R. B. Wilson, and M. L. Kaplan, "Relationship between the conduction-band discontinuities and band-gap differences of InGaAsP/InP hetero-junctions," *Appl. Phys. Lett.*, vol. 45, pp. 1199-1201, 1984.

[5] J. R. Flemish, H. Shen, K. A. Jones, M. Dutta, and V. S. Ban, "Determination of the composition of strained InGaAsP layers on InP substrates using photoreflectance and double-crystal X-ray diffractometry," *J. Appl. Phys.,* vol. 70, pp. 2152-2155, 1991.

[6] L. A. Coldren and S. W. Corzine, *"Diode lasers and photonic integrated circuits,"* John Wiley & Sons, Inc., New York, p. 12, 1995.

APPENDIX C

Coplanar Waveguide Circuit Elements

This appendix gives the transmission line circuit elements for coplanar waveguides both with and without lower ground plane. These circuit elements include the unit-length capacitance C, the unit-length inductance L, the microwave effective dielectric constant $\varepsilon_{r,eff}$, and the characteristic impedance Z_L. More accurate values can be obtained with LineCalc [1].

C.1 Coplanar waveguide without a lower ground plane (CPW)

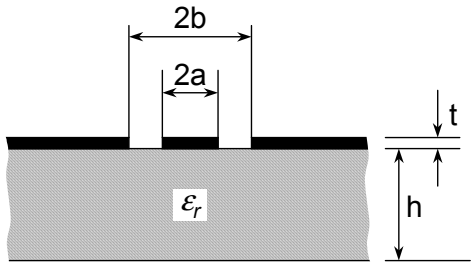

Fig. C.1 Coplanar waveguide without lower ground plane.

For a coplanar waveguide without a lower ground plane (Fig. C.1) the circuit elements are [2, 3]

$$\varepsilon_{r,eff} = 1 + \frac{\varepsilon_r - 1}{2} \frac{K(k')K(k_1)}{K(k)K(k_1')} \tag{C.1}$$

$$Z_L = \frac{30\pi}{\sqrt{\varepsilon_{r,eff}}} \frac{K(k')}{K(k)} \tag{C.2}$$

$$C = \frac{\sqrt{\mu_0 \varepsilon_0 \varepsilon_{r,eff}}}{Z_L} \tag{C.3}$$

$$L = Z_L \sqrt{\mu_0 \varepsilon_0 \varepsilon_{r,eff}} \tag{C.4}$$

Where ε_0 and μ_0 are the permittivity and permeability in vacuum and

$$k = a / b \tag{C.5}$$

$$k' = \sqrt{1 - k^2} \tag{C.6}$$

$$k_1 = \sinh(\pi a / 2h) / \sinh(\pi b / 2h) \tag{C.7}$$

$$k_1' = \sqrt{1 - k_1^2} \tag{C.8}$$

$K(k)$ is the complete elliptical integral of the first order with modulus *k*. It can be approximated as

$$K(k) = (\pi/2)\cdot\left\{1 + 2(k^2/8) + 9(k^2/8)^2 + 50(k^2/8)^3 + 306.250(k^2/8)^4 + ...\right\} \quad \text{(C.9)}$$

for $0 \le k \le 0.71$, and

$$K(k) = p + \{p-1\}(k'^2/4) + 9\{p-7/6\}(k'^4/64) + 25\{p-37/30\}(k'^6/256) + ... \quad \text{(C.10)}$$

$$p = \ln(4/k') = \ln\left(4/\sqrt{1-k^2}\right) \quad \text{(C.11)}$$

for $0.71 < k \le 1$.

These approximation has a maximum error of 0.3% at the crossover point.

C.2 Coplanar waveguide with a lower ground plane (CPWG)

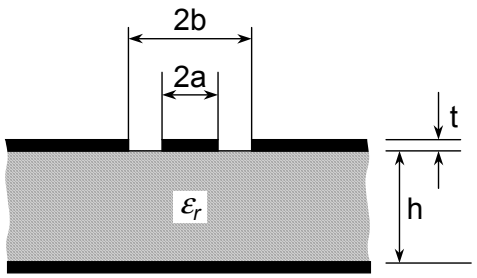

Fig. C.2 Coplanar waveguide with lower ground plane.

For a coplanar waveguide with a lower ground plane (Fig. C.2) the circuit elements are [4]

$$\varepsilon_{r,eff} = \frac{1 + \varepsilon_r \dfrac{K(k')K(k_1)}{K(k)K(k_1')}}{1 + \dfrac{K(k')K(k_1)}{K(k)K(k_1')}} \quad \text{(C.12)}$$

$$Z_L = \frac{60\pi}{\sqrt{\varepsilon_{r,eff}}} \frac{1}{K(k)/K(k') + K(k_1)/K(k_1')} \quad \text{(C.13)}$$

where

$$k = a/b \quad \text{(C.14)}$$

$$k' = \sqrt{1-k^2} \quad \text{(C.15)}$$

$$k_1 = \tanh(\pi a / 2h) / \tanh(\pi b / 2h) \tag{C.16}$$

$$k_1' = \sqrt{1 - k_1^2} \tag{C.17}$$

C.3 Metal thickness correction

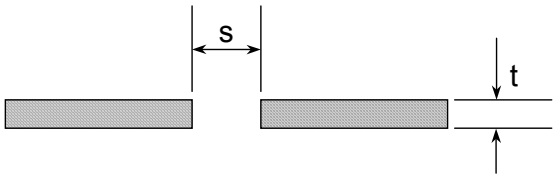

Fig. C.2 Coplanar waveguide with lower ground plane.

The previous circuit elements are derived assuming zero thickness for the conductors. The finite thickness of the conductors will introduce an extra capacitance. The incremental capacitance per unit length is [5]

$$\Delta C(t/s) = \frac{2\varepsilon_r \varepsilon_0}{\pi}\left[\frac{E(k) - (1/2)k'^2\, K(k)}{\sqrt{k}}\right] \tag{C.18}$$

where the parameters k and k' are solved from the following equations as functions of t/s

$$\frac{t}{s} = \frac{(1+k^2)\cdot K(k')/2 - E(k')}{2E(k) - k'^2 \cdot K(k)} \tag{C.19}$$

$$k' = \sqrt{1 - k^2} \tag{C.20}$$

E(k) is the complete elliptical integral of the second kind.

Considering the two ground conductors of the coplanar waveguide, the incremental capacitance per unit length is double of Eq. C.18.

References

[1] LineCalc, distributed by Hewlett Packard Company, Westlake Village, CA, 1996.

[2] G. Ghione and C. Naldi, "Analytical formulas for coplanar lines in hybrid and monolithic MICs," *Electron. Lett.*, vol. 20, pp. 179-181, 1984.

[3] R. K. Hoffmann, *Handbook of Microwave Integrated Circuits*. Boston: Artech House, Inc., pp. 355-356, 1987.

[4] G. Ghione and C. Naldi, "Parameters of coplanar waveguides with lower ground plane," *Electron. Lett.*, vol. 19, pp. 734-5, 1983.

[5] S. B. Cohn, "Thickness corrections for capacitive obstacles and strip conductors," *IRE Transactions on Microwave Theory and Techniques*, vol. 8, pp. 638-644, 1960.

APPENDIX D

Microwave Transmission Matrix Calculation

As discussed in Chapter 3, the TEAM can be considered as composed of a tapered transmission input feed line, an optical waveguide section, and a tapered output feed line. Each section can be modeled as a linear two-port network with a transmission matrix or a scattering matrix. This appendix discusses on how to obtain the voltage distribution on the waveguide section. With the driver and load connected, the two-port representation is shown at the bottom of Fig. D.1.

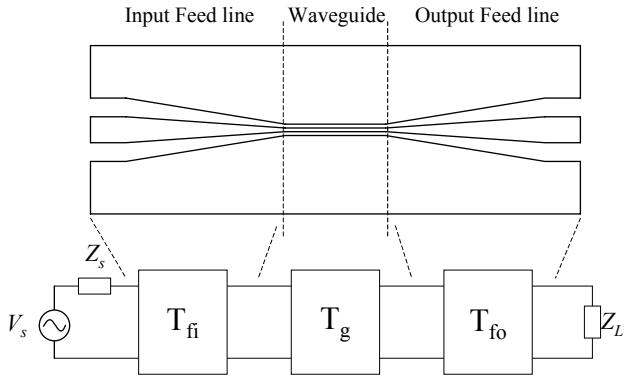

Fig. D.1 Transmission line and linear two-port representation of a TEAM.

When doing the calculation, each feed line section is divided into 50 sections, with each about 10 μm in length. Each small section is considered as a uniform coplanar waveguide and its transmission line properties can readily be calculated as discussed in Appendix C.

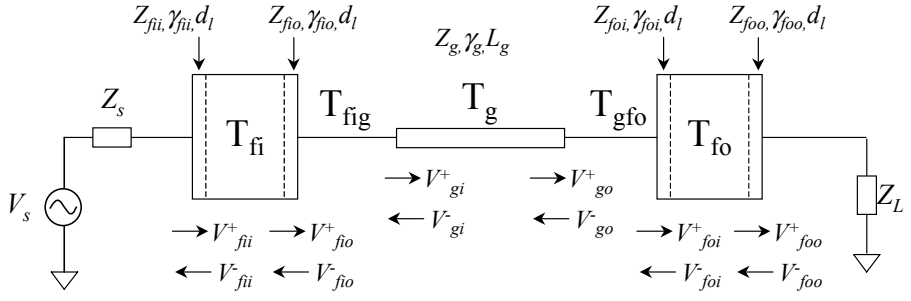

Fig. D.2 Transmission matrices for the calculation of a TEAM connected with source and load.

The overall transmission matrix of the device is a multiplication of five transmission matrices, T_{fi}, for the input feed line, T_{fig}, for the connection from the input feed line to the waveguide, T_g, for the waveguide section, T_{gfo}, for the connection from the waveguide to the output feed line, and T_{fo}, for the output feed line. Here, the subscript *'f'* means for feed line section, *'g'* means for waveguide section, *'i'* means for input, and 'o' means for output.

The tapered feed line matrix is found by calculating 50 cascaded transmission lines. Fig. D.3 shows the case of two cascaded lines. Z, γ, and l are the characteristic impedance, propagation constant and length of the line.

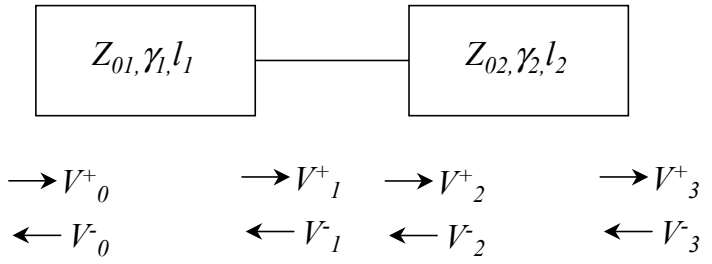

Fig. D.3 Transmission matrix of two cascaded lines.

The transmission matrix for a transmission line is related to its propagation constant, γ_1, and the length of the line, l_1, as

$$\begin{pmatrix} V_0^- \\ V_0^+ \end{pmatrix} = \begin{pmatrix} e^{-\gamma_1 l_1} & 0 \\ 0 & e^{+\gamma_1 l_1} \end{pmatrix} \begin{pmatrix} V_1^- \\ V_1^+ \end{pmatrix}, \tag{D.1}$$

The connection matrix from a transmission line with impedance of Z_{01}, to a transmission line with impedance of Z_{02} is

$$\begin{pmatrix} V_1^- \\ V_1^+ \end{pmatrix} = \begin{pmatrix} \frac{Z_{02}+Z_{01}}{2Z_{02}} & \frac{Z_{02}-Z_{01}}{2Z_{02}} \\ \frac{Z_{02}-Z_{01}}{2Z_{02}} & \frac{Z_{02}+Z_{01}}{2Z_{02}} \end{pmatrix} \begin{pmatrix} V_2^- \\ V_2^+ \end{pmatrix}, \tag{D.2}$$

Transmission matrix for the second transmission line is

$$\begin{pmatrix} V_2^- \\ V_2^+ \end{pmatrix} = \begin{pmatrix} e^{-\gamma_2 l_2} & 0 \\ 0 & e^{+\gamma_2 l_2} \end{pmatrix} \begin{pmatrix} V_3^- \\ V_3^+ \end{pmatrix}, \tag{D.3}$$

We can relate the input wave to the output wave as

$$\begin{pmatrix} V_0^- \\ V_0^+ \end{pmatrix} = \begin{pmatrix} A & B \\ C & D \end{pmatrix} \begin{pmatrix} V_3^- \\ V_3^+ \end{pmatrix} \tag{D.4}$$

where

$$\begin{pmatrix} A & B \\ C & D \end{pmatrix} = \begin{pmatrix} e^{-\gamma_1 l_1} & 0 \\ 0 & e^{+\gamma_1 l_1} \end{pmatrix} \begin{pmatrix} \frac{Z_{02}+Z_{01}}{2Z_{02}} & \frac{Z_{02}-Z_{01}}{2Z_{02}} \\ \frac{Z_{02}-Z_{01}}{2Z_{02}} & \frac{Z_{02}+Z_{01}}{2Z_{02}} \end{pmatrix} \begin{pmatrix} e^{-\gamma_2 l_2} & 0 \\ 0 & e^{+\gamma_2 l_2} \end{pmatrix} \tag{D.5}$$

By repeatedly doing this procedure numerically, we can obtain the transmission matrix of the whole tapered feed line.

Let's assume the output feed line is simply the horizontal flip of the input feed line, and assume the input feed line transmission matrix is

$$T_{fi} = \begin{pmatrix} T_{fi11} & T_{fi12} \\ T_{fi21} & T_{fi22} \end{pmatrix}, \tag{D.6}$$

then we will obtain the output feed line transmission matrix as

$$T_{fo} = \begin{pmatrix} \frac{T_{fi11}}{D} & -\frac{T_{fi12}}{D} \\ -\frac{T_{fi21}}{D} & \frac{T_{fi22}}{D} \end{pmatrix}, \tag{D.7}$$

where

$$D = T_{fi11}T_{fi22} - T_{fi12}T_{fi21}. \tag{D.8}$$

Assuming the last section of the input feed line has impedance of Z_{fio}, then the connection matrix from the input feed line to the waveguide is found as

$$\begin{aligned} \begin{pmatrix} V_{fio}^- \\ V_{fio}^+ \end{pmatrix} &= T_{fig} \begin{pmatrix} V_{gi}^- \\ V_{gi}^+ \end{pmatrix} \\ &= \begin{pmatrix} \frac{Z_g+Z_{fio}}{2Z_g} & \frac{Z_g-Z_{fio}}{2Z_g} \\ \frac{Z_g-Z_{fio}}{2Z_g} & \frac{Z_g+Z_{fio}}{2Z_g} \end{pmatrix} \begin{pmatrix} V_{gi}^- \\ V_{gi}^+ \end{pmatrix} \end{aligned} \tag{D.9}$$

Similarly, the connection matrix from the waveguide to the output feed line is

$$T_{gfo} = \begin{pmatrix} \dfrac{Z_{foi} + Z_g}{2Z_{foi}} & \dfrac{Z_{foi} - Z_g}{2Z_{foi}} \\ \dfrac{Z_{foi} - Z_g}{2Z_{foi}} & \dfrac{Z_{foi} + Z_g}{2Z_{foi}} \end{pmatrix} \tag{D.10}$$

The overall transmission matrix of the device is then found as

$$\begin{pmatrix} V_{fii}^- \\ V_{fii}^+ \end{pmatrix} = T \begin{pmatrix} V_{foo}^- \\ V_{foo}^+ \end{pmatrix} = \begin{pmatrix} T_{11} & T_{12} \\ T_{21} & T_{22} \end{pmatrix} \begin{pmatrix} V_{foo}^- \\ V_{foo}^+ \end{pmatrix} = T_{fi} T_{fig} T_g T_{gfo} T_{fo} \begin{pmatrix} V_{foo}^- \\ V_{foo}^+ \end{pmatrix} \tag{D.11}$$

Fig. D.4 shows the load end of the circuit. The relation between the two waves at the load end is

$$V_{foo}^- = \Gamma_L V_{foo}^+ , \tag{D.12}$$

where

$$\Gamma_L = \frac{Z_L - Z_{foo}}{Z_L + Z_{foo}} , \tag{D.13}$$

is the load reflection coefficient.

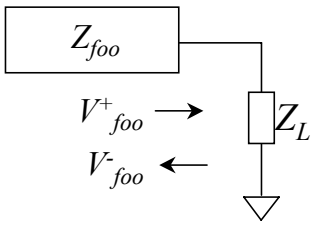

Fig. D.4 Circuit representation of the load end.

Fig. D.5 shows the source end of the circuit. The relation between the two waves at the source end is

$$V_{fii}^+ = \Gamma_s V_{fii}^- + T_s V_s , \tag{D.14}$$

where

$$\Gamma_s = \frac{Z_s - Z_{fii}}{Z_s + Z_{fii}} \tag{D.15}$$

$$T_s = \frac{Z_{fii}}{Z_{fii} + Z_s} \tag{D.16}$$

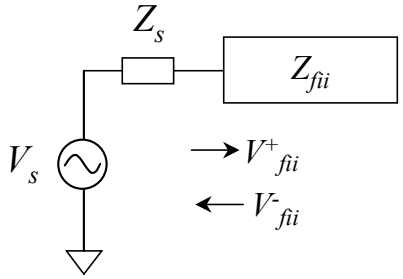

Fig. D.5 Circuit representation of the source end.

With Eqs. D.11-D.16, we can obtain V^+_{foo} as

$$V^+_{foo} = V_s T_s / \left[(T_{21} - T_{11}\Gamma_s)\Gamma_L + T_{22} - T_{12}\Gamma_s \right] \tag{D.17}$$

By plugging D.17 to D.12 and then plugging together with V^-_{foo} to D.11, we can obtain the other voltage values, V^-_{fii} and V^+_{fii}. With these, we can easily obtain the forward and backward wave voltages at the output point of the waveguide.

$$\begin{pmatrix} V^-_{go} \\ V^+_{go} \end{pmatrix} = T_{gfo} T_{fo} \begin{pmatrix} V^-_{foo} \\ V^+_{foo} \end{pmatrix} \tag{D.18}$$

Any wave voltages in the waveguide at a distance of *x* away from the output point of the waveguide is then

$$\begin{pmatrix} V^-_g(x) \\ V^+_g(x) \end{pmatrix} = \begin{pmatrix} e^{-\gamma_g x} & 0 \\ 0 & e^{+\gamma_g x} \end{pmatrix} \begin{pmatrix} V^-_{go} \\ V^+_{go} \end{pmatrix} \tag{D.19}$$

APPENDIX E

Measurement Configurations

This appendix describes the measurement configurations for photocurrent measurement, device mounting, and device testing.

E.1 Photocurrent measurement with a tunable laser

Fig. E.1 shows the photocurrent measurement setup configuration. This setup has been used for measuring photocurrent spectra shown in Figs. 4.4 and 4.5. The wavelength scan is achieved by using a tunable laser diode with a wavelength range of 1480-1570 nm [1]. The laser is internally modulated with a build-in modulation driver for lock-in amplification. The modulation signal is used as the reference signal for the lock-in amplifier. The laser light is focused to the waveguide via a lensed fiber [2]. A DC power supply is used for providing reverse bias voltage, and a 4.7 kΩ resistor is used for sampling the current signal. A computer with LabVIEW [3] controls the tunable laser and the lock-in amplifier for wavelength scanning and data taking.

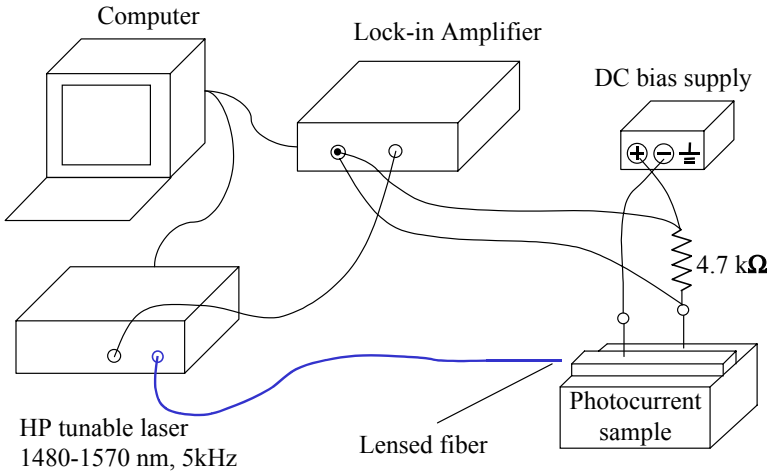

Fig. E.1 Setup for photocurrent measurement with a tunable laser as the light source.

E.2 Photocurrent measurement with a white light source

A photocurrent measurement system slightly different from the one using a tunable laser is shown in Fig. E.2. The advantage of using a tunable laser is that higher optical power is available; however, it limits the wavelength range to 1480 ~ 1570 nm. In order to obtain the information at a wider wavelength range, a halogen white light source combined with a monochromator [4] are used to generate wide-wavelength-range light source. The light is coupled into the waveguide through a lens. Chopper is used to chop the light for lock-in amplification. Prior to the real sample measurement, the lamp spectrum is first recorded and is used for the normalization of the real sample spectra. Fig. 5.4 shows the photocurrent spectra measured with this setup.

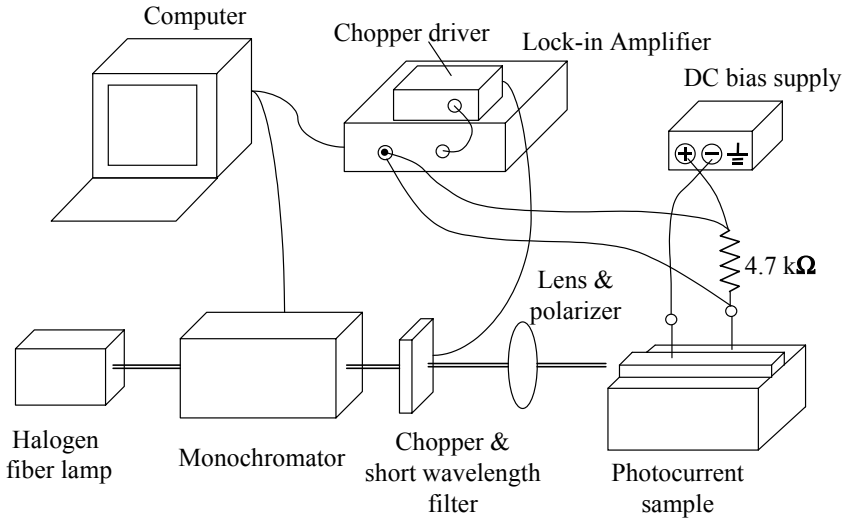

Fig. E.2 setup for wide wavelength range photocurrent measurement.

E.3 Modulator test setup

The traveling-wave EA modulators are first mounted on copper bars before they are put to the alignment and probing system. Fig. E.3 shows a device mounted on a copper bar. For high speed performance, a thin film resistor is also mount on the copper bar and it is connected to the modulator via short gold ribbons. The silver epoxy [5] is used to stick both the modulator and the resistor onto the copper bar.

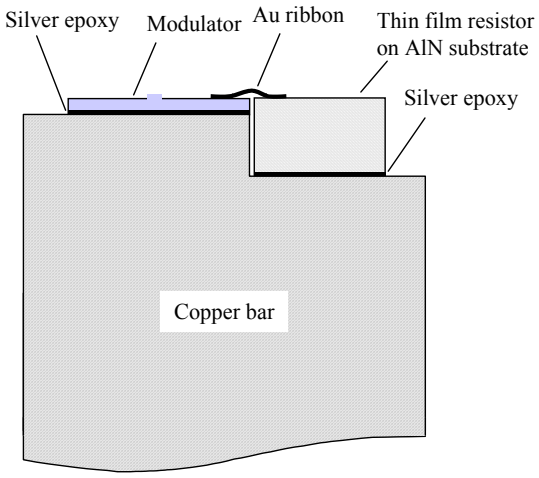

Fig. E. 3 Mounting configuration for a traveling-wave EA modulator ribbon bonded with a thin film resistor.

The device is then place in an alignment setup. Here, a lens pair is used to couple light from fiber to the waveguide and vice versa. The lens pair composes of two lenses, one with a numerical aperture of 0.16 to match to that of the single mode fiber, while the other with a numerical aperture of 0.55. Fig. E.4 shows the schematic of the coupling scheme. The lens pair has a working distance of 2.9 mm. Here the working distance is defined as the distance from the lens front facet at the device-side to the device.

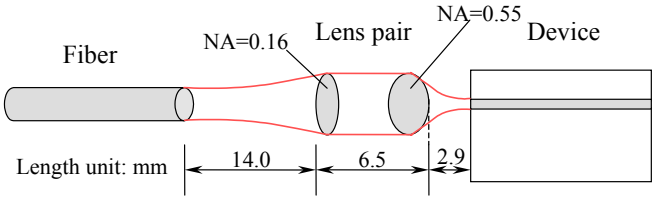

Fig. E.4 Lens pair is used to couple light from fiber to device, and vice versa.

The measurement setup for device characterization is similar to that for the photocurrent measurement (Fig. E.2). For polarization control, an in-line fiber polarization controller [6] is used to translate any polarization state into desired linear polarization [7]. A Cascade probe [8] is used to connect to the input port of the device. In the case of with an off-chip 50 Ω termination, the output port is probed with another Cascade probe, which is terminated with a standard 50 Ω load. High-frequency measurements were performed with an HP Lightwave Component Network Analyzer (HP 8703A), which can measure electrical to electrical,

electrical to optical, optical to electrical, and optical to optical responses from 0.13-20 GHz.

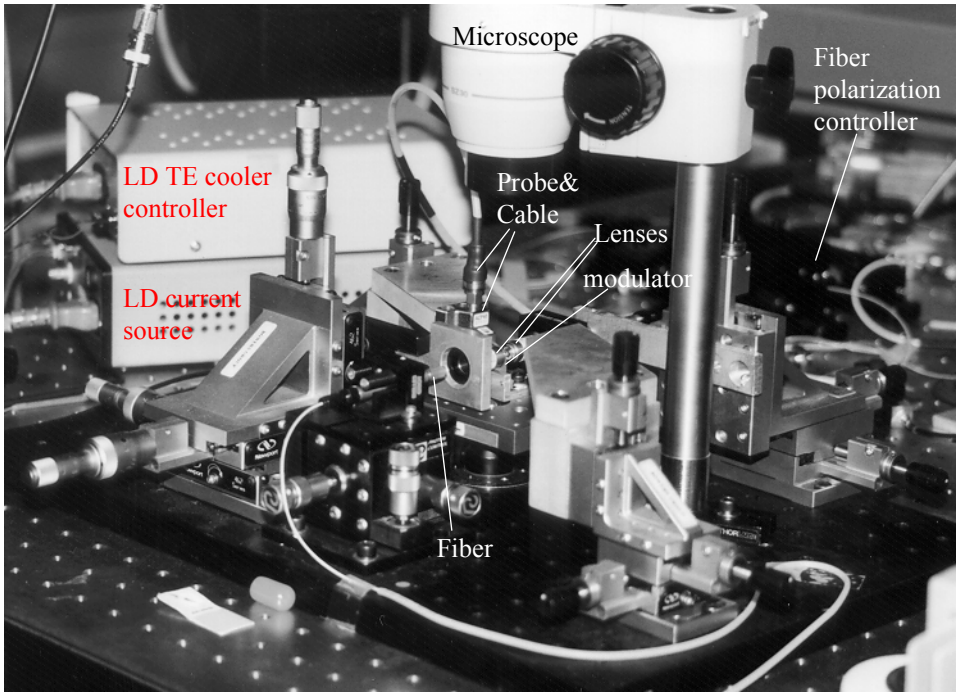

Fig. E.5 Setup for light coupling and microwave probing for TEAMs. Here only one microwave probe is shown.

Fig. E.5 shows the picture of the actual optical coupling and microwave probing setup.

References

[1] Tunable laser, HP 81680, manufactured by Hewlett Packard Company, Palo Alto, CA.

[2] Sphere-tipped lensed fiber, manufactured by KYOCERA, Japan.

[3] LabVIEW 3.1.1, distributed by National Instrument Company, Austin, TX.

[4] Monochromator, manufactured by ORIEL Instruments, Stratford, CT.

[5] Silver epoxy, H20E Part A&B, Epoxy Technology, Billerica, MA.

[6] Fiber polarization controller, manufactured by Thorlabs, Inc., MA.

[7] B. G. Koehler and J. E. Bowers, "In-line single-mode fiber polarization controllers at 1.55, 1.30, and 0.63 mu m," *Applied Optics*, vol. 24, pp. 349-53, 1985.

[8] ACP40-GSG Cascade probe with 100 micron contact pitch, manufactured by Cascade Microtech, Inc., Beaverton, Oregon.

APPENDIX F

Fabrication Process

F.1 General process steps

These general process steps are both used in InGaAs/InAlAs and InGaAsP/ InGaAsP TEAMs.

Solvent clean

1) Soak and spray with ACE, 2 min, use Q-tips for the first cleaning after growth
2) Soak and spray with ISO, 2 min, use Q-tips for the first cleaning after growth
3) Soak and spray with methanol, 2 min, use Q-tips for the first cleaning after growth
4) De-ionized (DI) water rinse and flush, 2 min
5) Nitrogen blow dry
6) Dehydration bake, 20 min at 120^{o}C in oven

AZ 4210 [1] photolithography

1) Spin @ 6 krpm, 40 sec
2) Hot plate soft bake 1 min @ 95^{o}C
3) Edge removal exposure 2'30", @ 7.5 mW/cm^2
4) Edge develop, AZ 400K [2]:DI = 1:3.8, ~ 50"
5) Pattern exposure 12", @ 7.5 mW/cm^2
6) Pattern develop, AZ 400K:DI = 1:3.8, ~ 45"

AZ 4330 [3] photolithography

1) Spin @ 6 krpm, 40 sec
2) Hot plate soft bake 1 min @ 95^{o}C
3) Edge removal exposure 2'30", @ 7.5 mW/cm^2
4) Edge develop, AZ 400K:DI = 1:3.8, ~ 50"
5) Pattern exposure 22", @ 7.5 mW/cm^2
6) Pattern develop, AZ 400K:DI = 1:3.8, ~ 55"

825+4210 double layer photolithography

1) Spin 825 [4] @ 5 krpm, 40 sec
2) Hot plate soft bake 1 min @ 95^{o}C
3) Flood exposure 9 sec, @ 7.5 mW/cm^2
4) Spin AZ4210 @ 5 krpm, 40 sec
5) Hot plate soft bake 1 min @ 95^{o}C
6) Edge removal exposure 2'30", @ 7.5 mW/cm^2

7) Edge develop, AZ 400K:DI = 1:3.8, ~ 50”

8) Pattern exposure 12”, 7.5 mW/cm^2

9) Pattern develop, AZ 400K:DI = 1:3.8, 35 ~ 45 sec

825+825+4210 triple layer photolithography (for final metal lift-off)

1) Spin 825 @ 4.5 krpm, 40 sec

2) Hot plate soft bake 1’30” @ 95^{o}C

3) Spin 825 @ 4.5 krpm, 40 sec

4) Hot plate soft bake 1’30” @ 95^{o}C

5) Flood exposure 7 sec, @ 7.5 mW/cm^2

6) Spin AZ4210 @ 5 krpm, 40 sec

7) Hot plate soft bake 1’30” @ 95^{o}C

8) Edge removal exposure 2’30”, @ 7.5 mW/cm^2

9) Edge develop, AZ 400K:DI = 1:3.8, ~ 50”

10) Pattern exposure 14”, @ 7.5 mW/cm^2

11) Pattern develop, AZ 400K:DI = 1:3.8, about 50” develop plus 10” overdevelop

O_2 plasma descum

PEIIA oxygen plasma etch for 10~20 sec, 300 mTorr, 100 W, low frequency

Double layer PMGI SF15 [5] spin-on

1) Spin @ 6 krpm, 50 sec

2) Oven cure @ 300^{o}C, 3 min, in large petri dish

3) Spin @ 5 krpm, 50 sec

4) Oven cure @ 300^{o}C, 3 min, in large petri dish

The as spun PMGI will be about 4.2 μm.

PMGI wet etch

1) Deep UV expose @ 1000 W, for 5 min

2) Straight SAL 101 [6] develop for 2 min

3) Repeat 1) and 2) until PMGI fully developed

Photo resist and PMGI removal

Method I

1) 1165 [7] boiled @ 80^{o}C for 10 min

2) DI water rinse and flush for 5 min

3) Nitrogen blow dry

Method II

1) Straight AZ400K soak for 2 min

2) DI water rinse and flush for 2 min

3) Nitrogen blow dry

F.2 Process steps for MBE grown InGaAs/InAlAs TEAMs

Wafer cleaving

Cleave wafer to about 11x11 mm per piece; write down the orientation of each piece, the ridge should lie at $(0\bar{1}\bar{1})$ orientation, which will reveal an inverse triangular-shaped ridge with anisotropy wet etching solutions.

p-contact formation – first mask

1) Solvent clean with Q-tip rub
2) 825+4210 double layer photolithography, align ridge at $(0\bar{1}\bar{1})$ orientation
3) O_2 plasma descum for 15 sec
4) Surface clean: HCl:DI = 1:1 dip for 30 sec
5) Thermal evaporation, Cr/Au/Zn/Au = 5/5/19/400 nm
6) E-beam evaporation, Ti/SiO_2 = 20/650 nm
7) Metal lift off in ACE with VERY WEAK ultra-sonic stir if necessary, followed by ISO, Methanol, DI rinse
8) O_2 plasma descum for 30 sec
9) Dektak metal thickness

Ridge etching

1) Dry etch in RIE, Cl_2/Ar = 7.5/4 sccm, 3 mTorr, 500 V/88W, pump pressure < 1×10^{-6} Torr before introducing gases; laser monitored; need calibration etch first. Fig. 4.11 shows the etching stop position.
2) Buffered HP dip for ~ 10 sec to remove residual SiO_2 and Ti.

n-contact formation – second mask

1) Solvent clean and dehydration baking
2) 825+4210 double layer photolithography
3) O_2 descum 15 sec
4) Surface clean: HCl:DI = 1:1 dip for 30 sec
5) E-beam evaporation Ni/AuGe/Ni/Au = 5/100/10/400 nm, or Ni/Ge/Au/Ni/Au = 5/17/30/20/400 nm,
6) Metal lift off in ACE with VERY WEAK ultra-sonic stir if necessary, followed by ISO, Methanol, DI rinse
7) O_2 plasma descum for 30 sec

Mesa etching – third mask

1) AZ4330 photolithography for mesa etching
2) O_2 descum 15 sec
3) Deep UV flood exposure for 5 min to harden photo resist surface
4) Dry etch in RIE, Cl_2/Ar = 7.5/4 sccm, 3 mTorr, 500 V/88W, pump pressure < 1×10^{-6} Torr before introducing gases; laser monitored; until etch through all epilayers.
5) Concentrated AZ400K developer dip for 2 min, DI rinse, nitrogen blow dry
6) O_2 descum 30 sec

Contact annealing

RTA, forming gas 3000 sccm, thermal coupler control

Step	Time (sec)	Temperature (^{o}C)
1	120	0
2	10	410
3	15	410
4	1	0
5	120	0

PMGI spin-on and edge removal

1) Dektak ridge and mesa height
2) Double layer PMGI SF15 spin-on
3) Spin on AZ 4210 @ 5.5 krpm, 40 sec
4) Hot plate soft bake 1'30" @ 95^{o}C
5) Edge removal exposure 2'30", @ 7.5 mW/cm^2
6) Edge develop, AZ400K:DI = 1:3.8, ~ 50"
7) O_2 descum 10 sec
8) Deep UV flood exposure for 5 min
9) Straight SAL 101 develop for 2 min
10) Repeat 8) and 9) for twice
11) Scratch away residual PMGI at edges using razor blade under microscope
12) Repeat 8) and 9) until edges fully cleaned
13) Strip off photo resist with ACE spray, followed by ISO, Methanol and DI rinse

PMGI bridge & planarization processing – fourth mask

1) Dektak ridge, mesa and edge PMGI height
2) Calculate PMGI thickness on top of ridge based on two Dektak measurement data, as shown in the bottom figure, the PMGI thickness on top of ridge is $h_4 = h_2+h_3-h_1$. Etch cycles = h_4/3.0 μm×14.0. As a rule of thumb, the number of cycles to etch away AZ4330 (3 μm thick) is about 14.

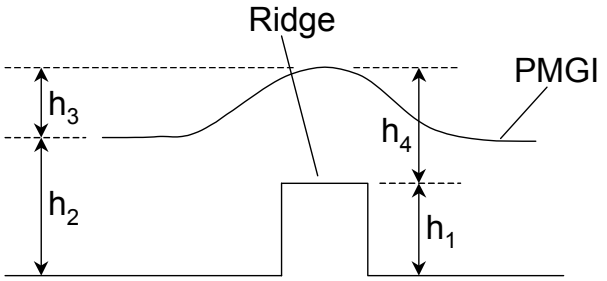

3) AZ4330 photolithography for PMGI bridge

4) RIE PMGI etch, O_2 = 7.5 sccm, 10 mTorr, 200 V/22W, pump pressure <~ 1×10^{-6} Torr before introducing gas; laser monitored; until reach desired cycles.

5) Inspect under microscope and Dektak ridge height. If ridges are not fully exposed, use PEIIA O_2 plasma to slightly etch PMGI at 300 mTorr, 50 W, low frequency. Repeat until ridges fully exposed.

6) Strip off photo resist with ACE spray followed with ISO, Methanol and DI spray

7) Dehydration bake at 120^{o}C in oven for 20 min

PMGI feed line region etch back – fifth mask

1) AZ4210 photolithography for PMGI etch back

2) O_2 descum 15 sec

3) Deep UV flood exposure for 5 min

4) Straight SAL 101 develop for 2 min

5) Repeat 3) and 4) until the PMGI at feed line region be fully developed

6) O_2 descum 2 min

7) Strip off photo resist with ACE spray, followed by ISO, Methanol and DI rinse

8) O_2 descum 15 sec

9) PMGI re-flow @ 300 ^{o}C in oven with large petri dish for ~ 1'30", inspect under microscope

Final metalization – sixth mask

1) 825+825+4210 triple layer photolithography for final metalization lift-off

2) O_2 descum 20 sec

3) HCl:DI = 1:1 dip for 30" followed by DI rinse

4) E-beam evaporation. Lower sample holder to reduce the distance from sample to source unit flat region to 18.5 cm. This will gives a ratio of about 3.0 of actual thickness compared to the monitor display. Rotation on for better coverage. Ti/Au = 28/700 nm (monitor display thickness), wait 10 min for cool down at 230 and 460 nm.

5) Lift-off with ACE followed by ISO, Methanol and DI rinse. Use VERY WEAK ultra sonic if needed.

6) Dehydration bake at 120^{o}C in oven for 20 min

Cleaving line etch – seventh mask

1) AZ4330 photolithography for cleaving line etch mask
2) O_2 descum 20 sec
3) Hard bake for 30 min at 120^{o}C in oven
3) Technic Strip Gold etchant etch for about 1'30" to etch away cleaving lines. **Cyanide, lethal when mixed with acid. AVOID ANY ACID, USE SPECIAL HOOD**. Rinse thoroughly with DI water.
4) Buffered HF etch for ~ 10" to etch away Ti
5) Deep UV flood exposure for 5 min
6) Straight SAL 101 develop for 2 min
7) Repeat 5) and 6) until the PMGI on top of the cleaving line region is fully developed

Lapping, cleaving, and testing

Lap down to ~70 μm
Cleave devices
Mount onto copper bars for testing

F.3 Process steps for MOCVD grown InGaAsP/InGaAsP TEAMs

Wafer cleaving

Same as MBE sample processing

p-contact formation – first mask

1) Solvent clean with Q-tip rub
2) 825+4210 double layer photolithography, align ridge at $(0\bar{1}\bar{1})$ orientation
3) O_2 plasma descum for 15 sec
4) Surface clean: HCl:DI = 1:1 dip for 30 sec
5) E-beam evaporation, Ti/Pt/Au/Si = 20/50/500/200 nm
7) Metal lift off in ACE with VERY WEAK ultra-sonic stir if necessary, followed by ISO, Methanol, DI rinse
8) O_2 plasma descum for 30 sec

Ridge formation

1) Dry etch in RIE,

Step	Gases	Flow rates (sccm)	Pressure (mTorr)	Voltage (V)	Etch time	Comment
1	O_2	20	125	500	30 min	Clean chamber
2	MHA	4/20/10	75	500	10 min	Pre-coat
3	MHA	4/20/10	75	500	~31 min	Etch
4	O_2	20	125	200	10 min	Polymer etch

MHA=CH_4/H_2/Ar, laser monitor; need calibration etch first. Fig. 5.5 shows the etching stop position. Polymer etch time ≅ etch time/3.

2) RIE CF_4/O_2 = 25/2 sccm, 35 mTorr, 300 V, 7 minutes to etch away residual Si mask
3) Dektak ridge height
4) H_3PO_4:HCl = 3:1 etch for 2~3 minutes to smooth side wall and to etch to the n-contact and etch stop layer. Use SEM to check with the side wall. Etch rate ~ 0.9 μm/min on (001) InP at room temperature, stops at InGaAsP, straight side wall on $(0\bar{1}\bar{1})$ oriented ridges.

n-contact formation – second mask

Same as MBE sample n-contact formation

Mesa etching – third mask

1) AZ4330 photolithography for mesa etching
2) O_2 descum 15 sec
3) Hard bake at 120°C in oven for 30 minutes
4) Dektak ridge height
5) H_3PO_4:HCl=3:1, 15 sec, room temperature to clean away residual InP on surface
6) H_3PO_4:H_2O_2:H_2O = 1:1:30, 2 min to break through InGaAsP layer and stop at InP
7) Dektak
8) H_3PO_4:HCl=3:1, ~15 sec to etch InP, this will etch away about 0.2 μm InP
9) Dektak ridge height
10) Repeat 8), 9) until etch through the layer and into substrate for ~ 0.2 μm
11) Strip off photo resist with ACE
12) O_2 descum 30 sec

Contact annealing

Same as MBE sample contact annealing

Contact testing

Use curve tracer to test the current-voltage characteristic of the test feature on mask

PMGI spin-on and edge removal

Same as MBE PMGI spin-on and edge removal

PMGI bridge & planarization processing – fourth mask

Same as MBE sample PMGI bridge & planarization processing

PMGI feed line region etch back – fifth mask

Same as MBE sample PMGI feed line region etch back

Final metalization – sixth mask

Same as MBE sample final metalization

Cleaving line etch – seventh mask

For the 2nd mask design, use the same method as MBE sample to make cleaving lines
For the 3rd mask design, the final metalization is designed to open at cleaving lines, in this case, following these steps
1) AZ4330 photolithography for PMGI cleaving line etch mask
2) O_2 descum 20 sec
3) Deep UV flood exposure for 5 min
4) Straight SAL 101 develop for 2 min
5) Repeat 3) and 4) until the PMGI on top of the cleaving line region is fully developed
6) Strip off ACE with ACE

Lapping, cleaving, and testing

Lap down to ~70 μm
Cleave devices
Mount on to copper bar for testing

References

[1] AZ P4210, distributed by Clariant Corporation, Somerville, NJ.

[2] AZ400K developer, distributed by Clariant Corporation, Somerville, NJ.

[3] AZ P4330, manufactured by Hoechst Celanese Corporation, Somervile, NJ.

[4] OCG825, manufactured by Olin Corporation, CT.

[5] PMGI SF15, manufactured by Micro Chem Corp., Newton, MA.

[6] Microposit SAL-101, manufactured by Shipley, Marlborough, MA.

[7] Microposit 1165 remover, manufactured by Shipley, Marlborough, MA.